

Copyright
by
Margaret Katherine Meadows
2016

**The Dissertation Committee for Margaret Katherine Meadows Certifies that this is
the approved version of the following dissertation:**

**Applications of Reversible Covalent Bonding Within the Context of
Spin Trapping, Boronate Ester Formation, Conjugate Addition of
Amines and Thiols, and the Synthesis of Natural Product Analogues**

Committee:

Eric V. Anslyn, Supervisor

Jonathan L. Sessler

Adrian Keatinge-Clay

Michael J. Rose

David W. Hoffman

**Applications of Reversible Covalent Bonding Within the Context of
Spin Trapping, Boronate Ester Formation, Conjugate Addition of
Amines and Thiols, and the Synthesis of Natural Product Analogues**

by

Margaret Katherine Meadows, B.S.

Dissertation

Presented to the Faculty of the Graduate School of

The University of Texas at Austin

in Partial Fulfillment

of the Requirements

for the Degree of

Doctor of Philosophy

The University of Texas at Austin

December 2016

Dedication

To my grandfathers, who are not here to see this but whom I will always love. You taught me so much – from card games to life lessons – and I cannot thank you enough. I love you and I miss you.

Acknowledgements

To Eric Anslyn: A huge thank you. You took me in when I needed a new lab, even though at the time I thought I wanted to be a synthetic chemist. You have since completely converted me to being a supramolecular chemist. You have been supportive and understanding and given me the chance to grow as a scientist and a teacher. You have helped me through projects that didn't work and celebrated victories with me. And you apparently wrote some really nice things in my recommendation letter. Eric, you have been the best advisor I could have hoped for, thank you.

To Brian Goess, Paul Wagenknecht, Greg Springsteen, TJ Banisaukas, Lon Knight, and the rest of the Furman Chemistry Department: Thank you for all your support and encouragement. You put up with grading my horrible handwriting and stayed long past your office hours to help me through practice problems. You taught me so much and have continued supporting me long past when I was your student. I'll see you at the next happy hour. FU all the time!

To Brette Chapin, Amber Johnson, and Rogelio Escamilla: Thank you for proofreading my chapters and not making fun of me when I clearly wrote them on too much caffeine and too little sleep. You have been my sanity checks so many times.

To Mr. and Mrs. Eicher and Mr. Newton: Thank you for being great teachers and giving me a love chemistry.

To the Anslyn group: You welcomed me in and have been great friends. Katharine, Alex, John, Brette, Amber, Baylie, and all the boys I will miss you SOOO much. (EAST SIDE!) There are so many other group members that I cannot list them all, but everyone has always made me feel like I am part of something special. Emma and

Stephanie, you have been great undergraduates and I have enjoyed working with you so much. Best of luck to you both.

To Tim Mack: You know you're my best friend but thank you for always picking up the phone when I call and making me laugh. You've been invaluable.

Krista, Darin, and Hillary: I know we're not (officially) family yet but you have welcomed me in whole-heartedly and I love you very much. Thank you for all your love and support.

Mom and Daddy: Thank you thank you thank you. I really don't have the words but I'll try. You have been so supportive of me ever since I was a stubborn little girl. You never had any doubt that I could do anything I put my mind to. You treated my getting this degree as inevitable and that faith has meant everything. You have encouraged me when I have called you crying and done your best to help me get through this even though you couldn't always be here in person. I know you have missed me while I've been in Texas but you never tried to stop me when I moved out here because you knew it was the right thing for me. You have been the best parents I could have ever asked for and I love you so much.

Austin: You have become my best friend, my partner, and my rock. You have comforted me and encouraged me and made me smile when all I wanted to do was cry. I am so happy to be marrying you and I love our family so much. I never thought I would find someone who would love our dogs more than I do, but I'm lucky enough to have found you. I'm so happy that you are moving with me to Chicago and I cannot wait to start our next adventure. I love you.

Tari and Lucy: My cuddle bugs, you make me so happy and I love you. You are so cute and right now you are both cuddled up next to me on the couch snoring. You are also such messes – aaand you just jumped off the couch to greet Austin and knocked over

my laundry and turned off the tv in the process. That perfectly sums up your effect on my life. You never fail to make me laugh. This is my equivalent of a bone parade just for you.

Applications of Reversible Covalent Bonding Within the Context of Spin Trapping, Boronate Ester Formation, Conjugate Addition of Amines and Thiols, and the Synthesis of Natural Product Analogues

Margaret Katherine Meadows, Ph.D.

The University of Texas at Austin, 2016

Supervisor: Eric V. Anslyn

Reversible covalent bonding is an essential chemical tool that incorporates the strength of covalent bonds and the dynamism of intermolecular interactions. This type of bonding has found applications across fields of chemistry, including sensing of small molecules, screening against target for the design of host/guest systems, and enzyme inhibition. Herein are discussed examples of reversible covalent bonding.

A three-component assembly incorporating 2-formylphenyl boronic acid, *N*-alkylhydroxylamine, and catechol was synthesized with the intention of acting as a reversible spin trap for nitric oxide detection. This assembly was further studied as a potential bioorthogonal method for specific chemical modification of amino acids within a peptide or protein. This system is amenable to a variety of substrates, including L-DOPA, a catechol-containing amino acid, which can readily be incorporated into proteins. This assembly is also compatible with existing bioorthogonal reactions, allowing for multiple labeling reactions to be conducted simultaneously.

The ability to reversibly crosslink two substrates under mild conditions has the potential for wide application. Our group has previously developed a conjugate acceptor,

derived from Meldrum's acid, that sequentially crosslinks an amine and a thiol under aqueous conditions at neutral pH. This crosslinking can be decoupled with a chemical trigger to regenerate the original species. We have since expanded this system to include the addition of aniline derivatives. We have further optimized this conjugate acceptor and studied the pK_a 's and reaction rates of the decoupling using different substrates.

The natural product piperlongumine has been found to induce apoptosis in cancer cells with little effect on normal cells and is thought to act through increasing the level of reactive oxygen species (ROS). This increase in ROS is proposed to occur through the reversible addition of glutathione into the more reactive Michael acceptor, followed by the addition of a glutathione-binding protein to the second Michael acceptor. We have synthesized piperlongumine using a route that can be easily modified to access derivatives with various substituents in order to study the potency of analogs and to test the proposed mechanism.

Table of Contents

List of Schemes.....	xiv
List of Figures.....	xvii
List of Tables.....	xxv
Chapter 1: An Overview of Reversible Covalent Bonding	1
1.1 Introduction.....	1
1.2 Applications of Reversible Covalent Bonding	2
1.2.1 Sensors.....	2
1.2.2 Dynamic combinatorial chemistry.....	4
1.2.3. Self-healing polymers	5
1.2.4 Molecular motors.....	6
1.2.5 Reversible enzyme inhibition	7
1.3 Reversible Covalent Bonding in this Dissertation.....	8
1.4 References.....	9
Chapter 2: Synthesis and Testing of a Spin Trap for Nitric Oxide Detection by Electron Paramagnetic Resonance Spectroscopy	11
2.1 Introduction.....	11
2.1.1 Reactive Oxygen Species and Nitric Oxide.....	11
2.1.2 NO Sensing.....	13
2.1.3 Electron Paramagnetic Resonance.....	16
2.1.4 Spin Trapping.....	19
2.2 Boronate Ester Spin Trap Synthesis and Reactivity	21
2.2.1 James/Bull Assembly and Synthesis of Spin Traps for NO Detection	21
2.2.2 NO Generation and EPR Spectroscopy	22
2.2.3 Absorbance Fine Structure.....	26
2.3 Conclusions.....	27
2.4 Experimental.....	28
2.4.1 Synthesis of spin traps 2.3 and 2.5.....	28

2.4.2 NO generation	29
2.4.3 NO cylinder.....	30
2.4.4 EPR	30
2.4.5 Absorbance	30
2.5 Acknowledgements.....	31
2.6 References.....	31
Chapter 3: Studies of a Semi-Bioorthogonal Labeling Method Using a Hydroxylamine Boronate Ester Assembly.....	
3.1 Introduction.....	34
3.1.1 Bioorthogonal labeling.....	34
3.1.2 Boronic acids and diol binding	38
3.1.2.1 Tony James’s amine and hydroxylamine assemblies	39
3.2 Application of Boronate Ester Assemblies to a Bioorthogonal Platform.....	41
3.2.1 Transition to aqueous conditions	41
3.2.2 <i>N</i> -alkylhydroxylamines and <i>O</i> -alkylhydroxylamines	42
3.2.3 Reversibility studies.....	43
3.2.4 Mechanistic insight	45
3.2.5 ¹¹ B-NMR studies “trapping” the amine complex	46
3.2.6 Substrate scope.....	50
3.2.6.1 Complex formation in the presence of saccharides	51
3.3 Bioorthogonality Studies	52
3.3.1 Orthogonality to common biological functional groups	52
3.3.2 Orthogonality to other bioorthogonal reactions.....	53
3.3.3 Peptide labeling.....	54
3.3.4 Protein labeling studies	59
3.4 Conclusion	61
3.5 Experimentals	61
3.5.1 General procedures for synthesis of compounds	61
3.5.2 Exchange studies.....	66
3.5.3 Mechanistic Studies	67

3.5.4 ^{11}B -NMR studies.....	67
3.5.5 Stability to other functional groups.....	67
3.5.6 Stability to current bioorthogonal reactions.....	68
3.5.7 Peptide synthesis.....	69
3.5.8 Fluorophore synthesis.....	70
3.5.9 Protein labeling.....	72
3.6 Acknowledgements.....	72
3.7 References.....	72
Chapter 4: Kinetic and Mechanistic Studies of a Reversible Conjugate Acceptor	74
4.1 Introduction.....	74
4.1.1 Click and de-click chemistry.....	74
4.1.2 Addition to α,β -unsaturated carbonyls.....	75
4.1.3 Previous studies with 4.3.....	78
4.2 Attempts to Improve Upon 4.3.....	79
4.2.1 Other alkylations of carbon disulfide.....	79
4.2.2 Addition to 4.3 of other types of amines.....	81
4.2.3 Synthesis of aniline-4.3 derivatives and exchange with NAC....	82
4.3 pK_a Determination of Aniline Derivatives.....	84
4.3.1 pH titrations.....	84
4.3.2 Linear Free Energy Relationships.....	91
4.4 Studies into the DTT-Mediated Decoupling Mechanism.....	94
4.4.1 Structural determination by ^1H -NMR.....	94
4.4.2 Pseudo-first order kinetics experiments.....	96
4.4.3 KinTek analysis of kinetics.....	99
4.4.4 pH and kinetics.....	117
4.5 Conclusion.....	124
4.6 Experimental.....	125
4.7 Acknowledgements.....	128
4.8 References.....	128

Chapter 5: Synthesis of Piperlongumine and Analogs for Cellular Testing.....	130
5.1 Introduction.....	130
5.1.1 Piperlongumine Discovery and Anticancer Activity	130
5.1.2 Reactive Oxygen Species and Cancer.....	131
5.1.3 Glutathione and the Suspected Mechanism of Action for Piperlongumine	132
5.1.4 Probing the Mechanism of Action through Synthetic Analogs	134
5.1.5 Prior Syntheses of Piperlongumine.....	134
5.2 Synthesis of Piperlongumine and Analogs	135
5.3 Conclusion	138
5.4 Experimental	138
5.4.1 General Procedures	138
5.4.2 Synthetic Procedures.....	139
5.5 Acknowledgements.....	144
5.6 References.....	144
Appendix.....	145
A.1 Crystallographic Data	145
A.2 References.....	158
References.....	159

List of Schemes

Scheme 1.1. Common reversible covalent bonds.	2
Scheme 1.2. Shinkai and James's sensor for saccharides.	4
Scheme 1.3. Disulfide bond network in a polymeric structure. ¹²	6
Scheme 1.4. A "walking" molecule utilizing reversible covalent bonds. ¹³	7
Scheme 2.1. Structure of DAF-FM and its product with NO.	14
Scheme 2.2. Lippard's probe binding NO and releasing dansyl amide to fluoresce.	15
Scheme 2.3. Reaction of NO with NO₅₅₀ causing a fluorescence turn on.	15
Scheme 2.4. James <i>et al.</i> 's hydroxylamine/boronate ester assembly.	21
Scheme 2.5. Proposed binding of NO by 2.3	22
Scheme 2.6. Synthesis of spin trap 2.3	22
Scheme 2.7. Possible hydrogen abstraction causing decay of the EPR signal.	26
Scheme 2.8. Proposed binding of NO ₂ radical to spin trap 2.3	27
Scheme 2.9. Two possibilities of the evolution of NO ₂ from NO.	27
Scheme 3.1. James <i>et al.</i> 's amine assembly.....	40
Scheme 3.2. James's hydroxylamine assembly.	40
Scheme 3.3. Proposed hydroxylamine exchange.....	44
Scheme 3.4. Proposed diol exchange.....	45
Scheme 3.5. Delayed addition of catechol provides only 3.2	45
Scheme 3.6. When catechol is one of the initially added reagents, 3.3 is formed.	46
Scheme 3.7. Complex equilibria of the three component amine assembly in water.	47
Scheme 3.8. Prior incubation with saccharides still leads to formation of 3.2	52
Scheme 3.9. Formation of 3.3 in the presence of common biological functional groups.....	53

Scheme 3.10. Formation of 3.3 and 3.13 in the same reaction vessel.	54
Scheme 3.11. Formation of 3.3 and 3.14 in the same reaction vessel.	54
Scheme 3.12. Assembly formation with peptide 3.15	55
Scheme 3.13. Schematic of proposed FRET interaction.	55
Scheme 3.14. Attempted synthesis of 3.20	56
Scheme 3.15. Synthetic route to 3.24	57
Scheme 3.16. Attempted synthesis of 3.26	57
Scheme 3.17. Proposed synthesis of 3.27	58
Scheme 3.18. Proposed synthesis of 3.28 and structure of 3.29	58
Scheme 3.19. Proposed synthesis of 3.30	59
Scheme 3.20. Proposed synthesis of 3.31	60
Scheme 3.21. Proposed synthesis of 3.32	61
Scheme 3.22. Synthesis of 3.33	70
Scheme 3.23. Synthesis of 3.34	71
Scheme 4.1. Complex equilibrium of dithiane scrambling.....	76
Scheme 4.2. Synthesis of 4.1-4.3	77
Scheme 4.3. Addition of one primary alkylamine followed by a thiol into 4.3	78
Scheme 4.4. Equilibration of multiple thiols added into conjugate acceptor 4.3 . .	78
Scheme 4.5. DTT decoupling.	79
Scheme 4.6. Thiol equilibration.....	80
Scheme 4.7. Synthesis of 4.4	80
Scheme 4.8. Attempted alkylation with <i>p</i> -chloronitrobenzene.....	81
Scheme 4.9. Addition of secondary amines into 4.3	81
Scheme 4.10. Addition of aniline and thiols into 4.3	82
Scheme 4.11. Deprotonation of aniline- 4.3 adduct.....	84

Scheme 4.12. Reference reaction for Hammett plots.	92
Scheme 4.13. Proposed decoupling mechanism upon addition of DTT to 4.6 . First, DTT addition occurs, followed by elimination of methane thiolate (4.15). The second thiol of DTT then adds to the β -position, precipitating elimination of the aniline. This seven-membered ring (4.16) then rearranges to give a more stable five-membered ring (4.17).	95
Scheme 4.14. Mechanistic model used for KinTek studies.	100
Scheme 4.15. More in depth mechanism of AnCA decoupling.	114
Scheme 4.16. Expanded mechanism for processes covered by k_1 (observed).....	115
Scheme 4.17. Expanded mechanism for processes covered by k_2 (observed).....	116
Scheme 4.18. Expanded mechanism for processes covered by k_3 (observed).....	117
Scheme 4.19. Complex equilibria of DTT decoupling mechanism.	118
Scheme 4.20. DTT, An, and methanethiol species present in solution.	119
Scheme 5.1. Glutathione (5.1) is in equilibrium with oxidized glutathione (5.2). Only reduced glutathione can act as a cofactor to modify substrates “R” (5.3).	133
Scheme 5.2. Boll et al.’s synthesis of piperlongumine.	135
Scheme 5.3. Synthesis of the α,β -unsaturated lactam.	136
Scheme 5.4. Coupling of 5.11 and 5.10 to provide piperlongumine.	137
Scheme 5.5. Synthesis of 5.13 and 5.15	137
Scheme 5.6. Synthesis of 5.17 and 5.19	138

List of Figures

Figure 1.1. Trigonal and tetrahedral boronic acid and boronate ester structures.....	3
Figure 1.2. (a) Formation of foldamers through a DCL, (b) self-assembly to form a micelle by a DCL, (c) DCL formation into potential hosts and, upon introduction of a target, binding of a guest, (d) DCL formation into potential guests, one of which is bound upon introduction of a host. ⁹	5
Figure 1.3. Shape recovery and self-healing of reversible covalent polymers. ¹²	6
Figure 1.4. (a) noncovalent enzyme inhibition, (b) irreversible covalent enzyme inhibition, (c) reversible covalent enzyme inhibition. ¹⁴	8
Figure 2.1. A selection of fluorescent sensors for ROS. ³	11
Figure 2.2. Schematic of NO production and reactivity. ⁷	13
Figure 2.3. Splitting of electron spin states according to the Zeeman effect. ¹²	17
Figure 2.4. (a) the absorption of energy from CW-EPR, (b) the first derivative of absorbance. ¹¹	18
Figure 2.5. Simulated EPR spectrum of a nitroxide radical (shown). ¹⁵	19
Figure 2.6. Commercially available spin traps <i>N</i> -tert-butyl- α -phenyl nitron (PBN), 5,5-dimethyl-pyrroline <i>N</i> -oxide (DMPO), and nitrosobenzene.	19
Figure 2.7. An example of an iron dithiocarbamate bound to NO.	20
Figure 2.8. Nitronyl nitroxide spin trap reaction with NO and the resulting change in splitting of the EPR spectrum. ¹⁷	20
Figure 2.9. Simulated and actual EPR spectra of 2.3 after bubbling with gas produced from NaNO ₂ and H ₂ SO ₄	23
Figure 2.10. Noise generated by EPR.	24
Figure 2.11. EPR signal generated from NO cylinder.	24

Figure 2.12. EPR signal generated after bubbling NO through NaOH solution....	25
Figure 2.13. Structure of spin trap 2.5	25
Figure 2.14. Absorbance of spin trap 2.3 and NO in ethanol.	26
Figure 2.15. Absorbance spectra of (a) <i>tert</i> -butyl nitrite and (b) <i>n</i> -butyl nitrite in ethanol.....	27
Figure 2.16. NO production setup.....	30
Figure 2.17. Absorbance spectra showing the fine structure from alkyl nitrite formation.....	31
Figure 3.1. Bioorthogonal selectivity. ⁴	34
Figure 3.2. Fluorescently stained endothelial cells showing the nuclei(blue), actin filaments (red), and microtubules(green). ⁶	35
Figure 3.3. Bioorthogonal reactions. <i>From top</i> : CuAAC, SPAAC, Staudinger ligation, and ketone/aminoether condensation.....	36
Figure 3.4. Incorporation of unnatural functional groups <i>via</i> direct modification, enzymatic incorporation, or RNA protein synthesis.....	37
Figure 3.5. Incorporation of unnatural metabolites into cells.....	37
Figure 3.6. Uses of dual labeling. ⁴	38
Figure 3.7. Geometries of boron.	39
Figure 3.8. Boronic acid-based sensor for diols that exhibits a fluorescence turn-on upon binding.	39
Figure 3.9. The different ¹ H-NMR shift of two enantiomers upon binding to James's assembly.....	41
Figure 3.10. Side-by-side comparison of James's hydroxylamine assembly and a solvent inserted analogue.....	42

Figure 3.11. <i>N</i> -functionalized hydroxylamines (left) and <i>O</i> -functionalized hydroxylamines (right).....	43
Figure 3.12. Absorbance change of 3.1 in water at basic pH over time. Time=0 is red and time=48 hours is purple. The released catechol is believed to cause the increase in absorbance.	44
Figure 3.13. ¹ H-NMR of 2-FPBA with increasing amounts of BnNH ₂ (<i>from bottom to top</i>). The penultimate spectrum is the addition of catechol and the final spectrum is addition of <i>t</i> -BuNHOH.	48
Figure 3.14. ¹¹ B-NMR of 2-FPBA with increasing amounts of BnNH ₂ (<i>from bottom to top</i>). The penultimate spectrum is the addition of catechol and the final spectrum is addition of <i>t</i> BuNHOH.	49
Figure 3.15. (<i>from bottom</i>) ¹ H-NMR of 3.2 , 3.3 , and 1:1 3.2:3.3	50
Figure 3.16. Complexes with a variety of catechol derivatives that were synthesized.	51
Figure 3.17. Assemblies formed with other diols.	51
Figure 3.18. Corresponding ¹ H-NMR spectra of species in Scheme 3.9. (<i>from bottom</i>) spectrum of 3.3 , spectrum of the reagents in Scheme 3.9 prior to addition of 2-FPBA, reaction in Scheme 3.9 after addition of 2-FPBA.	53
Figure 3.19. Visualization of the gel showing non-specific binding of the fluorophore to DOPA-DHFR and DHFR. (<i>from left</i>) 2-FPBA:NHOH:DOPA-DHFR in 1:1:1, 2:2:1, 3:3:1, 5:5:1, 5:5:DHFR, 5:0:1, 0:5:1, and 5:5:1 with glucose.	60
Figure 4.1. Schematic of a sacrificial unit used for coupling and decoupling. ⁷	75
Figure 4.2. Dynamic equilibrium of mono-activated conjugate acceptors.	77
Figure 4.3. Intramolecular hydrogen bond in the conjugate acceptor system.	82

Figure 4.4. Aniline derivatives synthesized and tested for thiol exchange.....	83
Figure 4.5. Carbonyl aniline derivatives of 4.3	83
Figure 4.6. pH titration of 4.6 . Red indicates lowest pH's (0.65), purple indicates highest (13.52). Calculated $pK_a = 6.02$	85
Figure 4.7. Absorbance change at 260 nm for pH titration of 4.6 . Gives a pK_a value of 5.93.....	85
Figure 4.8 Absorbance change at 320 nm for pH titration of 4.6 . Gives a pK_a value of 6.10.....	86
Figure 4.9. pH titration of 4.7 . Red indicates lowest pH's (2.41), purple indicates highest (12.7). Calculated $pK_a = 6.51$	86
Figure 4.10. pH titration of 4.8 . Red indicates lowest pH's (0.87), purple indicates highest (11.64). Calculated $pK_a = 6.54$	87
Figure 4.11. pH titration of 4.9 . Red indicates lowest pH's (0.68), purple indicates highest (10.51). Calculated $pK_a = 5.56$	87
Figure 4.12 pH titration of 4.10 . Red indicates lowest pH's (1.21), purple indicates highest (11.11). Calculated $pK_a = 4.34$	88
Figure 4.13. pH titration of 4.13 . Red indicates lowest pH's (0.85), purple indicates highest (11.33). Calculated $pK_a = 4.54$	88
Figure 4.14. pH titration of 4.12 . Red indicates lowest pH's (1.66), purple indicates highest (11.11).	89
Figure 4.15. Absorbance change at 370 nm for pH titration of 4.12	89
Figure 4.16. Absorbance change at 260 nm for pH titration of 4.12	90
Figure 4.17. Absorbance change at 260 nm for pH titration of 4.12	90
Figure 4.18. Hammett plot with all pK_a 's included.	93
Figure 4.19. Hammett plot without 4.8 and 4.12	94

Figure 4.20. LCMS of 4.12 two hours after DTT addition.....	96
Figure 4.21. ¹ H-NMR of 4.3 combined with DTT. (<i>from bottom</i>): 5 min after addition, 3 hr after addition showing both 4.15 and 4.17 , 48 hrs after addition showing 4.17	96
Figure 4.22. Change in absorbance over time for 4.7 upon addition of DTT.....	98
Figure 4.23. Change in absorbance over time for 4.8 upon addition of DTT.....	98
Figure 4.24. Change in absorbance over time for 4.12 upon addition of DTT.....	99
Figure 4.25. Change in absorbance over time for 4.13 upon addition of DTT.....	99
Figure 4.26. (a) 4.6 with 1 mM DTT before subtraction and (b) truncated and subtracted data used for kinetics work. Each shows spectra over 2400 min with t = 0 as red and t = 2400 as purple.....	101
Figure 4.27. Absorbance spectra of 4.6 with 2 mM DTT over 2400 min with t = 0 as red and t = 2400 as purple.....	102
Figure 4.28. Absorbance spectra of 4.6 with 5 mM DTT over 2400 min with t = 0 as red and t = 2400 as purple.....	102
Figure 4.29. Absorbance spectra of 4.6 with 10 mM DTT over 2400 min with t = 0 as red and t = 2400 as purple.....	103
Figure 4.30. Eigenvectors for 4.6 with 1 mM DTT. The significance values for each vector are 22.25 (pink), 2.43 (green), 0.056 (purple), 0.023 (orange), and 0.010 (blue). Vectors are fitted in order of their significance values.	104
Figure 4.31. Concentration of each component over time for 4.6 with 1 mM DTT. Red is AnCA , green is AnCADTT , blue is An , yellow is I , and cyan is CADTT	104

Figure 4.32. Concentration of each component over time for **4.6** with 10 mM DTT.
 Red is **AnCA**, green is **AnCADTT**, blue is **An**, yellow is **I**, and cyan is **CADTT**.....105

Figure 4.33. Simulated spectra of each component. Red is **AnCA**, green is **AnCADTT**, blue is **An**, yellow is **I**, and cyan is **CADTT**.....105

Figure 4.34. Reconstructed absorbance spectra for **4.6** with 1 mM DTT.....106

Figure 4.35. Residual absorbance not accounted for in the reconstructed spectra in Figure 4.34.106

Figure 4.36. Simulated concentrations of each compound with 1 mM showing that the reaction is still mostly reactants. Red is **AnCA**, green is **AnCADTT**, blue is **An**, yellow is **I**, and cyan is **CADTT**.....107

Figure 4.37. Calculated concentrations of each compound with 10 mM. Red is **AnCA**, green is **AnCADTT**, blue is **An**, yellow is **I**, and cyan is **CADTT**.....108

Figure 4.38. Simulated absorbance for each component from the addition of 5 mM of DTT with **4.10**. Red is **AnCA**, green is **AnCADTT**, blue is **An**, yellow is **I**, and cyan is **CADTT**.108

Figure 4.39. Residual absorbance spectra for **4.10** with 5 mM DTT.....109

Figure 4.40. Eigenvectors for the reaction of **4.10** with 10 mM of DTT.....109

Figure 4.41. Calculated concentrations of each species for the reaction of **4.8** with 1 mM DTT. Red is **AnCA**, green is **AnCADTT**, blue is **An**, yellow is **I**, and cyan is **CADTT**.....110

Figure 4.42. Calculated concentrations of each species for the reaction of **4.8** with 10 mM DTT. Red is **AnCA**, green is **AnCADTT**, blue is **An**, yellow is **I**, and cyan is **CADTT**.....110

Figure 4.43. Simulated absorbance for each component from the addition of 5 mM of DTT with 4.8 . Red is AnCA , green is AnCADTT , blue is An , yellow is I , and cyan is CADTT .	111
Figure 4.44. Hammett plot for k_1 values.	112
Figure 4.45. Hammett plot for k_2 values.	112
Figure 4.46. Hammett plot for k_3 values.	113
Figure 4.47. Absorbance spectra of 4.7 (100 μ M) with 20 eq of DTT in pH 3.61 citrate buffer.	119
Figure 4.48. Absorbance spectra of 4.7 (100 μ M) with 20 eq of DTT in pH 4.56 acetate buffer.	120
Figure 4.49. Absorbance change of 4.7 with DTT at pH 5.50. $t = 0$ is red, $t = 50$ hrs is purple.	121
Figure 4.50. Absorbance change of 4.7 with DTT at pH 5.50.	121
Figure 4.51. Absorbance change of 4.7 with DTT at pH 6.25. $t = 0$ is red, $t = 50$ hrs is purple.	122
Figure 4.52. Absorbance change of 4.7 with DTT at pH 6.25.	122
Figure 4.53. Absorbance change of 4.7 with DTT at pH 7.12. $t = 0$ is red, $t = 50$ hrs is purple.	123
Figure 4.54. Absorbance change of 4.7 with DTT at pH 7.12.	123
Figure 4.55. Absorbance change of 4.7 with DTT at pH 8.37. $t = 0$ is red, $t = 50$ hrs is purple.	124
Figure 4.56. Absorbance change of 4.7 with DTT at pH 8.37.	124
Figure 5.1. Piperlongumine (piplartine).	130
Figure 5.2. Mouse melanoma model.	131
Figure 5.3. Piperlongumine tested in normal and tumor cells.	131

Figure 5.4. The two Michael acceptor's in piperlongumine. The red is proposed to react before the blue.....134

List of Tables

Table 3.1. Reduction conditions tried with 3.19	56
Table 4.1. pKa's of the aniline-conjugate acceptor series.	91
Table 4.2. Hammett values, pKa, and log(K _X /K _H) used for Hammett plots.....	93
Table 4.3. Rate constants calculated from KinTek analysis.	111
Table A1. Crystal data and structure refinement for 3.3	146
Table A2. Atomic coordinates (x 10 ⁴) and equivalent isotropic displacement parameters (Å ² x 10 ³) for 3.3 . U(eq) is defined as one third of the trace of the orthogonalized U ^{ij} tensor.....	147
Table A3. Bond lengths [Å] and angles [°] for 3.3	148
Table A4. Anisotropic displacement parameters (Å ² x 10 ³) for 3.3	152
Table A5. Hydrogen coordinates (x 10 ⁴) and isotropic displacement parameters (Å ² x 10 ³).....	154
Table A6. Torsion angles [°] for 3.3	156

Chapter 1: An Overview of Reversible Covalent Bonding¹

1.1 INTRODUCTION

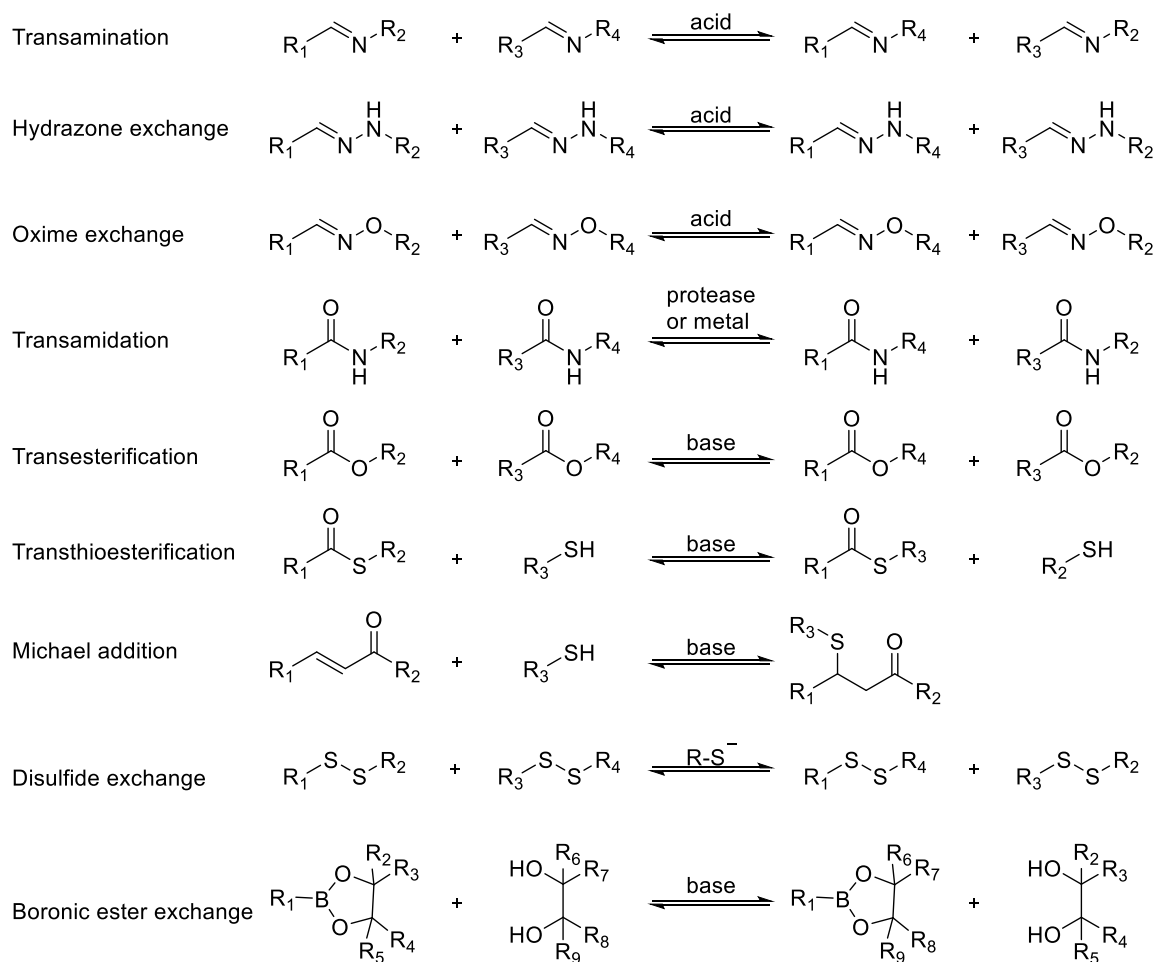
In introductory chemistry, students are taught that there are two types of bonding: covalent and ionic. In more advanced classes, students are introduced to non-covalent interactions, which include hydrogen bonding, van der Waals forces, dipole-dipole interactions, and the mechanical bond.¹ Covalent bonding is often the purview of more traditional disciplines such as synthesis,^{2,3} whereas intermolecular interactions tend to be the specialty of supramolecular chemists.⁴ Covalent bonding is appealing due to the strength of the interaction; intermolecular forces are appealing in their reversibility. Between these two forces lies the reversible covalent bond.

Ideally, reversible covalent bonding combines the strength of the covalent bond with the dynamism of intermolecular forces.⁵ Traditionally, organic synthesis uses irreversible covalent bonds to generate products and the irreversibility of these bonds implies that products are often formed under kinetic control. In contrast, reversible covalent bonds give products based on thermodynamic control; here the products are those that are the most thermodynamically stable rather than the ones that are formed from the lowest energy transition states. This thermodynamic control offers the opportunity to select the most stable products, or the most stable receptor-substrate adducts.

Reversible covalent bonding also has advantages over intermolecular forces. Covalent interactions are more discriminating than most non-covalent interactions, a greater specificity that derives from reactions between specific functional groups. Receptors that use covalent interactions instead of non-covalent interactions often have a greater change in geometry upon

¹ This chapter in part adapted from section 2.4 in Diehl, K. L.; Bachman, J. L.; Chapin, B. M.; Edupuganti, R.; Escamilla, P. R.; Gade, A. M.; Hernandez, E. T.; Jo, H. H.; Johnson, A. M.; Kolesnichenko, I. V.; Lim, J.; Lin, C.-Y.; Meadows, M. K.; Seifert, H. M.; Zamora-Olivares, D.; Anslyn, E. V. Design and Synthesis of Synthetic Receptors for Biomolecule Recognition. In *Synthetic Receptors for Biomolecules: Design Principles and Applications*; Smith B., Ed.; Royal Society of Chemistry: London, UK, 2015; 39-85. Section 2.4 was written by Margaret K. Meadows.

binding a substrate, such as a change from an sp^2 to an sp^3 center. This structural change can be used to incorporate a signaling mechanism into sensor design, often by conjugation of the receptor to a chromophore or fluorophore. Common reversible covalent bonds are shown in Scheme 1.1.



Scheme 1.1. Common reversible covalent bonds.

1.2 APPLICATIONS OF REVERSIBLE COVALENT BONDING

1.2.1 Sensors

Reversible covalent bonding has become widely known in the field of saccharide sensing by taking advantage of boronate ester formation. Boronic acids readily form reversible covalent bonds with various nucleophiles and Lewis bases, and are able to switch from three ligands to

four due to boron's unique electronics. (Figure 1.1) Boronic acids were first used as receptors by Lorand and Edwards in 1959 to study the binding of saccharides.⁶ It was not until the early 1990s that boronic acids were further utilized in sensor design. Since then, these versatile functional groups have been used to bind diols, α -aminoacids, aminoalcohols, α -hydroxyl acids, fluoride, and cyanide.⁷

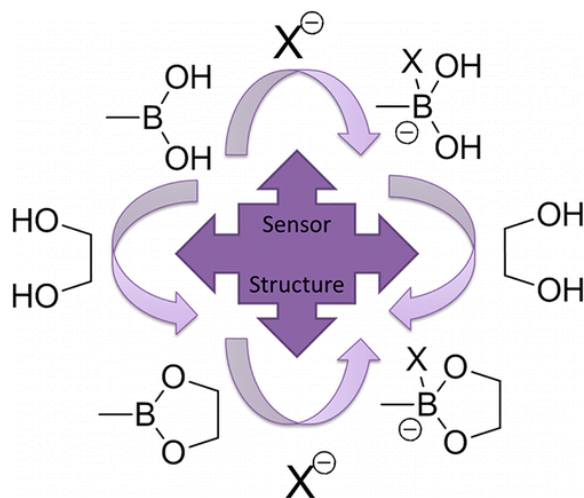
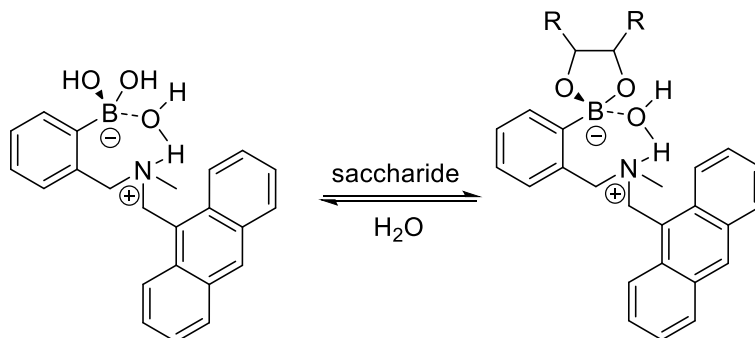


Figure 1.1. Trigonal and tetrahedral boronic acid and boronate ester structures.

The most widely studied application of boronate ester formation is in the sensing of glucose and fructose.⁷ These sensing schemes are based on work by Shinkai and James⁸ and use variation on their original scaffold using *ortho*-aminomethyl phenylboronic acids with anthracene as a signaling molecule. (Scheme 1.2) This motif uses the reversible covalent bonding between boron and diols in order to reversibly measure saccharide concentrations.



Scheme 1.2. Shinkai and James's sensor for saccharides.

1.2.2 Dynamic combinatorial chemistry

Perhaps the fastest growing field making use of reversible covalent bonds is that of dynamic combinatorial chemistry.^{9,10} Dynamic combinatorial chemistry (DCC) uses libraries of molecules that can reversibly bond to each other under a complex series of equilibria. These libraries can be used for a variety of applications, including templation for host-guest chemistry, synthesis of macrocycles, and sensor optimization.⁵

A dynamic combinatorial library (DCL) on its own forms a mixture of monomers, dimers, trimers, and cyclic and linear oligomers, all of which are under equilibration. Changing the conditions of the reaction mixture can induce more complex structures such as folding or micelle formation. (Figure 1.2a and 1.2b) Alternatively, introduction of a target can induce templation of the library against the target. (Figure 1.2c and 1.2d) This approach takes advantage of the reversibility of the system and allows the library to come to a new equilibrium, where the product can be further studied and is already a good host (or guest) for the target by the very nature of its synthesis.

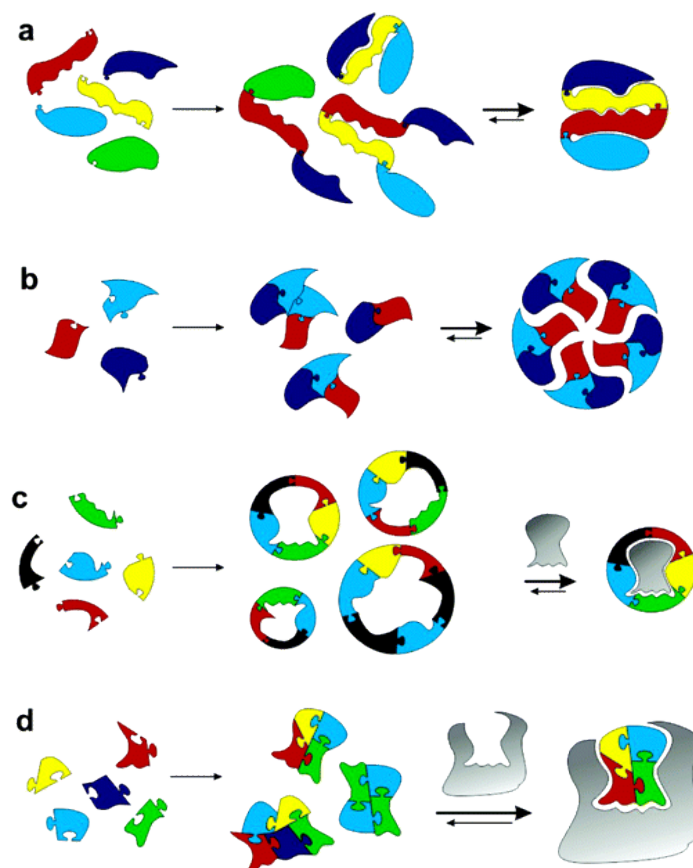


Figure 1.2. (a) Formation of foldamers through a DCL, (b) self-assembly to form a micelle by a DCL, (c) DCL formation into potential hosts and, upon introduction of a target, binding of a guest, (d) DCL formation into potential guests, one of which is bound upon introduction of a host.⁹

1.2.3. Self-healing polymers

Reversible covalent bonds have recently been employed in the synthesis of self-healing polymers.¹¹ Self-healing polymers are polymers that are able to reconnect after being torn or scratched. (Figure 1.3) This self-healing is really the reconnection of covalent bonds through the network of the polymer; since the bonds used to form the polymer are readily reversible, they are also able to reform without re-synthesizing the original material. Disulfide bonds are often used in this application. (Scheme 1.3)

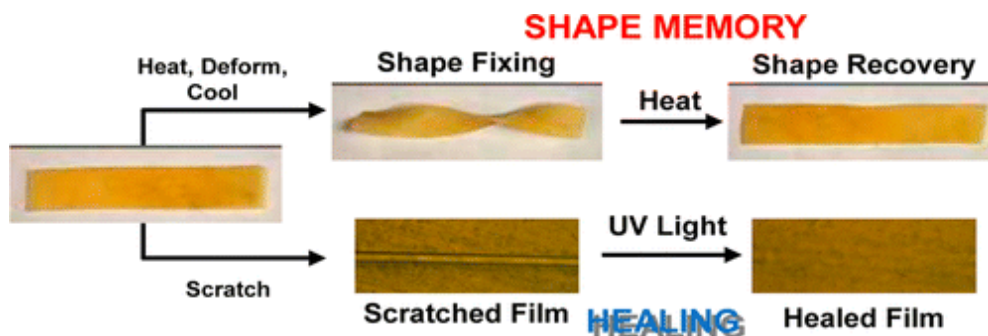
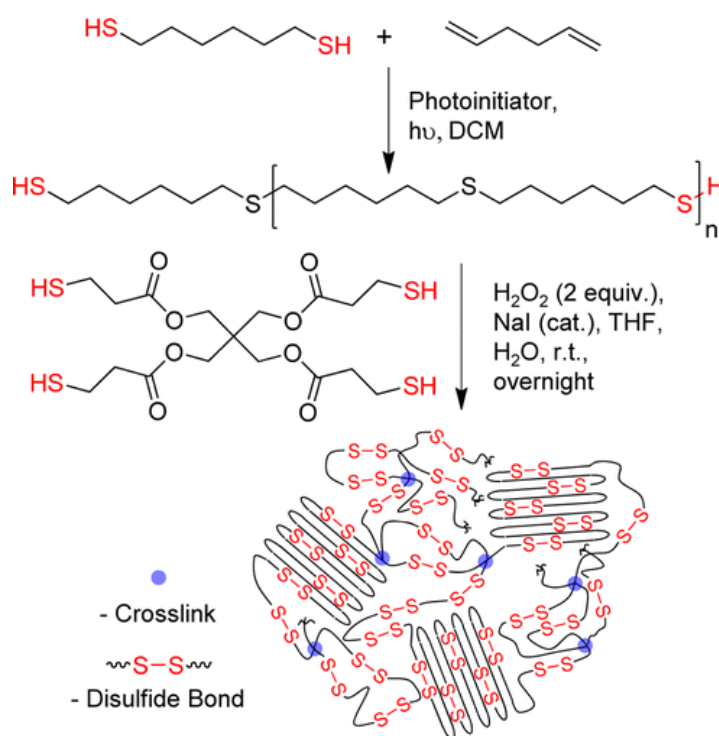


Figure 1.3. Shape recovery and self-healing of reversible covalent polymers.¹²

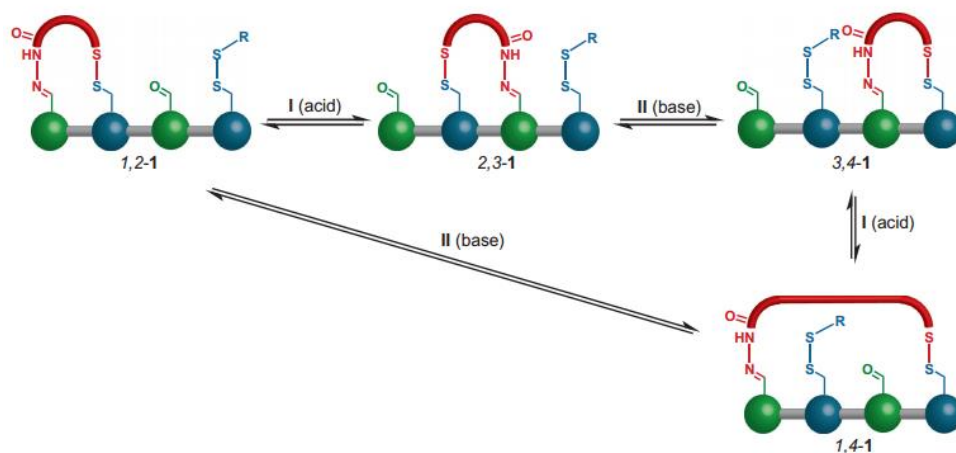


Scheme 1.3. Disulfide bond network in a polymeric structure.¹²

1.2.4 Molecular motors

Reversible covalent bonds have also been applied to the field of molecular motors.¹³ David Leigh published a system where, using disulfide bonds and hydrazone formation, a bipodal linker is able to “walk” along a chain. (Scheme 1.4) Acidic conditions make the hydrazone labile and allows it to switch from position 1 to position 3. A change in pH to basic conditions halts the reversibility of the hydrazone but allows the disulfide to reversibly move

from position 2 to position 4 along the linear polymer. Thus, through the use of controllable, reversible covalent bonds, Leigh was able to produce a “walking” molecule.



Scheme 1.4. A “walking” molecule utilizing reversible covalent bonds.¹³

1.2.5 Reversible enzyme inhibition

In the design and synthesis of pharmaceuticals, reversible inhibitors have many advantages over more traditional enzymatic inhibitors.¹⁴ Reversible inhibitors can dramatically reduce the off-target effects of the drug while still retaining the pharmacological activity of covalent modification. (Figure 1.4) Irreversible inhibitors bind through strong covalent bonds which prevents the enzymatic target from any further activity; however, these same irreversible inhibitors can also bind to non-targeted enzymes (*i.e.* off-target binding). This off-target inhibition can have toxic side effects and limit the possible dosages of the drug. Noncovalent inhibitors avoid this off-target covalent modification, but, as they do not covalently modify the target, are generally less effective inhibitors. Reversible covalent inhibitors occupy the space between these two more traditional types of inhibition. They can covalently react with the target of interest, increasing their potency compared to noncovalent inhibitors; however, if the inhibitor reacts with a non-targeted species, the covalent modification is reversible, so the toxicity of the inhibitor is lowered compared to irreversible inhibitors. These reversible covalent inhibitors have been gaining interest as a compromise between the more traditional methods.

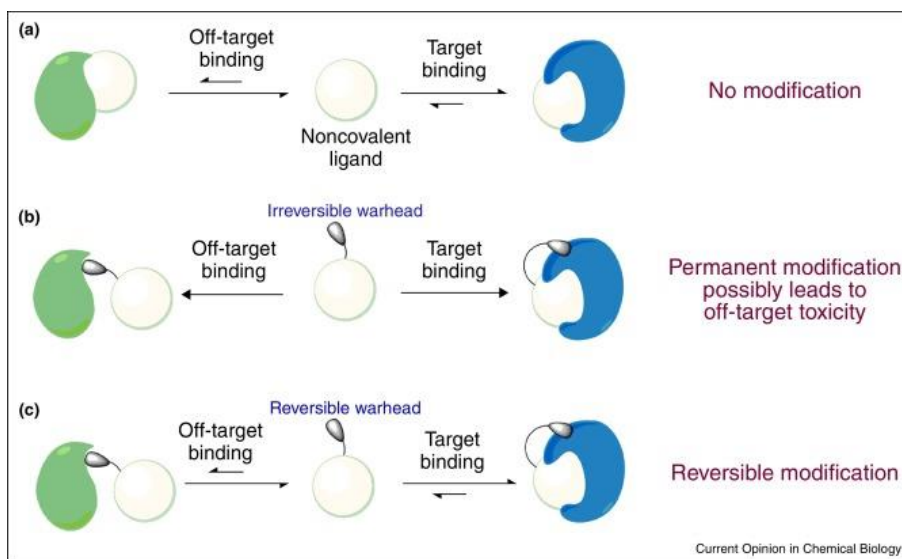


Figure 1.4. (a) noncovalent enzyme inhibition, (b) irreversible covalent enzyme inhibition, (c) reversible covalent enzyme inhibition.¹⁴

1.3 REVERSIBLE COVALENT BONDING IN THIS DISSERTATION

This dissertation covers a selection of different uses of reversible covalent bonding. Each chapter is devoted to a different application of reversible covalent bonding.

Spin traps are molecules that are used to trap short-lived radical species in order to observe them by electron paramagnetic resonance. Chapter 2 discusses the development of a spin trap with the end goal of reversibly binding nitric oxide, an important signaling molecule in cells. Detection of nitric oxide reversibly would allow for monitoring of nitric oxide levels over time, instead of only at one time-point.

Bull and James have previously developed a three-component assembly that utilizes the reversibility of boronate ester formation and the reversibility of imine formation. Chapter 3 seeks to expand upon a similar three-component assembly that forms oximes instead of imines. Ostensibly, this three-component assembly should also be reversible; however, this was found not to be the case. This three-component oxime assembly was instead studied for purposes of bioorthogonal labeling, among other purposes.

Chapter 4 discusses a conjugate addition of amines and thiols to a Meldrum's acid derivative that allows for reversible exchange of different thiols as well as decoupling of both the amine and thiol. The kinetics and pK_a 's of this system are measured, discussed, and compared to different derivatives.

Chapter 5 discusses the synthesis of various analogues of the natural product piperlongumine which is thought to react through two additions of thiols in a 1,4-conjugate fashion. These additions are typically reversible and the analogues synthesized are intended to test the cytotoxicity of these molecules.

1.4 REFERENCES

- (1) Varshey, D. B.; Sander, J. R. G.; Friscic, T.; MacGillivray, L. R. Supramolecular Interactions. In *Supramolecular Chemistry: From Molecules to Nanomaterials*; Gale, P. A., Steed, J. W., Eds.; 2012; pp 9–24.
- (2) Nicolaou, K. C.; Sorensen, E. J. *Classics in Total Synthesis: Targets, Strategies, Methods*; VCH, 1996.
- (3) Corey, E. J. The Logic of Chemical Synthesis: Multistep Synthesis of Complex Carbogenic Molecules (Nobel Lecture). *Angewandte Chemie International Edition in English* **1991**, *30* (5), 455–465.
- (4) Steed, J. W.; Atwood, J. L.; Gale, P. A. Definition and Emergence of Supramolecular Chemistry. In *Supramolecular Chemistry: From Molecules to Nanomaterials*; Gale, P. A., Steed, J. W., Eds.; 2012; pp 3–8.
- (5) Gasparini, G.; Molin, M. D.; Lovato, A.; Prins, L. J. Dynamic Covalent Chemistry. In *Supramolecular Chemistry: From Molecules to Nanomaterials*; Gale, P. A., Steed, J. A., Eds.; 2012; pp 1497–1526.
- (6) Lorand, J. P.; Edwards, J. O. Polyol Complexes and Structure of the Benzeneboronate Ion. *The Journal of Organic Chemistry* **1959**, *24* (6), 769–774.
- (7) Bull, S. D.; Davidson, M. G.; van den Elsen, J. M. H.; Fossey, J. S.; Jenkins, A. T. A.; Jiang, Y.-B.; Kubo, Y.; Marken, F.; Sakurai, K.; Zhao, J.; et al. Exploiting the Reversible Covalent Bonding of Boronic Acids: Recognition, Sensing, and Assembly. *Accounts of chemical research* **2013**, *46* (2), 312–326.
- (8) James, T. D.; Samankumara Sandanayake, K. R. A.; Shinkai, S. Chiral Discrimination of Monosaccharides Using a Fluorescent Molecular Sensor. *Nature* **1995**, *374* (6520), 345–347.
- (9) Corbett, P. T.; Leclaire, J.; Vial, L.; West, K. R.; Wietor, J.-L.; Sanders, J. K. M.; Otto, S. Dynamic Combinatorial Chemistry. *Chemical Reviews* **2006**, *106* (9), 3652–3711.
- (10) Li, J.; Nowak, P.; Otto, S. Dynamic Combinatorial Libraries: From Exploring Molecular

- Recognition to Systems Chemistry. *Journal of the American Chemical Society* **2013**, *135* (25), 9222–9239.
- (11) Wojtecki, R. J.; Meador, M. A.; Rowan, S. J. Using the Dynamic Bond to Access Macroscopically Responsive Structurally Dynamic Polymers. *Nature Materials* **2011**, *10* (1), 14–27.
- (12) Michal, B. T.; Jaye, C. A.; Spencer, E. J.; Rowan, S. J. Inherently Photohealable and Thermal Shape-Memory Polydisulfide Networks. *ACS Macro Letters* **2013**, *2* (8), 694–699.
- (13) Von Delius, M.; Geertsema, E. M.; Leigh, D. A. These Molecules Are Made for Walking: A Synthetic Small Molecule That Can Walk down a Track. *Nature Chemistry* **2010**, *2* (2), 96–101.
- (14) Bandyopadhyay, A.; Gao, J. Targeting Biomolecules with Reversible Covalent Chemistry. *Current Opinion in Chemical Biology* **2016**, *34*, 110–116.

Chapter 2: Synthesis and Testing of a Spin Trap for Nitric Oxide Detection by Electron Paramagnetic Resonance Spectroscopy

2.1 INTRODUCTION

2.1.1 Reactive Oxygen Species and Nitric Oxide

Small reactive oxygen-containing species (ROS) are prevalent throughout biological systems, performing many roles including signaling, homeostasis, and metabolism.^{1,2} ROS such as superoxide ($O_2^{\bullet-}$), hydroxyl (HO^{\bullet}), hydrogen peroxide, singlet oxygen (1O_2), and nitric oxide (NO^{\bullet}) derive from mitochondrial respiration. Increased levels of ROS, which induce a state called oxidative stress, are often indicative of disease states and as such have been the target of many sensing motifs.³ The desire for reliable, real-time measurement of oxidative stress has been a driving factor in a large body of research. Sensing systems have been developed for ROS such as hydrogen peroxide, hydroxyl radical, and superoxide, typically with fluorescence being the predominant signaling motif. (Figure 2.1)

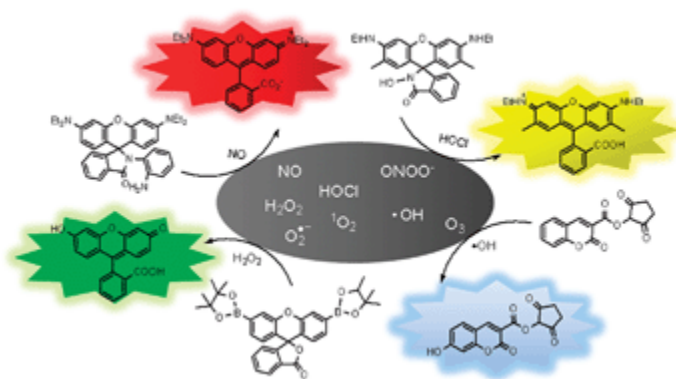


Figure 2.1. A selection of fluorescent sensors for ROS.³

One ROS of particular interest to our research is nitric oxide radical (NO), a simple, diatomic gas of great significance in biological systems. The primary biological role of NO was first discovered in 1980 by Furchgott and Zawadzki, who found that an unknown substance produced in endothelial cells caused a relaxation of blood vessels in response to muscarinic agonists – a substance that they called the endothelium-derived relaxing factor (EDRF).⁴ The

structure of NO was not elucidated until 1987 by Ignarro,⁵ who later shared the 1998 Nobel Prize in Medicine with Furchgott and Ferid Murad for this contribution. Through his own studies and the work of others, Ignarro was able to prove the structure of EDRF as NO radical. Since the elucidation of its structure, NO research has been prominent in biological, chemical, and medicinal research with thousands of citations. Although the initial discovery of biological NO was in relation to muscle relaxation and blood flow, this small molecule also acts as a neurotransmitter and as part of the immune system to fight infection.⁶

In mammalian systems, NO is produced mainly through three isoforms of nitric oxide synthases: endothelial (eNOS), neuronal (nNOS), and inducible (iNOS). All three NOS enzymes produce NO through the oxidation of L-arginine to L-citrulline utilizing NADPH cofactor, producing 1 equivalent of NO for every oxidized arginine molecule.⁷ (Figure 2.2) NO can then react with O₂ to give peroxynitrite (ONOO⁻), with cysteine or glutathione to give *S*-nitrosylation products, and with other biological species including metalloproteins to give metal nitrosyl complexes. eNOS and nNOS production of NO is dependent upon Ca²⁺ levels, which leads to relatively constant NO production at low concentrations.⁶ Changes in this production can be the result of vascular or neurodegenerative diseases, respectively.

iNOS differs from the other two isoforms. Its expression can be induced as an inflammatory response (e.g. in response to bacterial lipopolysaccharides) and, although it is primarily found in macrophages, expression of iNOS can be found across all cell types. Additionally, iNOS is not regulated by Ca²⁺ concentrations, but instead continually produces NO. Although NO production can be a successful defense against harmful pathogens, increased iNOS expression is also indicative of disease states and overproduction of NO can damage healthy cells. When studying potential sensors or pharmaceuticals related to NO, iNOS production is typically the pathway studied as NO production is easily stimulated.

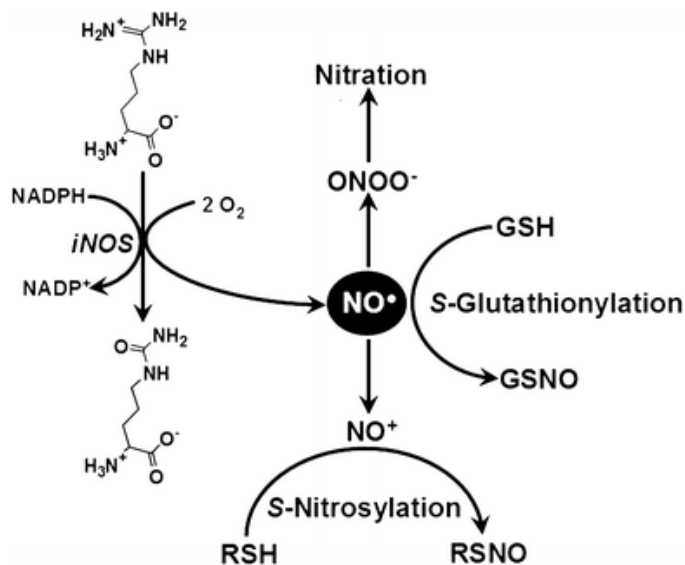
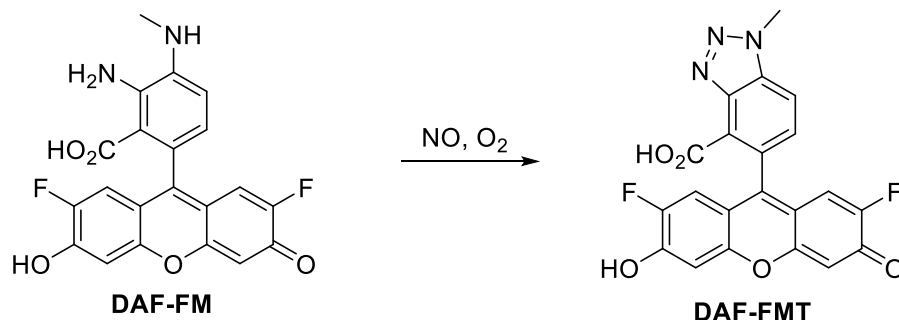


Figure 2.2. Schematic of NO production and reactivity.⁷

2.1.2 NO Sensing

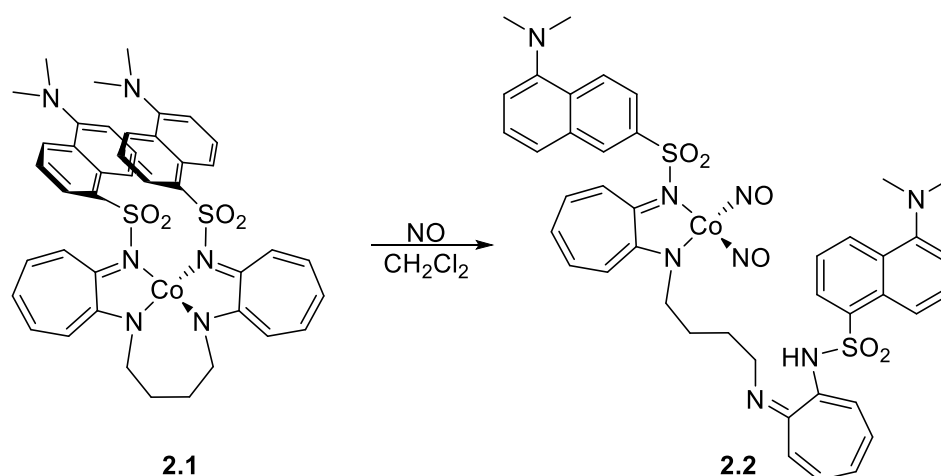
Several NO sensors have been developed over the past few decades, each with their advantages and flaws. The most common fluorescent sensor for NO is **DAF-FM**, synthesized by the Nagano group.⁸ **DAF-FM** was the best performing sensor of a series of *o*-phenylenediamine fluorescein derivatives that operate by binding oxidation products of NO, species that are equivalent to “NO⁺”. In **DAF-FM**, the free diamine quenches the fluorescence of the fluorescein core through photoinduced electron transfer, or PET. Nitrosation of **DAF-FM** by “NO⁺” at one amine is followed by a dehydration, leading to formation of a triazole (**DAF-FMT**), which is less able to participate in PET quenching (Scheme 2.1). This results in a 160-fold turn on of fluorescence for the probe. Earlier generations of the probe lacked the fluorine moieties, which were incorporated to lower the pK_a of the fluorophore significantly below physiological pH in order to reduce pH sensitivity and to decrease photobleaching. Additionally, **DAF-FM** is also a quantitative sensor that irreversibly binds NO, technically a dosimeter rather than a true sensor; this creates larger error in intracellular concentrations than a reversible sensor would and disturbs NO concentrations within the system. **DAF-FM** has the problem of reacting with other electrophiles, leading to false positives. Another critique of **DAF-FM** is that it is rapidly pumped

out of cells, creating a large extracellular fluorescence signal, and reducing the time that NO can be visualized following treatment of the system of interest. Despite these drawbacks, **DAF-FM** is capable of being used *in vitro* and is the predominate sensor in the field.



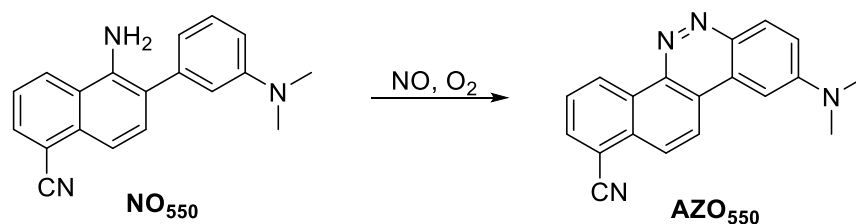
Scheme 2.1. Structure of **DAF-FM** and its product with NO.

Lippard and coworkers took a different approach to NO sensing, employing known NO binding to transition metal cores in the design of a series of transition metal-containing probes.⁹ The first in this series was **2.1**, which uses a tetradentate ligand bound to cobalt that quenches via the partially filled d-orbitals of Co^{II}, a common mechanism in paramagnetic transition metal complexes. In the presence of excess NO, two of the bound nitrogens from the ligand are displaced, allowing for fluorescence from the dansyl amide fluorophore. (Scheme 2.2) This probe is a direct sensor of NO, in contrast to the “NO⁺” sensed by **DAF-FM**, and is unaffected by O₂ present in solution. Unfortunately, Lippard’s probe is insoluble in water and shows low sensitivity as well as a slow response rate, making it unsuitable for *in vivo* imaging. Subsequent sensors based on the same signaling motif have displayed faster response rates to NO but still had low sensitivities and poor water-compatibility.



Scheme 2.2. Lippard's probe binding NO and releasing dansyl amide to fluoresce.

Our group's first foray into NO sensing was in 2010. We developed an irreversible sensor that bound "NO⁺," similar to **DAF-FM**.¹⁰ **NO₅₅₀** is non-fluorescent at an excitation wavelength of 450 nm due to non-radiative relaxation after excitation, but upon reaction with NO, the more conjugated product (**AZO₅₅₀**) has an excitation maximum at this same wavelength, which allows for the measurement of NO levels. (Scheme 2.3) Although **NO₅₅₀** exhibits a turn-on of 1500-fold fluorescence at 450 nm excitation, it is less reactive than other probes, leading to an overall smaller signal turn-on when exposed to NO. **NO₅₅₀** has been used for *in vitro* NO detection, but still exhibits low water solubility. Current efforts are ongoing in the Anslyn group and with collaborators to improve both water solubility and sensitivity, however, these are outside the scope of this body of work.



Scheme 2.3. Reaction of NO with **NO₅₅₀** causing a fluorescence turn on.

As discussed in this section, fluorescence has been the predominate method in sensing of ROS. It is a widely used technique with many benefits, but the literature has yet to find a sensitive, ratiometric fluorescent sensor for use *in vivo*.

2.1.3 Electron Paramagnetic Resonance

In our efforts to develop a ratiometric sensor, rather than the existing dosimetric-style sensing scheme, we turned to electron paramagnetic resonance spectroscopy. Electron paramagnetic resonance (EPR), also called electron spin resonance (ESR), is an analysis technique used to study species with unpaired electrons, also known as paramagnetic species or free radicals. EPR excites electron spins ($+ \frac{1}{2}$ and $- \frac{1}{2}$) using microwave radiation combined with a magnetic field and the resulting signal reflects the environment around the unpaired electron.¹¹ An advantage of EPR over other techniques is that only paramagnetic species give a signal in the spectrum, which allows these experiments to be conducted in complex media with minimal background signal.

EPR signals result from the excitation of electrons within a magnetic field. Each electron has a magnetic moment (m_s) which, when an external magnetic field is applied, aligns either parallel ($m_s = - \frac{1}{2}$) or antiparallel ($m_s = + \frac{1}{2}$) to the magnetic field, creating an energy gap in the formerly degenerate states. These alignments have differing energies due to the Zeeman effect, where a spectral line is split into several components when in the presence of a static magnetic field.¹¹ The Zeeman effect of an unpaired free electron is represented by Equation 2.1, where ΔE is the difference between the energies of the two electron spin states inside a magnetic field (Figure 2.3). g_e is the g-factor of an electron ($g_e = 2.0023$) which characterizes the magnetic moment and gyromagnetic ratio of the electron. μ_B is the Bohr magneton constant (9.274×10^{-24} J/T) which expresses the magnetic dipole moment of an electron and B_0 is the strength of the magnetic field. Equation 2.2 and 2.3 relate frequency (ν) to magnetic field, which is the basis for EPR spectroscopy. An electron occupying the lower ($- \frac{1}{2}$) state can absorb energy equal to $h\nu$ to jump to the higher $+ \frac{1}{2}$ spin state, which results in an EPR signal.

Equation 2.1. $\Delta E = g_e \mu_B B_0$

Equation 2.2. $\Delta E = h\nu$

Equation 2.3. $h\nu = g_e \mu_B B_0$

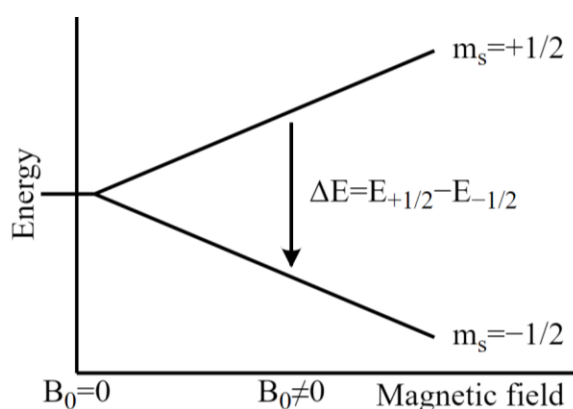


Figure 2.3. Splitting of electron spin states according to the Zeeman effect.¹²

Although theoretically a large combination of frequencies and magnetic fields could be used for EPR, most instruments operate in the X-band microwave region (8000 and 12,000 MHz) and 3500 G (0.35 T) magnetic field. After application of the correct magnetic field and frequency, an electron can switch spin states, absorbing or emitting energy as it does. In systems with only paired electrons, these absorptions and emissions cancel each other out, resulting in no signal. In a paramagnetic species, however, there is more absorbance than emission due to greater electron population in lower energy states. This absorbance is monitored and reflected in the resulting EPR signal.

There are two methods used with EPR spectroscopy: continuous wave (CW) or pulsed EPR. CW-EPR, which is more commonly used, uses continuous microwave radiation at a constant frequency while varying the magnetic field until the magnetic field widens the gap

between electron spin states until it matches the energy of the radiation.¹³ The slope of the absorbance is measured as the magnetic field is modulated, which results in an output equal to the first derivative of absorbance. (Figure 2.4) In contrast, pulsed EPR utilizes a constant magnetic field and pulses oscillating microwave radiation.¹⁴ The alignment of electron spins is perturbed and the resulting emission is measured; this yields data about spin relaxation times and the dynamic properties of the studied species.

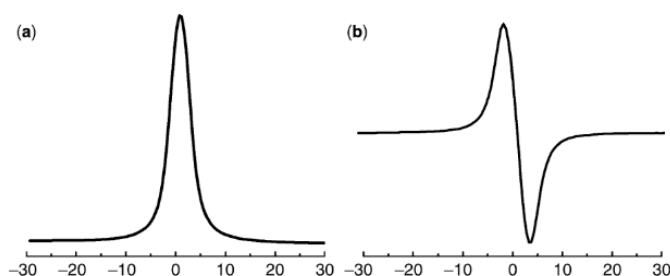


Figure 2.4. (a) the absorption of energy from CW-EPR, (b) the first derivative of absorbance.¹¹

EPR yields additional information about the nature of the paramagnetic species in the form of hyperfine coupling. Hyperfine coupling is the interaction between the unpaired electron and adjacent nuclei. Nuclei, like electrons, also have spin angular momentum (J). Nuclei with non-zero nuclear spin result in splitting of the EPR spectrum in a $2I + 1$ pattern.¹¹ For example, nuclei with $I = \frac{1}{2}$ (^1H , ^{13}C , ^{31}P , ^{15}N) split the EPR spectrum into 2 components ($2I + 1 = 2$). Figure 2.5 shows a simulated EPR spectrum of a nitroxide radical. ^{14}N has a nuclear spin of 1, producing a three component splitting in the spectrum.

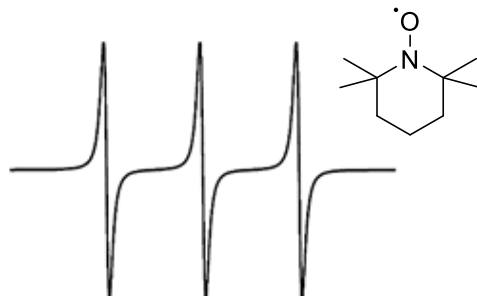


Figure 2.5. Simulated EPR spectrum of a nitroxide radical (shown).¹⁵

2.1.4 Spin Trapping

Since many paramagnetic species are short-lived, spin traps have been developed for EPR spectroscopy. Spin traps are diamagnetic molecules that bind the paramagnetic species of interest and create a longer-lived, more stable radical.¹⁶ This radical is then the species that is shown in the EPR spectrum. Spin traps need to be stable to the experiment conditions and specific to the analyte of interest, and they should undergo radical addition rapidly to yield long-lasting spin adducts. Common organic spin traps are often nitrones (PBN and DMPO) or nitroso compounds (nitrosobenzene). (Figure 2.6)

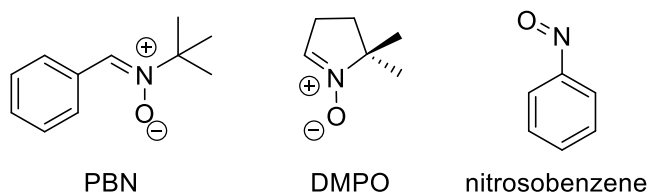


Figure 2.6. Commercially available spin traps *N*-*tert*-butyl- α -phenyl nitron (PBN), 5,5-dimethyl-pyrroline *N*-oxide (DMPO), and nitrosobenzene.

EPR has been used to detect NO directly in the gas phase, but the signal is too broad and noisy for direct detection in the liquid phase.¹⁷ Spin trapping, in theory, could sharpen the signal, but NO is unusual in its reactivity in that it, unlike other ROS, does not react with traditional spintraps such as PBN or DMPO. Current EPR methods for detection of NO in the liquid phase have focused on metal coordination of NO (Figure 2.7) and NO reacting with a radical species to produce a change in EPR spectrum that can be monitored (Figure 2.8).

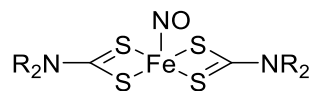


Figure 2.7. An example of an iron dithiocarbamate bound to NO.

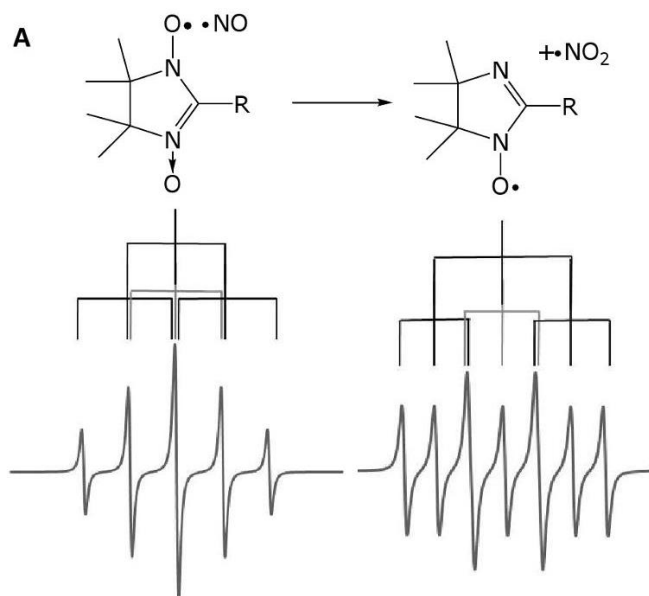


Figure 2.8. Nitronyl nitroxide spin trap reaction with NO and the resulting change in splitting of the EPR spectrum.¹⁷

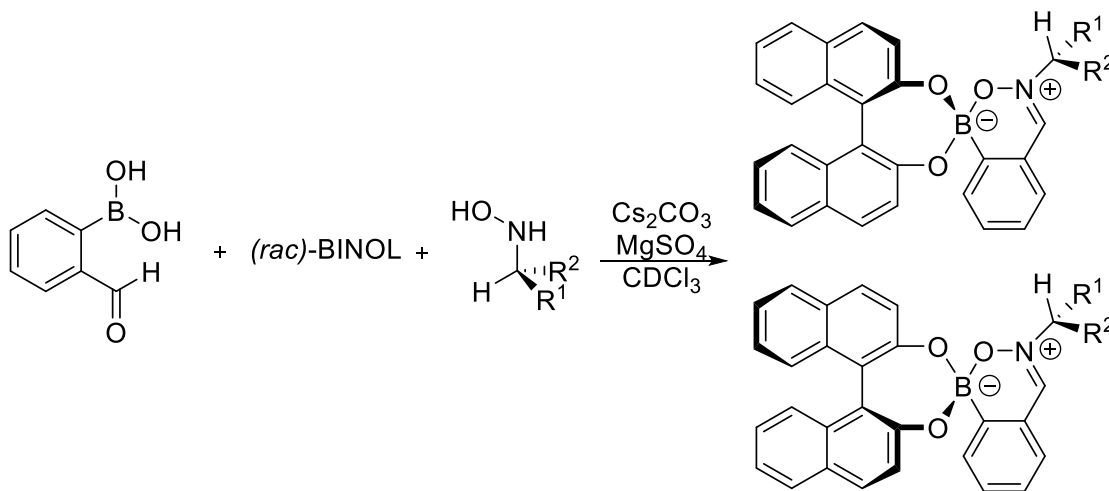
Since EPR has the added benefit of measuring paramagnetic species in cloudy or complex media, it seems ideal for measuring NO concentrations in tissue samples. Dinitrosyl iron complexes and heme complexes have been used for *in vitro* and *in vivo* measurement of NO.¹⁷ Signals from dinitrosyl iron complexes have been detected in activated macrophages and cancer cells after NO exposure; it is believed that these complexes form as part of the S-nitrosylation pathway in cells. Heme nitrosyl concentrations are too low to be detected in human tissue, but have been used in rodents, which have a larger NO component to their inflammatory response.

In our efforts to expand upon the existing literature for NO sensing, we hypothesized that EPR would be a good method to study NO levels by spin trapping in a reversible fashion. Sequential EPR spectra would allow us to visualize changing NO levels over time.

2.2 BORONATE ESTER SPIN TRAP SYNTHESIS AND REACTIVITY

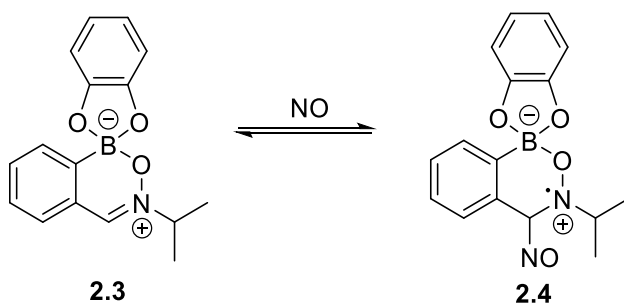
2.2.1 James/Bull Assembly and Synthesis of Spin Traps for NO Detection

In designing a reversible sensor, we looked at systems that were readily synthesized in high yields that would be stable to aqueous conditions, and, in particular, we turned to a boronate ester assembly originally published by James *et al.*¹⁸ James published a simple, three component assembly that is formed rapidly from 2-formylphenylboronic acid (2-FPBA), racemic 1,1'-Bi-2-naphthol (BINOL), and *N*-alkyl hydroxylamines. (Scheme 2.4) This assembly is discussed further in section 3.1.2.1.



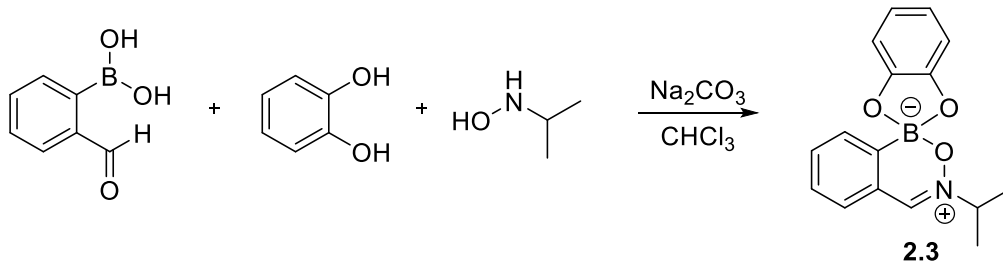
Scheme 2.4. James *et al.*'s hydroxylamine/boronate ester assembly.

We hypothesized that NO could add reversibly to the nitrene-like functionality in complex **2.3** to form the spin adduct **2.4**. (Scheme 2.5) The addition of NO would create a nitrogen-centered radical that we hoped to visualize using EPR spectroscopy. This addition would likely be reversible which would allow for the monitoring of NO levels over time, which was our original goal with this project.



Scheme 2.5. Proposed binding of NO by **2.3**.

Proposed spin trap **2.3** was synthesized using 2-FPBA, catechol, and *N*-isopropylhydroxylamine. (Scheme 2.6) The *N*-isopropylhydroxylamine (iPrNHOH) was synthesized from acetone in a two-step procedure from the literature.^{19,20} Catechol was used with the intention of acting as a truncated version of the original BINOL that would not complicate the reaction with stereoisomeric products. The product was recovered by filtration and used with no further purification in future experiments.



Scheme 2.6. Synthesis of spin trap **2.3**.

2.2.2 NO Generation and EPR Spectroscopy

In our first NO binding studies, spin trap **2.3** was dissolved in CH_2Cl_2 and NO was bubbled through the solution. The NO was produced using the same method that had been previously applied to our **NO**₅₅₀ studies discussed in section 2.1.2; this method reacts H_2SO_4 with aqueous NaNO_2 via dropwise addition. The resulting gas is then bubbled through basic solution and then sparged through the solution containing the spin trap. During this first study, we obtained an EPR spectrum that matched what we were expecting to see. We saw a nitrogen-

centered radical shown by the 1:1:1 splitting pattern. This spectrum was matched with the calculated spectrum provided by Minh Nguyen in the Holliday Group at The University of Texas at Austin. (Figure 2.9)

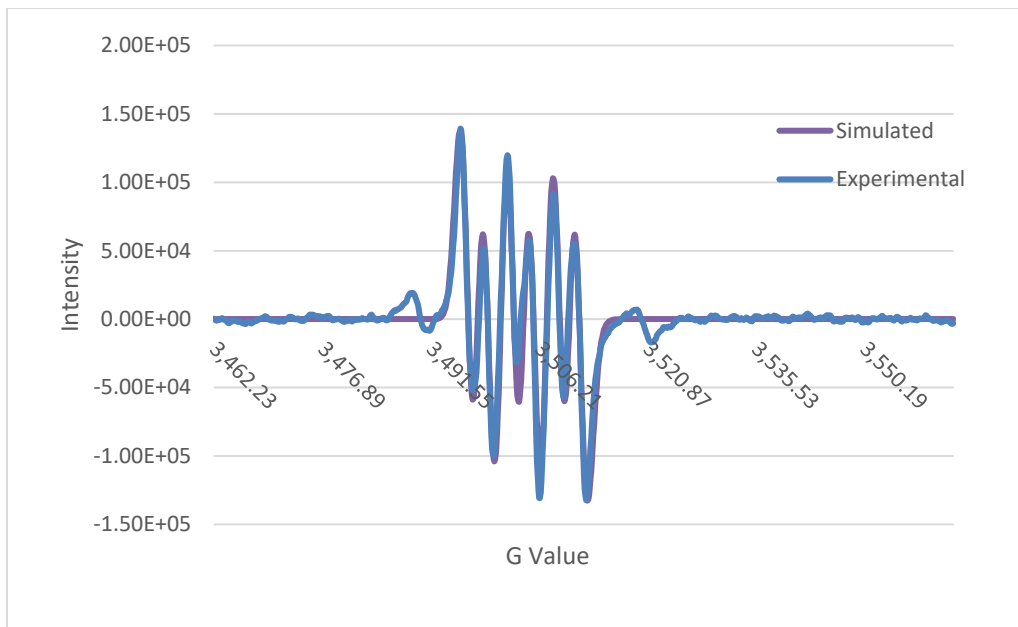


Figure 2.9. Simulated and actual EPR spectra of **2.3** after bubbling with gas produced from NaNO_2 and H_2SO_4 .

Although these initial results seemed positive, we encountered great difficulty in reproducing this spectrum. Most of our efforts resulted in no discernible EPR signal, only noise. (Figure 2.10) Under the hypothesis that excess oxygen was decaying NO before it was able to bind to the spin trap, different methods of deoxygenation of the spin trap solutions were tried, with little improvement.

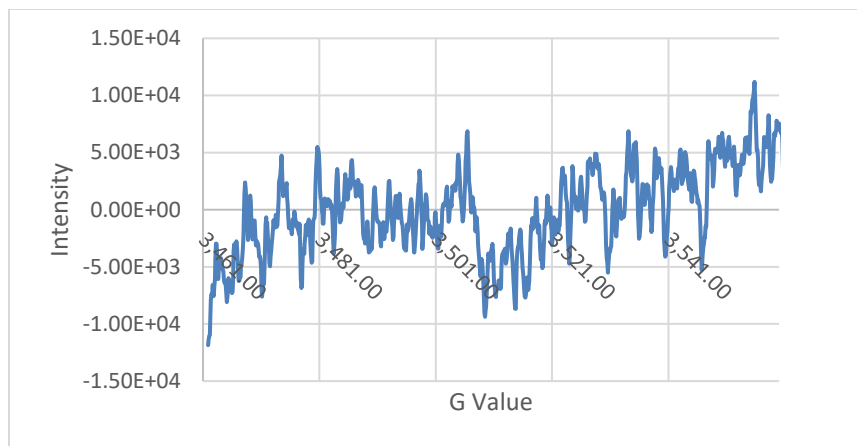


Figure 2.10. Noise generated by EPR.

While trying to eliminate potential sources for oxygen, we changed our source of NO to a NO gas cylinder and bubbled this directly into a solution of spin trap **2.3**. This yielded the EPR signal in Figure 2.11. We were able to improve this signal by using an airtight EPR tube and by bubbling the NO through 7 M NaOH prior to the spin trap solution. (Figure 2.12)

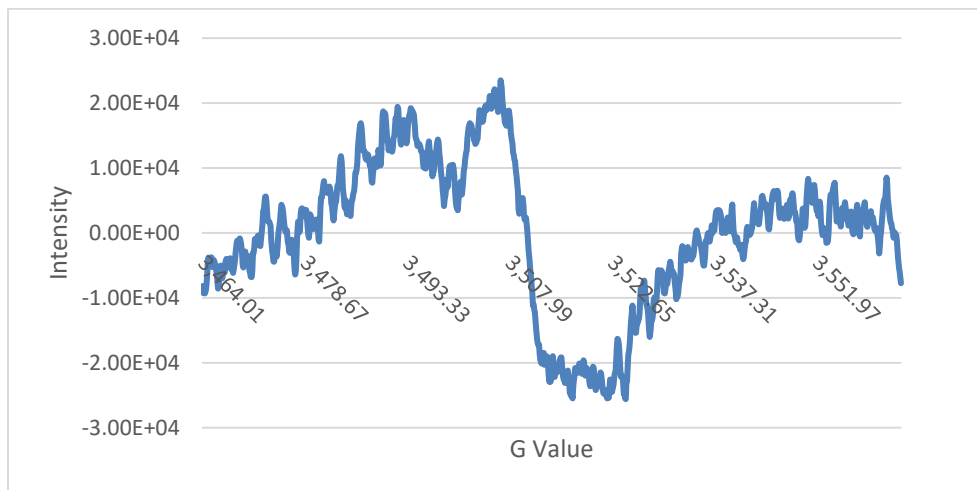


Figure 2.11. EPR signal generated from NO cylinder.

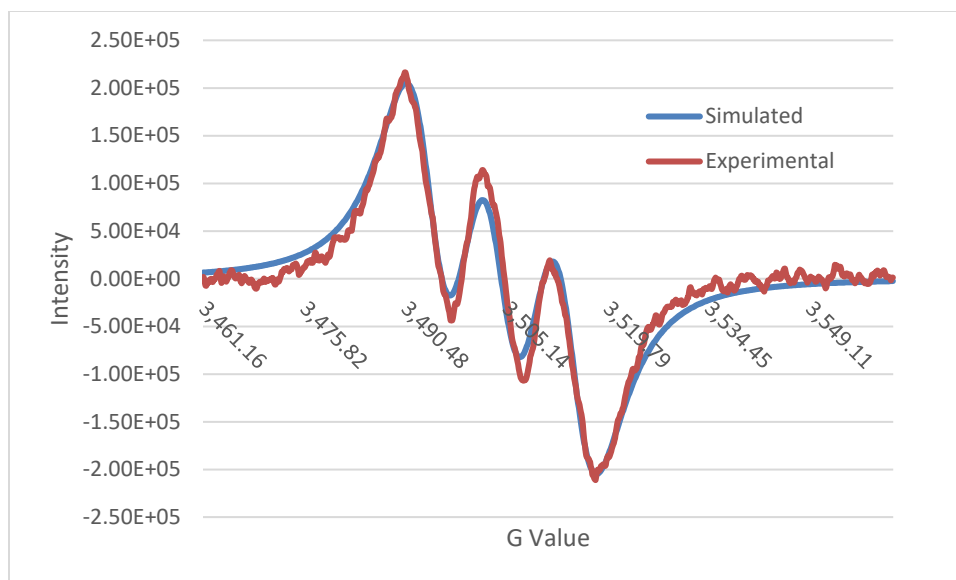


Figure 2.12. EPR signal generated after bubbling NO through NaOH solution.

An alternate spin trap was synthesized (structure **2.5**, Figure 2.13) due to remove the possibility of signal decay through hydrogen abstraction. (Scheme 2.7) This spin trap was synthesized in the same manner at **2.3**, but with *N-tert*-butylhydroxylamine. Spin trap **2.5** did not improve the EPR signal significantly.

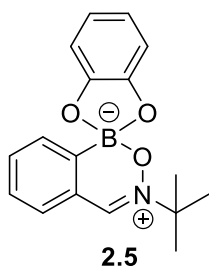
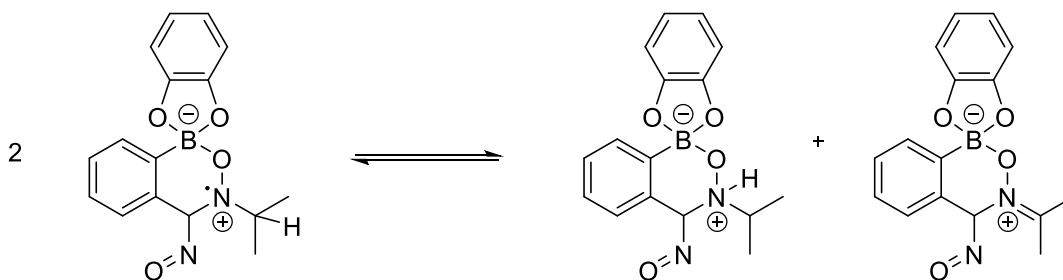


Figure 2.13. Structure of spin trap **2.5**.



Scheme 2.7. Possible hydrogen abstraction causing decay of the EPR signal.

2.2.3 Absorbance Fine Structure

Despite our efforts we were unable to reproduce our original experiment. In a UV-Vis titration of NO into spin trap **2.3**, we saw an unusual fine structure in the absorbance plot. (Figure 2.14) We had switched solvents from dichloromethane to ethanol in order to move to a polar, protic solvent system, a necessity for any relevant biological studies.

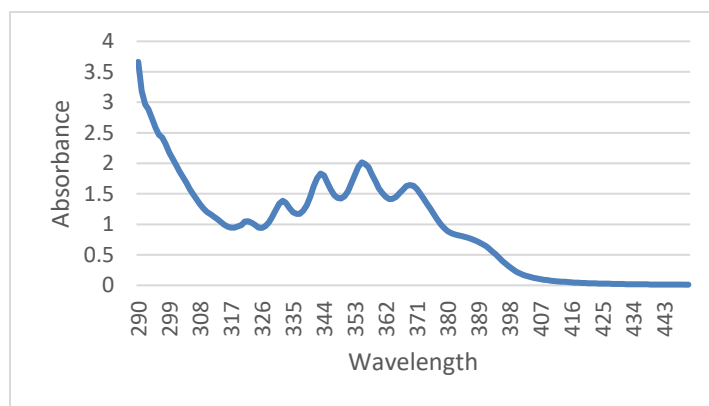


Figure 2.14. Absorbance of spin trap **2.3** and NO in ethanol.

Upon investigation of the literature, we found that this fine structure is characteristic of alkyl nitrites.^{21,22} (Figure 2.15) We proposed that this unusual fine structure that we observed in the absorbance curve was therefore due to the binding of the radical nitrogen dioxide, NO₂. (Scheme 2.8) NO₂ is a known byproduct of the reaction of NO with molecular oxygen and by NO decay over time. (Scheme 2.9)

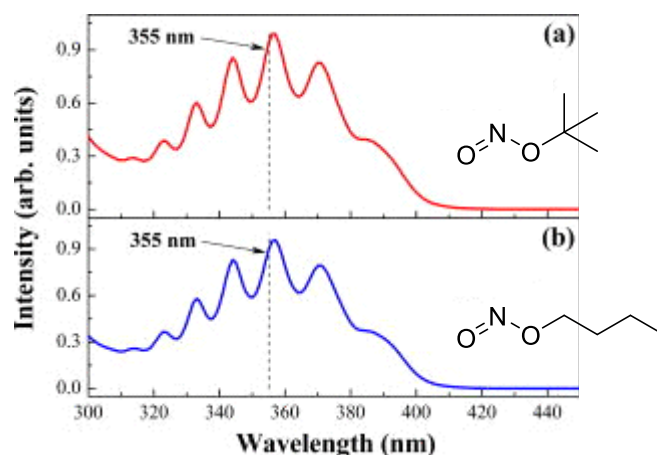
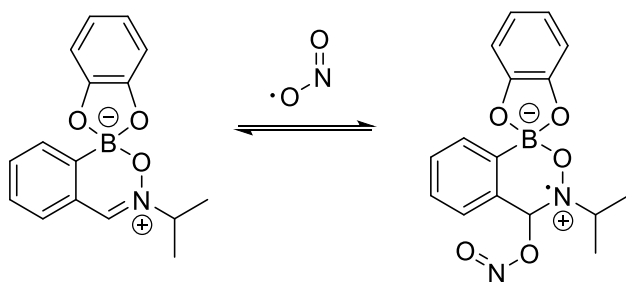
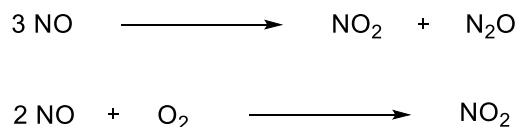


Figure 2.15. Absorbance spectra of (a) *tert*-butyl nitrite and (b) *n*-butyl nitrite in ethanol.



Scheme 2.8. Proposed binding of NO_2 radical to spin trap **2.3**.



Scheme 2.9. Two possibilities of the evolution of NO_2 from NO .

2.3 CONCLUSIONS

We synthesized a boronate ester based spin trap, compound **2.3**, that although unable to bind NO to any great extent, did bind NO_2 in sufficient quantities to be observed by both EPR and UV-Vis spectroscopy. We were unable to visualize an EPR spectrum when degassing our solutions since NO was unable to be oxidized to NO_2 and the decomposition of NO to NO_2 did not occur on the timescale we were observing. When we did not degas our solution, we observed

EPR spectra characteristic of nitrogen centered radicals, which we believe to be the result of NO₂ addition to **2.3**. This is corroborated by the fine structure characteristic of alkyl nitrites observed in our absorbance spectra.

2.4 EXPERIMENTAL

2.4.1 Synthesis of spin traps **2.3** and **2.5**

Synthesis of 2-propanone oxime: Acetone (136 mmol, 10 mL) and hydroxylamine hydrochloride (204 mmol, 14.2 g) were dissolved in a RBF containing 272 mL H₂O. Sodium carbonate (245 mmol, 25.95 g) was slowly added. The reaction was stirred at room temperature overnight (~16 hrs). Diethyl ether was added and the reaction mixture was transferred to a separatory funnel. The reaction mixture was extracted 5x with diethyl ether. The organic layers were combined, dried over MgSO₄, and filtered. The filtrate was concentrated under reduced pressure to give 9.13 g of fluffy white powder (yield = 92%). ¹H-NMR (400 MHz, CDCl₃): δ = 9.18 (bs, 1H), 1.89 (dd, 6H, *J*=1.79, 4.76 Hz).

Synthesis of *N*-isopropyl hydroxylamine: 2-propanone oxime (125 mmol, 9.13 g) was dissolved in 178 mL MeOH. NaBH₃CN (137 mmol, 8.63 g) was added followed by a small amount of bromocresol green as a colorimetric indicator. 2M HCl in MeOH was added dropwise (~70 mL) until a yellow-green color persisted (pH = 3.5-4). The reaction was stirred overnight then solvent was removed under vacuum. The resulting residue was dissolved in CH₂Cl₂ and transferred to a separatory funnel. The reaction mixture was washed with saturated aqueous NaHCO₃ solution. The organic layer was dried over MgSO₄, and filtered. The filtrate was concentrated under reduced pressure to yield 1.76 g of the desired product (19% yield). ¹H-NMR (400 MHz, CDCl₃): δ = 3.15 (heptet, 1H, *J*=6.33 Hz), 1.08 (d, 6H, *J*=6.35 Hz).

Synthesis of **2.3**: *N*-isopropyl hydroxylamine (23 mmol, 1.76 g) was dissolved in 233 mL of CHCl₃. To this solution was added catechol (26 mmol, 2.84 g), 2-formylphenylboronic acid (23 mmol, 3.51 g), cesium carbonate (26 mmol, 8.46 g), and MgSO₄ (47 mmol, 5.63 g). The reaction mixture was stirred for 15 min at room temperature then filtered. Filtrate was

concentrated under reduced pressure to yield a bright yellow solid in quantitative yield (6.46 g). $^1\text{H-NMR}$ (400 MHz, CDCl_3): δ = 8.12 (s, 1H), 7.78 (d, 1H, $J=7.28$ Hz), 7.70 (m, 1H), 7.46 (m, 2H), 6.82 (m, 2H), 6.76 (m, 2H), 4.30 (heptet, 1H, $J=6.53$), 1.58 (d, 6H, $J=6.59$). UV-Vis absorbance: λ_{max} = 284 nm (CHCl_3), 277 nm (H_2O).

Synthesis of **2.5**: *N-t*-butylhydroxylamine hydrochloride (1.99 mmol, 0.25 g) was dissolved in 20 mL of CHCl_3 . To this was added catechol (2.00 mmol, 0.22 g) and 2-formylphenylboronic acid (2.00 mmol, 0.30 g). The reaction mixture was stirred for 15 min at room temperature then solvent removed under reduced pressure to yield a bright yellow solid in quantitative yield (0.59 g). $^1\text{H-NMR}$ (400 MHz, CDCl_3): δ = 8.22 (s, 1H), 7.76 (d, 1H, $J=7.4$ Hz), 7.68 (m, 1H), 7.46 (m, 2H), 6.80 (m, 2H), 6.73 (m, 2H), 1.62 (s, 9H). $^{13}\text{C-NMR}$ (400 MHz, CDCl_3): δ = 151.61, 141.76, 135.94, 131.66, 128.86, 128.30, 126.92, 118.83, 109.40, 69.92, 27.39.

2.4.2 NO generation

NO was generated through the following process, based on literature precedent.¹⁰ NaNO_2 (725 mmol, 50 g) was dissolved in 30 mL H_2O in a 3-neck RBF. A N_2 line was fitted to one neck, an addition funnel to the second neck, and a line to a bubbler filled with 30% NaOH solution was fitted to the third neck. In the addition funnel was placed 50 mL of 2M H_2SO_4 . The bubbler was vented into a filter flask with H_2O , which was in turn connected to an Erlenmeyer flask with CH_2Cl_2 and spin trap **2.3** or **2.5**. (Figure 2.16) After purging with nitrogen, H_2SO_4 was slowly dripped into the RBF and the resulting gas bubbled through the 30% NaOH soln, the H_2O , then the spin trap soln.

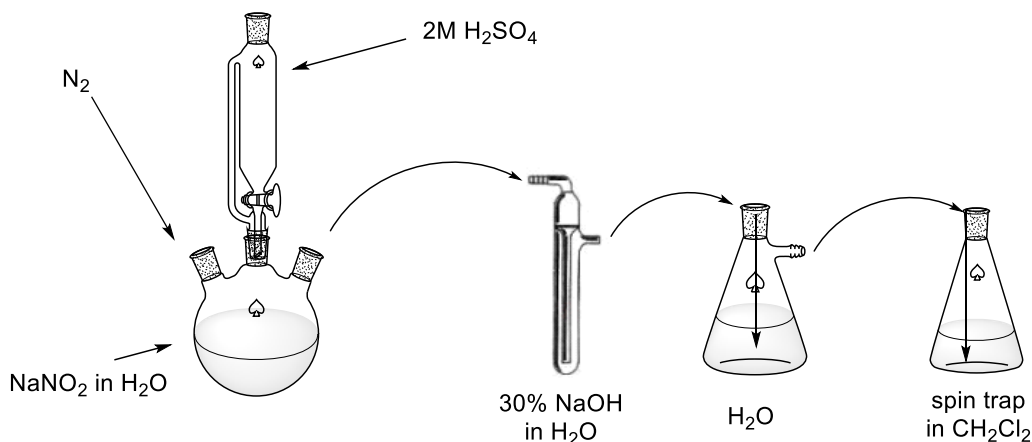


Figure 2.16. NO production setup.

2.4.3 NO cylinder

With degassing: A screw-top EPR tube was charged with CH₂Cl₂ and **2.3** or **2.5** and connected to a bubbler containing 7 M NaOH aqueous solution. Argon was purged for 30 min through the bubbler, into the solution of spintrap, and vented through a vent needle at the top of the EPR tube. The NO cylinder was then opened and NO allowed to bubble through the system in the same fashion. After 30 min, the EPR sample was removed and taken to the spectrometer.

2.4.4 EPR

All EPR spectra were collected on a Bruker EMX Plus continuous wave spectrometer using X-band frequencies and 10 mm o.d. EPR tubes.

2.4.5 Absorbance

Titration of **2.3** with NO/NO₂ produced as described in 2.4.2: NO was bubbled into ethanol and was titrated into a solution containing **2.3** in ethanol ([**2.3**] = 0.11 mM). Absorbance spectra were collected after waiting 20 min after each addition of NO soln. (Figure 2.17) The legend describes each consecutive volume of NO/NO₂ solution added, however [NO] and [NO₂] are unknown.

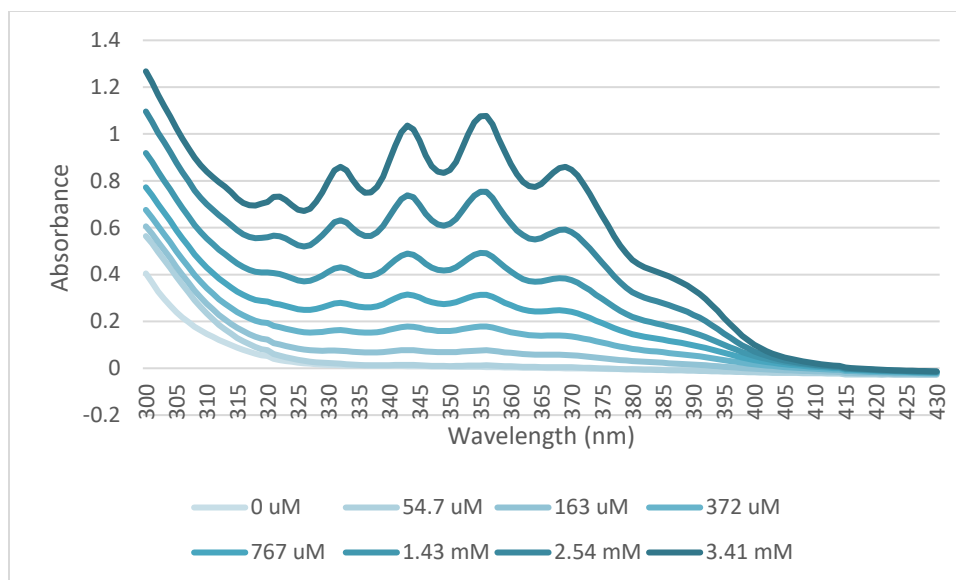


Figure 2.17. Absorbance spectra showing the fine structure from alkyl nitrite formation.

2.5 ACKNOWLEDGEMENTS

Dr. Minh Nguyen is gratefully acknowledged for his help with interpretation of EPR spectra and providing simulated spectra for reference.

2.6 REFERENCES

- (1) Ray, P. D.; Huang, B.-W.; Tsuji, Y. Reactive Oxygen Species (ROS) Homeostasis and Redox Regulation in Cellular Signaling. *Cellular Signalling* **2012**, *24*, 981–990.
- (2) Schieber, M.; Chandel, N. S. Review ROS Function in Redox Signaling and Oxidative Stress. *CURBIO* **2014**, *24*, R453–R462.
- (3) Chen, X.; Tian, X.; Shin, I.; Yoon, J. Fluorescent and Luminescent Probes for Detection of Reactive Oxygen and Nitrogen Species. *Chemical Society Reviews* **2011**, *40* (9), 4783.
- (4) Furchgott, R. F.; Zawadzki, J. V. The Obligatory Role of Endothelial Cells in the Relaxation of Arterial Smooth Muscle by Acetylcholine. *Nature* **1980**, *288* (5789), 373–376.
- (5) Ignarro, L. J.; Byrns, R. E.; Buga, G. M.; Wood, K. S. Endothelium-Derived Relaxing Factor from Pulmonary Artery and Vein Possesses Pharmacologic and Chemical Properties Identical to Those of Nitric Oxide Radical. *Circulation research* **1987**, *61* (6), 866–879.
- (6) Förstermann, U.; Sessa, W. C. Nitric Oxide Synthases: Regulation and Function. *European heart journal* **2012**, *33* (7), 829–37, 837a–837d.
- (7) Singh, S.; Gupta, A. K. Nitric Oxide: Role in Tumour Biology and iNOS/NO-Based Anticancer Therapies. *Cancer Chemotherapy and Pharmacology* **2011**, *67* (6), 1211–

1224.

- (8) Kojima, H.; Urano, Y.; Kikuchi, K.; Higuchi, T.; Hirata, Y.; Nagano, T. Fluorescent Indicators for Imaging Nitric Oxide Production. *Angewandte Chemie International Edition* **1999**, *38* (21), 3209–3212.
- (9) Franz, K. J.; Singh, N.; Lippard, S. J. Metal-Based NO Sensing by Selective Ligand Dissociation. *Angewandte Chemie International Edition* **2000**, *39* (12), 2120–2122.
- (10) Yang, Y.; Seidlits, S. K.; Adams, M. M.; Lynch, V. M.; Schmidt, C. E.; Anslyn, E. V.; Shear, J. B. A Highly Selective Low-Background Fluorescent Imaging Agent for Nitric Oxide. *Journal of the American Chemical Society* **2010**, *132* (38), 13114–13116.
- (11) Corvaja, C. Introduction to Electron Paramagnetic Resonance. In *Electron Paramagnetic Resonance: A Practitioner's Toolkit*; Brustolon, M., Giamello, E., Eds.; 2009; pp 3–35.
- (12) Wikipedia: The Free Encyclopedia. Electron Paramagnetic Resonance https://en.wikipedia.org/wiki/Electron_paramagnetic_resonance (accessed Sep 6, 2016).
- (13) Hofer, P. Basic Experimental Methods in Continuous Wave Electron Paramagnetic Resonance. In *Electron Paramagnetic Resonance: A Practitioner's Toolkit*; Brustolon, M., Giamello, E., Eds.; 2009; pp 37–82.
- (14) Bowman, M. K. Pulsed Electron Paramagnetic Resonance. In *Electron Paramagnetic Resonance: A Practitioner's Toolkit*; Brustolon, M., Giamello, E., Eds.; 2009; pp 159–194.
- (15) Gescheidt, G. EPR Spectroscopy in the Liquid Phase. In *Electron Paramagnetic Resonance: A Practitioner's Toolkit*; Brustolon, M., Giamello, E., Eds.; 2009; p 128.
- (16) Alberti, A.; Macciantelli, D. Spin Trapping. In *Electron Paramagnetic Resonance: A Practitioner's Toolkit*; Brustolon, M., Giamello, E., Eds.; 2009; pp 287–323.
- (17) Hogg, N. Detection of Nitric Oxide by Electron Paramagnetic Resonance Spectroscopy. *Free radical biology & medicine* **2010**, *49* (2), 122–129.
- (18) Tickell, D. A.; Mahon, M. F.; Bull, S. D.; James, T. D. A Simple Protocol for NMR Analysis of the Enantiomeric Purity of Chiral Hydroxylamines. *Organic letters* **2013**, *15* (4), 860–863.
- (19) Pohjakallio, A.; Pihko, P. M. Enantioselective Synthesis of 2-Isoxazolines by a One-Flask Conjugate Addition/Oxime-Transfer Process. *Chemistry - A European Journal* **2009**, *15* (16), 3960–3964.
- (20) Kurtzweil, M. L.; Loo, D.; Beak, P. The Endocyclic Restriction Test: Determination of the Transition-Structure Geometry for the Transfer of Oxygen from N,N-Dialkylhydroxylamines to Triarylphosphines. *Journal of the American Chemical Society* **1993**, *115* (2), 421–427.
- (21) Ji, M.; Zhen, J.; Zhang, Q.; Chen, Y. Photolysis of N-Butyl Nitrite and Isoamyl Nitrite at 355 Nm: A Time-Resolved Fourier Transform Infrared Emission Spectroscopy and Ab Initio Study. *The Journal of chemical physics* **2009**, *130* (17), 174314.
- (22) Brisset, J.-L.; Pawlat, J. Chemical Effects of Air Plasma Species on Aqueous Solutes in Direct and Delayed Exposure Modes: Discharge, Post-Discharge and Plasma Activated

Water. *Plasma Chemistry and Plasma Processing* **2016**, 36, 355–381.

Chapter 3: Studies of a Semi-Bioorthogonal Labeling Method Using a Hydroxylamine Boronate Ester Assembly

3.1 INTRODUCTION

3.1.1 Bioorthogonal labeling

Bioorthogonal labeling is the use of chemical modification of a biological moiety of interest in order to introduce a new moiety so that the original species can be more easily monitored. The term “bioorthogonal” was popularized by Carolyn Bertozzi with her pioneering research into the field.¹ Bioorthogonal modification can be accomplished through a variety of techniques including genetic modification to introduce a fluorescent protein such as green fluorescent protein (GFP), enzymatic modification in which an enzyme is used to covalently attach a label to a cell surface protein, or chemical introduction of a label utilizing chemistry that is selective and stable to biological conditions and functional groups.² This work primarily focuses on the chemical introduction of fluorescent labels through bioorthogonal reactions.

Bioorthogonal reactions must be biologically inert (i.e., stable to aqueous conditions and unreactive to biologically relevant functional groups).³ (Figure 3.1) They must have selective reactivity under physiological conditions with few or no byproducts, all of which must be nontoxic. Ideally these reactions are also rapid and high-yielding.

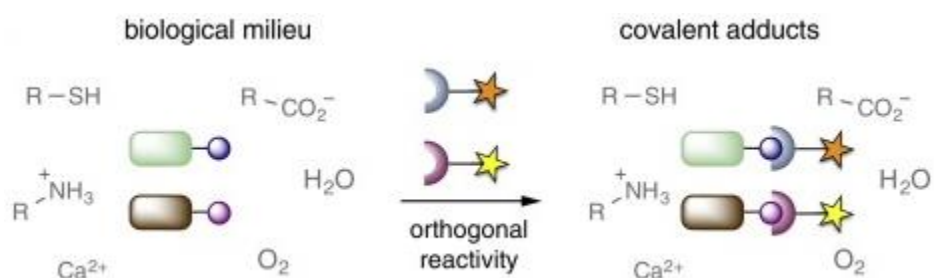


Figure 3.1. Bioorthogonal selectivity.⁴

Bioorthogonal chemistry is most often used to covalently link fluorescent tags to molecules of interest. Fluorescent tags allow for easier study of non-fluorescent biomolecules through a nondestructive method of analysis. Many fluorophores can be visualized at low concentrations in real-time. These fluorescent tags have been used to study the environment, properties, and interactions of labeled species.⁵ (Figure 3.2)

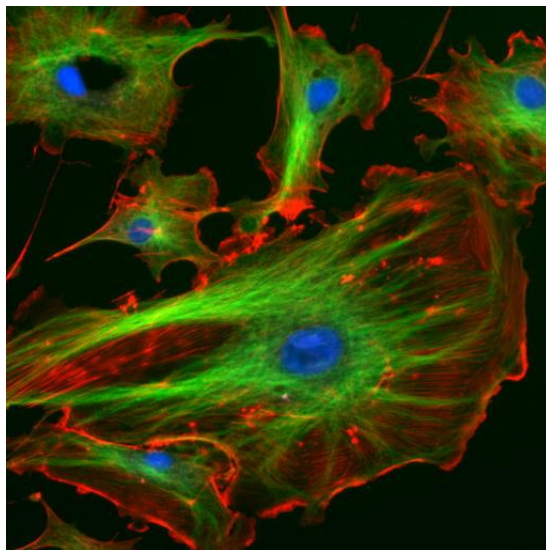


Figure 3.2. Fluorescently stained endothelial cells showing the nuclei(blue), actin filaments (red), and microtubules(green).⁶

Common bioorthogonal, or semi-bioorthogonal, reactions include copper-catalyzed alkyne-azide cycloadditions (CuAAC), strain-promoted alkyne-azide cycloaddition (SPAAC), Staudinger ligations, ketone/aminoether condensations, and a variety of others. (Figure 3.3) The CuAAC is a [3 + 2] cycloaddition that has been known in the literature for many years, but was recently adapted for aqueous conditions and used to label cell-surface proteins.⁷ The necessity of Cu^I catalysis limits the biological utility of this reaction as higher Cu^I concentrations can be toxic to living systems and lower Cu^I concentrations greatly reduce the reaction rate. The SPAAC was introduced by Bertozzi in 2004 as an analogous [3 + 2] cycloaddition that avoided using copper as a catalyst.⁸ Cyclooctynes are strained enough that they will react with azides without the use

of copper. The SPAAC has been used both *in vitro* and *in vivo* with good success.¹ The Staudinger ligation also uses azides to label biomolecules, but typically has a slower reaction rate than other bioorthogonal reactions. It has been used both *in vitro* and *in vivo*.⁹ One of the earliest bioorthogonal reactions explored was the addition of aminoethers to aldehydes and ketones. This condensation proceeds best under mildly acidic conditions (pH = 4-6) or with catalytic aniline, which limits its utility to whole animal or intracellular systems. It has been used successfully with both *in vitro* and cell surface labeling.¹⁰

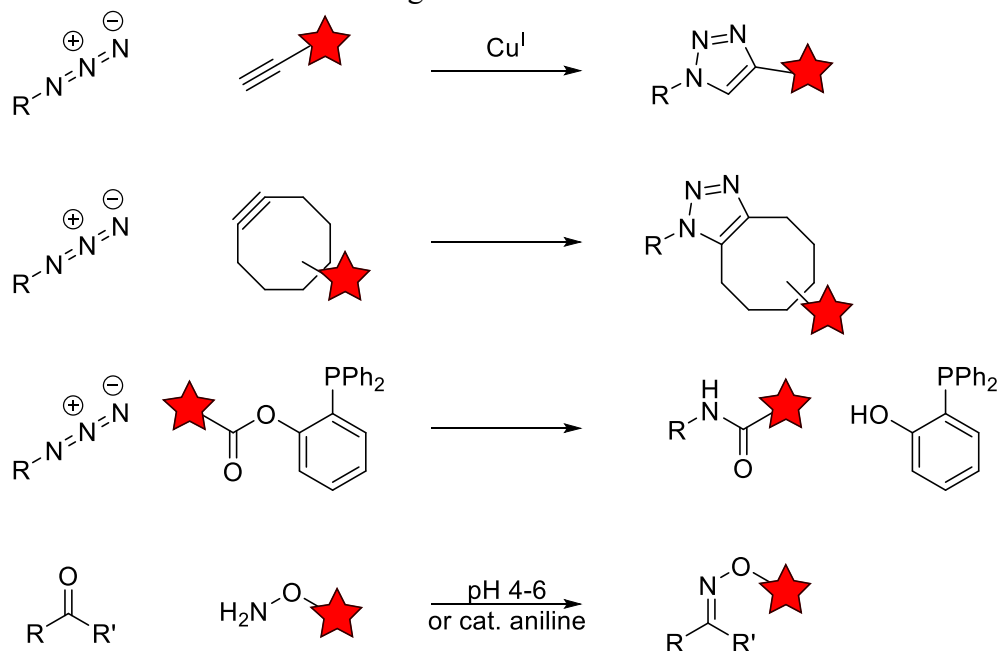


Figure 3.3. Bioorthogonal reactions. *From top:* CuAAC, SPAAC, Staudinger ligation, and ketone/aminoether condensation.

Most of these bioorthogonal transformations necessarily react with functional groups not often found in biology; this therefore requires the incorporation of unnatural amino acids or chemical modification of one of the common 20 amino acids, in the case of protein labeling. This can be accomplished through a variety of methods including post-translational modification, incorporation of the unnatural amino acid by a nonspecific enzyme, or chemical derivitization of existing amino acids.¹¹ (Figure 3.4) Alternatively, unnatural biomolecules can be incorporated

into cellular processes by growing the cells in media containing the biomolecule of interest. (Figure 3.5)

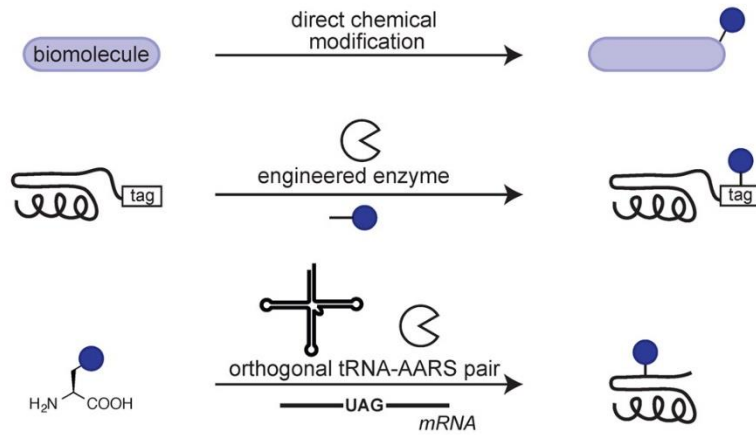


Figure 3.4. Incorporation of unnatural functional groups *via* direct modification, enzymatic incorporation, or RNA protein synthesis.

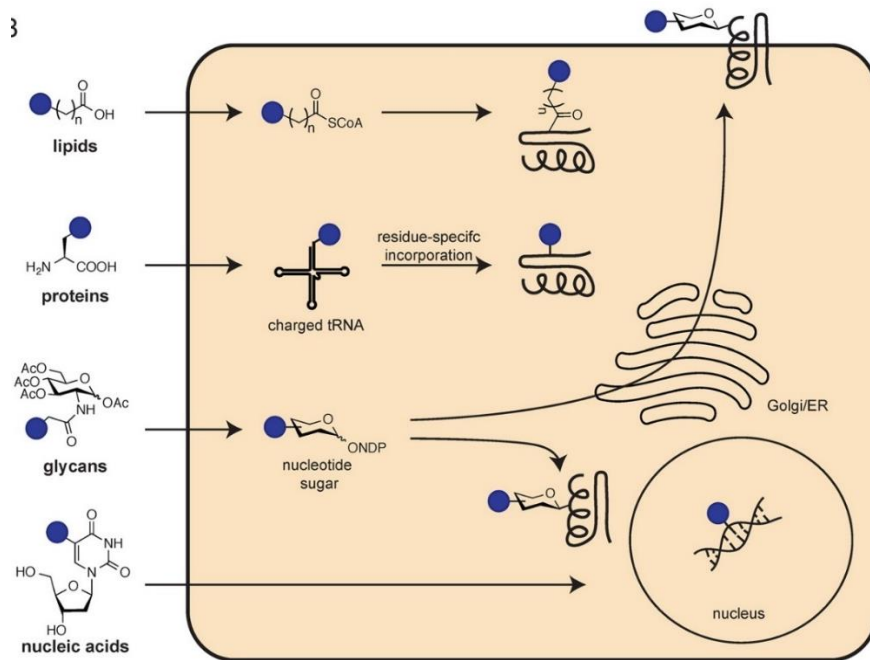


Figure 3.5. Incorporation of unnatural metabolites into cells.

With the popularization of bioorthogonal chemistries and the increasing ease of their introduction into living systems, there has been increased interest in bioorthogonal reactions that are orthogonal to each other. These mutually exclusive bioorthogonal reactions have the potential to be used for dual labeling, which greatly increases the scope of biomolecules and biomolecular interactions that can be studied.¹² (Figure 3.6) In one example, this dual labeling has been accomplished *via* introduction of an azide for SPAAC chemistry and a ketone for aminoether condensation in *E. Coli* cells; the majority of other research has been limited to the study of cell lysate or isolated proteins.

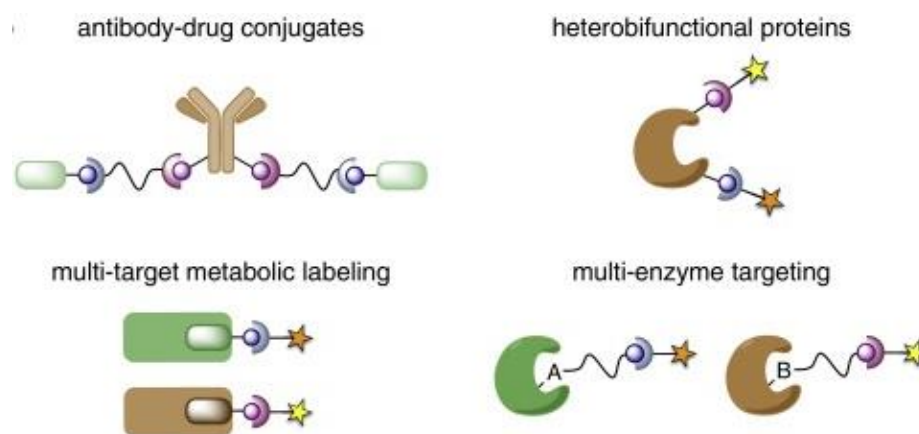


Figure 3.6. Uses of dual labeling.⁴

Our group was interested in exploring a new bioorthogonal scheme that we hoped to also be orthogonal to existing labeling schemes. For this, we turned to boronate ester formation, an area with which our group has previous experience.¹³

3.1.2 Boronic acids and diol binding

Boronic acids were first discovered to bind diols by Lorand and Edwards in the 1950s.¹⁴ Lorand and Edwards were trying to identify the structure of phenylboronic acid and found that the boronic acid readily formed complexes with diols. Due to its unique electronics, boron is able to exist in both a 6-electron trigonal planar geometry and an 8-electron tetrahedral geometry.

(Figure 3.7) Since these original studies, boronic acids have been extensively used to bind diols as sensors for saccharides, chiral shift reagents, and many other uses.^{13,15-17} (Figure 3.8)

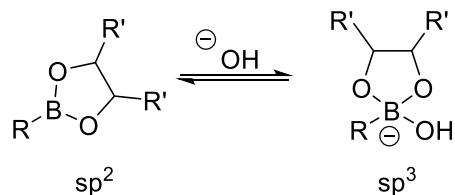


Figure 3.7. Geometries of boron.

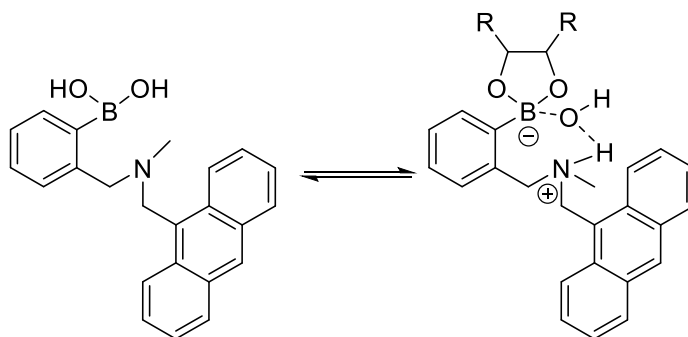
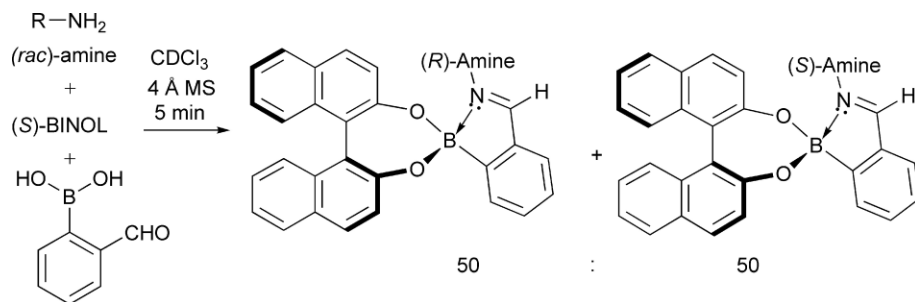


Figure 3.8. Boronic acid-based sensor for diols that exhibits a fluorescence turn-on upon binding.

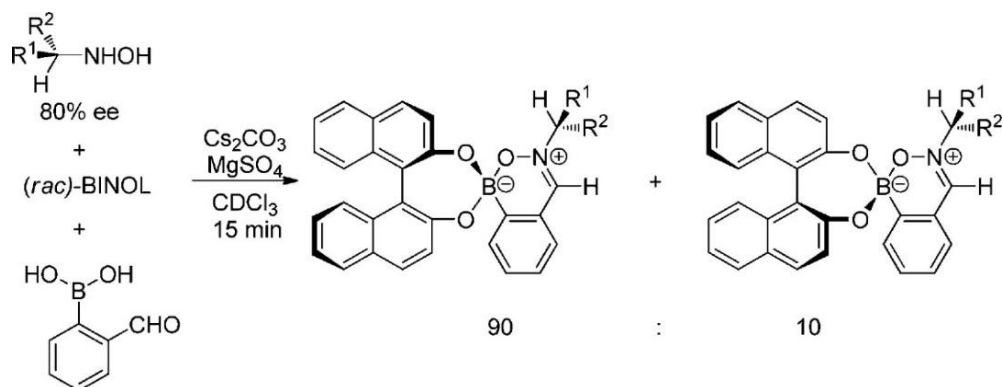
3.1.2.1 Tony James's amine and hydroxylamine assemblies

One use of boronate esters has been as chiral shift reagents for enantiomeric excess (*ee*) determination. In 2006, Tony James *et al.* published a three-component assembly utilizing 2-formylphenylboronic acid (2-FPBA), BINOL, and chiral amines.¹⁸ (Scheme 3.1) By using only one stereoisomer of BINOL, they were able to differentiate enantiomers of the amines through the formation of diastereomeric complexes which were visualized *via* ¹H-NMR. The reaction was rapid, occurring in only 5 minutes upon combination of the three components in CDCl₃ with 4 Å molecular sieves. Since 2006 this assembly has been studied by many research groups including ours.¹³



Scheme 3.1. James *et al.*'s amine assembly.

Tony James's research group followed up on this work with a similar assembly that incorporated chiral *N*-alkylhydroxylamines.¹⁹ This assembly included the introduction of Cs_2CO_3 and $MgSO_4$ instead of molecular sieves to remove water. (Scheme 3.2) This assembly was also used to determine *ee*. (Figure 3.9)



Scheme 3.2. James's hydroxylamine assembly.

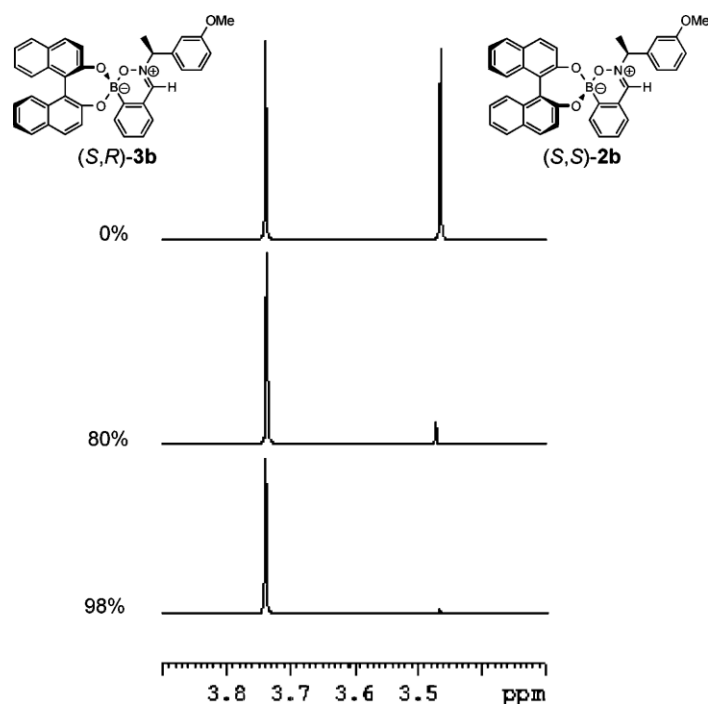


Figure 3.9. The different ^1H -NMR shift of two enantiomers upon binding to James's assembly.

3.2 APPLICATION OF BORONATE ESTER ASSEMBLIES TO A BIOORTHOGONAL PLATFORM

3.2.1 Transition to aqueous conditions

We hypothesized that this hydroxylamine assembly would be more water stable than the previous amine assembly. Similar aminoboronate assemblies have been studied and found, in protic solvents, to incorporate a solvent molecule to stabilize the boronate ester formation, as shown in Figure 3.8.¹³ We hypothesized that the hydroxyl group of the hydroxylamine would be analogous to the inserted solvent and increase the stability of these complexes in water. (Figure 3.10) Since we began work on this system, other groups have also found that these types of complexes are water stable.²⁰

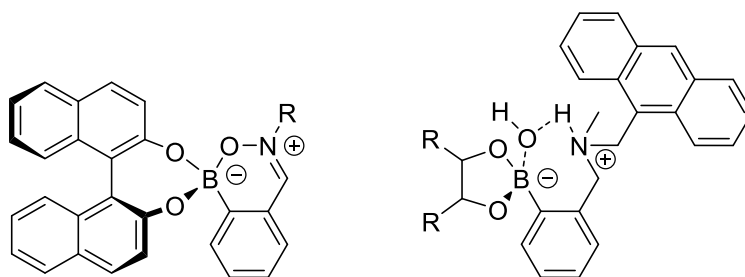
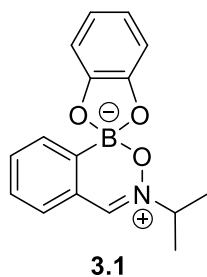


Figure 3.10. Side-by-side comparison of James's hydroxylamine assembly and a solvent inserted analogue.

We found that the assembly with catechol (**3.1**) was formed in water and methanol as well as pH 7 phosphate buffer, pH 5.5 acetate buffer, and pH 9 bicarbonate buffer. We also found that the addition of Na_2CO_3 was not necessary, although it did speed assembly formation.



Because boronic acids generally have even higher affinities to catechols than alkyl diols and are known to bind catechols relatively well in water, we realized that this three component assembly had the potential to assemble catechol-functionalized biological compounds, such as the amino acid L-DOPA, with virtually anything that carried a hydroxylamine group. Although L-DOPA is not one of the common 20 amino acids, it has been incorporated into both peptides and proteins,²¹ and therefore provides a readily available coupling partner in a semi-bioorthogonal fashion.

3.2.2 *N*-alkylhydroxylamines and *O*-alkylhydroxylamines

Another avenue we were interested in exploring was the difference in reactivity between *N*-functionalized hydroxylamines (RNHOH) and *O*-functionalized hydroxylamines, also called

aminoethers (RONH₂). (Figure 3.11) Aminoethers have been previously reported in bioorthogonal couplings, as mentioned in section 3.1.1, but have different reactivity than hydroxylamines; we hypothesized that these two isomeric functional groups could potentially be paired together while retaining their orthogonal reactivity.

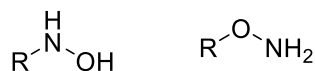


Figure 3.11. *N*-functionalized hydroxylamines (left) and *O*-functionalized hydroxylamines (right).

3.2.3 Reversibility studies

Previous assemblies with aminoboronate esters have been shown to form reversibly and are capable of exchanging both diol and amine under equilibrium conditions.¹⁵ We found that this system is not nearly as reversible as the previously reported amine assembly. Once formed and isolated, **3.1** is stable to neutral methanol/water mixtures for more than 72 hours with no detectable change by ¹H-NMR. Although the bound catechol is slowly displaced by hydroxyl groups under strongly basic conditions (pH=13) (Figure 3.12), the hydroxylamine addition is irreversible and stable to acid (pH=1), base (pH=13), and heat (50 °C) over 24 hrs.

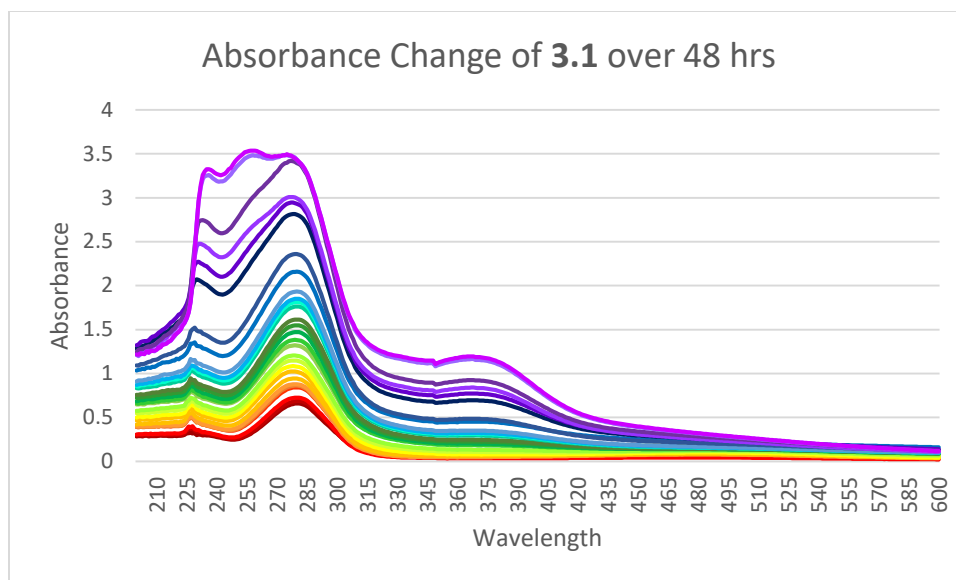
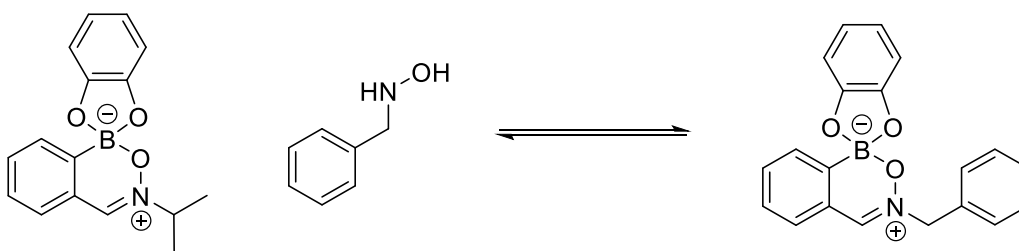
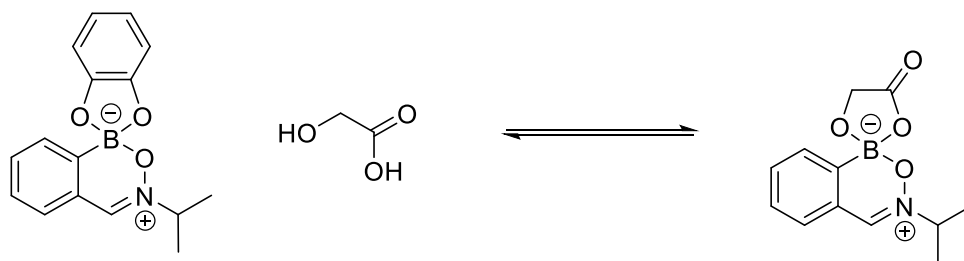


Figure 3.12. Absorbance change of **3.1** in water at basic pH over time. Time=0 is red and time=48 hours is purple. The released catechol is believed to cause the increase in absorbance.

Additionally, we found that over a period of 24 hours we were unable to exchange the hydroxylamine in **3.1** for *N*-benzylhydroxylamine. This was found to be the case under neutral aqueous conditions at room temperature or at 50 °C, and in CDCl₃ with or without base. (Scheme 3.3) We also found that we were unable to exchange the catechol with glycolic acid under neutral or basic aqueous conditions or with heating at 50 °C. (Scheme 3.4)



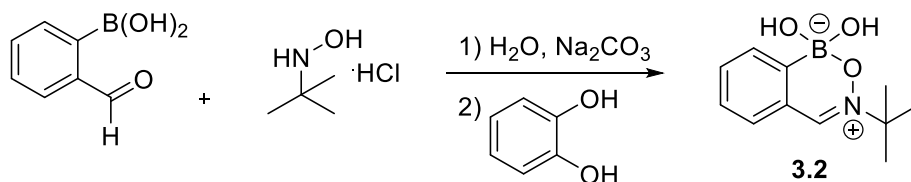
Scheme 3.3. Proposed hydroxylamine exchange.



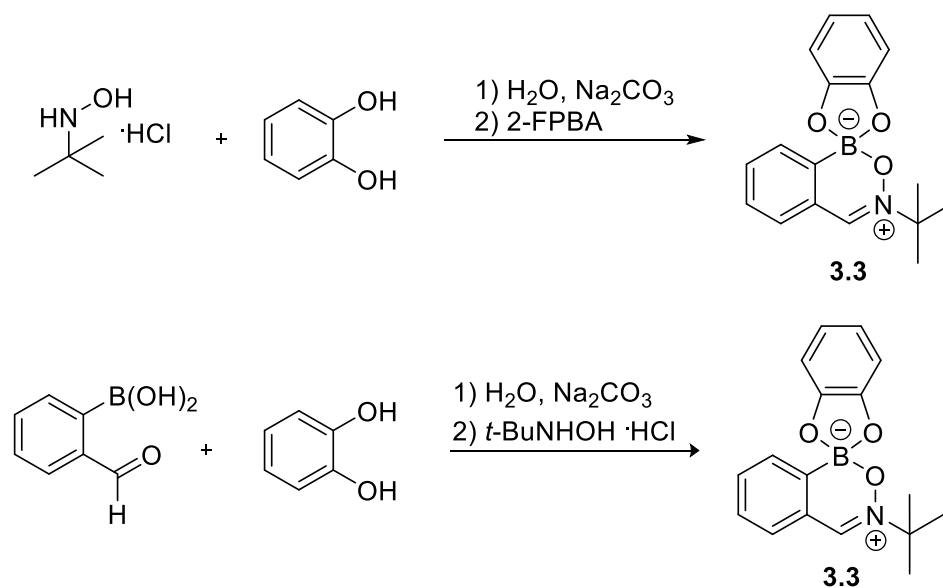
Scheme 3.4. Proposed diol exchange.

3.2.4 Mechanistic insight

We found that the order of addition in water was extremely important for formation of the desired complex. Combination of 2-FPBA with *N-t*-butylhydroxylamine hydrochloride (*t*-BuNHOH) prior to the addition of catechol forms the water complex **5.2**. (Scheme 3.5) *t*-BuNHOH was used instead of *i*PrNHOH due to commercial availability. Combination of catechol and 2-FPBA or catechol and *i*PrNHOH prior to the addition of the third component both result in complex formation of **3.3** with the desired catechol. (Scheme 3.6) This importance of order of addition leads us to propose that once the hydroxylamine binds, the diol, alcohol, or hydroxyl group attached to the boron atom is essentially locked in place.



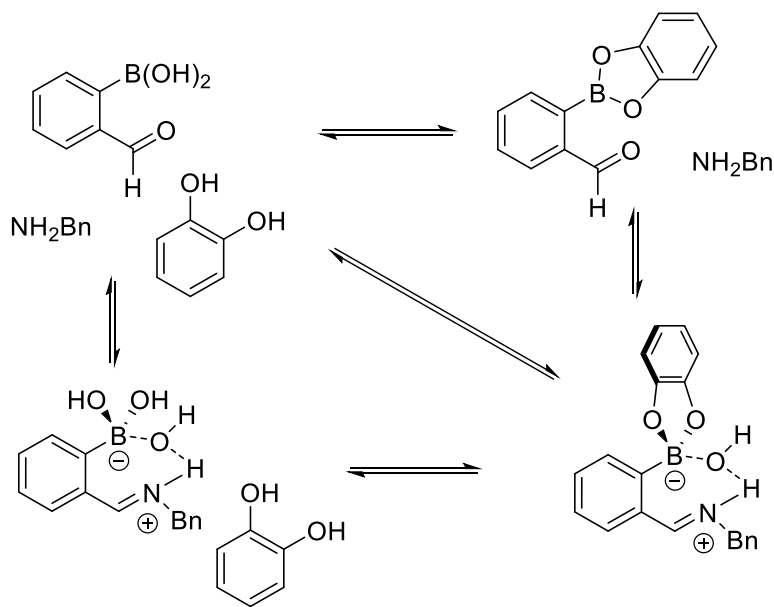
Scheme 3.5. Delayed addition of catechol provides only **3.2**.



Scheme 3.6. When catechol is one of the initially added reagents, **3.3** is formed.

3.2.5 ^{11}B -NMR studies “trapping” the amine complex

The amine complex mentioned in section 3.1.2.1 exists as a series of complex equilibria in aqueous and methanolic solutions. (Scheme 3.7) Our group has studied the equilibria between these three species before¹³ and we hypothesized that we would be able to add in a *N*-alkylhydroxylamine to “trap” the complexes that formed and bring a halt to the dynamic equilibrium.



Scheme 3.7. Complex equilibria of the three component amine assembly in water.

We studied the effects of combining benzylamine, catechol, 2-FPBA, and *t*-BuNHOH. We used a 50:50 CD₃OD:D₂O solution and ¹¹B- and ¹H-NMR spectroscopy to study the complex reaction. We monitored the effects of increasing amounts of benzylamine in the presence of 2-FPBA, followed by addition of catechol in the penultimate spectra, with the final spectra showing the addition of *t*-BuNHOH. (Figures 3.13 and 3.14) Both ¹H- and ¹¹B-NMR spectra show a gradual shift from 2-FPBA aldehyde to imine formation with benzylamine as more benzylamine is added. Upon addition of catechol, new peaks are observed, which correspond to the three component assembly with benzylamine, catechol, and 2-FPBA. Once *t*-BuNHOH was added, peaks corresponding to hydroxylamine complex are formed; $\delta = 8.5$ for ¹H-NMR and 5.0 for ¹¹B-NMR. Although we were clearly able to see the species from the complex equilibria of benzylamine, catechol, and 2-FPBA and we are able to see the formation of a hydroxylamine complex, in our solvent system we were unable to resolve which hydroxylamine complex we had formed, **3.2** or **3.3**. In order to identify the structure formed, we independently synthesized **3.2** and **3.3** and compared the ¹H- and ¹¹B-NMR spectra in methanol. (Figure 3.15) We found that, in our solvent system, **3.2** and **3.3** are indistinguishable in both the ¹H- and ¹¹B-NMR spectra.

Therefore, although we do seem to be able to “trap” the amine complex with the addition of the hydroxylamine and bring a halt to the equilibrium, we decided not to continue with this due to the difficulty of characterization.

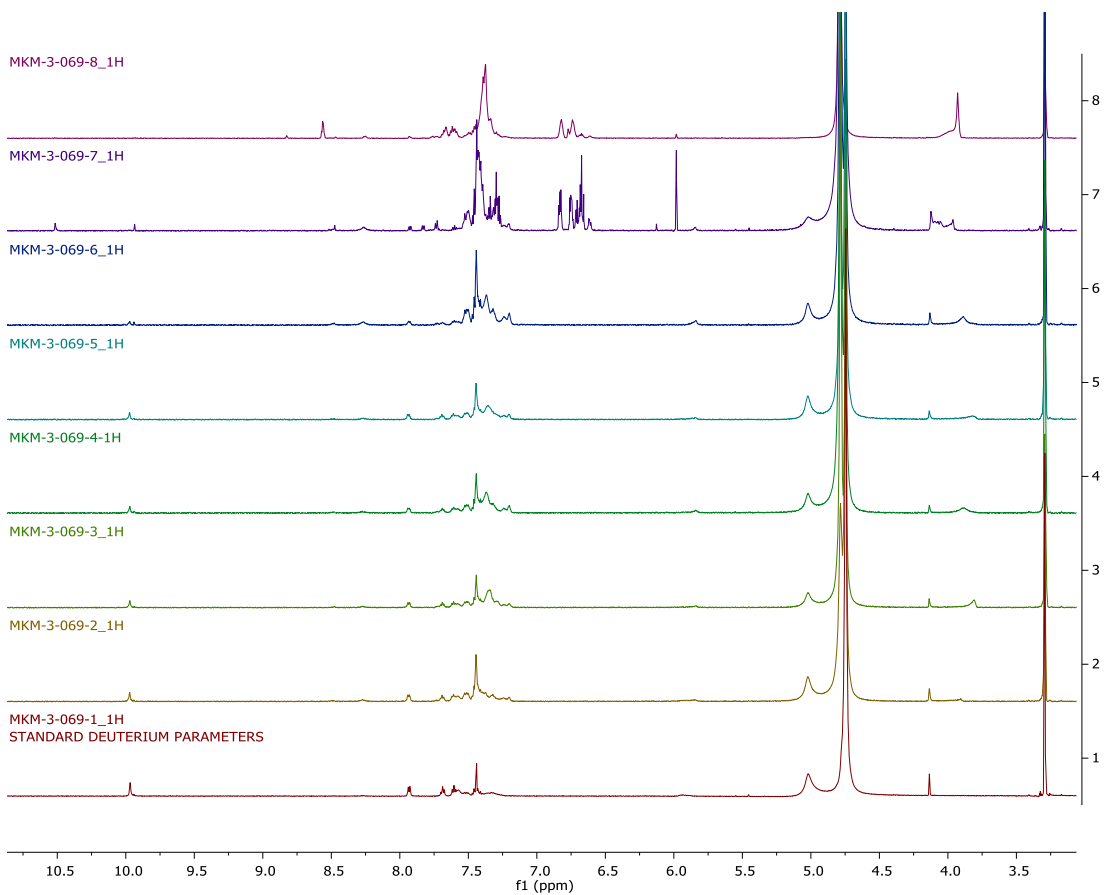


Figure 3.13. ¹H-NMR of 2-FPBA with increasing amounts of BnNH₂ (from bottom to top). The penultimate spectrum is the addition of catechol and the final spectrum is addition of *t*-BuNHOH.

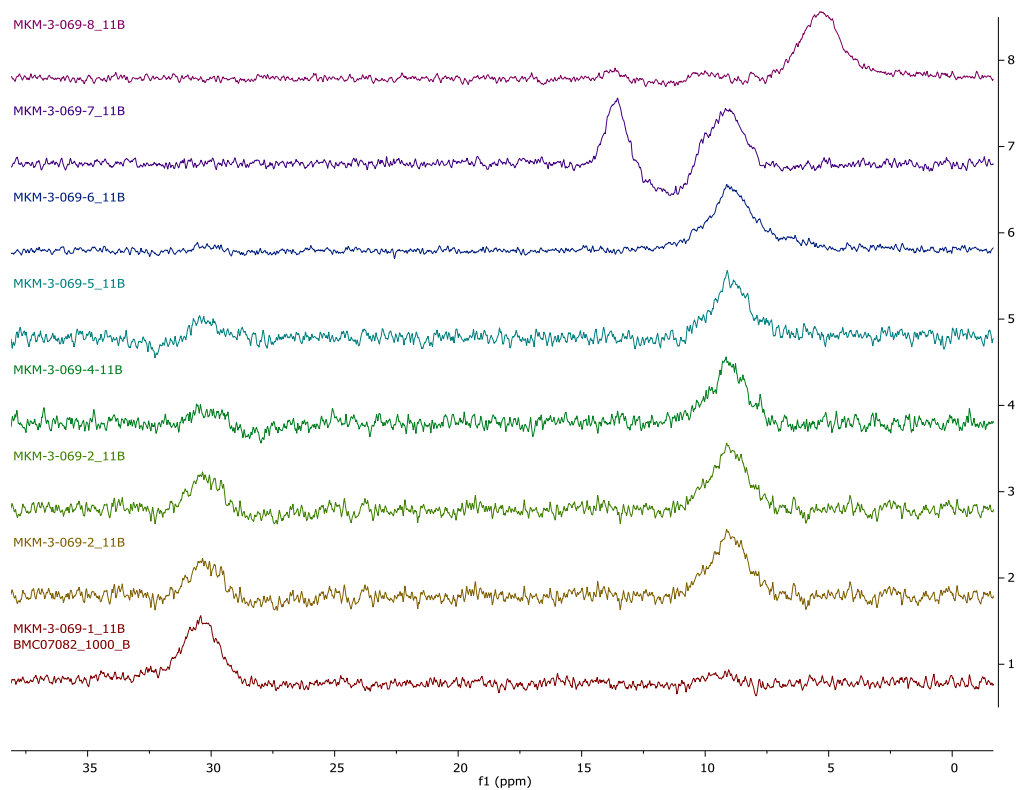


Figure 3.14. ^{11}B -NMR of 2-FPBA with increasing amounts of BnNH_2 (from bottom to top). The penultimate spectrum is the addition of catechol and the final spectrum is addition of tBuNHOH .

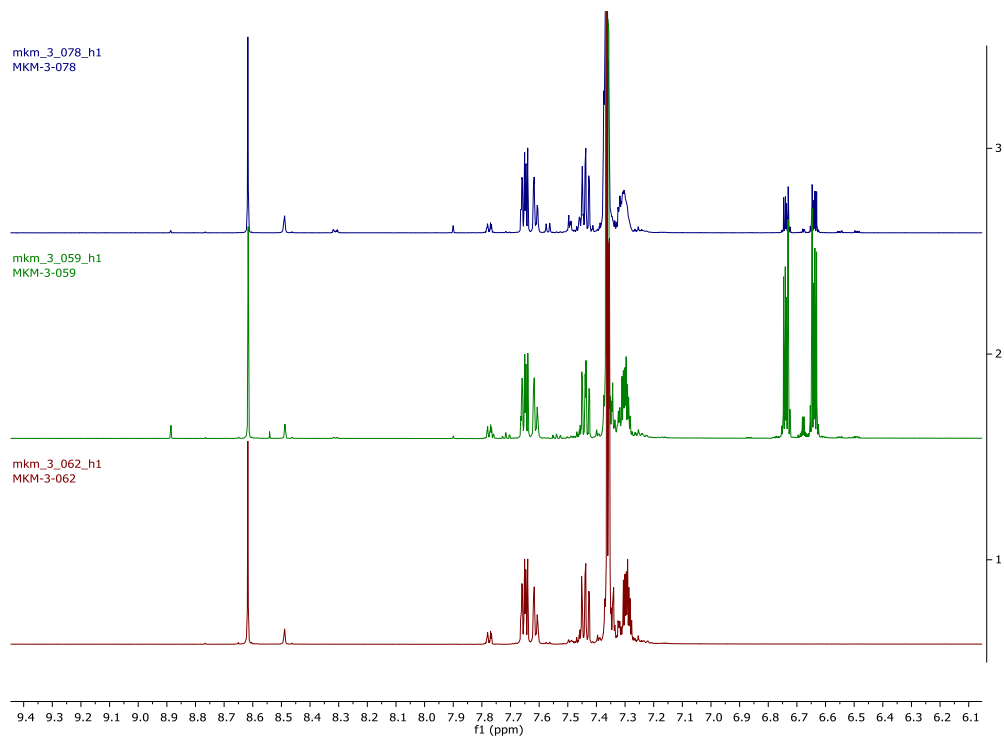


Figure 3.15. (from bottom) ¹H-NMR of **3.2**, **3.3**, and 1:1 **3.2:3.3**.

3.2.6 Substrate scope

Varying the substitution on the catechol provided a range of assemblies in addition to complex **3.3**. (Figure 3.16) We were also able to complex α -hydroxy acids and *cis*-cyclopentane-1,2-diol (Figure 3.17). The determining factors in assembly formation seem to be solubility of the diol and strength of binding to 2-FPBA. Those diols that were less soluble or bound poorly were unable to out-compete formation of complex **3.2**.

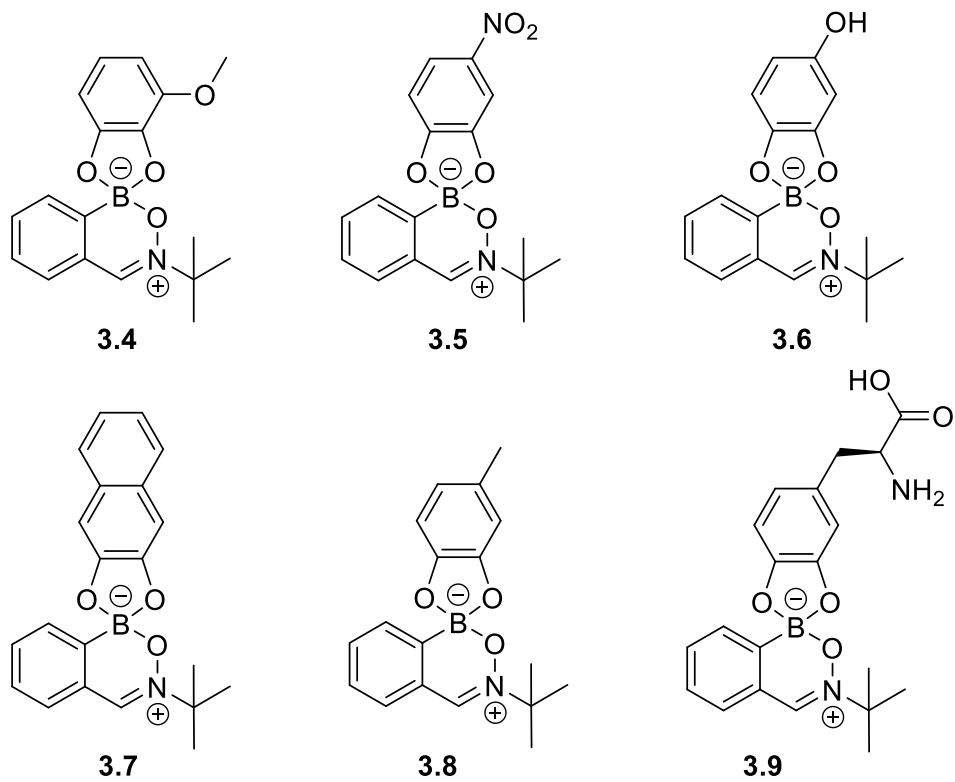


Figure 3.16. Complexes with a variety of catechol derivatives that were synthesized.

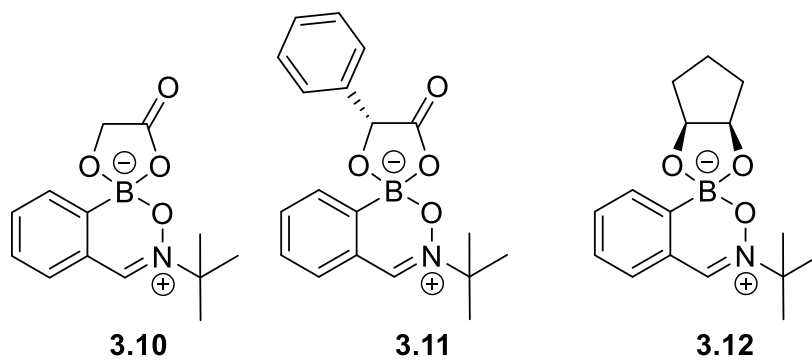
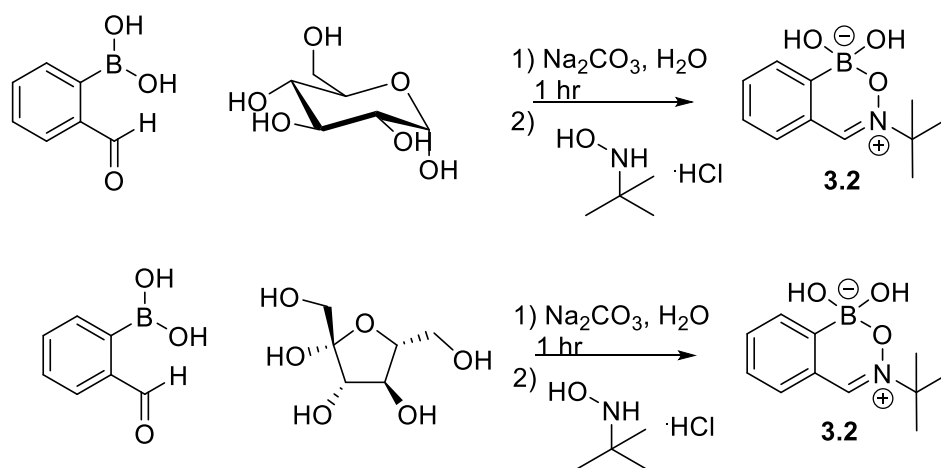


Figure 3.17. Assemblies formed with other diols.

3.2.6.1 Complex formation in the presence of saccharides

Although boronic acid complexes are most well known for their ability to reversibly bind sugars, the hydroxylamine assembly did not show the same affinity. We hypothesize that this is

due to the low binding constants of 2-FPBA with sugars without the assistance of an *ortho*-methylamine to increase binding. Even prior incubation of glucose or fructose with 2-FPBA and Na₂CO₃ yielded only complex **3.2**. (Scheme 3.8) In CDCl₃ with no competing water, we observed very little complex formation.

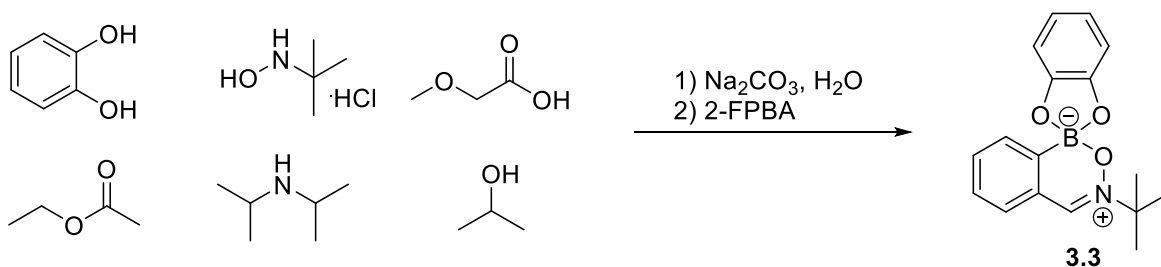


Scheme 3.8. Prior incubation with saccharides still leads to formation of **3.2**.

3.3 BIOORTHOGONALITY STUDIES

3.3.1 Orthogonality to common biological functional groups

With our desire to transition this assembly to a more bio-compatible platform, we tested the robustness of our complex to the presence of common biological functional groups. (Scheme 3.9) Catechol and *t*-BuNHOH were combined in a flask with isopropanol, diisopropylamine, ethyl acetate, and 2-methoxyacetic acid. These were stirred under basic conditions with no visible reaction as observed by ¹H-NMR after 12 hours. 2-FPBA was then added and complex formation was achieved in under 15 minutes as detected by ¹H-NMR. (Figure 3.18) We also combined **3.3** with *N*-acetylcysteine under basic conditions to see if the thiol would add in a nucleophilic fashion, with no addition observed, likely due to the thermodynamic stability of complex **3.3**.



Scheme 3.9. Formation of **3.3** in the presence of common biological functional groups.

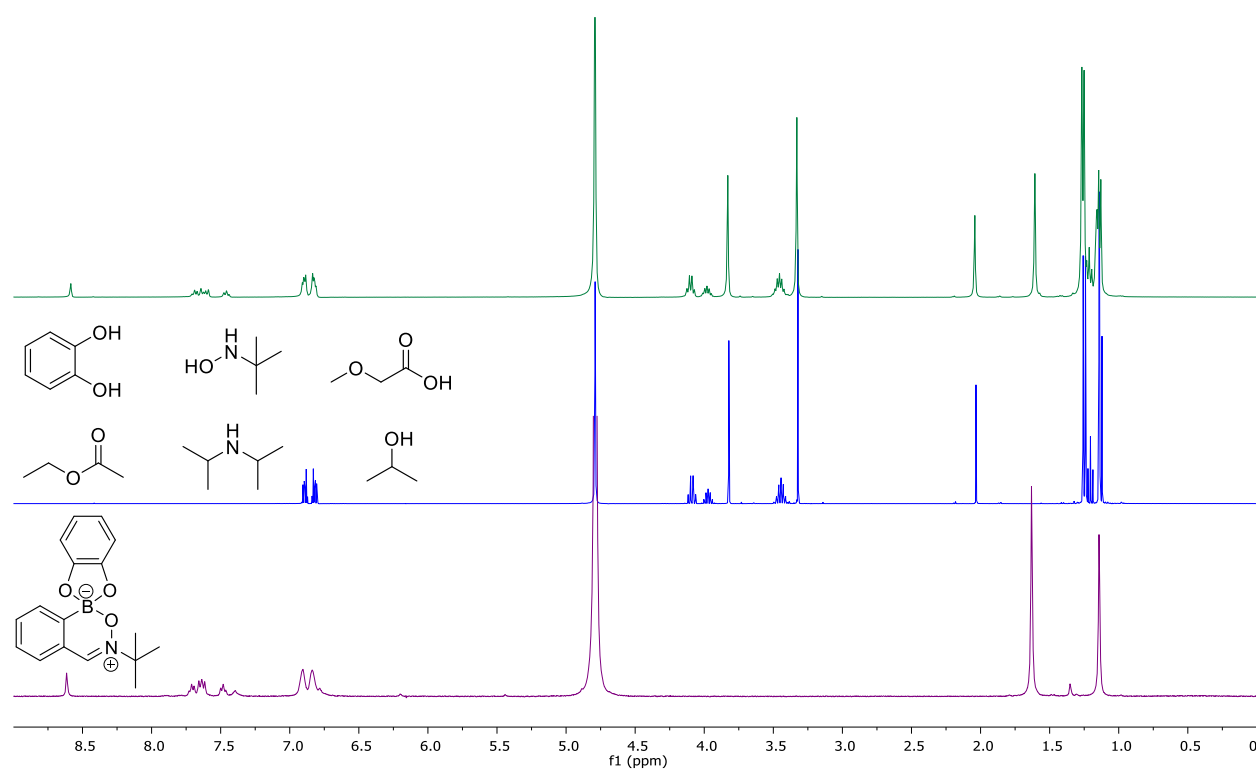
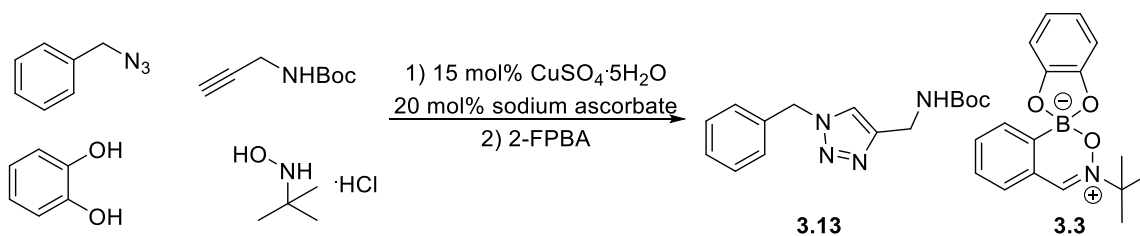


Figure 3.18. Corresponding ^1H -NMR spectra of species in Scheme 3.9. (*from bottom*) spectrum of **3.3**, spectrum of the reagents in Scheme 3.9 prior to addition of 2-FPBA, reaction in Scheme 3.9 after addition of 2-FPBA.

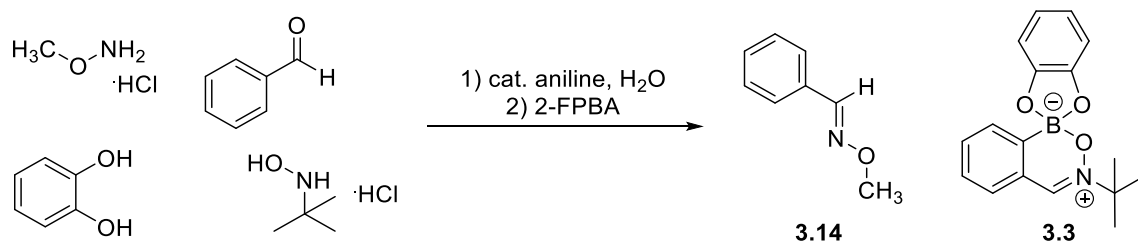
3.3.2 Orthogonality to other bioorthogonal reactions

We endeavored to test the orthogonality of our system with bioorthogonal reactions known in the literature. We chose the CuAAC and aminoether/aldehyde condensation as these are commonly used and the aminoether/aldehyde condensation provides an additional level of

complexity to our studies; we would be able to contrast the reactivity of *O*-alkyl hydroxylamine with a *N*-alkyl hydroxylamine. We found that our assembly formation was indeed compatible with other common bioorthogonal coupling reactions. (Schemes 3.10 and 3.11)



Scheme 3.10. Formation of **3.3** and **3.13** in the same reaction vessel.

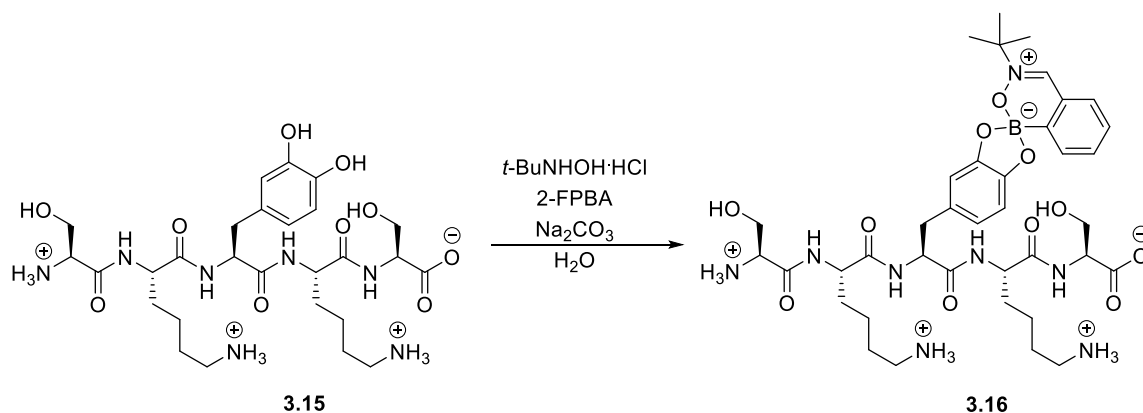


Scheme 3.11. Formation of **3.3** and **3.14** in the same reaction vessel.

3.3.3 Peptide labeling

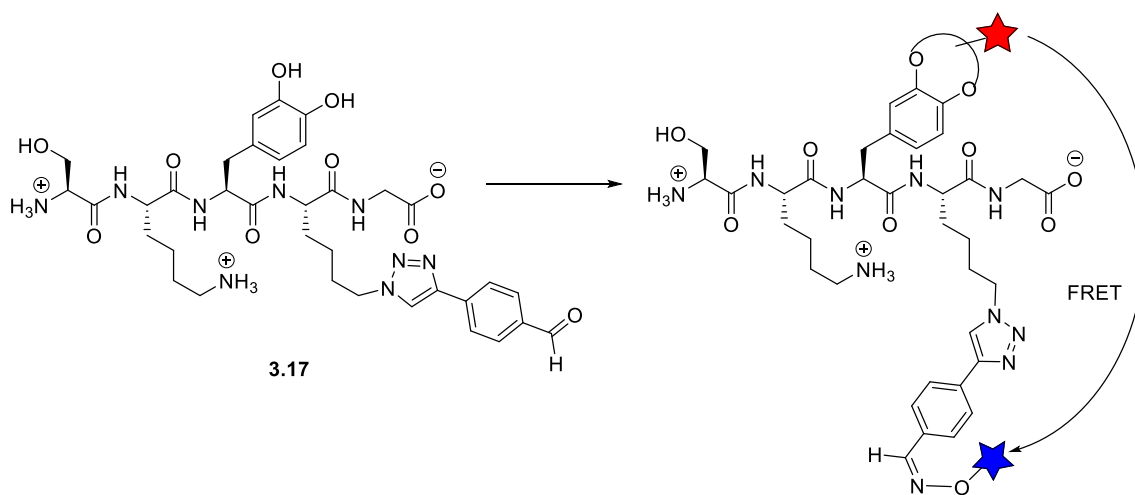
In order to further explore this opportunity for orthogonal reactivity, we moved to a peptide scaffold. We were able to label the non-essential amino acid L-DOPA. (Figure 3.16) L-DOPA is a naturally-occurring precursor to dopamine, norepinephrine, and epinephrine. It also happens to be an amino acid containing a catechol, which makes it appropriate for a labeling target.

We synthesized a short, pentameric peptide containing L-DOPA (**3.15**) and we were able to form a boronate ester complex with *t*-BuNHOH and 2-FPBA. (Scheme 3.12)



Scheme 3.12. Assembly formation with peptide **3.15**.

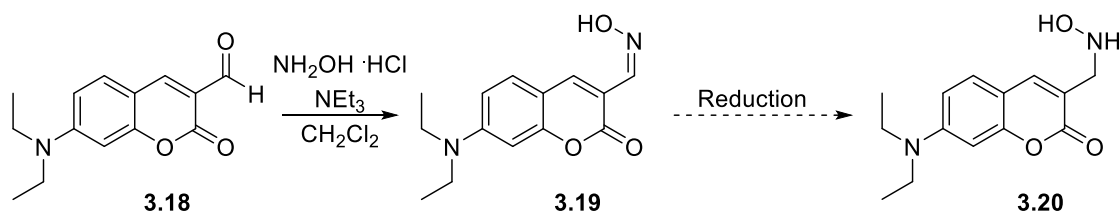
We then sought to show the orthogonality to other bioorthogonal reactions with a similar platform. Peptide **3.17** was synthesized using azidolysine in order to covalently attach an aldehyde. Our goal was to label the catechol and aldehyde with fluorophores which would display Förster resonance energy transfer (FRET), showing a successful dual-labeling.²² (Scheme 3.13) We chose a fluorescein/coumarin FRET pair which has been used in the literature.²²



Scheme 3.13. Schematic of proposed FRET interaction.

In order to label our peptide, we needed to synthesize a coumarin hydroxylamine, which proved more complicated than anticipated. Although addition of the oxime into the aldehyde of

3.18 was facile, the reduction of **3.19** proved difficult. (Scheme 3.14) Traditionally, this transformation is accomplished through reduction *via* sodium cyanoborohydride, but this was not a strong enough reductant for our system. (Table 3.1) We hypothesize that the oxime is far more stable than the hydroxylamine due to conjugation, which is corroborated by the air-oxidation of the hydroxylamine back to the oxime.

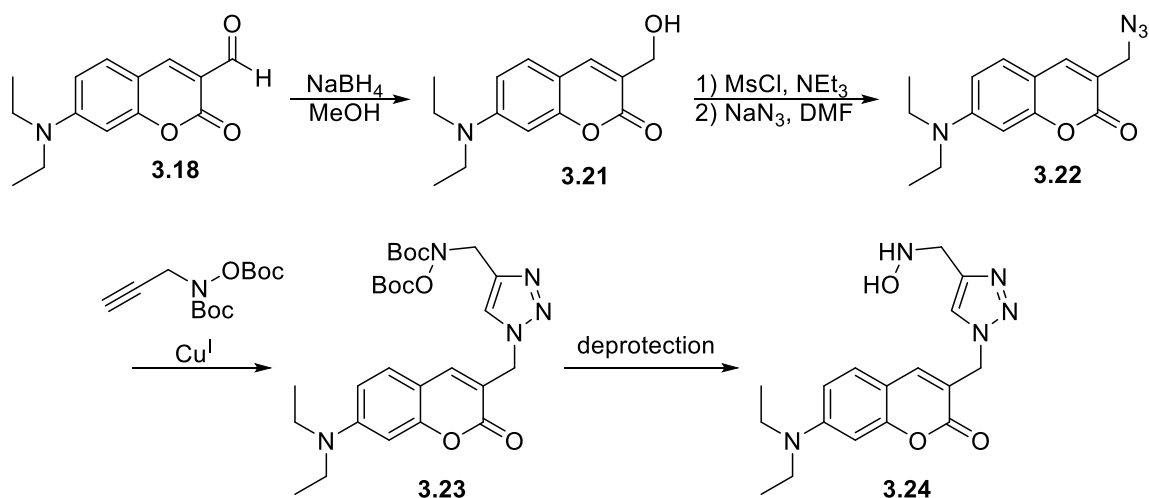


Scheme 3.14. Attempted synthesis of **3.20**.

Reduction Conditions	Result
NaCNBH ₃ (1 eq, 3 eq, or 5 eq), MeOH, pH=4	Only oxime recovered
NaBH ₄ , MeOH	Loss of fluorescence, probable decomposition of coumarin core
BH ₃ ·THF	Reduced to hydroxylamine which oxidized back upon work up

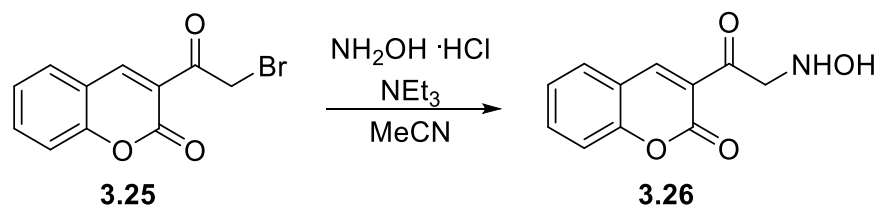
Table 3.1. Reduction conditions tried with **3.19**.

The next route we tried was through a CuAAC to add the hydroxylamine to the coumarin. (Scheme 3.15) We had previously found that unprotected primary hydroxylamines oxidized to the oxime in the presence of Cu^I so we used a di-Boc protected hydroxylamine. Reduction of **3.18** to the corresponding alcohol was readily achieved *via* sodium borohydride. Subsequent mesylation and displacement with azide needed to be conducted in one pot to prevent hydrolysis of the mesylate. The CuAAC proceeded well to yield **3.23**, but we found difficulty with the deprotection. Using 5% TFA resulted in no deprotection but neat TFA decomposed the molecule.



Scheme 3.15. Synthetic route to **3.24**.

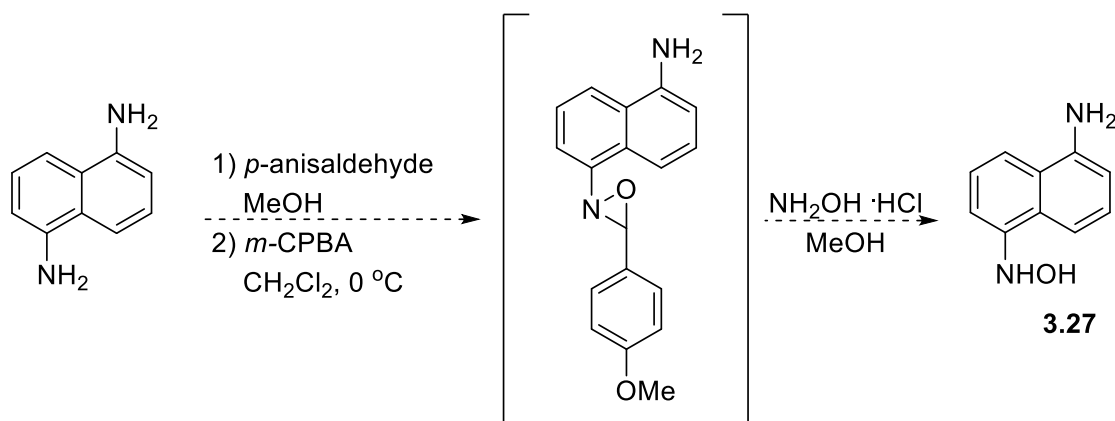
We next tried a simple $\text{S}_{\text{N}}2$ displacement using hydroxylamine hydrochloride and **3.25** under basic conditions. (Scheme 3.16) Although we isolated a product that contained the predicted $^1\text{H-NMR}$ spectrum of a $\text{S}_{\text{N}}2$ product of **3.25**, we were unable to characterize the end product due to poor ionization for MS and therefore unable to determine which nucleophile had added to **3.25**, hydroxylamine, chloride, or unwanted water. This led us to try another strategy since poor characterization would make our end goal of peptide labeling more difficult.



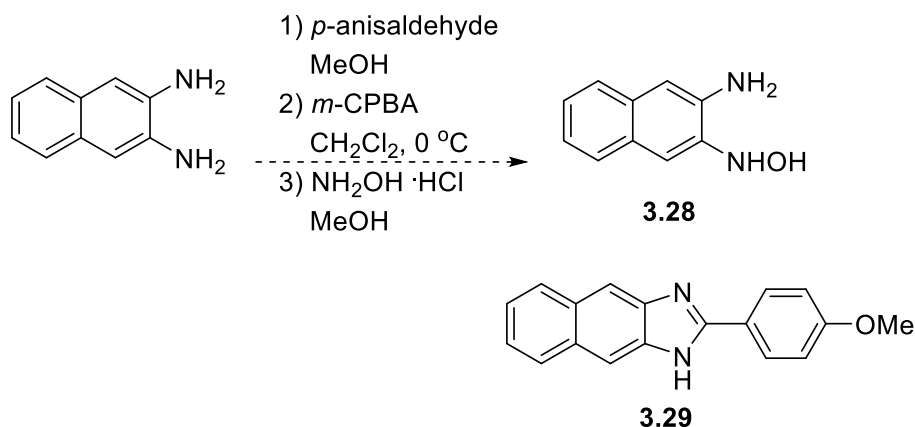
Scheme 3.16. Attempted synthesis of **3.26**.

Our next efforts at synthesizing a fluorescent hydroxylamine used diamionaphthalenes.¹⁹ (Schemes 3.17 and 3.18) Although naphthalene/fluorescein interactions have not been as studied as coumarin/fluorescein FRET pairs, we hypothesized that we would

still be able to observe an effect from the dual labeling of our peptide. 1,5-diaminonaphthalene showed no reaction whereas, under the same reaction conditions, 2,3-diaminonaphthalene formed a compound believed to be **3.29** based on LCMS analysis.

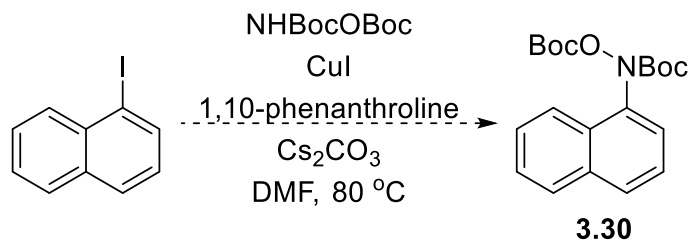


Scheme 3.17. Proposed synthesis of **3.27**.



Scheme 3.18. Proposed synthesis of **3.28** and structure of **3.29**.

Our final attempt at synthesizing a fluorescent hydroxylamine for peptide labeling was through a copper catalyzed coupling with 1-iodonaphthalene and *N,O*-di-Boc-hydroxylamine.²⁴ (Scheme 3.19) The reaction resulted in protonated naphthalene and no addition of the protected hydroxylamine. This is believed to be due to steric hindrance from the adjoining phenyl ring.



Scheme 3.19. Proposed synthesis of **3.30**.

3.3.4 Protein labeling studies

We wanted to apply this labeling technique to larger biomolecules, specifically proteins. We collaborated with the Ellington group to attempt to label a protein which had been modified with L-DOPA residues in place of Tyr residues. The protein we used was *E. coli* dihydrofolate reductase (DHFR). The *E. coli* cells were grown in media containing L-DOPA, thus producing a DHFR protein that contains L-DOPA residues in place of Tyr residues (DOPA-DHFR). The protein was isolated and then purified by fast protein liquid chromatography prior to labeling studies.

The protein was used at 1 mg/ml concentrations, which equates to approximately 50 μM . We initially tried labeling with a coumarin hydroxylamine, but found that this exhibited poor water solubility and bound the protein non-specifically after visualization of the results of gel electrophoresis. (Figure 3.19) Fluorescent protein can be visualized across each lane of the gel that contained the fluorophore, including controls that had no 2-FPBA or no DOPA-DHFR. Following this, we theorized that a fluorescein derivative would be more water soluble and less likely to bind the protein non-specifically. We tested unmodified fluorescein with the DOPA-DHFR and found that it showed no appreciable binding to the protein.

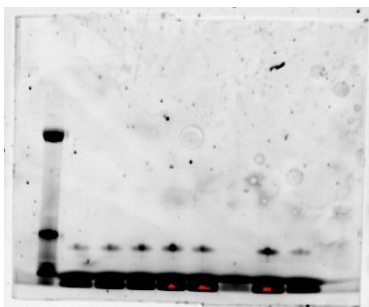
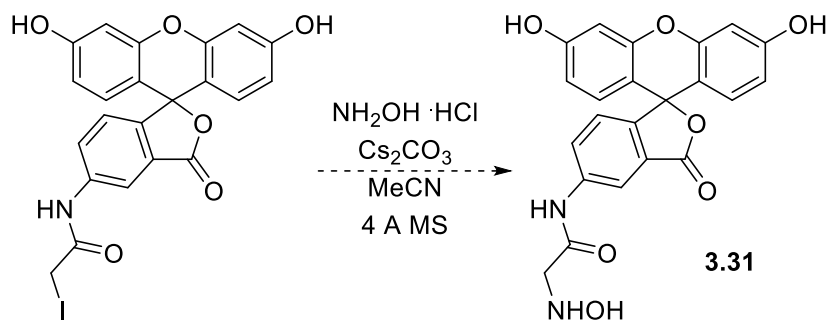
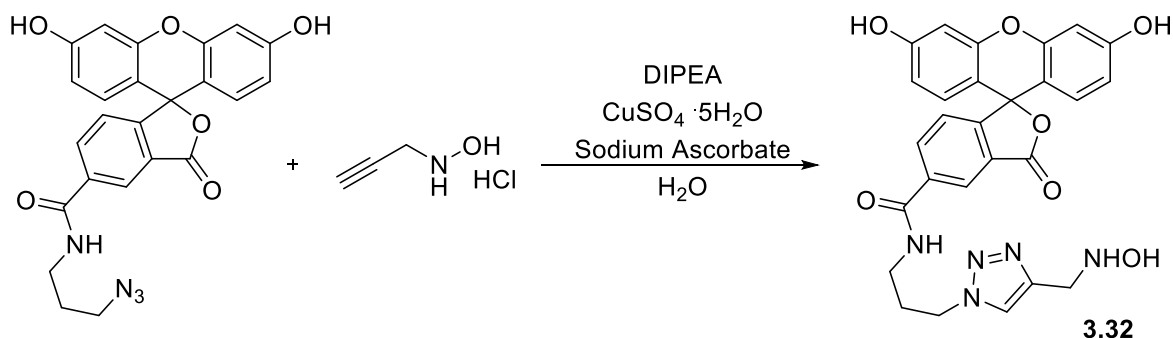


Figure 3.19. Visualization of the gel showing non-specific binding of the fluorophore to DOPA-DHFR and DHFR. (from left) 2-FPBA:NHOH:DOPA-DHFR in 1:1:1, 2:2:1, 3:3:1, 5:5:1, 5:5:DHFR, 5:0:1, 0:5:1, and 5:5:1 with glucose.

This prompted us to synthesize a fluorescein dye containing a hydroxylamine. (Scheme 3.20) Unfortunately, we observed no desired product from this method so we turned to CuAAC attachment of a hydroxylamine to our fluorophore. (Scheme 3.21) This CuAAC resulted in oxidation of the hydroxylamine to give the oxime, which was then reduced using NaBH_3CN in MeOH to give **3.32**.



Scheme 3.20. Proposed synthesis of **3.31**.



Scheme 3.21. Proposed synthesis of **3.32**.

Once we obtained this hydroxylamine fluorescein derivative, we again attempted to label the DOPA-DHFR. The protein was incubated with 2-FPBA for 1 hour prior to addition of the hydroxylamine fluorophore. Upon addition of the fluorophore, the protein was again incubated for 1 hour then analyzed using gel electrophoresis techniques. Unfortunately, we did not observe appreciable labeling of DOPA-DHFR by our system; although the DOPA-DHFR was separated from the reaction mixture by gel electrophoresis, all fluorophore stayed at the baseline.

3.4 CONCLUSION

In our research, we expanded upon a boronate ester assembly that was used for *ee* determination by utilizing it to bind a variety of catechol derivatives with the intention of transitioning to a bioorthogonal labeling scheme. We were able to demonstrate the orthogonality of our assembly against common biological functional groups and existing bioorthogonal reactions. The future directions of this project include coupling of a PEG-modified hydroxylamine provided by Prof. Jeff Bode at ETH-Zurich and modifying this system to work at lower concentrations.

3.5 EXPERIMENTALS

3.5.1 General procedures for synthesis of compounds

Synthesis of 2-propanone oxime: Acetone (136 mmol, 10 mL) and hydroxylamine hydrochloride (204 mmol, 14.2 g) were dissolved 272 mL H_2O . Sodium carbonate (245 mmol,

25.95 g) was slowly added. The reaction was stirred at room temperature overnight (~16 hrs). 100 mL of diethyl ether was added and the reaction mixture was transferred to a separatory funnel. The reaction mixture was extracted 5x with 50 mL of diethyl ether. The organic layers were combined, dried over MgSO₄, and filtered. The filtrate was concentrated under reduced pressure to give 9.13 g of fluffy white powder (92% yield). ¹H-NMR (400 MHz, CDCl₃): δ = 9.18 (bs, 1H), 1.89 (dd, 6H, *J*=1.79, 4.76 Hz).

Synthesis of *N*-isopropyl hydroxylamine: 2-propanone oxime (125 mmol, 9.13 g) was dissolved in 178 mL MeOH. NaBH₃CN (137 mmol, 8.63 g) was added followed by a small amount of bromocresol green as a colorimetric indicator. 2M HCl in MeOH was added dropwise (~70 mL) until a yellow-green color persisted (pH = 3.5-4). The reaction was stirred overnight and then solvent was removed under vacuum. The resulting residue was dissolved in CH₂Cl₂ and transferred to a separatory funnel. The reaction mixture was washed with saturated aqueous NaHCO₃ solution. The organic layer was dried over MgSO₄, and filtered. The filtrate was concentrated under reduced pressure to yield 1.76 g of the desired product (19% yield). ¹H-NMR (400 MHz, CDCl₃): δ = 3.15 (heptet, 1H, *J*=6.33 Hz), 1.08 (d, 6H, *J*=6.35 Hz).

Synthesis of **3.1**: *N*-isopropyl hydroxylamine (23 mmol, 1.76 g) was dissolved in 233 mL of CHCl₃. To this solution was added catechol (26 mmol, 2.84 g), 2-formylphenylboronic acid (23 mmol, 3.51 g), cesium carbonate (26 mmol, 8.46 g), and MgSO₄ (47 mmol, 5.63 g). The reaction mixture was stirred for 15 min at room temperature then filtered. Filtrate was concentrated under reduced pressure to yield a bright yellow solid in quantitative yield (6.46 g). ¹H-NMR (400 MHz, CDCl₃): δ = 8.12 (s, 1H), 7.78 (d, 1H, *J*=7.28 Hz), 7.70 (m, 1H), 7.46 (m, 2H), 6.82 (m, 2H), 6.76 (m, 2H), 4.30 (heptet, 1H, *J*=6.53), 1.58 (d, 6H, *J*=6.59). UV-Vis absorbance: λ_{max} = 284 nm (CHCl₃), 277 nm (H₂O).

Synthesis of **3.2**: 2-formylphenylboronic acid (2.00 mmol, 0.30 g) was dissolved in 20 mL of H₂O. To this was added *N*-*t*-butylhydroxylamine hydrochloride (1.99 mmol, 0.25 g). The reaction mixture was stirred for 15 min at room temperature then the solvent was removed under reduced pressure. The desired product was purified *via* reverse-phase chromatography (5-95%

CH₃CN/H₂O). ¹H-NMR (400 MHz, D₂O): δ = 8.44 (s, 1H), 7.54 (td, 1H, *J*=7.3,1.1 Hz), 7.47 (m, 2H), 7.30 (td, 1H, *J*=7.5,1.5 Hz), 1.46 (s, 9H). ¹³C-NMR (400 MHz, D₂O): δ = 143.52, 135.03, 139.90, 129.42, 127.60, 127.11, 69.16, 26.26. HRMS (ESI): *m/z* calculated for C₁₁H₁₆BNO₃ [M+Na]⁺: 244.1118, found 244.1116.

Representative procedure for compounds **3.3**, **3.4**, **3.5**, **3.7**, **3.8**, and **3.11**: Catechol (2.00 mmol, 0.22 g) was dissolved in 20 mL of H₂O. To this was added 2-formylphenylboronic acid (2.00 mmol, 0.30 g), followed by *N-t*-butylhydroxylamine hydrochloride (1.99 mmol, 0.25 g). The reaction mixture was stirred for 15 min at room temperature then filtered to give the desired product as a solid.

Representative procedure for compounds **3.6**, **3.10**, **3.12**: 1,2,4-trihydroxy benzene (2.00 mmol, 0.25 g) was dissolved in 20 mL of H₂O. To this was added 2-formylphenylboronic acid (2.00 mmol, 0.30 g), followed by *N-t*-butylhydroxylamine hydrochloride (1.99 mmol, 0.25 g). The reaction mixture was stirred for 15 min at room temperature then extracted with CH₂Cl₂. The organic layers were combined, dried over MgSO₄, and filtered. The filtrate was concentrated under reduced pressure to give the desired product. Purification was accomplished through reverse-phase chromatography (5-95% CH₃CN/H₂O).

3.3: ¹H-NMR (400 MHz, CDCl₃): δ = 8.22 (s, 1H), 7.76 (d, 1H, *J*=7.4 Hz), 7.68 (m, 1H), 7.46 (m, 2H), 6.80 (m, 2H), 6.73 (m, 2H), 1.62 (s, 9H). ¹³C-NMR (400 MHz, CDCl₃): δ = 151.61, 141.76, 135.94, 131.66, 128.86, 128.30, 126.92, 118.83, 109.40, 69.92, 27.39. HRMS (ESI): *m/z* calculated for C₁₇H₁₈BNO₃ [M+Na]⁺: 318.1275, found 318.1274. For crystallographic data and procedures, see Appendix.

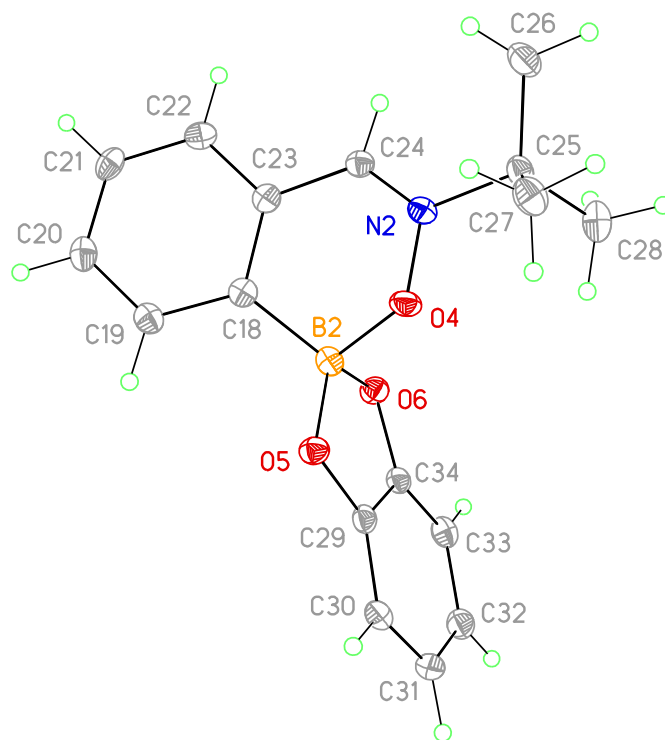


Figure 3.20. Crystal structure of **3.3**.

3.4: $^1\text{H-NMR}$ (400 MHz, CDCl_3): δ = 8.23 (s, 1H), 7.78 (dd, 1H, $J=7.29, 1.04$ Hz), 7.67 (ddd, 1H, $J=7.42, 6.53, 2.00$ Hz), 7.46 (m, 2H), 6.69 (dd, 1H, $J=8.34, 7.77$ Hz), 6.57 (dd, 1H, $J=7.74, 1.17$ Hz), 6.48 (dd, 1H, $J=8.37, 1.18$), 1.63 (s, 9H). $^{13}\text{C-NMR}$ (400 MHz, CDCl_3): δ = 152.71, 144.47, 141.71, 135.75, 131.87, 128.68, 128.18, 126.97, 118.23, 104.43, 103.86, 69.83, 56.15, 27.41. HRMS (ESI): m/z calculated for $\text{C}_{18}\text{H}_{20}\text{BNO}_4$ $[\text{M}+\text{Na}]^+$: 348.1381, found 348.1391.

3.5: $^1\text{H-NMR}$ (400 MHz, CDCl_3): δ = 8.29 (s, 1H), 7.84 (dd, 1H, $J=8.56, 2.50$ Hz), 7.74 (m, 2H), 7.62 (d, 1H, $J=2.48$ Hz), 7.54 (m, 2H), 6.76 (d, 1H, $J=8.56$ Hz), 1.67 (s, 9H). $^{13}\text{C-NMR}$ (400 MHz, CDCl_3): δ = 158.50, 151.82, 141.99, 136.46, 131.56, 129.28, 128.91, 126.58, 117.97, 107.96, 104.84, 70.32, 27.41. HRMS (CI): m/z calculated for $\text{C}_{17}\text{H}_{17}\text{BN}_2\text{O}_5$ $[\text{M}+\text{H}]^+$: 341.1303, found 341.1302.

3.6: $^1\text{H-NMR}$ (400 MHz, CD_3OD): $\delta = 8.62$ (s, 1H), 7.64 (m, 3H), 7.44 (td, 1H, $J=7.22, 1.68$ Hz), 6.57, (d, 1H, $J=8.50$ Hz), 6.30 (d, 1H, $J=2.80$ Hz), 6.11 (dd, 1H, $J=8.51, 2.83$), 1.69 (s, 9H). $^{13}\text{C-NMR}$ (400 MHz, CD_3OD): $\delta = 150.28, 141.94, 137.79, 134.22, 130.42, 129.80, 128.55, 127.23, 115.30, 115.20, 105.25, 102.93, 69.77, 26.33$. HRMS (CI): m/z calculated for $\text{C}_{17}\text{H}_{18}\text{BNO}_4$ $[\text{M}+\text{H}]^+$: 312.1407, found 312.1402.

3.7: $^1\text{H-NMR}$ (400 MHz, CDCl_3): $\delta = 8.23$ (s, 1H), 7.80 (m, 1H), 7.65 (m, 2H), 7.49 (m, 1H), 7.24 (m, 2H), 7.10 (s, 2H), 1.63 (s, 9H). $^{13}\text{C-NMR}$ (400 MHz, CDCl_3): $\delta = 152.39, 141.80, 136.17, 131.162, 130.07, 129.06, 128.57, 126.82, 126.40, 126.13, 123.85, 122.58, 104.00, 70.09, 27.37$. HRMS (ESI): m/z calculated for $\text{C}_{21}\text{H}_{20}\text{BNO}_3$ $[\text{M}+\text{Na}]^+$: 368.1432, found 368.1447.

3.8: $^1\text{H-NMR}$ (400 MHz, CDCl_3): $\delta = 8.22$ (s, 1H), 7.76 (m, 1H), 7.69 (ddd, 1H, $J=7.40, 6.26, 2.22$), 7.46 (m, 2H), 6.70 (d, 1H, $J=7.69$), 6.66 (d, 1H, $J=1.82$), 6.54 (dt, 1H, $J=7.64, 1.77$), 2.29 (s, 3H), 1.64 (s, 9H). $^{13}\text{C-NMR}$ (400 MHz, CDCl_3): $\delta = 151.57, 149.37, 141.68, 135.89, 131.68, 128.79, 128.25, 126.91, 118.64, 110.47, 108.64, 69.89, 27.39, 21.32$. HRMS (CI): m/z calculated for $\text{C}_{18}\text{H}_{21}\text{BNO}_3$ $[\text{M}+\text{H}]^+$: 310.1609, found 310.1580.

3.10: $^1\text{H-NMR}$ (400 MHz, CDCl_3): $\delta = 8.36$ (s, 1H), 7.70 (m, 2H), 7.52 (dt, 1H, $J=7.73, 0.98$ Hz), 7.44 (ddd, 1H, $J=7.73, 6.79, 1.77$ Hz), 4.44 (m, 2H), 1.56 (s, 9H). $^{13}\text{C-NMR}$ (400 MHz, CDCl_3): $\delta = 178.25, 142.55, 135.86, 130.95, 129.56, 128.51, 127.20, 69.84, 65.69, 27.21$. HRMS (CI): m/z calculated for $\text{C}_{13}\text{H}_{16}\text{BNO}_4$ $[\text{M}+\text{H}]^+$: 262.1251, found 262.1256.

3.11: (*a mixture of 2 diastereomers*) $^1\text{H-NMR}$ (400 MHz, CDCl_3): $\delta = 8.31$ (s, 1H), 8.28 (s, 1H), 7.84, (dd, 2H, $J=12.67, 7.37$), 7.75 (m, 4H), 7.66 (d, 2H, $J=7.64$), 7.50 (m, 4H), 7.38 (m, 4H), 7.30 (m, 2H), 5.53 (s, 1H), 5.51 (s, 1H), 1.67 (s, 9H), 1.58 (s, 9H). HRMS (CI): m/z calculated for $\text{C}_{19}\text{H}_{20}\text{BNO}_4$ $[\text{M}+\text{H}]^+$: 338.1564, found 338.1566.

3.12: $^1\text{H-NMR}$ (400 MHz, CD_3OD): $\delta = 8.64$ (s, 1H), 7.63 (m, 3H), 7.44 (m, 1H), 4.69 (m, 2H), 1.82 (m, 3H), 1.64 (s, 9H), 1.56 (m, 3H). $^{13}\text{C-NMR}$ (400 MHz, CD_3OD): $\delta = 134.34, 130.46, 129.84, 129.25, 127.46, 127.28, 73.59, 34.81, 29.93, 26.34, 22.19, 19.02$. HRMS (CI): m/z calculated for $\text{C}_{16}\text{H}_{22}\text{BNO}_3$ $[\text{M}+\text{H}]^+$: 288.1771, found 288.1770.

Synthesis of **3.9**: L-DOPA (2.00 mmol, 0.39 g) was dissolved in 20 mL of H₂O. To this was added 2-formylphenylboronic acid (2.00 mmol, 0.30 g), followed by *N*-*t*-butylhydroxylamine hydrochloride (1.99 mmol, 0.25 g). The reaction mixture was stirred for 15 min at room temperature then the solvent was removed under reduced pressure. The product was produced in a mixture with **3.2**. ¹H-NMR (400 MHz, D₂O): δ = 8.68 (s, 1H), 7.63 (m, 1H), 7.47 (m, 2H), 7.43 (m, 1H), 6.75 (d, 1H, *J*=7.93), 6.67 (m, 1H), 6.57 (dd, 1H, *J*=8.04,2.10 Hz), 3.70 (m, 1H), 2.82 (m, 2H), 1.58 (s, 9H). HRMS (ESI): *m/z* calculated for C₂₀H₂₃BN₂O₅ [M-H]: 381.1631, found 381.1635.

3.5.2 Exchange studies

Synthesis of *N*-benzyl oxime: Benzaldehyde (47.1 mmol, 4.8 mL) and hydroxylamine hydrochloride (70.5 mmol, 4.9 g) were dissolved in a RBF containing 94 mL H₂O and 40 mL methanol. Sodium carbonate (84.8 mmol, 8.99 g) was slowly added. The reaction was stirred at room temperature overnight (16 hrs). Diethyl ether was added and the reaction mixture was transferred to a separatory funnel. The reaction mixture was extracted 5x with diethyl ether. The organic layers were combined, dried over MgSO₄, and filtered. The filtrate was concentrated under reduced pressure to give 5.7 g of fluffy white powder (quant. yield). ¹H-NMR (400 MHz, CDCl₃): δ = 8.17 (s, 1H), 7.58 (m, 2H), 7.38 (m, 3H).

Synthesis of *N*-benzyl hydroxylamine: *N*-benzyl oxime (47 mmol, 5.7 g) was dissolved in 70 mL MeOH. NaBH₃CN (51.9 mmol, 3.26 g) was added followed by a small amount of bromocresol green as a colorimetric indicator. 2M HCl in MeOH was added dropwise until a yellow-green color persisted (pH = 3.5-4). The reaction was stirred overnight and then solvent was removed under vacuum. The resulting residue was dissolved in CH₂Cl₂ and transferred to a separatory funnel. The reaction mixture was washed with saturated aqueous NaHCO₃ solution. The organic layer was dried over MgSO₄, and filtered. The filtrate was concentrated under reduced pressure and purified *via* column chromatography (5% methanol in CH₂Cl₂) to yield 2.5

g of the desired product (43% yield). ¹H-NMR (400 MHz, CDCl₃): δ = 7.34 (m, 5H), 3.78 (s, 2H).

Exchange of **3.1** with *N*-benzyl hydroxylamine: **3.1** (0.178 mmol, 50 mg) and *N*-benzyl hydroxylamine (0.650 mmol, 80 mg) were combined in 2 mL H₂O. The reaction mixture was stirred for 24 hours at room temperature or 50 °C, then extracted with CH₂Cl₂ 2x. The organic layers were combined and solvent removed under reduced pressure to show no exchange.

Exchange of **3.1** with glycolic acid: **3.1** (0.178 mmol, 50 mg) and glycolic acid (0.650 mmol, 54 mg) were combined in 2 mL H₂O. The reaction mixture was stirred for 24 hours at room temperature or 50 °C, then extracted with CH₂Cl₂ 2x. The organic layers were combined and solvent removed under reduced pressure to show no exchange.

3.5.3 Mechanistic Studies

Delayed addition of *t*-BuNHOH: 2-FPBA (0.080 mmol, 12 mg), catechol (0.080 mmol, 8.8 mg), and Na₂CO₃ (0.080 mmol, 8.4 mg) were combined in 1 mL D₂O. After an hour *t*BuNHOH (0.080 mmol, 10 mg) was added and **3.3** formed.

Delayed addition of catechol: 2-FPBA (0.080 mmol, 12 mg), *t*-BuNHOH (0.080 mmol, 10 mg), and Na₂CO₃ (0.080 mmol, 8.4 mg) were combined in 1 mL D₂O. **3.2** formed. After an hour catechol (0.080 mmol, 8.8 mg) was added. No exchange observed.

3.5.4 ¹¹B-NMR studies

Representative procedure: Stock solution of 70 mM were made for each reagent. 2-FPBA (100 μL, 10 mM), catechol (100 μL, 10 mM), and benzylamine (120 μL, 12 mM) were combined in a quartz NMR tube with 380 μL of 1:1 D₂O:CD₃OD. This was stored in a refrigerator overnight. Then *t*-BuNHOH (100 μL, 10 mM) was added. After 1 hour, ¹H-NMR and ¹¹B-NMR spectra were taken.

3.5.5 Stability to other functional groups

Addition of *N*-Acetylcysteine into **3.1** in ethanol: **3.1** (0.356 mmol, 0.10 g) was dissolved in ethanol (4 mL). To this was added K₂CO₃ (0.534 mmol, 49 mg) and *N*-acetylcysteine (0.356

mmol, 58 mg). The reaction mixture was stirred for 24 hours then filtered. ¹H-NMR showed only **3.1**.

Addition of *N*-Acetylcysteine into **3.1** in CD₃OD: **3.1** (0.010 mmol, 2.75 mg) was dissolved in CD₃OD (1 mL). To this was added 1,8-Diazabicyclo[5.4.0]undec-7-ene (DBU) (0.010 mmol, 1.50 mg) and *N*-acetylcysteine (0.010 mmol, 1.60 mg). The reaction mixture was monitored by ¹H-NMR which showed no appreciable change over 24 hours.

Formation of **3.3**: *t*-BuNHOH (0.080 mmol, 10 mg), catechol (0.080 mmol, 8.8 mg), methoxyacetic acid (0.080 mmol, 6.1 μL), isopropanol (0.080 mmol, 6.1 μL), ethyl acetate (0.080 mmol, 7.8 μL), diisopropylamine (0.080 mmol, 11.2 μL), and Na₂CO₃ (0.080 mmol, 8.4 mg) were combined in 1 mL D₂O. After ¹H-NMR taken, 2-FPBA (0.080 mmol, 12 mg) added, resulting in formation of **3.3**.

3.5.6 Stability to current bioorthogonal reactions

Synthesis of **3.13**: Benzylamine (0.370 mmol, 50 mg), *N*-Boc-propargylamine (0.370 mmol, 58 mg), copper (II) sulfate pentahydrate (0.056 mmol, 14 mg), and sodium ascorbate (0.076 mmol, 15 mg) were combine in a flask with 38 mL H₂O. This was stirred under N₂ for 16 hours then transferred to a separatory funnel. The reaction mixture was extracted 3x with CH₂Cl₂, the organic layers combined and washed with saturated aqueous EDTA. The organic layer was dried over MgSO₄, and filtered. The filtrate was concentrated under reduced pressure to give **3.13**. ¹H-NMR (400 MHz, CDCl₃): δ = 7.43 (s, 1H), 7.35 (m, 3H), 7.24 (m, 2H), 5.48 (s, 5.48), 4.35 (d, 2H, *J*=5.87), 1.40 (s, 9H).

Synthesis of **3.3** and **3.13**: Benzylamine (0.370 mmol, 50 mg), *N*-Boc-propargylamine (0.370 mmol, 58 mg), copper (II) sulfate pentahydrate (0.056 mmol, 14 mg), sodium ascorbate (0.076 mmol, 15 mg), *t*-BuNHOH (0.370 mmol, 47 mg), and catechol (0.370 mmol, 41 mg) were combine in a flask with 38 mL H₂O. This was stirred under N₂ for 16 hours then 2-FPBA (0.370 mmol, 56 mg) was added. After 1 hour, the reaction mixture transferred to a separatory funnel and extracted 3x with CH₂Cl₂. The organic layers were combined and washed with saturated

aqueous EDTA. The organic layer was dried over MgSO₄, and filtered. The filtrate was concentrated under reduced pressure to give **3.13** and **3.3**.

Synthesis of **3.14**: *O*-methylhydroxylamine hydrochloride (0.075 mmol, 6.26 mg) and benzaldehyde (0.075 mmol, 7.19 mg) were combined in a borosilicate NMR tube with catalytic aniline (0.0075 mmol, 0.7 mg) and 0.75 mL D₂O. Within 30 minutes, starting material had disappeared and oxime **3.14** had formed as observed by ¹H-NMR.

Synthesis of **3.3** and **3.14**: *O*-methylhydroxylamine hydrochloride (0.037 mmol, 3.1 mg), benzaldehyde (0.037 mmol, 7.7 μL), *t*-BuNHOH (0.037 mmol, 9.0 mg), and catechol (0.037 mmol, 8.3 mg) were combined in a borosilicate NMR tube with catalytic aniline (0.0075 mmol, 0.7 mg) and 1.5 mL D₂O. Within 30 minutes, starting material had disappeared and oxime **3.14** had formed as observed by ¹H-NMR. 2-FPBA (0.037 mmol, 11 mg) was added and within 15 min, formation of **3.3** was observed.

3.5.7 Peptide synthesis

Peptides were synthesized on a CEM microwave peptide synthesizer using Fmoc-protected amino acids and Wang resins with the first residue covalently attached. Following synthesis, the peptide on the resin was transferred to a fritted syringe and washed 3x each with glacial acetic acid, CH₂Cl₂, and methanol, successively.

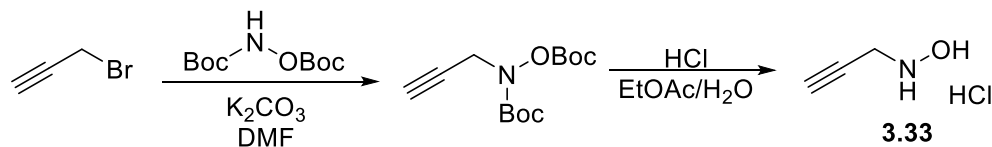
Peptide **3.15** was cleaved from the resin *via* incubation with 10 mL of a cleaving solution (95% trifluoroacetic acid, 2.5% H₂O, 2.5% triisopropylsilane). After 2.5 hrs, this was filtered through a fritted syringe. The filtrate was collected and the solvent was evaporated to 3 mL. and cold diethylether was added to precipitate the peptide. The vial was capped and centrifuged at 7500 rpm for 10 min at 1 °C. The ether was decanted and the peptide lyophilized. The peptide was then purified *via* HPLC. ¹H-NMR (400 MHz, D₂O): δ = 6.63 (d, 1H, *J*=8.10 Hz), 6.55 (d, 1H, *J*=2.02 Hz), 6.48 (dd, 1H, *J*=8.15,2.09 Hz), 4.36 (dd, 1H, *J*=8.75,6.99 Hz), 4.29 (dd, 1H, *J*=4.53,3.99 Hz), 4.13 (dd, 1H, *J*=7.83,6.42 Hz), 4.07 (t, 1H, *J*=7.15 Hz), 3.96, dd, 1H,

$J=5.41, 4.58$ Hz), 3.75-3.85 (m, 3H), 3.70 (dd, 1H, $J=11.75, 4.01$ Hz), 2.61-2.83 (m, 6H), 1.38-1.66 (m, 8H), 1.19 (m, 2H), 1.05 (m, 2H).

Peptide complex **3.16**: Peptide 3.15 (0.013 mmol, 8.41 mg), *t*-BuNHOH (0.013 mmol, 1.68 mg), and Na_2CO_3 (0.013 mmol, 1.42 mg) were combined in a borosilicate NMR tube with 0.75 mL D_2O . 2-FPBA (0.013 mmol, 2.01 mg) was added and complex formation observed by $^1\text{H-NMR}$. $^1\text{H-NMR}$ (400 MHz, D_2O): δ = 8.45 (s, 1H), 7.55 (td, 1H, $J=7.34, 1.17$ Hz), 7.47 (m, 2H), 7.32 (td, 1H, $J=7.51, 1.45$ Hz), 6.67 (d, 1H, $J=8.10$ Hz), 6.60 (d, 1H, $J=2.02$ Hz), 6.52 (dd, 1H, $J=8.15, 2.09$ Hz), 4.42 (m, 1H), 4.15 (dd, 1H, $J=7.89, 6.23$ Hz), 4.08 (m, 2H), 3.84 (m, 1H), 3.73 (d, 2H, $J=7.45$ Hz), 3.68 (d, 2H, $J=4.87$ Hz), 2.65-2.92 (m, 6H), 1.38-1.74 (m, 19H), 1.21 (m, 2H).

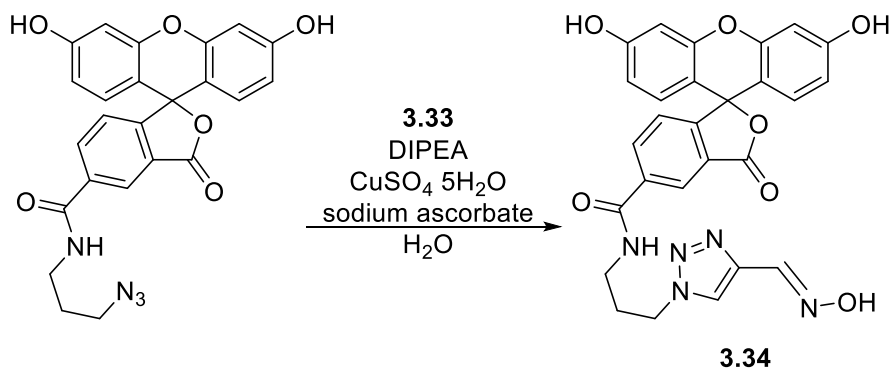
Peptide **3.17** was synthesized using Fmoc protected azidolysine and then acetylbenzaldehyde was covalently attached through CuAAC while still on the resin. 4-ethynylbenzaldehyde (4 eq), tris[(1-benzyl-1H-1,2,3-triazol-4-yl)methyl]amine (TBTA) (0.5 eq), copper (I) iodide (0.25 eq), and sodium ascorbate (0.5 eq) were added to peptide **3.17** under nitrogen in 3 mL DMF. This was wrapped in aluminum foil then placed on the shaker for 16 hrs. Resin was washed 3x with DMF, CH_2Cl_2 , and methanol, successively. Then the peptide was cleaved using 10 mL of cleaving solution (95% trifluoroacetic acid and 5% H_2O), followed by filtration through a fritted syringe. The filtrate was evaporated and the residue purified via HPLC. HRMS (ESI): m/z calculated for $\text{C}_{41}\text{H}_{59}\text{N}_{11}\text{O}_{11}$ $[\text{M}+\text{H}]^+$: calculated 882.4468, found 882.4446.

3.5.8 Fluorophore synthesis



Scheme 3.22. Synthesis of **3.33**.

Synthesis of **3.33**: K_2CO_3 (5.82 mmol, 0.805 g) and *N,O*-diBoc-hydroxylamine (4.29 mmol, 1.00 g) were dissolved in 36 mL anhydrous DMF. Propargyl bromide (0.529 mL, 80% in toluene) was gradually added and the reaction was stirred at room temperature for 16 hours. Water was added and the mixture transferred to a separatory funnel. The mixture was extracted 3x with CH_2Cl_2 . The organic layers were combined, dried over MgSO_4 , and filtered. Solvent was removed under reduced pressure to give *N,O*-diBoc-propargylhydroxylamine in quantitative yield which was carried on to the next step with no further purification. *N,O*-diBoc-propargylhydroxylamine (4.28 mmol, 1.16 g) was dissolved in 2:1 ethyl acetate:water (30 mL). 10.3 mL of 12 M HCl was added and this was stirred over 3 hours. Solvent was evaporated to yield a yellow oil (293 mg, 64%). $^1\text{H-NMR}$ (400 MHz, D_2O): $\delta = 4.00$ (s, 2H), 2.85 (s, 1H).



Scheme 3.23. Synthesis of **3.34**.

Synthesis of **3.34**: Azidofluorescein (0.015 mmol, 7 mg), **3.33** (0.017, 5.03 mg), diisopropylethylamine (0.018 mmol, 8.9 μL), copper (II) sulfate pentahydrate (0.002 mmol, 1.6 mg), and sodium ascorbate (0.003 mmol, 1.7 mg) were combined in 4 mL water. This was stirred for 7 days at room temperature. LCMS showed oxime and unreacted starting material. The solvent was lyophilized and the crude reaction carried straight to reduction.

Synthesis of **3.32**: **3.34** was dissolved in methanol (1 mL) and NaBH_3CN (4 eq) added. Reaction mixture was stirred overnight (16 hrs) and then the solvent was removed under reduced

pressure. The desired product was purified *via* reverse-phase chromatography (CH₃OH/H₂O). HRMS (ESI): *m/z* calculated for C₂₇H₂₃N₅O₇ [M+H]⁺: calculated 530.1670, found 530.1657. λ_{ex} = 500 nm, λ_{em} = 540 nm.

3.5.9 Protein labeling

DOPA-DHFR was incubated at 50 μM with 2-FPBA and the hydroxylamine in 1:1, 1:2, 1:3, and 1:5 ratios in pH 7 phosphate buffer. Controls lacking 2-FPBA, hydroxylamine, or DHFR without DOPA residues were conducted simultaneously. After 1 hr, the mixture was prepared for gel electrophoresis, separated *via* gel electrophoresis, and the gel was visualized.

3.6 ACKNOWLEDGEMENTS

Dr. Brette Chapin is gratefully acknowledged for her help with ¹¹B-NMR spectroscopy. Dr. Ross Thyer is gratefully acknowledged for his work with the protein labeling studies. Emily Roesner is gratefully acknowledged for her help with compound synthesis and characterization.

3.7 REFERENCES

- (1) Sletten, E. M.; Bertozzi, C. R. From Mechanism to Mouse: A Tale of Two Bioorthogonal Reactions. *Accounts of Chemical Research* **2011**, *44* (9), 666–676.
- (2) Sahoo, H. Fluorescent Labeling Techniques in Biomolecules: A Flashback. *RSC Advances* **2012**, *2* (18), 7017.
- (3) Lang, K.; Chin, J. W. Bioorthogonal Reactions for Labeling Proteins. *ACS chemical biology* **2014**, *9* (1), 16–20.
- (4) Patterson, D. M.; Prescher, J. A. Orthogonal Bioorthogonal Chemistries. *Current Opinion in Chemical Biology* **2015**, *28*, 141–149.
- (5) Dean, K. M.; Palmer, A. E. Advances in Fluorescence Labeling Strategies for Dynamic Cellular Imaging. *Nature Chemical Biology* **2014**, *10* (7), 512–523.
- (6) Wikipedia: The Free Encyclopedia. DAPI <https://en.wikipedia.org/wiki/DAPI> (accessed Sep 23, 2016).
- (7) Hong, V.; Steinmetz, N. F.; Manchester, M.; Finn, M. G. Labeling Live Cells by Copper-Catalyzed Alkyne--Azide Click Chemistry. *Bioconjugate chemistry* **2010**, *21* (10), 1912–1916.
- (8) Agard, N. J.; Prescher, J. A.; Bertozzi, C. R. A Strain-Promoted [3 + 2] Azide–Alkyne Cycloaddition for Covalent Modification of Biomolecules in Living Systems. **2004**.
- (9) van Berkel, S. S.; van Eldijk, M. B.; van Hest, J. C. M. Staudinger Ligation as a Method

- for Bioconjugation. *Angewandte Chemie (International ed. in English)* **2011**, *50* (38), 8806–8827.
- (10) Rashidian, M.; Song, J. M.; Pricer, R. E.; Distefano, M. D. Chemoenzymatic Reversible Immobilization and Labeling of Proteins without Prior Purification. *Journal of the American Chemical Society* **2012**, *134* (20), 8455–8467.
 - (11) Patterson, D. M.; Nazarova, L. A.; Prescher, J. A. Finding the Right (Bioorthogonal) Chemistry. *ACS Chemical Biology* **2014**, *9* (3), 592–605.
 - (12) Ramil, C. P.; Lin, Q.; Shimomura, O.; Johnson, F. H.; Saiga, Y.; Tsien, R. Y.; Giepmans, B. N. G.; Adams, S. R.; Ellisman, M. H.; Tsien, R. Y.; et al. Bioorthogonal Chemistry: Strategies and Recent Developments. *Chemical Communications* **2013**, *49* (94), 11007.
 - (13) Collins, B. E.; Metola, P.; Anslyn, E. V. On the Rate of Boronate Ester Formation in Ortho-Aminomethyl Functionalized Phenyl Boronic Acids. *Supramolecular chemistry* **2013**, *25* (2), 79–86.
 - (14) Lorand, J. P.; Edwards, J. O. Polyol Complexes and Structure of the Benzeneboronate Ion. *The Journal of Organic Chemistry* **1959**, *24* (6), 769–774.
 - (15) Bull, S. D.; Davidson, M. G.; van den Elsen, J. M. H.; Fossey, J. S.; Jenkins, A. T. A.; Jiang, Y.-B.; Kubo, Y.; Marken, F.; Sakurai, K.; Zhao, J.; et al. Exploiting the Reversible Covalent Bonding of Boronic Acids: Recognition, Sensing, and Assembly. *Accounts of chemical research* **2013**, *46* (2), 312–326.
 - (16) Xu, X.-D.; Cheng, H.; Chen, W.-H.; Cheng, S.-X.; Zhuo, R.-X.; Zhang, X.-Z. In Situ Recognition of Cell-Surface Glycans and Targeted Imaging of Cancer Cells. *Scientific reports* **2013**, *3*, 2679.
 - (17) Nishiyabu, R.; Kubo, Y.; James, T. D.; Fossey, J. S. Boronic Acid Building Blocks: Tools for Self Assembly. *Chemical communications (Cambridge, England)* **2011**, *47* (4), 1124–1150.
 - (18) Pérez-Fuertes, Y.; Kelly, A. M.; Johnson, A. L.; Arimori, S.; Bull, S. D.; James, T. D. Simple Protocol for NMR Analysis of the Enantiomeric Purity of Primary Amines. *Organic letters* **2006**, *8* (4), 609–612.
 - (19) Tickell, D. A.; Mahon, M. F.; Bull, S. D.; James, T. D. A Simple Protocol for NMR Analysis of the Enantiomeric Purity of Chiral Hydroxylamines. *Organic letters* **2013**, *15* (4), 860–863.
 - (20) Schmidt, P.; Stress, C.; Gillingham, D.; Patterson, D. M.; Nazarova, L. A.; Prescher, J. A.; Saito, F.; Noda, H.; Bode, J. W.; Blackman, M.; et al. Boronic Acids Facilitate Rapid Oxime Condensations at Neutral pH. *Chem. Sci.* **2015**, *6* (6), 3329–3333.
 - (21) Alfonta, L.; Zhang, Z.; Uryu, S.; Loo, J. A.; Schultz, P. G. Site-Specific Incorporation of a Redox-Active Amino Acid into Proteins. *Journal of the American Chemical Society* **2003**, *125* (48), 14662–14663.
 - (22) Albers, A. E.; Okreglak, V. S.; Chang, C. J. A FRET-Based Approach to Ratiometric Fluorescence Detection of Hydrogen Peroxide. *Journal of the American Chemical Society* **2006**, *128* (30), 9640–9641.

Chapter 4: Kinetic and Mechanistic Studies of a Reversible Conjugate Acceptor

4.1 INTRODUCTION

4.1.1 Click and de-click chemistry

Coupling reactions have a long history in chemistry. Coupling can be simply defined as the formation of strong, covalent bonds between two or more starting molecules. A subsection of these types of reactions can be classified under “click chemistry,” a term coined by K. Barry Sharpless in 1998. Under Sharpless’s definition, “click” reaction must adhere to a set of guidelines: reactions must involve simple procedures, benign solvents such as water, little prior derivatization of components, high yields of products that require no chromatographic purification, and proceed in mild conditions of temperature, pressure and atmosphere.¹ The classic example of this type of reaction, and one that is often referred to only as a “click reaction”, is the Huisgen copper-catalyzed azide-alkyne cycloaddition or CuAAC, as discussed in Section 3.1.²

Typically click reactions are not readily reversible. The formation of strong covalent bonds necessitates the creation of thermodynamically stable products, which are unlikely to be easily reversible. Previous efforts at reversing coupling reactions include mechanochemical decoupling^{3,4} or heating at high temperatures,^{5,6} neither of which fall under Sharpless’s definition of click reactions. These methods also severely limit substrate scope and applicability.

One method that has been employed to decouple reactions is to use a sacrificial linker. This method couples two components together and decouples them at a different part of the molecule. (Figure 4.1) Although these strategies have been used for many applications, they require more intensive synthesis and are not truly reversible.

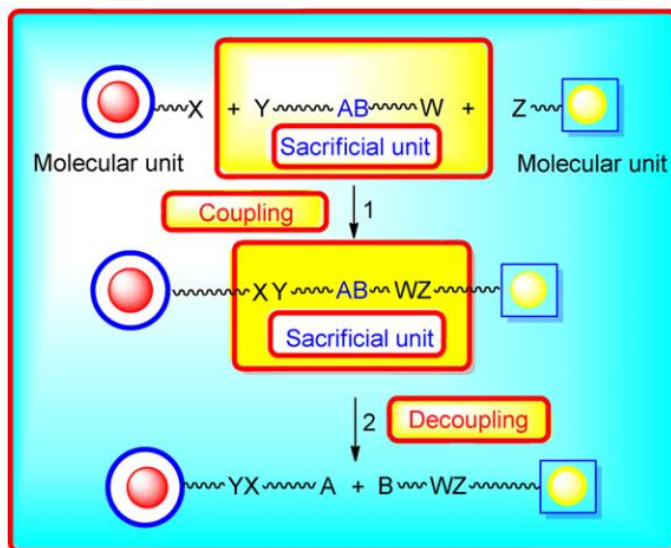
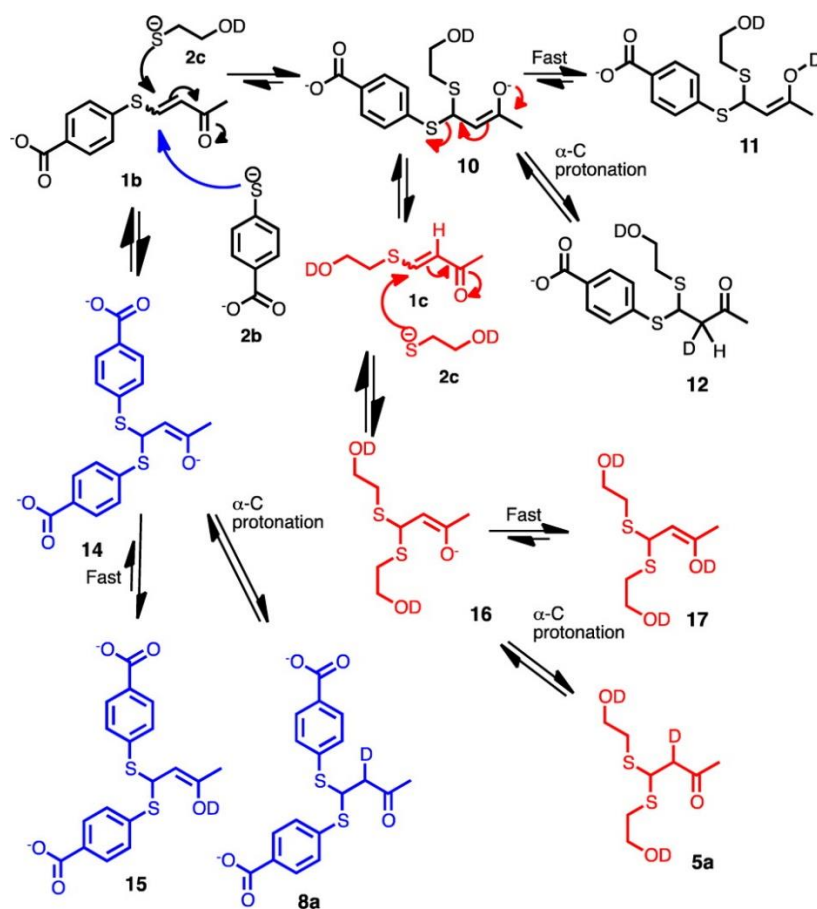


Figure 4.1. Schematic of a sacrificial unit used for coupling and decoupling.⁷

4.1.2 Addition to α,β -unsaturated carbonyls

The Anslyn group, among others, has explored 1,4-addition to unsaturated carbonyls as a method of reversible coupling. α,β -unsaturated carbonyls have been known for many years to undergo 1,4-addition. Our group showed the reversibility of this process by scrambling different thiols into β -sulfido- α,β -unsaturated carbonyls to generate dithianes.⁸ (Scheme 4.1) In DMSO or H₂O/DMSO mixtures, this system was dynamic, readily exchanging at room temperature over the course of a few hours to a few days.



Scheme 4.1. Complex equilibrium of dithiane scrambling.

In order to increase the rates of exchanges, our group examined a series of α,β -unsaturated carbonyls activated by electron withdrawing groups such as carbonyls, nitriles, and chlorides. (Figure 4.2) We found that the electron withdrawing groups indeed increased the rate of exchange of thiols in acetonitrile/water mixtures at neutral pH.

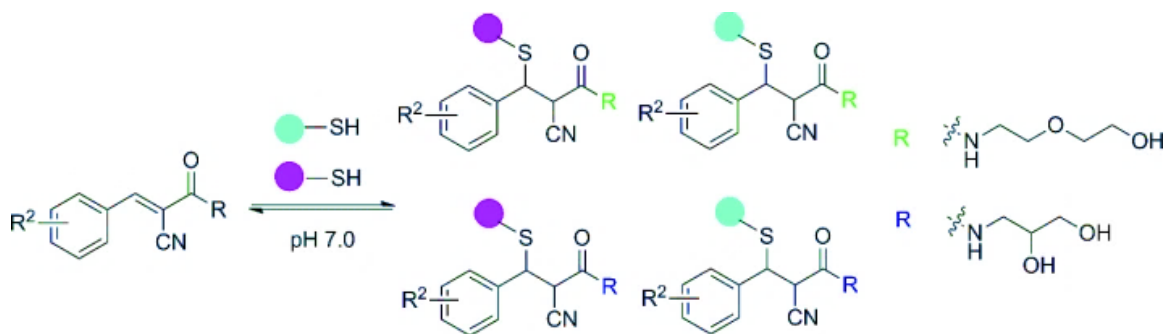
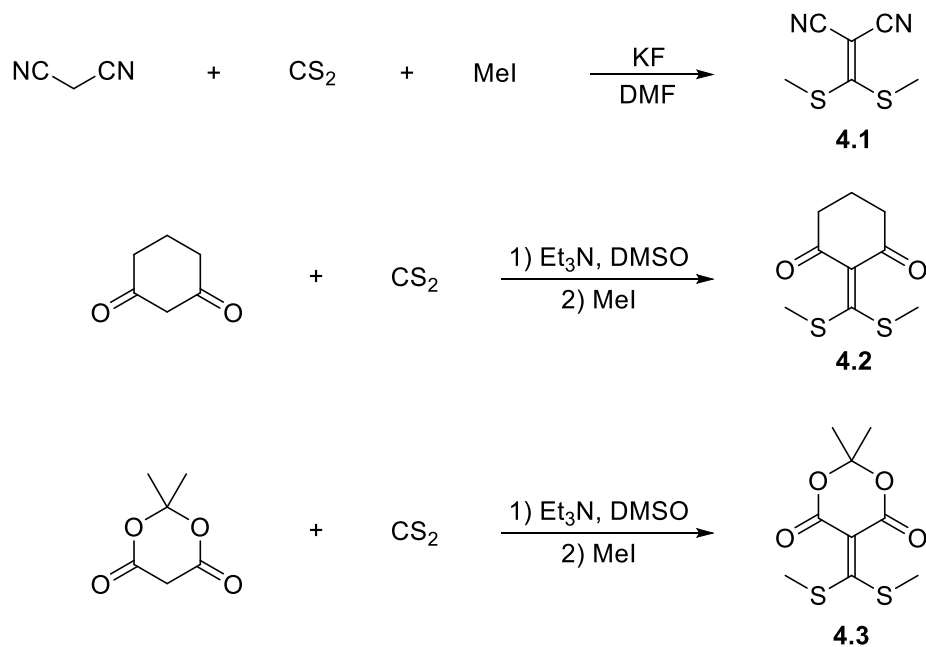


Figure 4.2. Dynamic equilibrium of mono-activated conjugate acceptors.

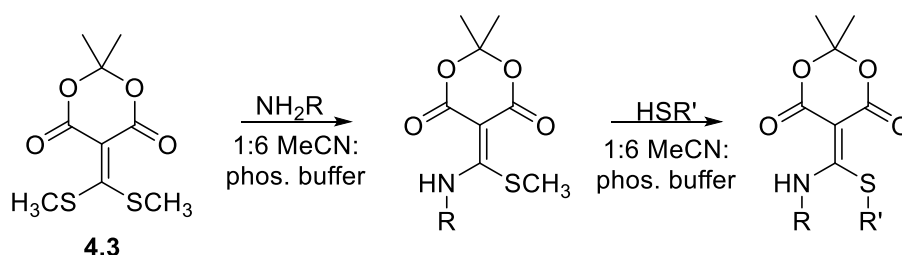
After observing the effects of monoactivation of these conjugate acceptors, we examined bisactivation. (Scheme 4.2) Conjugate acceptor **4.1** hydrolyzed faster than thiol exchange could occur and thiol exchange with **4.2** occurred on a timescale that was in excess of a week. **4.3** was found to readily exchange thiols as well as resist hydrolysis.⁹



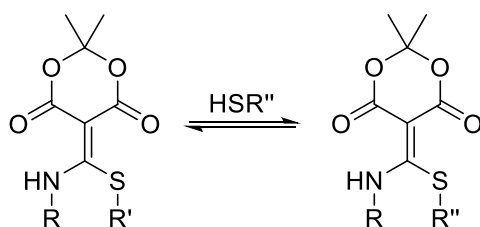
Scheme 4.2. Synthesis of **4.1-4.3**.

4.1.3 Previous studies with 4.3

Conjugate acceptor **4.3** was found to add two equivalents of primary alkyl amines in organic solvent, but in primarily aqueous conditions (6:1 water:acetonitrile), **4.3** was found to add only one equivalent of primary alkyl amine. Following this single amine addition, a thiol can then be exchanged at room temperature over the span of either a few hours or a few days. (Scheme 4.3) Additional thiols can also be scrambled into the conjugate acceptor, creating an equilibrium that is dictated by the relative stabilities of the products. (Scheme 4.4)



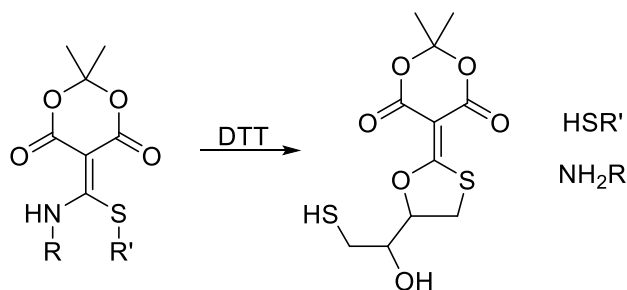
Scheme 4.3. Addition of one primary alkylamine followed by a thiol into **4.3**.



Scheme 4.4. Equilibration of multiple thiols added into conjugate acceptor **4.3**.

As shown above, **4.3** is successful at coupling together amines and thiols. The additions in **4.3** follow many of the “click” chemistry requirements: addition is achieved in mild solvent conditions, the only byproduct is methyl mercaptan which requires no chromatography for removal, no extensive derivatization of the reagents is necessary, and the reactions proceed in good yields. The next step our group was interested in was the decoupling, or “declick,” of these coupling partners.

We found that the addition of dithiothreitol (DTT) provided the original thiol and amine back in unaltered forms. (Scheme 4.5) This method of decoupling has many advantages over using a sacrificial linker: there is no derivatization of the amine and thiol needed prior to addition; if mixing together many different thiols and then screening against a potential target, thiols from potential hits are easily characterized; finally, the substrate scope is not limited to only readily-modified compounds.



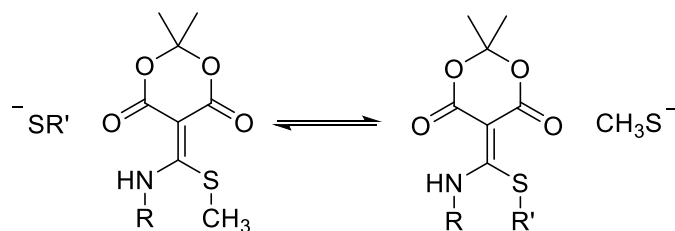
Scheme 4.5. DTT decoupling.

This system is currently being studied for a variety of applications including bioconjugation, macrocyclization of peptides, and decomposable polymers; however, these applications are beyond the scope of this dissertation and thus will not be further discussed in this chapter.

4.2 ATTEMPTS TO IMPROVE UPON 4.3

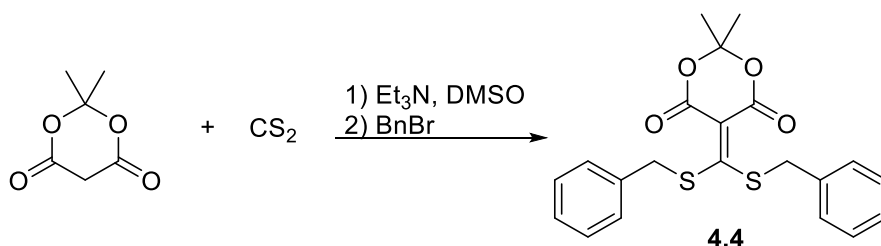
4.2.1 Other alkylations of carbon disulfide

One of the difficulties with addition into **4.3** is the equilibration upon adding a thiol and displacing methane thiol. (Scheme 4.6) Methane thiolate is very nucleophilic so it readily adds back into **4.3** upon displacement. This is typically overcome through sparging with inert gas; however, this becomes difficult with small scale experiments using small volumes of solvent and when comparing separate experiments since sparging is difficult to reliably reproduce.



Scheme 4.6. Thiol equilibration.

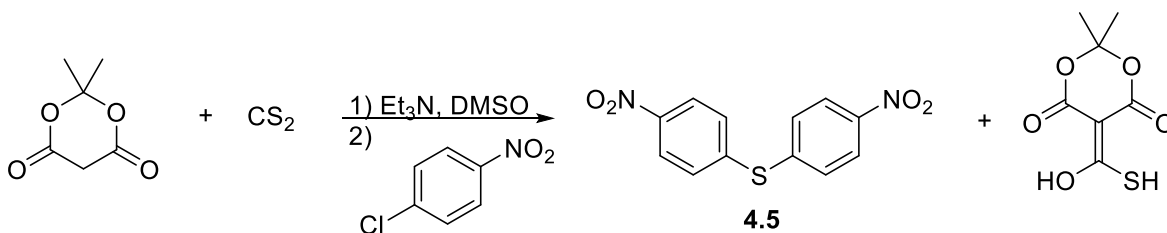
Alkylation with bromobenzene was achieved using the same methodology to make **4.3** in order to give **4.4**. (Scheme 4.7) Addition of amines into **4.4** proceeded well, but both **4.4** and the amine adducts were water insoluble and precipitated out of solution. This made them less than ideal for our purposes of thiol exchange under aqueous conditions, so we turned to less hydrophobic alkylating reagents.



Scheme 4.7. Synthesis of **4.4**.

Acylation with acetyl chloride provided an unknown product that appeared to rapidly hydrolyze as observed by $^1\text{H-NMR}$. *N,N*-Dimethylcarbamoyl chloride reacted under our conditions, but did not alkylate the adduct formed from Meldrum's acid and CS_2 .

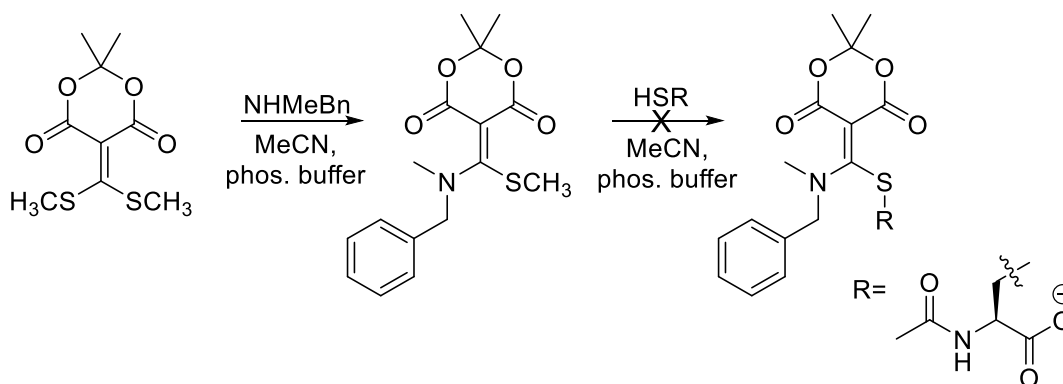
Alkylation with *p*-chloronitrobenzene via nucleophilic aromatic substitution did not provide the expected product, but rather **4.5** and hydrolysis of the Meldrum's acid and CS_2 adduct. (Scheme 4.8)



Scheme 4.8. Attempted alkylation with *p*-chloronitrobenzene.

4.2.2 Addition to 4.3 of other types of amines

Initial studies of **4.3** concerned only the addition of primary alkyl amines. We hypothesized that addition of a secondary amine into **4.3** might increase the rate of exchange due to less donation of the nitrogen lone pair into the conjugated system caused by the sterically-hindered amine rotating out of plane. Although the secondary amine added, thiol exchange did not occur. (Scheme 4.9)



Scheme 4.9. Addition of secondary amines into **4.3**.

This observation led us to the conclusion that the intramolecular hydrogen bond between the amine hydrogen and the carbonyl oxygen was essential for activating the system for thiol exchange. (Figure 4.3) The second alkyl group on secondary amines cannot activate the carbonyl in this way.

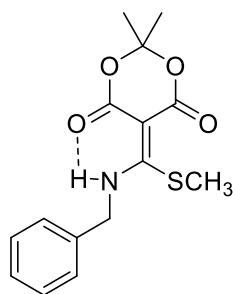
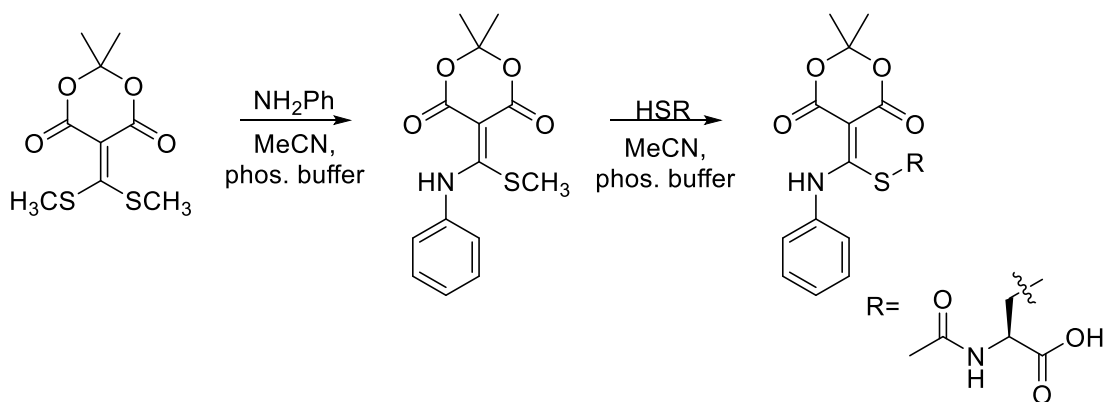


Figure 4.3. Intramolecular hydrogen bond in the conjugate acceptor system.

Another class of amines that we looked to test with this conjugate acceptor system was anilines. We used primary anilines, which could hydrogen bond in a similar manner as above, and could also provide extended conjugation of our system. (Scheme 4.10) We found that aniline added readily to **4.3** and that subsequent thiol exchange was also possible under a similar timescale to primary alkyl amines.



Scheme 4.10. Addition of aniline and thiols into **4.3**.

4.2.3 Synthesis of aniline-**4.3** derivatives and exchange with NAC

A range of aniline derivatives with **4.3** were synthesized and tested for addition of *N*-acetylcysteine (NAC) using the procedure shown in Scheme 4.10. (Figure 4.4) A range of *p*-substituted anilines were used with both electron donating and electron withdrawing groups present (**4.6-4.14**). All of these were tested for the addition of NAC and each showed thiol

exchange. Addition of 4-aminobenzaldehyde or 4-aminoacetophenone into **4.3** was poor yielding and difficult to purify so these derivatives were not tested for thiol exchange. (Figure 4.5)

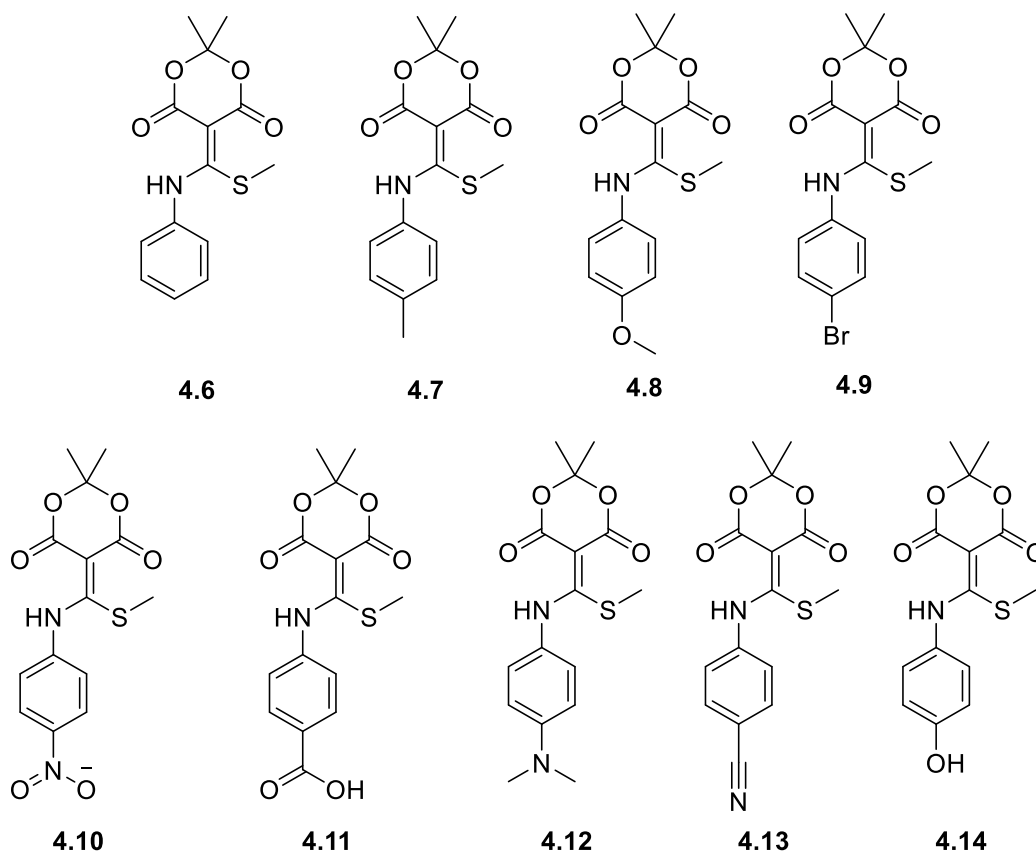


Figure 4.4. Aniline derivatives synthesized and tested for thiol exchange.

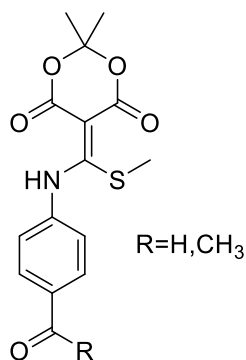
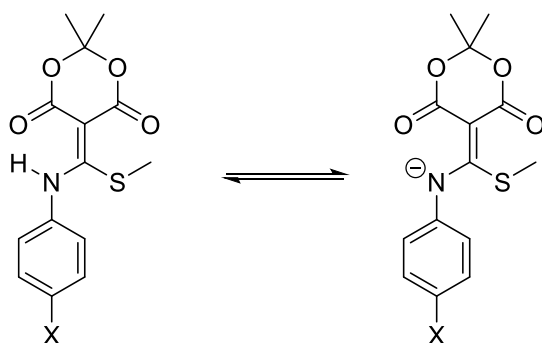


Figure 4.5. Carbonyl aniline derivatives of **4.3**.

4.3 pK_a DETERMINATION OF ANILINE DERIVATIVES

4.3.1 pH titrations

The pK_a's of multiple derivatives of the aniline-conjugate acceptor series shown above were determined. It was found that when using primary alkylamines, thiol exchange slowed dramatically at pH's above the pK_a of the aminofunctionalized **4.3**; we were interested to see if this was the same once the anilino nitrogen was deprotonated. (Scheme 4.11) **4.11** and **4.14** were omitted due to the likelihood of complexity from multiple pK_a's.



Scheme 4.11. Deprotonation of aniline-**4.3** adduct.

The pK_a of each aniline-**4.3** derivative was determined using absorbance spectroscopy. (Figures 4.6, 4.9-4.13) The change in absorbance at two separate wavelengths was plotted and a cubic polynomial fitted to the data. (Figures 4.7 and 4.8) The second derivative of this polynomial was taken and the value of d^2x/dt^2 where $x=0$ was found. This value was then used in the original fit equation to find the inflection point, or the pK_a of each species. Since two separate wavelengths were used, the average of the two is the reported pK_a.

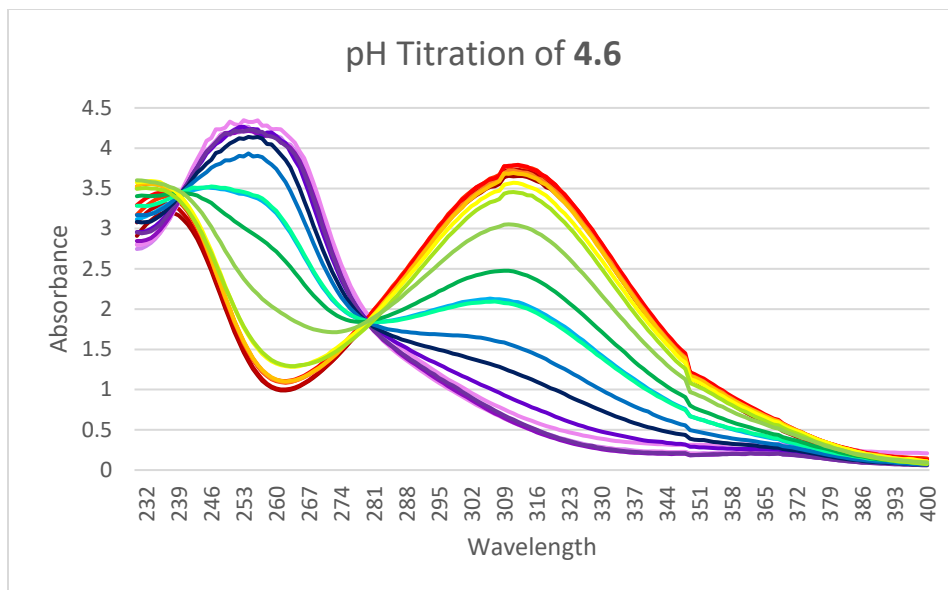


Figure 4.6. pH titration of **4.6**. Red indicates lowest pH's (0.65), purple indicates highest (13.52). Calculated $pK_a = 6.02$.

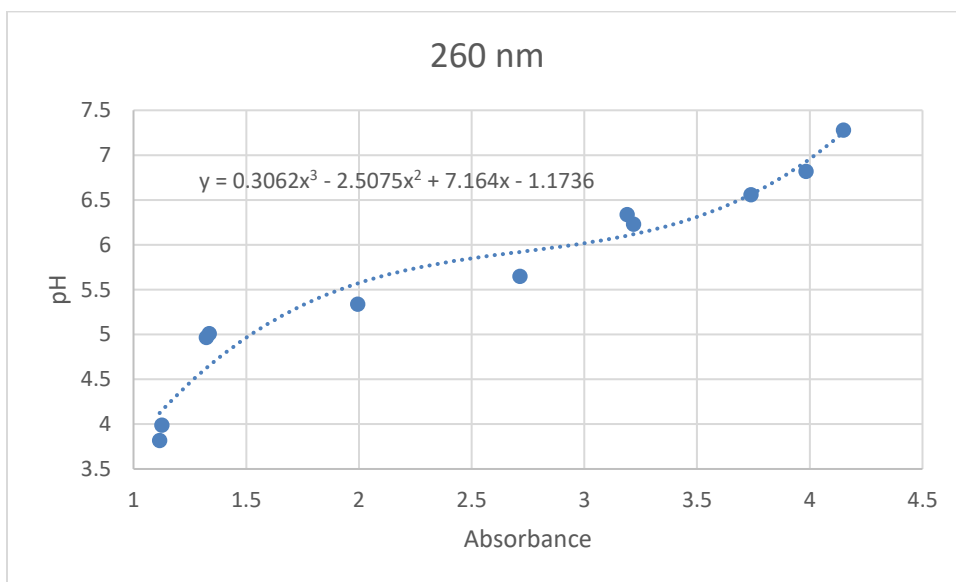


Figure 4.7. Absorbance change at 260 nm for pH titration of **4.6**. Gives a pK_a value of 5.93.

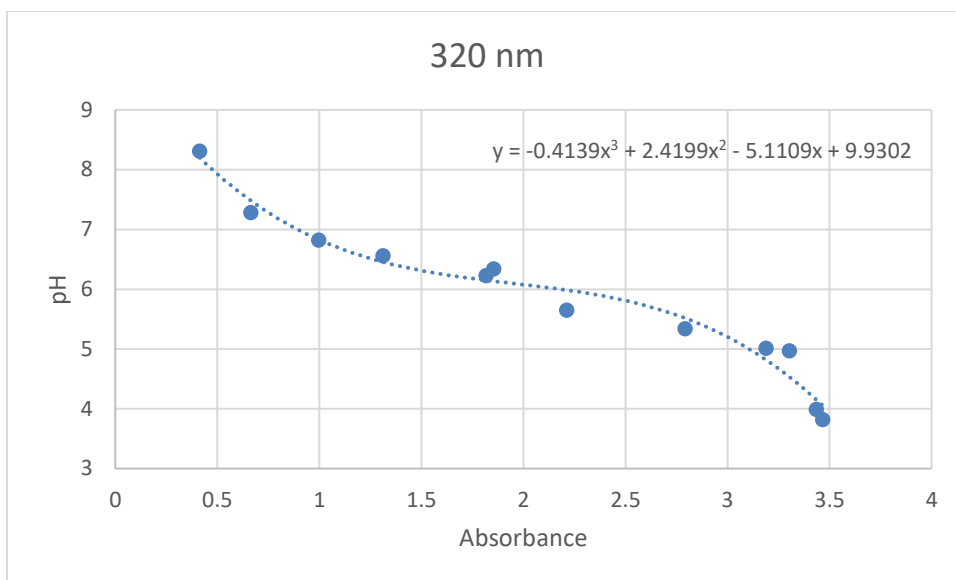


Figure 4.8 Absorbance change at 320 nm for pH titration of **4.6**. Gives a pK_a value of 6.10.

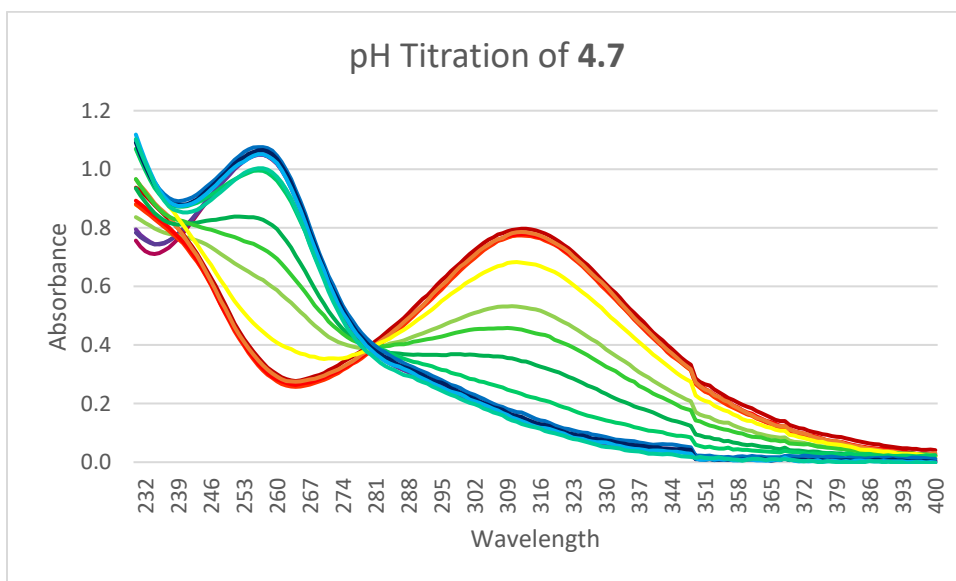


Figure 4.9. pH titration of **4.7**. Red indicates lowest pH's (2.41), purple indicates highest (12.7). Calculated $pK_a = 6.51$.

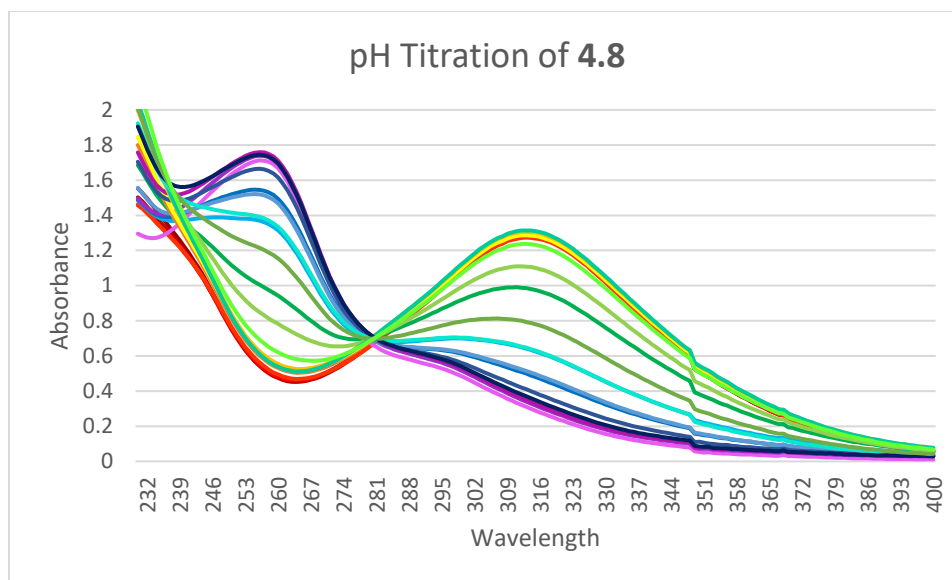


Figure 4.10. pH titration of **4.8**. Red indicates lowest pH's (0.87), purple indicates highest (11.64). Calculated $pK_a = 6.54$.

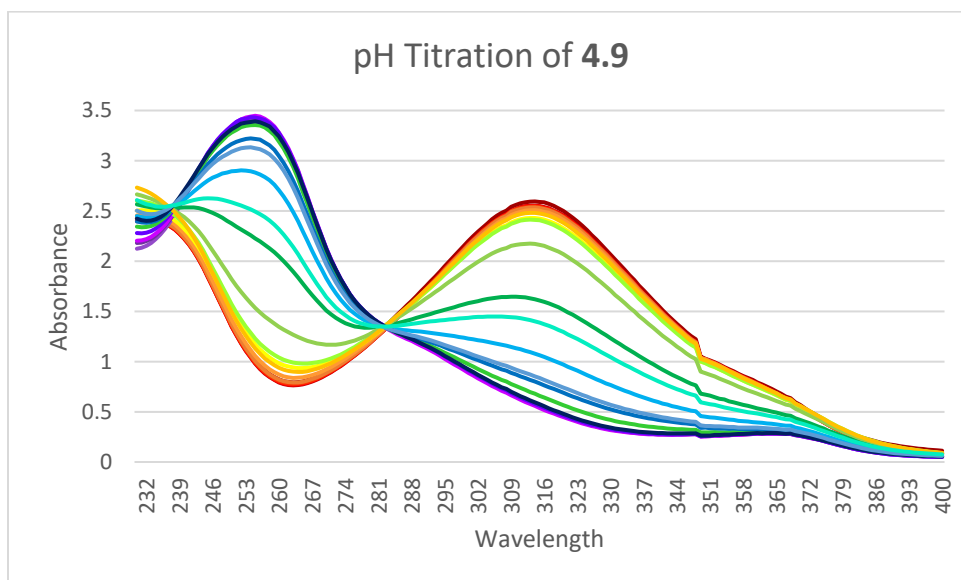


Figure 4.11. pH titration of **4.9**. Red indicates lowest pH's (0.68), purple indicates highest (10.51). Calculated $pK_a = 5.56$.

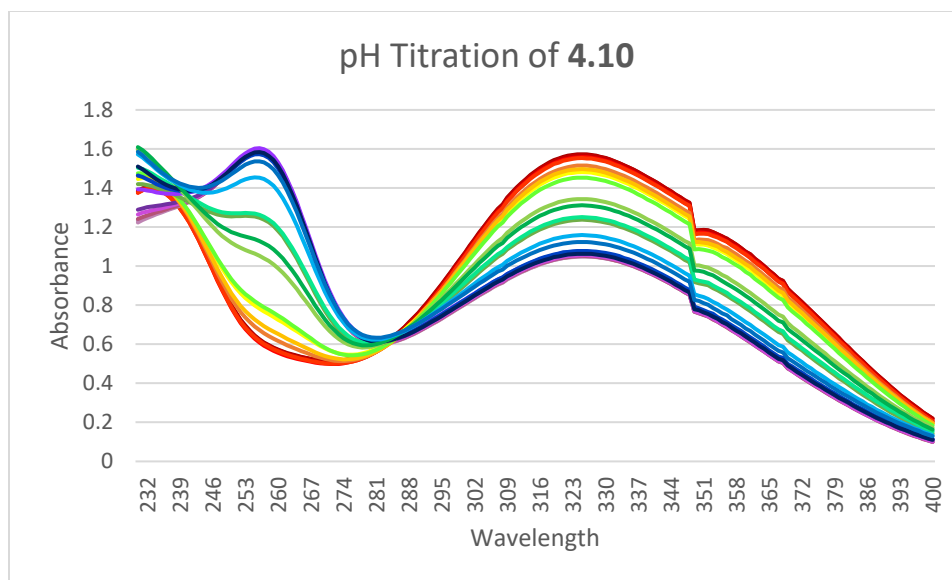


Figure 4.12 pH titration of **4.10**. Red indicates lowest pH's (1.21), purple indicates highest (11.11). Calculated $pK_a = 4.34$.

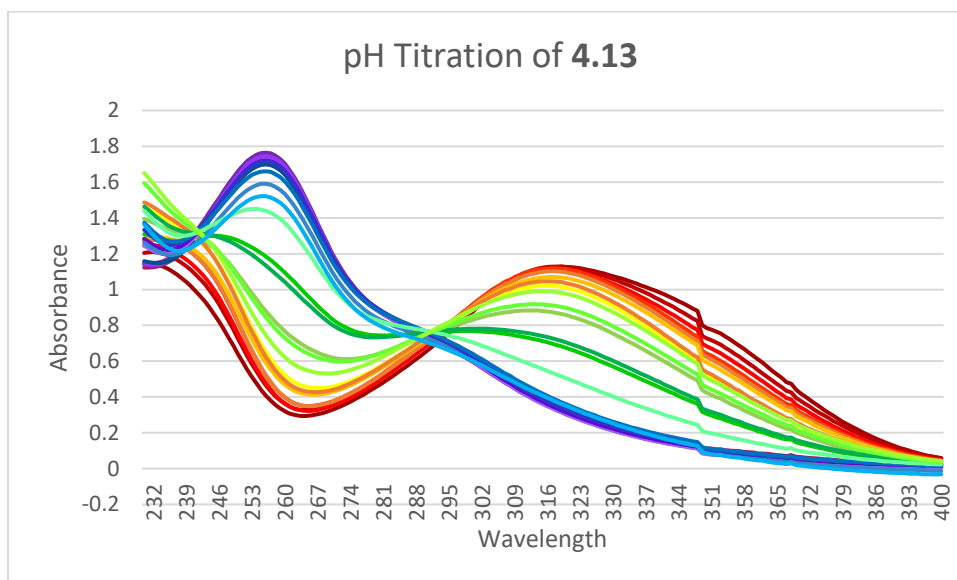


Figure 4.13. pH titration of **4.13**. Red indicates lowest pH's (0.85), purple indicates highest (11.33). Calculated $pK_a = 4.54$.

The pH titration of **4.12** was more complex than the previous titrations shown. (Figure 4.14) Over the range of pH's measured (1.28-10.79), there are clearly two pK_a 's which makes calculation of the individual pK_a 's difficult. (Figures 4.15-4.17)

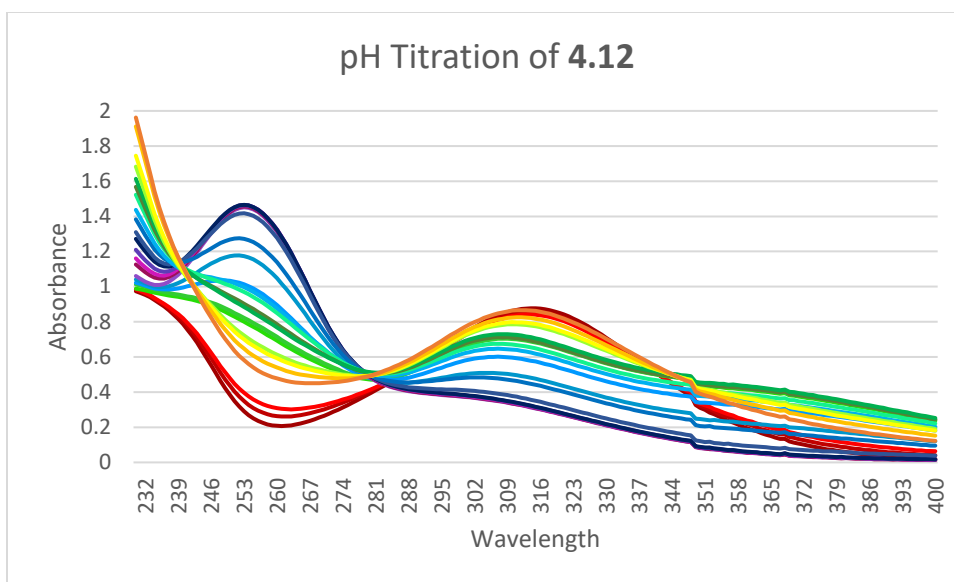


Figure 4.14. pH titration of **4.12**. Red indicates lowest pH's (1.66), purple indicates highest (11.11).

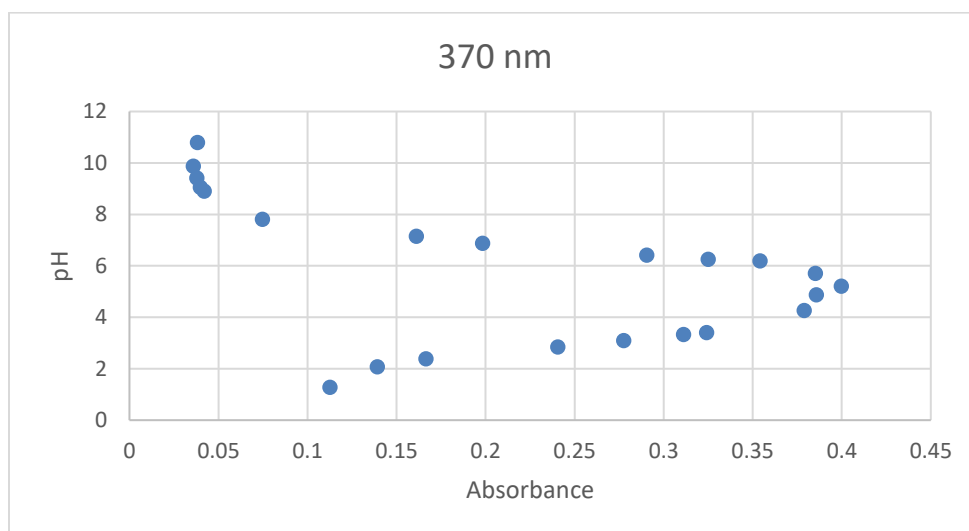


Figure 4.15. Absorbance change at 370 nm for pH titration of **4.12**.

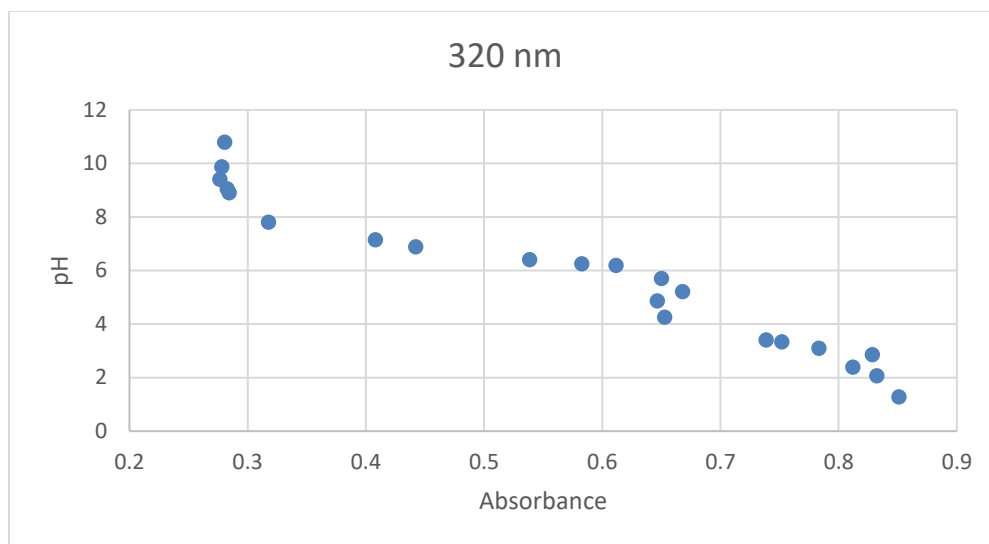


Figure 4.16. Absorbance change at 260 nm for pH titration of **4.12**.

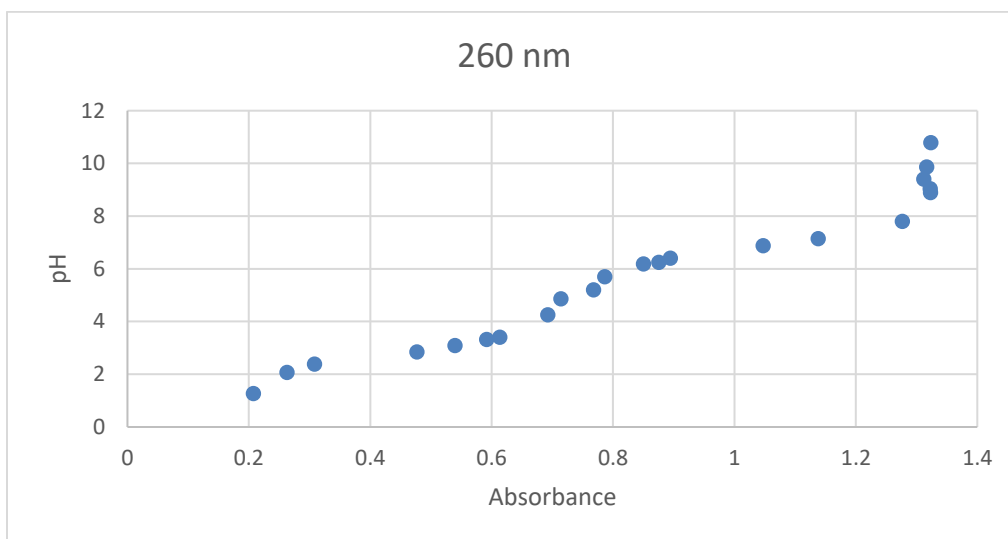


Figure 4.17. Absorbance change at 260 nm for pH titration of **4.12**.

By dividing each wavelength into two separate graphs each with their own cubic fit functions, the two pK_a 's were calculated and averaged from the values obtained from change in absorbance at 370, 320 and 260 nm for the higher pK_a and 370 and 260 nm for the lower pK_a since the change in absorbance at 320 nm is minimal at low pH. The two pK_a 's obtained for **4.12**

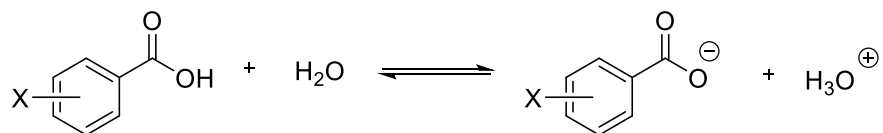
were 6.65 and 2.88, respectively. All pK_a 's determined in this section are compiled into Table 4.1.

Conjugate Acceptor (<i>para</i> -substitution)	Calculated pK_a
4.6 (H)	6.02
4.7 (Me)	6.51
4.8 (OMe)	6.54
4.9 (Br)	5.56
4.10 (NO ₂)	4.34
4.12 (NMe ₂)	2.28, 6.65
4.13 (CN)	4.54

Table 4.1. pK_a 's of the aniline-conjugate acceptor series.

4.3.2 Linear Free Energy Relationships

In order to compare the different pK_a 's found for compounds **4.6-4.13**, we turned to linear free energy relationships (LFERs). LFERs are used as a quantitative method to describe structure-activity relationships.¹⁰ Each LFER utilizes a reference reaction for which there are values for a range of substituents. The most common LFER used is the Hammett Plot, which uses the deprotonation of benzoic acid derivatives as the reference reaction. (Scheme 4.12) This reference reaction is used to define the substituent parameter σ_X , which can be used to determine the effect resonance and inductive effects have on the reaction of interest. σ_H is defined as 0; negative σ values mean that the substituted benzoic acid is less acidic than benzoic acid itself, and the opposite applies to positive σ values.



Scheme 4.12. Reference reaction for Hammett plots.

Hammett plots allow for the study of substituent effects for reactions of interest and for comparison to the reference reaction. Both equilibrium constants (K) and rate constants (k) can be compared to the deprotonation of benzoic acid. (Equations 4.1 and 4.2) ρ is the slope of the Hammett plot and also compares the studied reaction with the reference reaction; a positive ρ means that negative charge is building (as it does in the deprotonation of benzoic acid) and a negative ρ means that positive charge is building. A $|\rho|$ value above 1 indicates that the studied reaction is more sensitive to changes in substituent than the reference reaction, and a $|\rho|$ value of less than 1 indicates that the studied reaction is less sensitive to substituent changes.

Equation 4.1
$$\log\left(\frac{K_X}{K_H}\right) = \rho\sigma_X$$

Equation 4.2
$$\log\left(\frac{k_X}{k_H}\right) = \rho\sigma_X$$

The pK_a 's determined in Section 4.3.1 were used to compile a Hammett plot. (Table 4. 2 and Figure 4.18) Conjugate acceptors **4.8** (OMe) and **4.12** (NMe₂) do not follow the same trend as the other compounds used so these were omitted from the second Hammett plot. (Figure 4.19)

	Hammett Value	pK _a	K _a	log(K _X /K _H)
H	0	6.02	9.54993E-07	0
Me	-0.15	6.51	3.0903E-07	-0.49
NO ₂	0.71	4.34	4.57088E-05	1.68
Br	0.23	5.56	2.75423E-06	0.46
CN	0.66	4.54	2.88403E-05	1.48
OMe	-0.27	6.54	2.88403E-07	-0.52
NMe ₂	-0.83	6.65	2.23872E-07	-0.63

Table 4.2. Hammett values, pK_a, and log(K_X/K_H) used for Hammett plots.

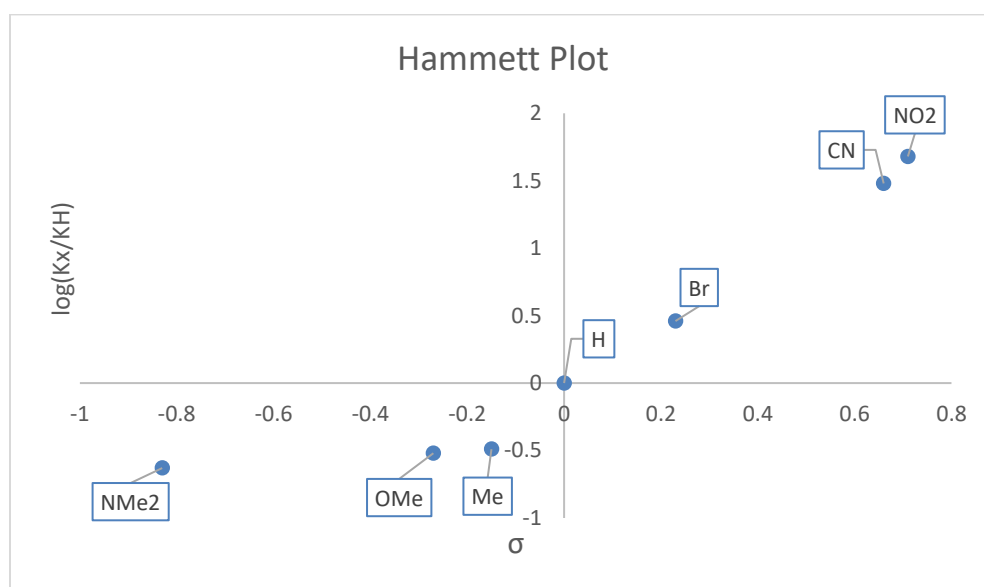


Figure 4.18. Hammett plot with all pK_a's included.

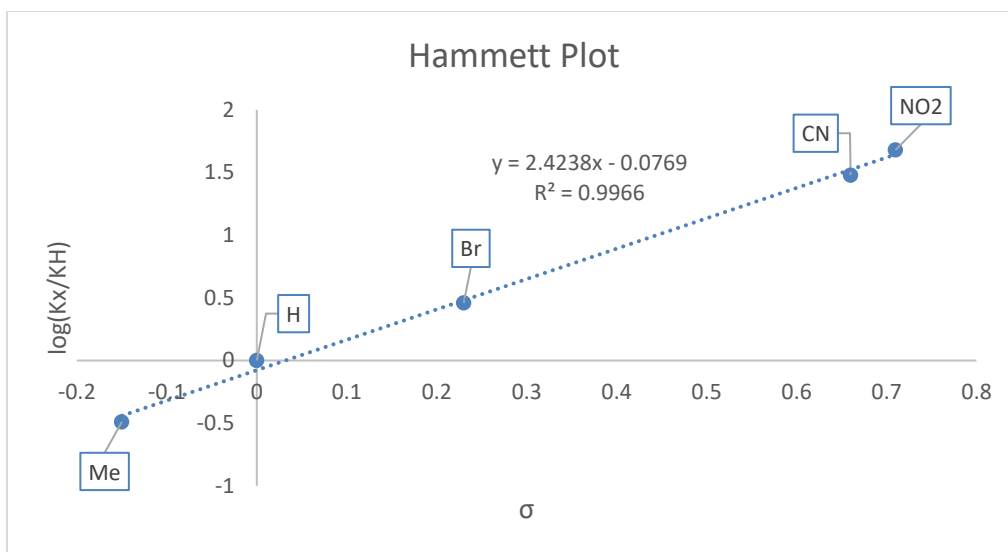


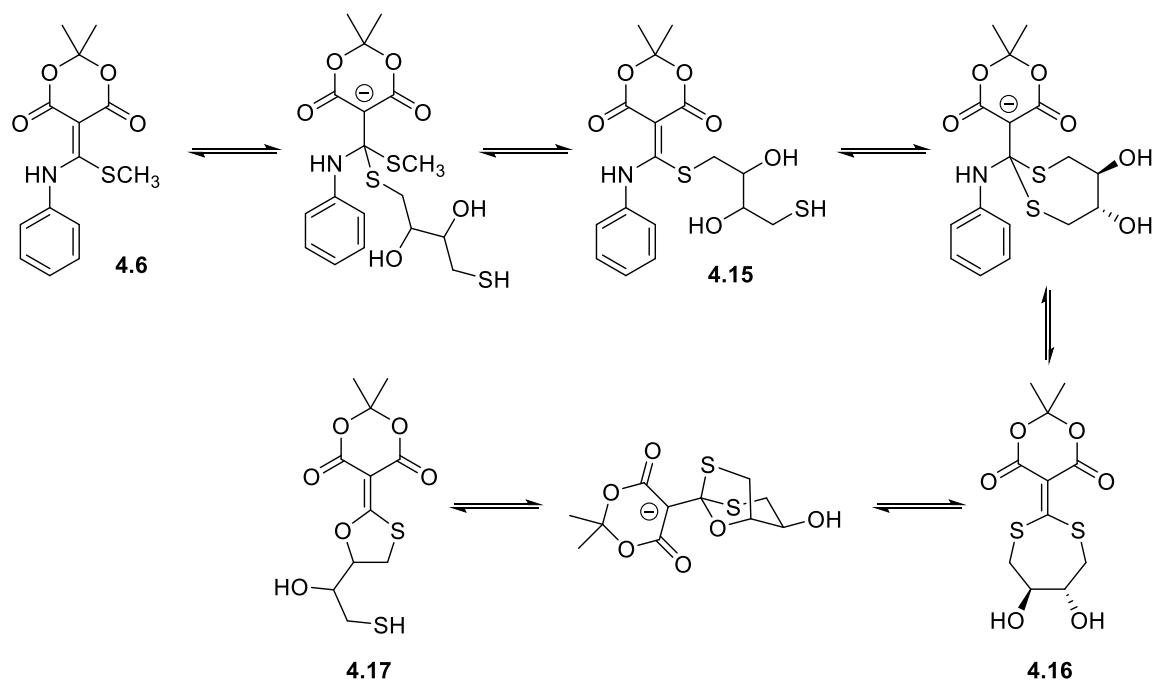
Figure 4.19. Hammett plot without **4.8** and **4.12**.

With the omission of **4.8** and **4.12**, the Hammett plot shows a linear relationship ($R^2 = 0.9966$). ρ is 2.42 which indicates that the deprotonation of the conjugate acceptors is more sensitive than the deprotonation of benzoic acid, and confirms that there is building negative charge which is as expected. The effect of this range of pKa's on decoupling will be discussed later in this chapter.

4.4 STUDIES INTO THE DTT-MEDIATED DECOUPLING MECHANISM

4.4.1 Structural determination by ¹H-NMR

After the addition of a thiol and amine into **4.3**, these can be decoupled through the addition of DTT. The final product (**4.17**) was characterized by ¹H-NMR and COSY 2D-NMR. The proposed mechanism for decoupling of compounds such as **4.6** is shown in Scheme 4.13.



Scheme 4.13. Proposed decoupling mechanism upon addition of DTT to **4.6**. First, DTT addition occurs, followed by elimination of methanethiolate (**4.15**). The second thiol of DTT then adds to the β -position, precipitating elimination of the aniline. This seven-membered ring (**4.16**) then rearranges to give a more stable five-membered ring (**4.17**).

The reaction of **4.12** and DTT was monitored by LCMS; two hours after DTT addition, LCMS analysis showed four major species. (Figures 4.20) The two peaks that absorb at 254 nm have masses corresponding to **4.12** and **4.15**; the two non-absorbant peaks have the same mass of 309 ($[M+3]^-$) but different retention times, which indicates that they have different structures. This is the type of product distribution we would expect to see from our proposed mechanism.

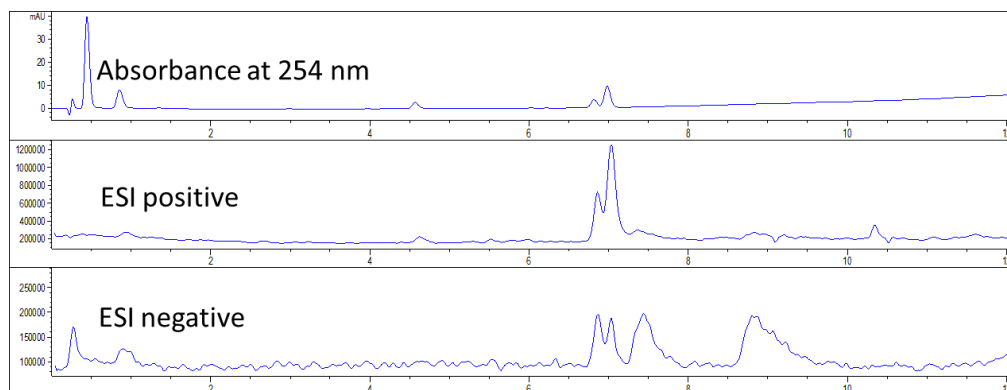


Figure 4.20. LCMS of **4.12** two hours after DTT addition.

$^1\text{H-NMR}$ can also be used to follow the reaction progress. An intermediate that correlates with **4.15** is visible after a few hours. (Figure 4.21) Although no signals with the symmetry that **4.16** should have are visible, the final product is easily characterized as **4.17**.

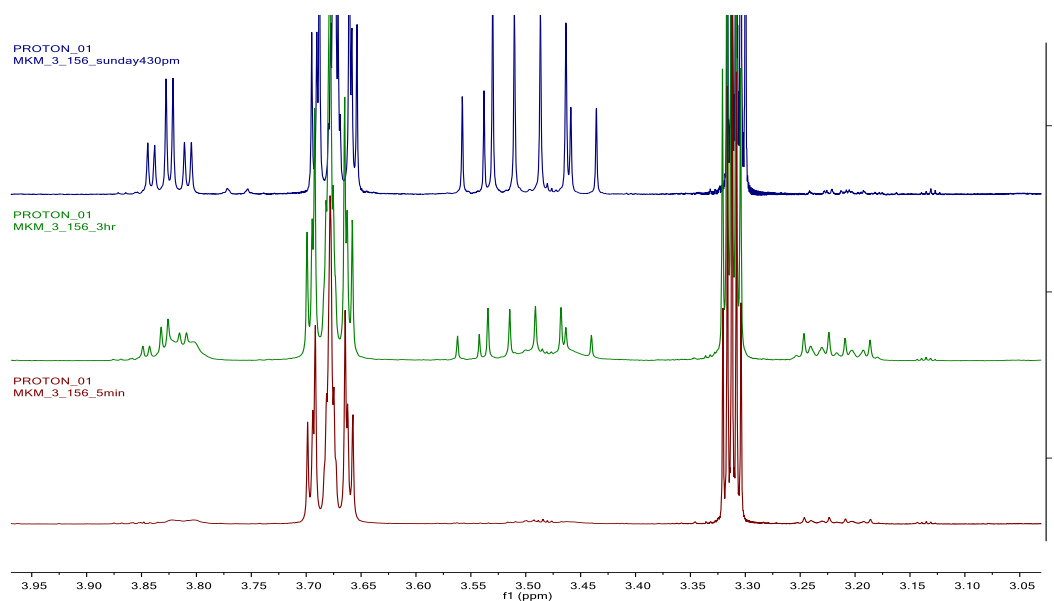


Figure 4.21. $^1\text{H-NMR}$ of **4.3** combined with DTT. (from bottom): 5 min after addition, 3 hr after addition showing both **4.15** and **4.17**, 48 hrs after addition showing **4.17**.

4.4.2 Pseudo-first order kinetics experiments

We were interested in learning more about the mechanistic pathway of decoupling and looked to kinetic studies for this. Reaction kinetics can be a way of validating a mechanistic model; rate constants can provide data about the rate-determining step and the dependence on

concentration for each reactant. We hypothesized that we would have second order kinetics based off our mechanism proposed above, with both the aniline-modified conjugate acceptor (AnCA) and DTT being first order. (Equation 4.3) By using the steady state approximation, we can simplify the rate law by assuming that any intermediates formed are relatively transient, meaning that their concentrations are small and constant during the reaction. We also hypothesized that we would be able to apply pseudo-first order kinetics to simplify our studies; pseudo-first order kinetics simplifies second order kinetics by using an excess of one reactant to the point where the approximate concentration is constant throughout the experiment. These two simplifications provide Equation 4.4 for measuring kinetics where k_{obs} is a combination of all rate constants and $[DTT]_0$ is the initial concentration of DTT.

Equation 4.3
$$\frac{d[P]}{dt} = k[AnCA][DTT]$$

Equation 4.4
$$\frac{d[P]}{dt} = k_{obs}[AnCA][DTT]_0$$

We monitored the decoupling of **4.7**, **4.8**, **4.12**, and **4.13** with 100 eq of DTT. (Figures 4.22-4.25) The change in absorbance, however, is not linear as was expected. This non-linearity means that the simplifications we applied to the rate law were not correct. Given this, we turned to a more complex analysis method for our kinetics.

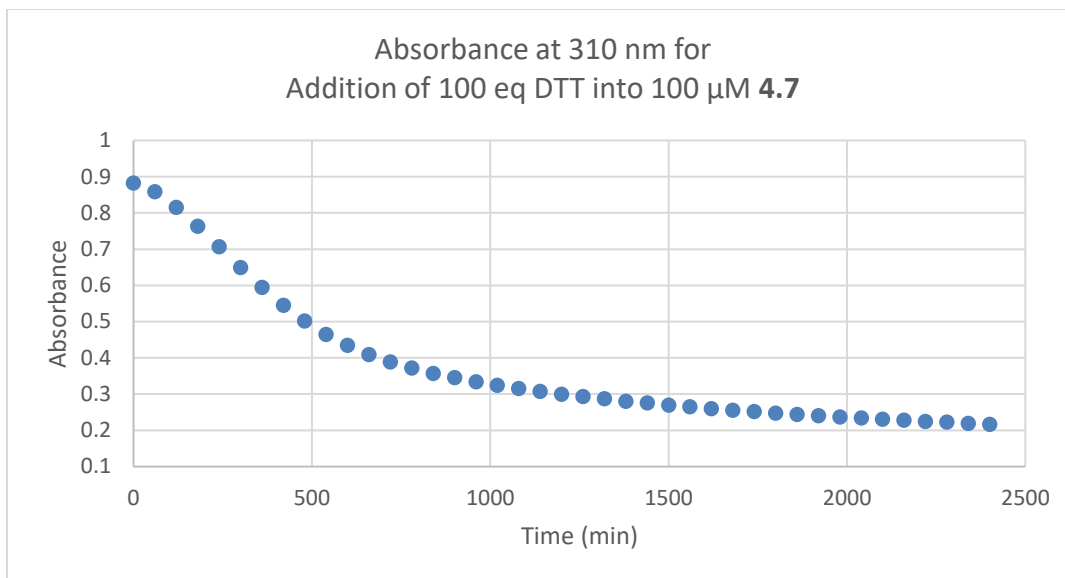


Figure 4.22. Change in absorbance over time for **4.7** upon addition of DTT.

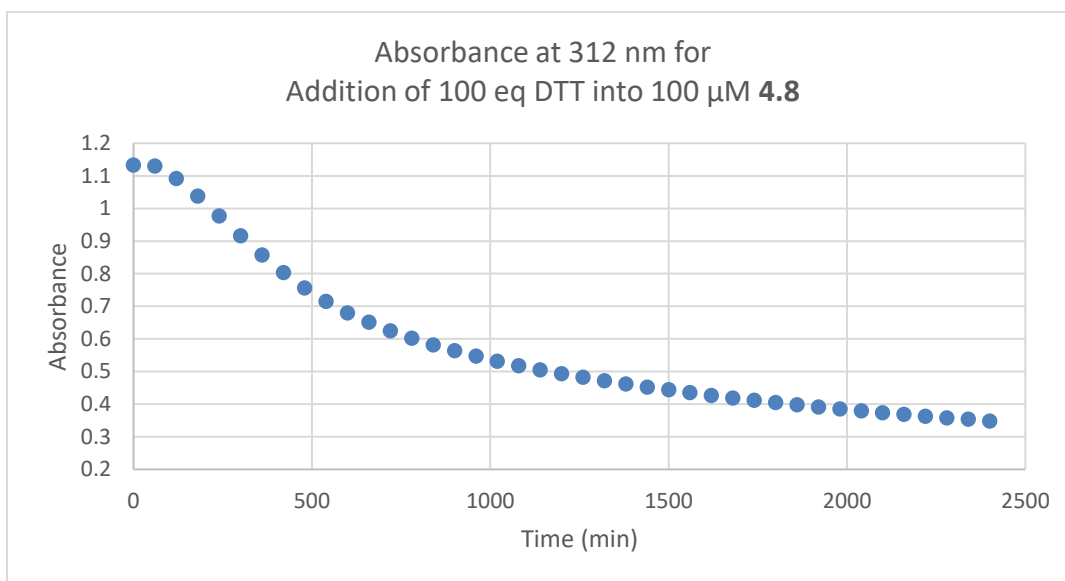


Figure 4.23. Change in absorbance over time for **4.8** upon addition of DTT.

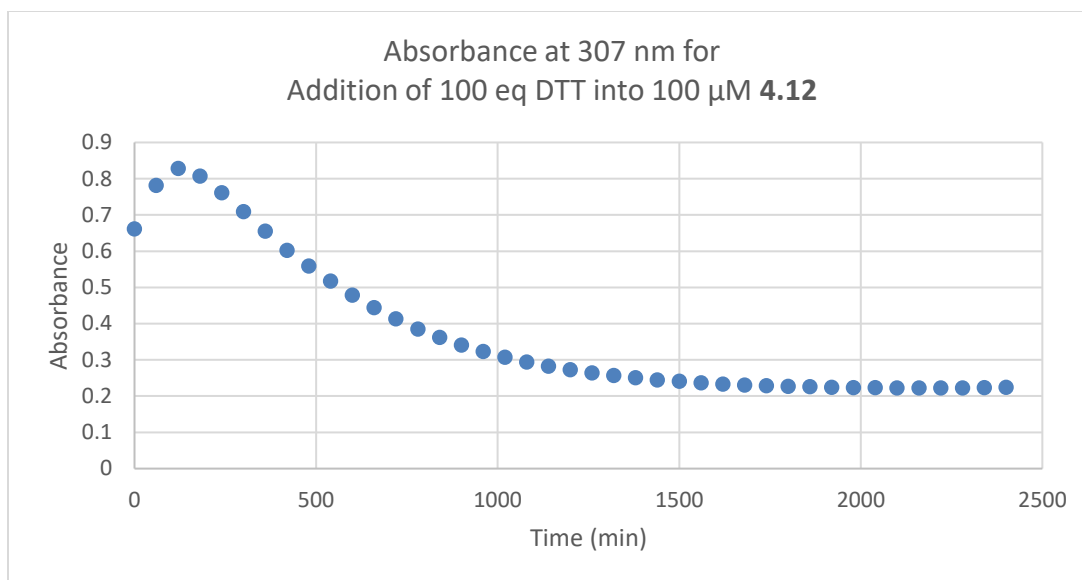


Figure 4.24. Change in absorbance over time for **4.12** upon addition of DTT.

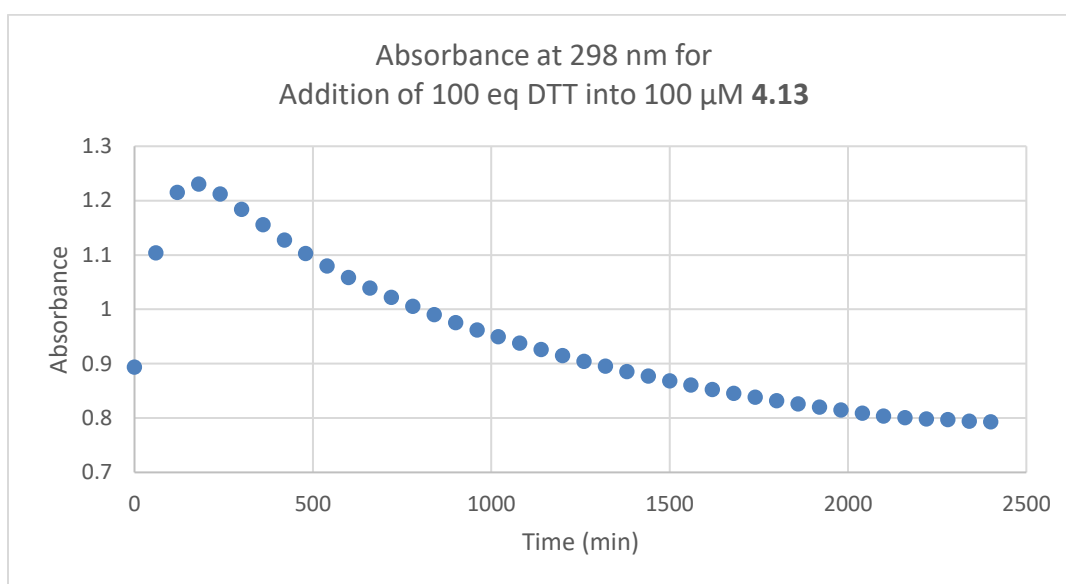
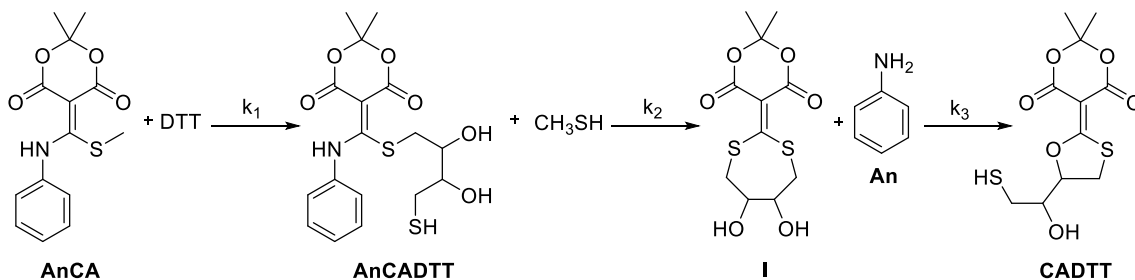


Figure 4.25. Change in absorbance over time for **4.13** upon addition of DTT.

4.4.3 KinTek analysis of kinetics

More complex kinetics can be analyzed using KinTek, a kinetics software program developed by Dr. Ken Johnson at the Institute for Cellular and Molecular Biology at the University of Texas at Austin. The software analyzes spectra, including absorbance spectra, by

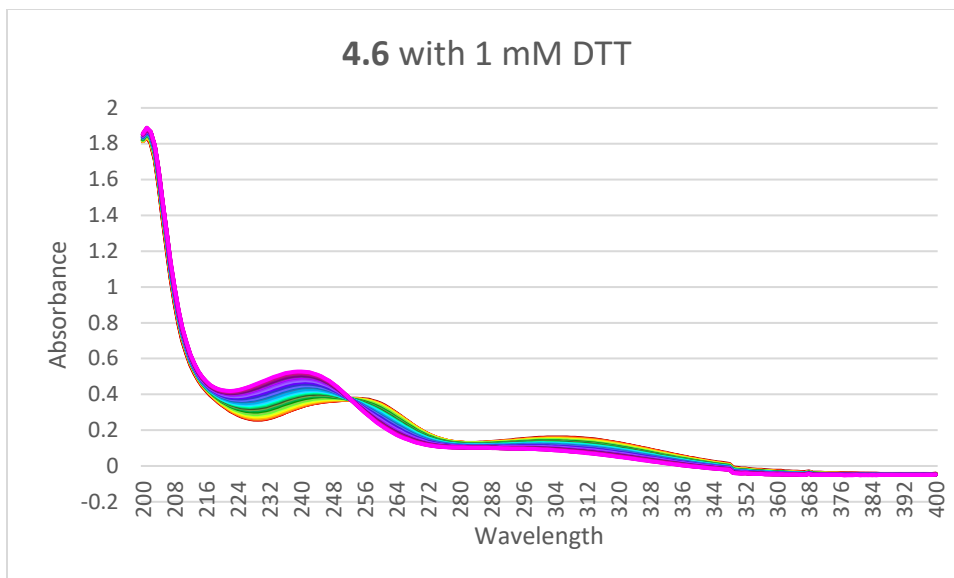
measuring the change over time. Each spectra is subjected to singular value decomposition (SVD) which deconvolutes any redundancy in the data to obtain the time-dependence of individual species. The SVD analysis produces eigenvectors that correspond to changes in the data and assigns significance values to each eigenvector. These eigenvectors are not representations of the physical species, but represent the mathematical analysis. From these eigenvectors and the calculated extinction coefficients of each component, the program rebuilds the initial spectra and plots the concentrations of each species over the progression of the reaction. For this analysis, we used a simplified mechanistic model that includes the major intermediates. (Scheme 4.14)



Scheme 4.14. Mechanistic model used for KinTek studies.

After addition of DTT to each AnCA and monitoring absorbance over 2400 min, a series of spectra for each AnCA was obtained. In order to prepare the spectra to be input into the program, the absorbance of DTT was subtracted from each and the data truncated to only include wavelengths from 220 nm to 345 nm to remove error from the subtraction and from the change in light source from the instrument. (Figure 4.26)

(a)



(b)

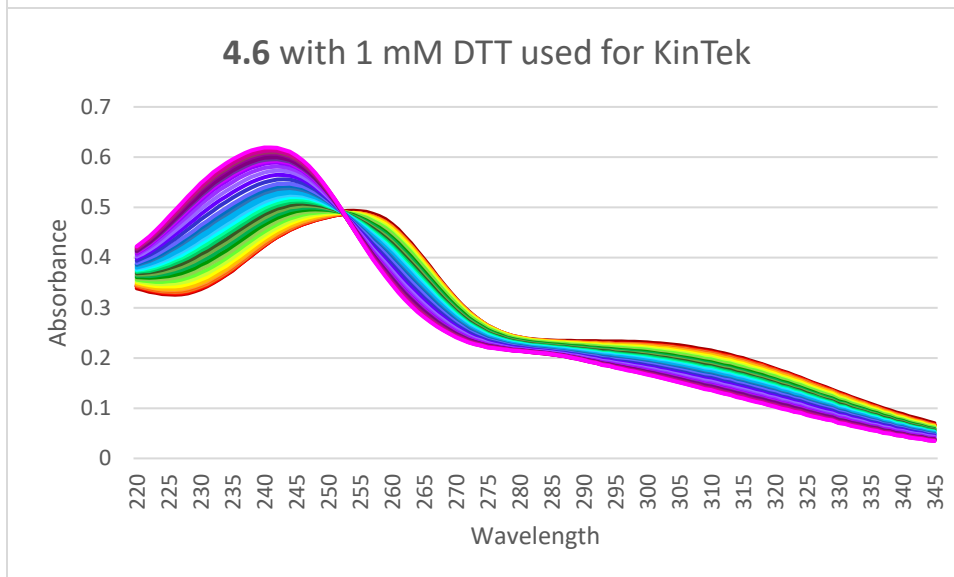


Figure 4.26. (a) **4.6** with 1 mM DTT before subtraction and (b) truncated and subtracted data used for kinetics work. Each shows spectra over 2400 min with $t = 0$ as red and $t = 2400$ as purple.

The experiment was repeated with different concentrations of DTT added to **4.6**, each over a period of 2400 minutes. Both the experiments at 2 mM and 5 mM DTT were subtracted and truncated as described above, eliminating the background from DTT. (Figures 4.27 and 4.28) 10 mM was truncated to 230 nm to remove the extra noise from the high concentration of DTT. (Figure 4.29)

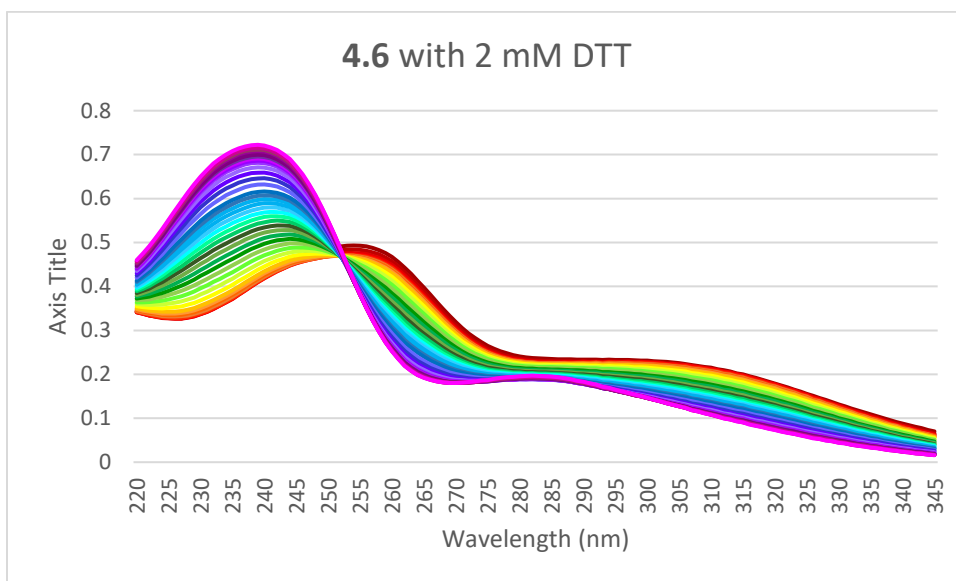


Figure 4.27. Absorbance spectra of **4.6** with 2 mM DTT over 2400 min with $t = 0$ as red and $t = 2400$ as purple.

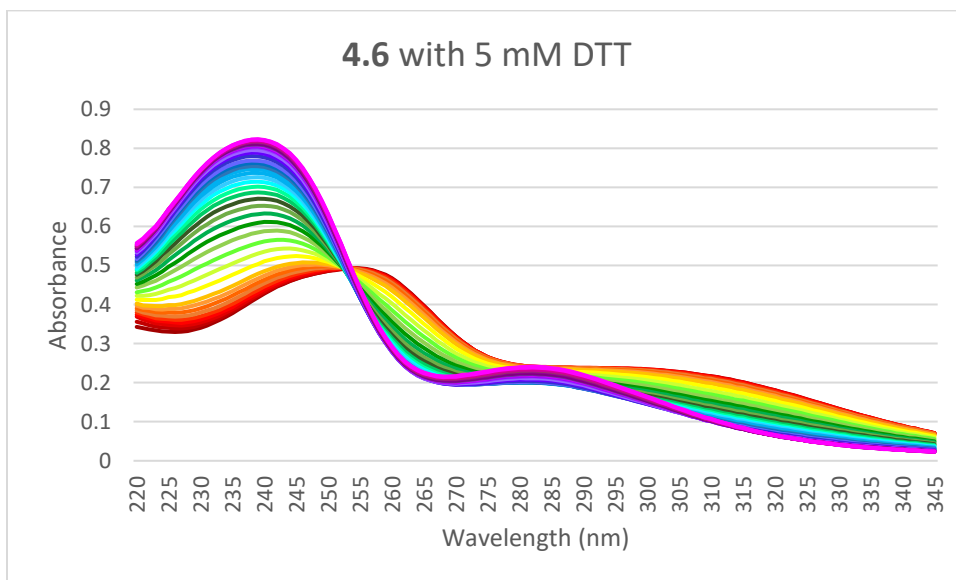


Figure 4.28. Absorbance spectra of **4.6** with 5 mM DTT over 2400 min with $t = 0$ as red and $t = 2400$ as purple.

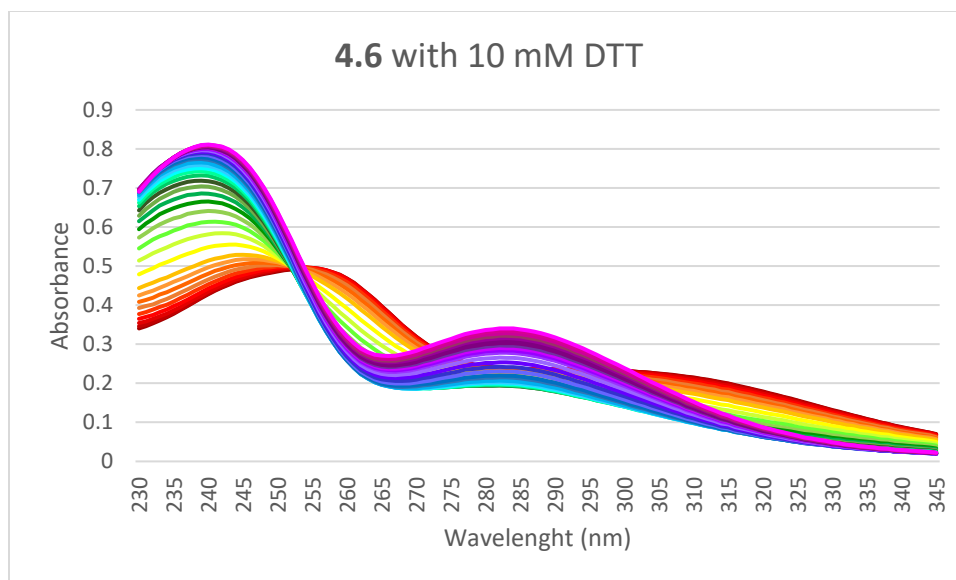


Figure 4.29. Absorbance spectra of **4.6** with 10 mM DTT over 2400 min with $t = 0$ as red and $t = 2400$ as purple.

The rate constants calculated for this model were $k_1 = 3.82 \times 10^{-7} \mu\text{M}^{-1}\cdot\text{min}^{-1}$, $k_2 = 4.5 \times 10^{-3} \text{ min}^{-1}$, and $k_3 = 8.92 \times 10^{-4} \text{ min}^{-1}$. Each rate constant represents the combination of the forward (k_f) and reverse (k_r) rates for each step; each k is actually $k_f + k_r$. Analysis of the four spectra with KinTek gave five eigenvectors to fit. (Figure 4.30) The concentration of each species was calculated over the course of the experiment for each concentration (Figures 4.31 and 4.32) and the absorbance per μM calculated for each component. (Figure 4.33) The reconstruction of the original absorbance spectra is based on the extinction coefficients for each component and their relative concentrations over time. (Figure 4.34) The residual absorbance that is unaccounted for in the reconstruction is shown in Figure 4.35.

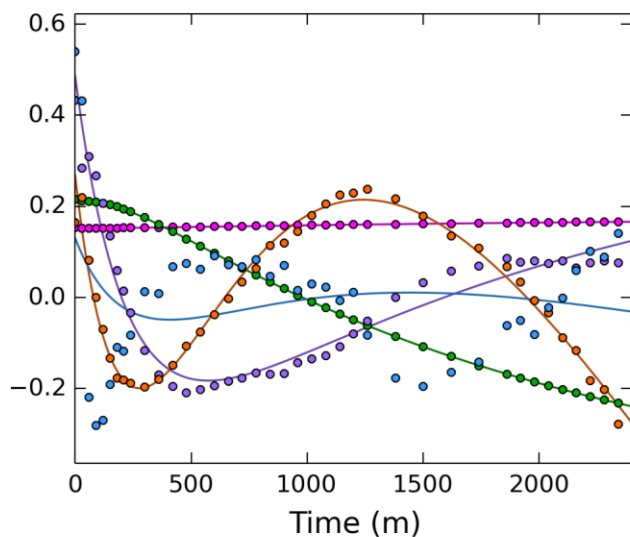


Figure 4.30. Eigenvectors for **4.6** with 1 mM DTT. The significance values for each vector are 22.25 (pink), 2.43 (green), 0.056 (purple), 0.023 (orange), and 0.010 (blue). Vectors are fitted in order of their significance values.

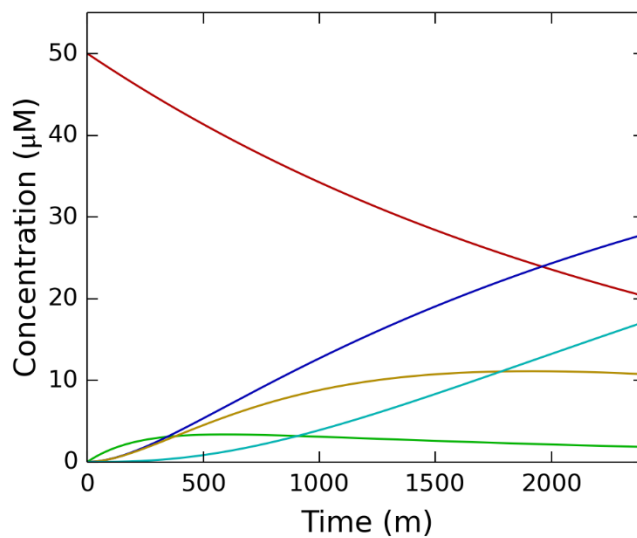


Figure 4.31. Concentration of each component over time for **4.6** with 1 mM DTT. Red is **AnCA**, green is **AnCADTT**, blue is **An**, yellow is **I**, and cyan is **CADTT**.

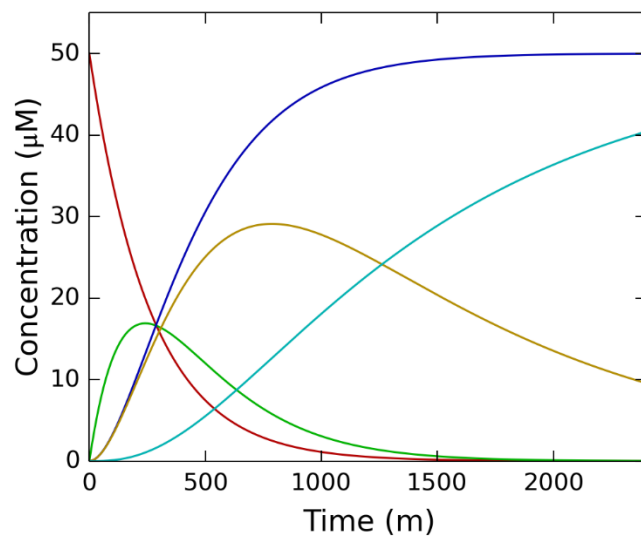


Figure 4.32. Concentration of each component over time for **4.6** with 10 mM DTT. Red is **AnCA**, green is **AnCADTT**, blue is **An**, yellow is **I**, and cyan is **CADTT**.

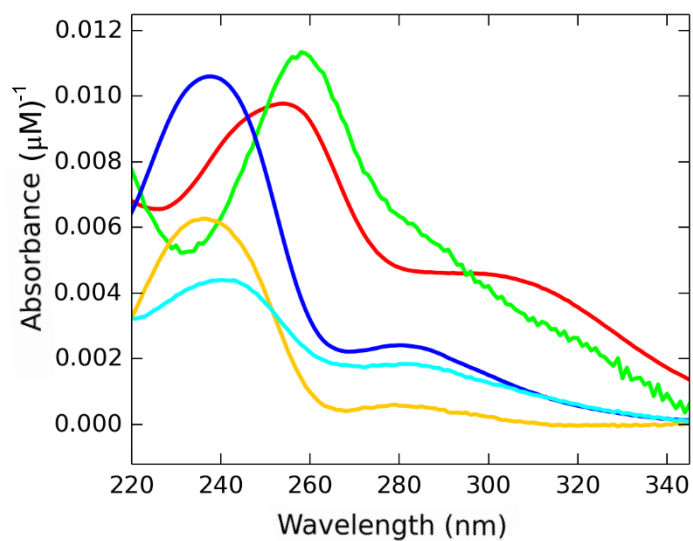


Figure 4.33. Simulated spectra of each component. Red is **AnCA**, green is **AnCADTT**, blue is **An**, yellow is **I**, and cyan is **CADTT**.

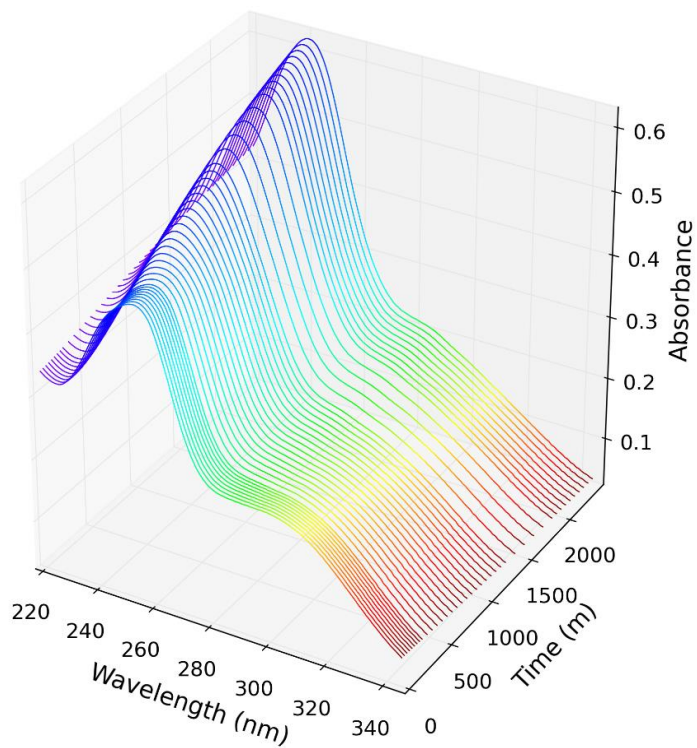


Figure 4.34. Reconstructed absorbance spectra for **4.6** with 1 mM DTT.

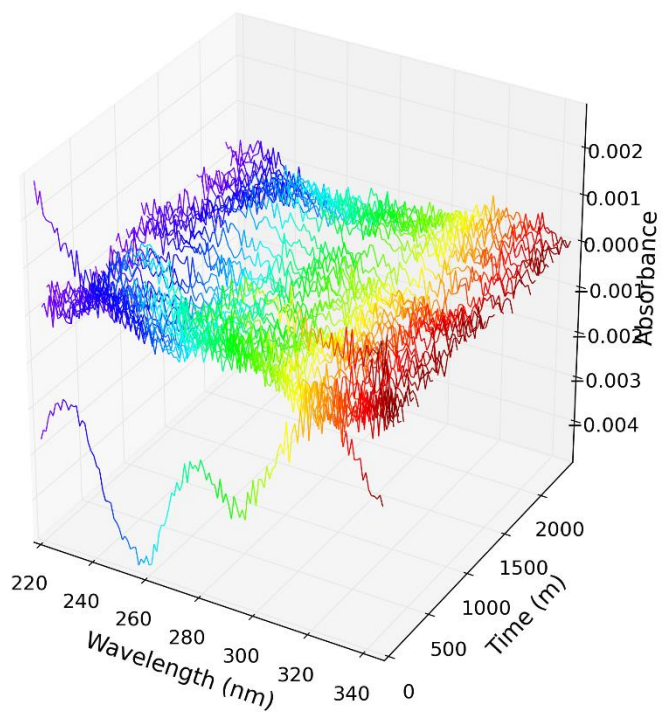


Figure 4.35. Residual absorbance not accounted for in the reconstructed spectra in Figure 4.34.

The same set of kinetics experiments were repeated with **4.10**. LCMS analysis of each reaction at the end time point showed very little **CADTT** formation at 1 mM and 2 mM DTT so these were omitted from the global fitting. (Figures 4.36 and 4.37) Although the simulated spectra for each component were not as accurate as the ones in Figure 4.33, the residual absorbance was still minimal. (Figures 4.38 and Figure 4.39) The rate constants obtained were $k_1 = 1.94 \times 10^{-7} \mu\text{M}^{-1}\cdot\text{min}^{-1}$, $k_2 = 1.14 \times 10^{-3} \text{ min}^{-1}$, and $k_3 = 8.78 \times 10^{-4} \text{ min}^{-1}$. The significance values for each vector for 10 mM are 11.7935 (pink), 1.64724 (green), 0.082456 (purple), 0.029335 (orange), and 0.022643 (blue), which are less than that of the experiments with **4.6**, which creates a larger error in calculating rate constants. (Figure 4.40)

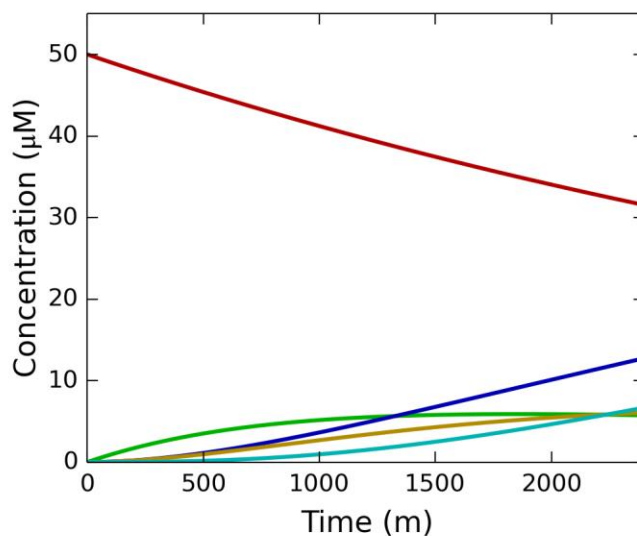


Figure 4.36. Simulated concentrations of each compound with 1 mM showing that the reaction is still mostly reactants. Red is **AnCA**, green is **AnCADTT**, blue is **An**, yellow is **I**, and cyan is **CADTT**.

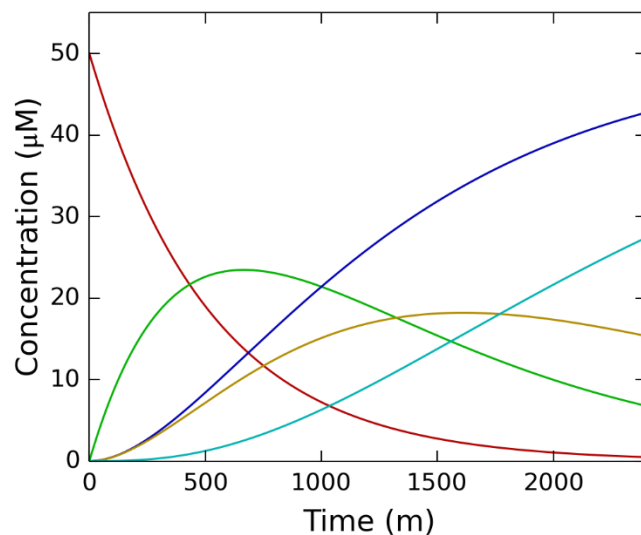


Figure 4.37. Calculated concentrations of each compound with 10 mM. Red is **AnCA**, green is **AnCADTT**, blue is **An**, yellow is **I**, and cyan is **CADTT**.

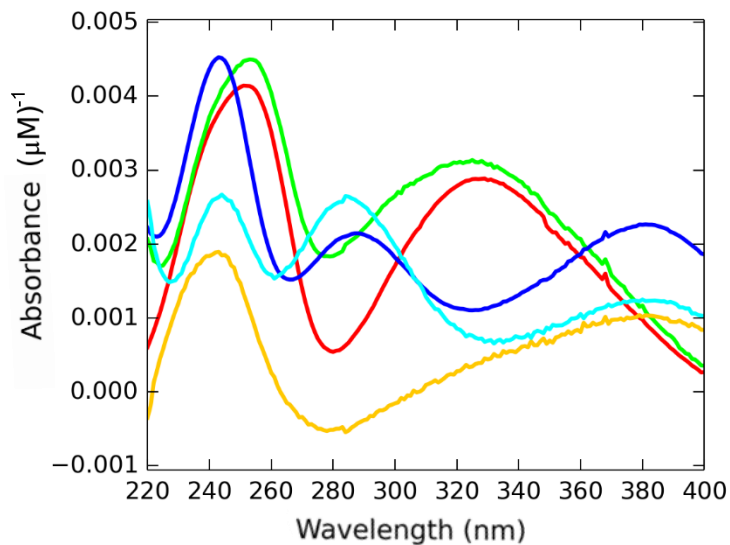


Figure 4.38. Simulated absorbance for each component from the addition of 5 mM of DTT with **4.10**. Red is **AnCA**, green is **AnCADTT**, blue is **An**, yellow is **I**, and cyan is **CADTT**.

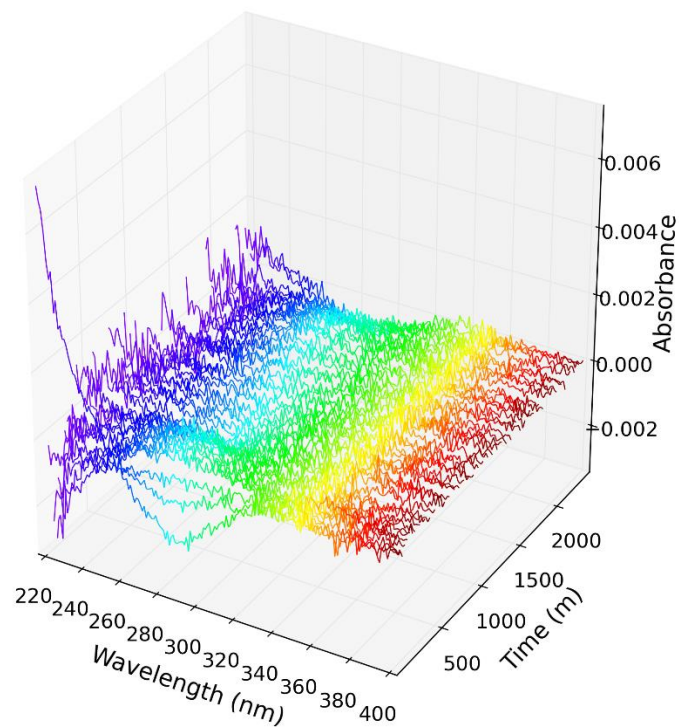


Figure 4.39. Residual absorbance spectra for **4.10** with 5 mM DTT.

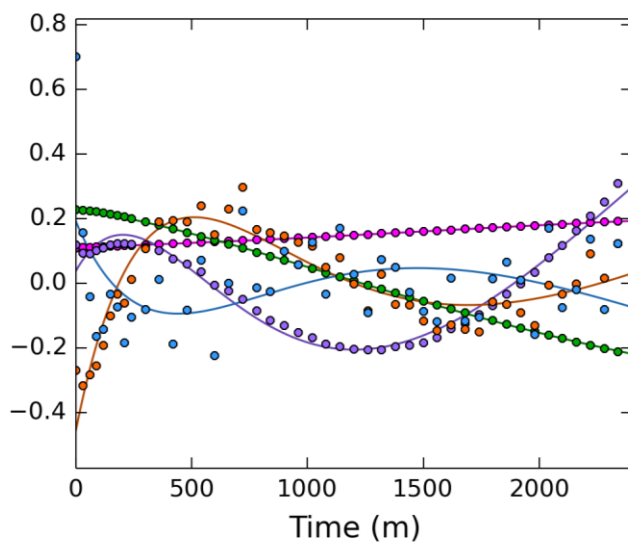


Figure 4.40. Eigenvectors for the reaction of **4.10** with 10 mM of DTT.

The reaction of DTT with **4.8** was also subjected to the same analysis. This time all four DTT concentrations were able to be used as the reaction generated enough product (**CADTT**) for

analysis even at 1 mM DTT. (Figures 4.41 and 4.42) The rate constants obtained were $k_1 = 4.31 \times 10^{-7} \mu\text{M}^{-1}\cdot\text{min}^{-1}$, $k_2 = 4.73 \times 10^{-3} \text{ min}^{-1}$, and $k_3 = 8.92 \times 10^{-4} \text{ min}^{-1}$. The relative absorbance of each component was also computed. (Figure 4.43)

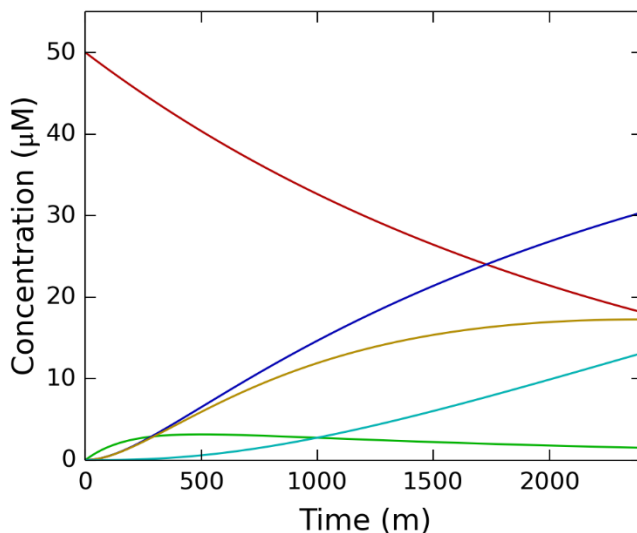


Figure 4.41. Calculated concentrations of each species for the reaction of **4.8** with 1 mM DTT. Red is **AnCA**, green is **AnCADTT**, blue is **An**, yellow is **I**, and cyan is **CADTT**.

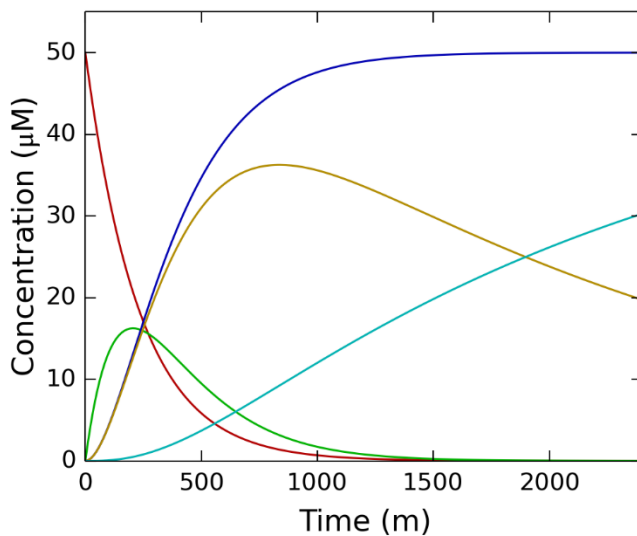


Figure 4.42. Calculated concentrations of each species for the reaction of **4.8** with 10 mM DTT. Red is **AnCA**, green is **AnCADTT**, blue is **An**, yellow is **I**, and cyan is **CADTT**.

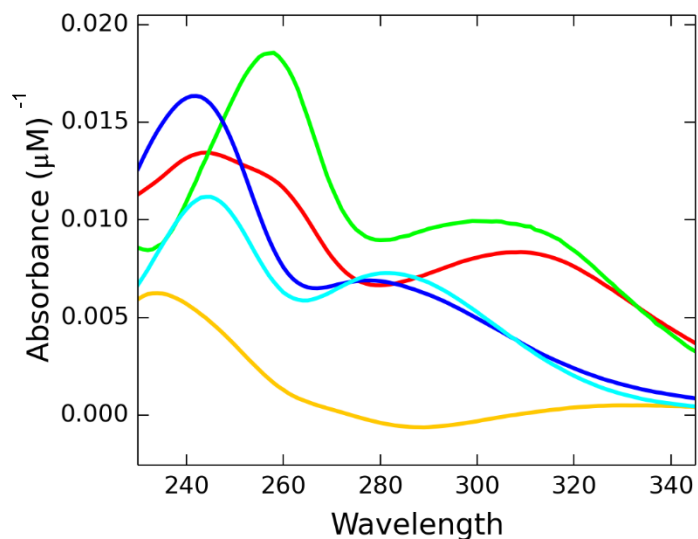


Figure 4.43. Simulated absorbance for each component from the addition of 5 mM of DTT with **4.8**. Red is **AnCA**, green is **AnCADTT**, blue is **An**, yellow is **I**, and cyan is **CADTT**.

The same kinetics experiments were conducted for **4.7** and **4.9**. The calculated rate constants are tabulated in Table 4.3. The rate determining step in each case is the first step.

Substituent	k_1 ($\mu\text{M}^{-1}\cdot\text{min}^{-1}$)	k_2 (min^{-1})	k_3 (min^{-1})
H	3.82×10^{-7}	4.50×10^{-3}	8.92×10^{-4}
Br	2.77×10^{-7}	3.58×10^{-3}	8.82×10^{-4}
NO_2	1.94×10^{-7}	1.14×10^{-3}	8.78×10^{-4}
Me	4.14×10^{-7}	4.78×10^{-3}	8.69×10^{-4}
OMe	4.31×10^{-7}	4.73×10^{-3}	8.92×10^{-4}

Table 4.3. Rate constants calculated from KinTek analysis.

The variance in each rate constant by substituent was analyzed by the construction of a Hammett Plot. (Figures 4.44, 4.45, 4.46) k_1 and k_2 show a linear dependence on substituent, whereas k_3 shows no significant dependence on substituent, as expected from the model.

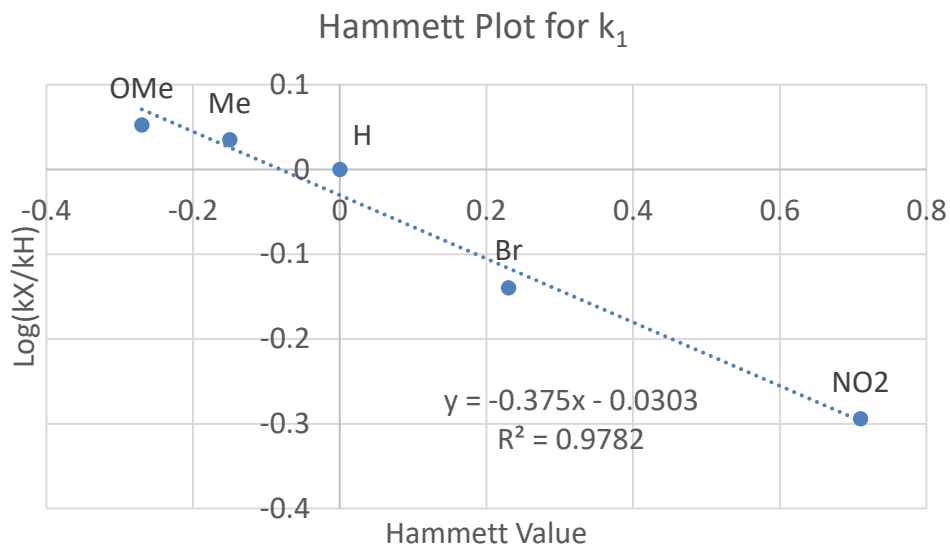


Figure 4.44. Hammett plot for k_1 values.

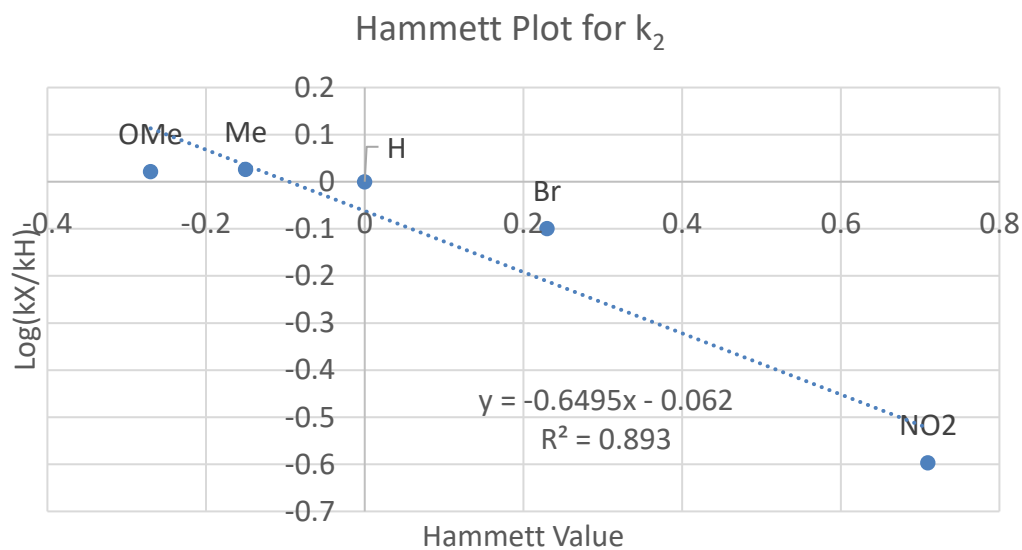


Figure 4.45. Hammett plot for k_2 values.

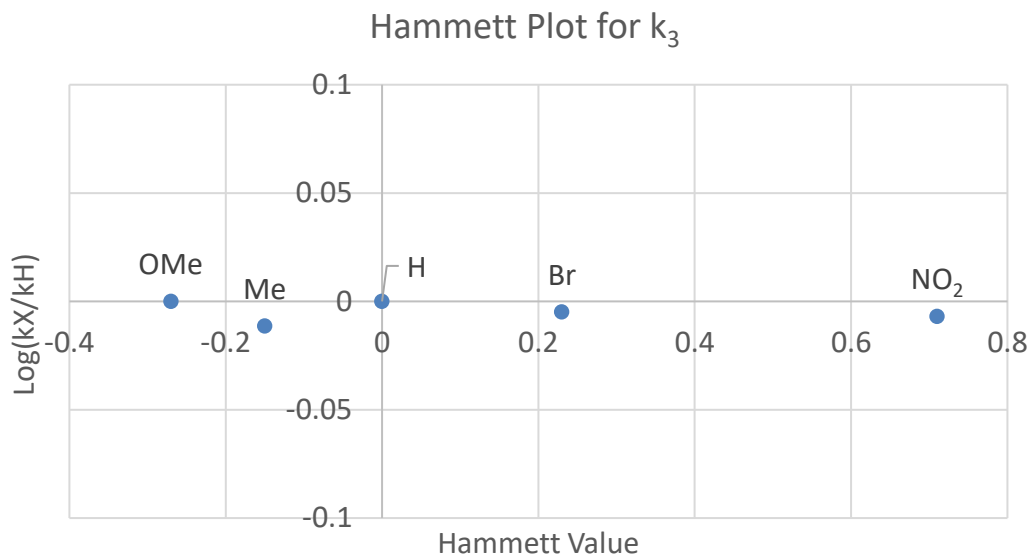
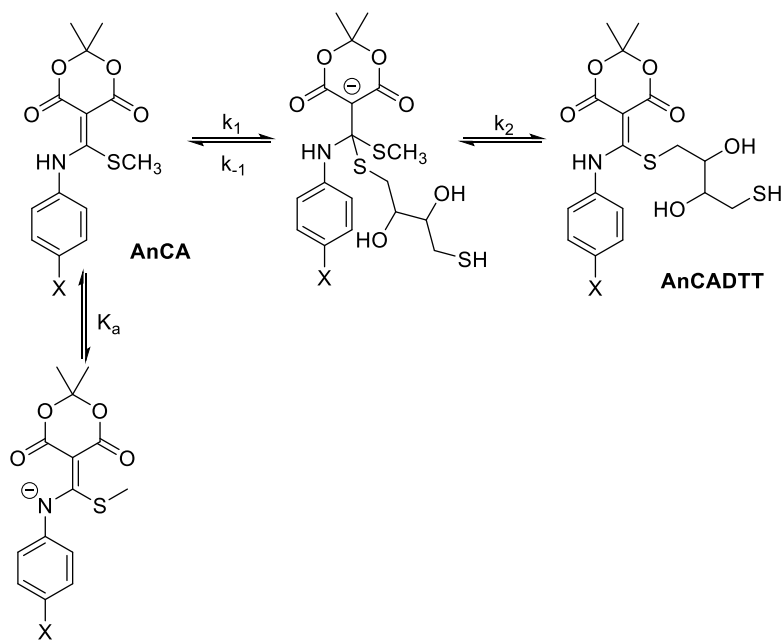


Figure 4.46. Hammett plot for k_3 values.

The negative slopes (ρ) in Figure 4.44 and 4.45 indicate that negative charge is decreasing during the indicated process. The ρ value in the Hammett plot for k_2 is steeper than for k_1 , indicating that the transformations covered by k_2 are more affected by substituent changes than those for k_1 . Additionally, the plot for k_1 shows a more linear relationship than for k_2 . This information was incorporated into a more detailed proposed mechanism. (Scheme 4.15)

AnCA, which explains the linearity shown in the Hammett plot. The negative slope indicates an overall loss of negative charge which is a result of the equilibrium between **AnCA** and **AnCA⁻** (which is mostly negative) to **AnCADTT** (which is neutral).



Scheme 4.16. Expanded mechanism for processes covered by k_1 (observed).

Equation 4.5

$$\frac{d[P]}{dt} = \frac{K_a k_1 k_2 [AnCA] [DTT]_0}{k_{-1} + k_2}$$

Equation 4.6

$$\frac{d[P]}{dt} = \frac{k_1 k_2 [H_3O^+] [AnCA^-] [AnCA] [DTT]_0}{[AnCA] (k_{-1} + k_2)}$$

Equation 4.7

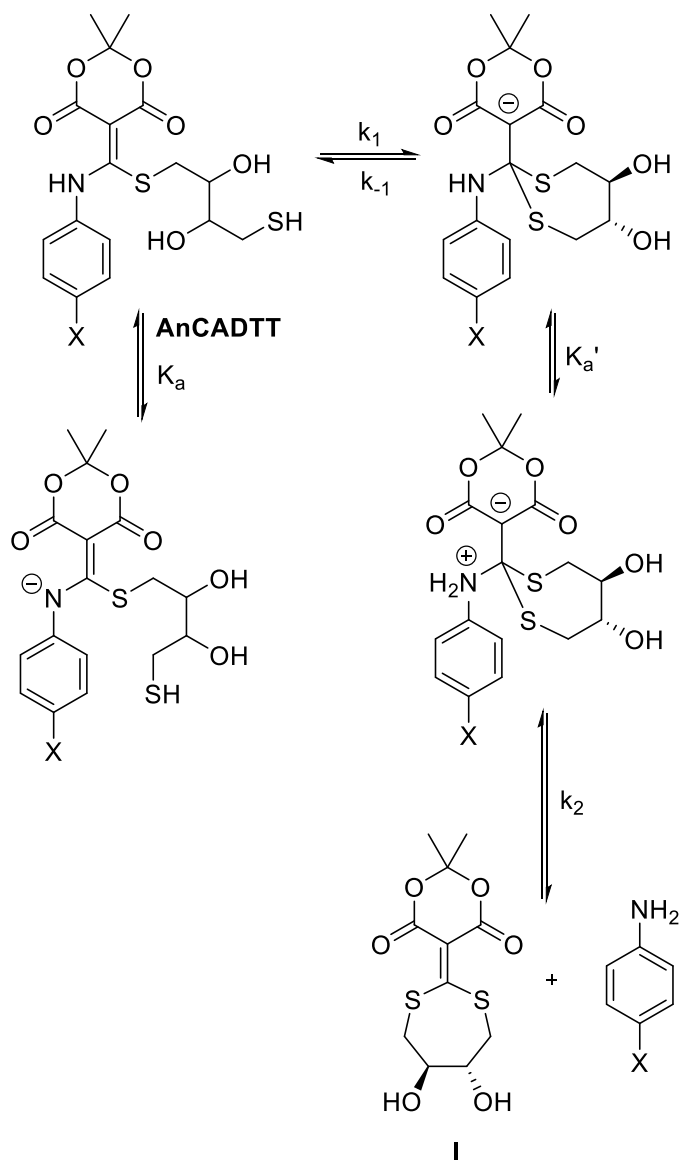
$$\frac{d[P]}{dt} = \frac{k_1 k_2 [H_3O^+] [AnCA^-] [DTT]_0}{k_{-1} + k_2}$$

Equation 4.8

$$k_{obs} = \frac{k_1 k_2 [H_3O^+]}{k_{-1} + k_2}$$

The integrated rate law for k_2 (observed) is shown in Equation 4.9. By substituting for K_a (Equation 4.10), the rate law can be simplified to Equation 4.11. The observed rate constant is the product of multiple constants. (Equation 4.12) The rate law shows a dependence on identity

of the **AnCADTT**, which explains the dependence on substituent shown in the Hammett plot. The negative slope indicates an overall loss of negative charge which is a result of the equilibrium between **AnCADTT** and **AnCADTT⁻** (which is mostly negative) to the protonated, zwitterionic intermediate and finally to **I** (which is neutral). The reduced linearity of the data of Figure 4.45 compared to 4.46 is attributed to the complexity of the k_{obs} value.



Scheme 4.17. Expanded mechanism for processes covered by $k_2(\text{observed})$.

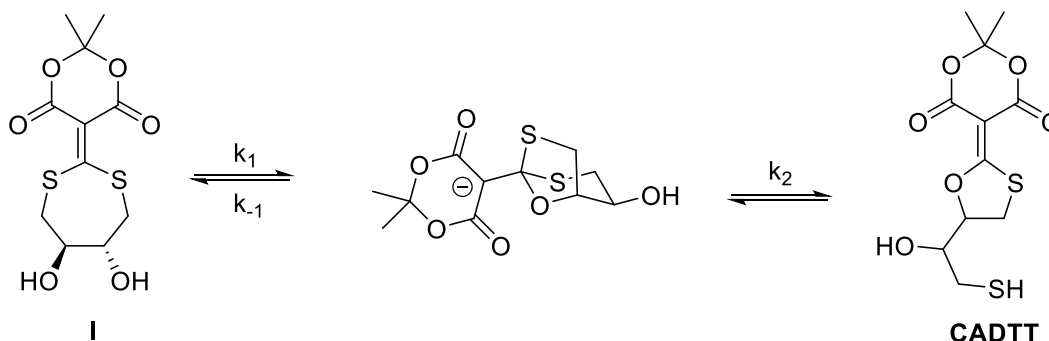
Equation 4.9
$$\frac{d[P]}{dt} = \frac{K_a K_a' k_1 k_2 [AnCADTT]}{k_{-1} + k_2}$$

Equation 4.10
$$\frac{d[P]}{dt} = \frac{K_a' k_1 k_2 [H_3O^+] [AnCADTT^-] [AnCADTT]}{[AnCADTT] (k_{-1} + k_2)}$$

Equation 4.11
$$\frac{d[P]}{dt} = \frac{K_a' k_1 k_2 [H_3O^+] [AnCADTT^-]}{k_{-1} + k_2}$$

Equation 4.12
$$k_{obs} = \frac{K_a' k_1 k_2 [H_3O^+]}{k_{-1} + k_2}$$

The integrated rate law for k_3 (observed) is shown in Equation 4.13. The rate law shows a dependence only on identity of the **I**, which explains the lack of substituent effect shown in the Hammett plot.



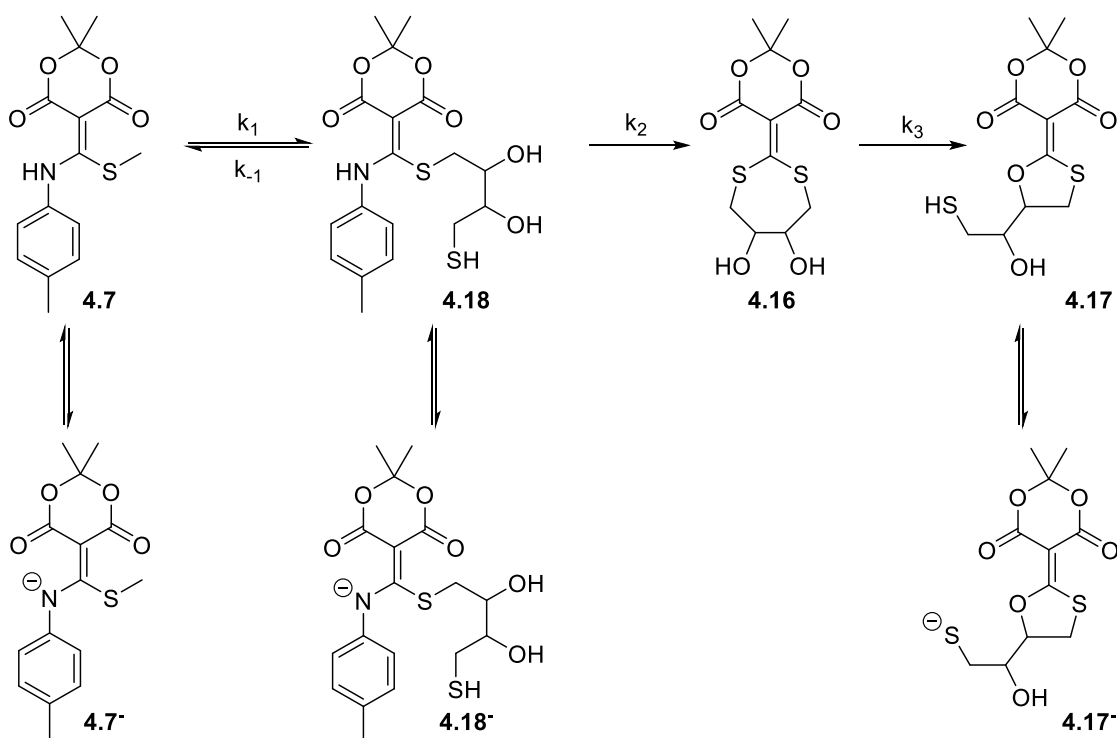
Scheme 4.18. Expanded mechanism for processes covered by k_3 (observed).

Equation 4.13
$$\frac{d[P]}{dt} = \frac{k_1 k_2 [I]}{k_{-1} + k_2}$$

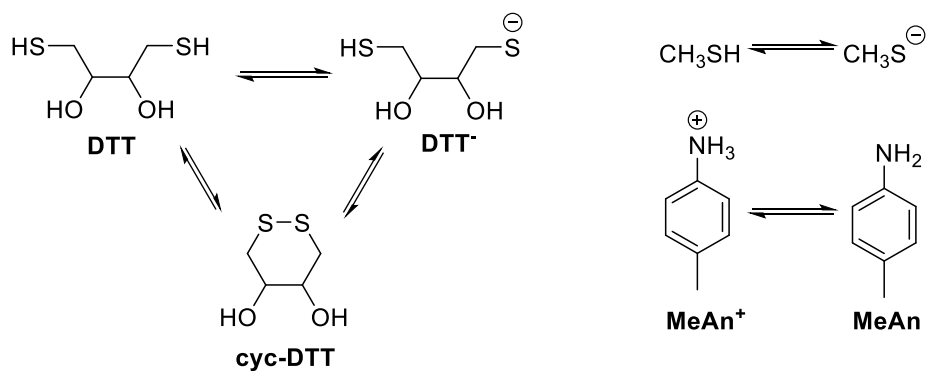
4.4.4 pH and kinetics

Many reactions show a rate dependence on pH including the decoupling of the primary amine-conjugated **4.3**. Above the pK_a of the amine, thiol exchange does not occur due the decreased electrophilicity of the deprotonated conjugate acceptor. We were interested in seeing if

this was true for the aniline derivatives as well. Cursory studies showed that the aniline-CA derivatives decoupled at a wider range of pH since thiol exchange occurred in pH 7 phosphate buffer, pH 5 acetate buffer, and pH 9 bicarbonate buffer. For a more accurate analysis, we used **4.7** and measured change in absorbance upon addition of DTT. There are a series of complex equilibria between the intermediates and their conjugate bases. (Scheme 4.19) The DTT, methanethiol, and 4-toluidine (**MeAn**) also have pKa's that are relevant across the range we are interested in (9.2, 10.4, and 5.10, respectively). (Scheme 4.20)



Scheme 4.19. Complex equilibria of DTT decoupling mechanism.



Scheme 4.20. DTT, An, and methanethiol species present in solution.

Decoupling with DTT was conducted in 2:1 mixture of buffer and methanol. Below pH 5, we saw very little decoupling, even with 20 equivalents of DTT. (Figures 4.47 and 4.48)

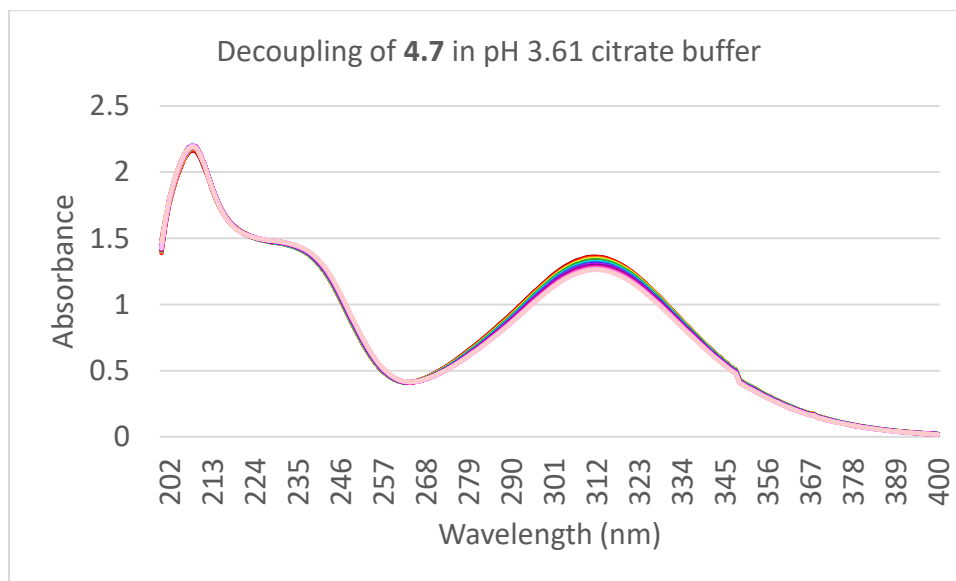


Figure 4.47. Absorbance spectra of **4.7** (100 μ M) with 20 eq of DTT in pH 3.61 citrate buffer.

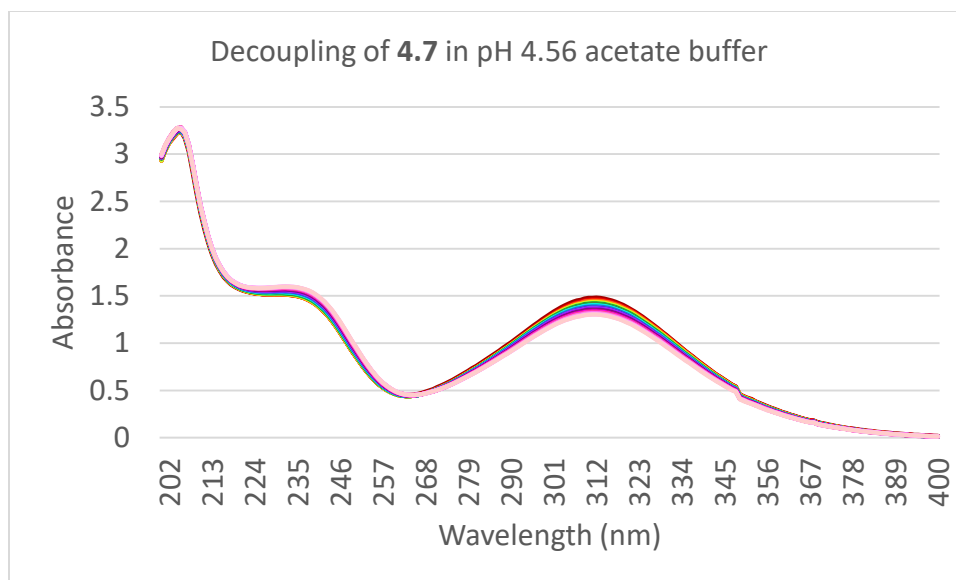


Figure 4.48. Absorbance spectra of **4.7** (100 μ M) with 20 eq of DTT in pH 4.56 acetate buffer.

At pH 5.50, we saw decoupling but it was considerably slower than at pH's above 6, not approaching equilibrium even after 50 hours. (Figures 4.49 and 4.50) Above pH 6, the decoupling reaction achieved equilibrium within the allotted time and, although it is clear that there is more deprotonated conjugate acceptor, it is unclear the effect the changes in pH have on the relative abundance of each species. (Figures 4.51-4.56) Phosphate buffer is not recommended below pH 6; therefore, acetate buffer was used and the change in the type of buffer may have also contributed to the change in rates. Further analysis using KinTek will need to be conducted in the future.

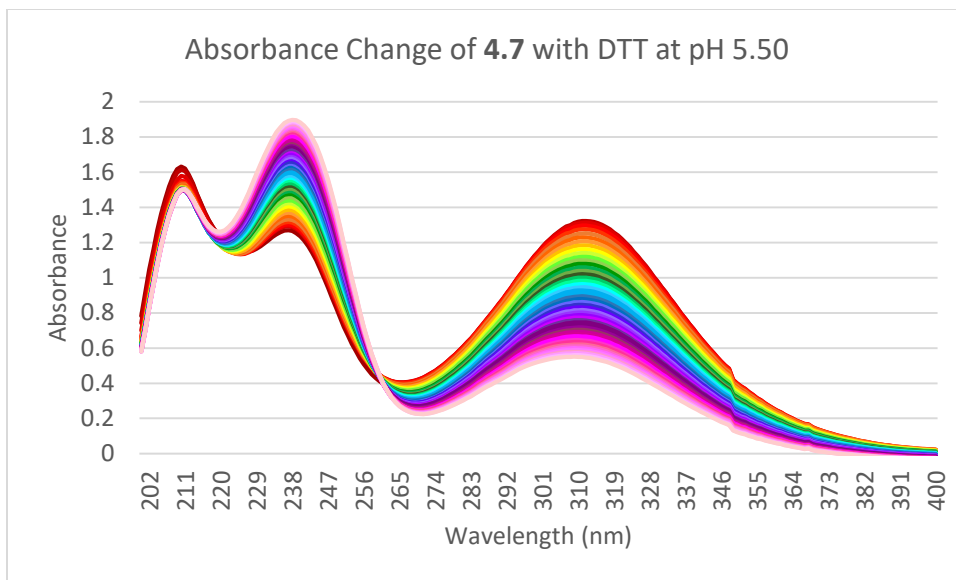


Figure 4.49. Absorbance change of 4.7 with DTT at pH 5.50. t = 0 is red, t = 50 hrs is purple.

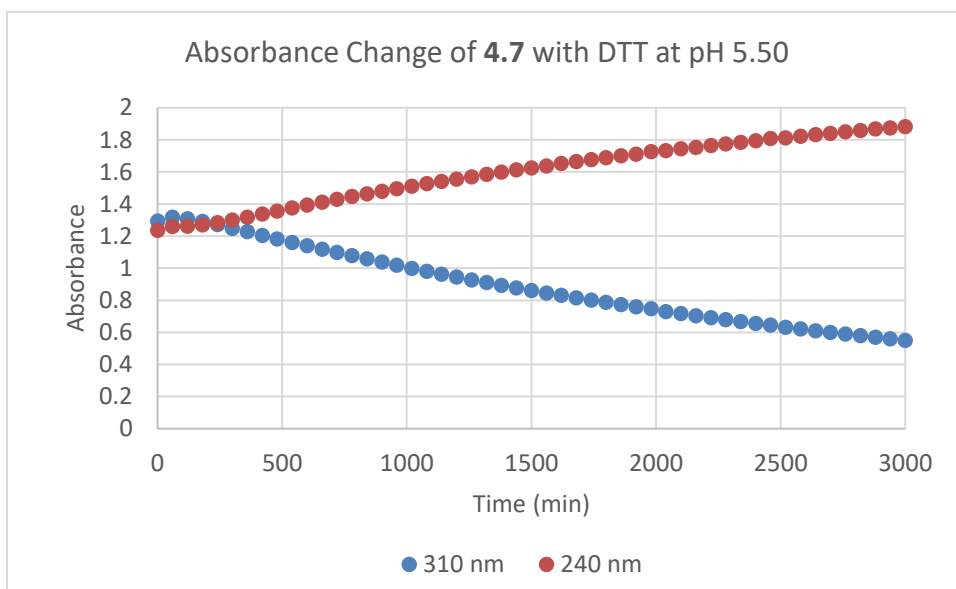


Figure 4.50. Absorbance change of 4.7 with DTT at pH 5.50.

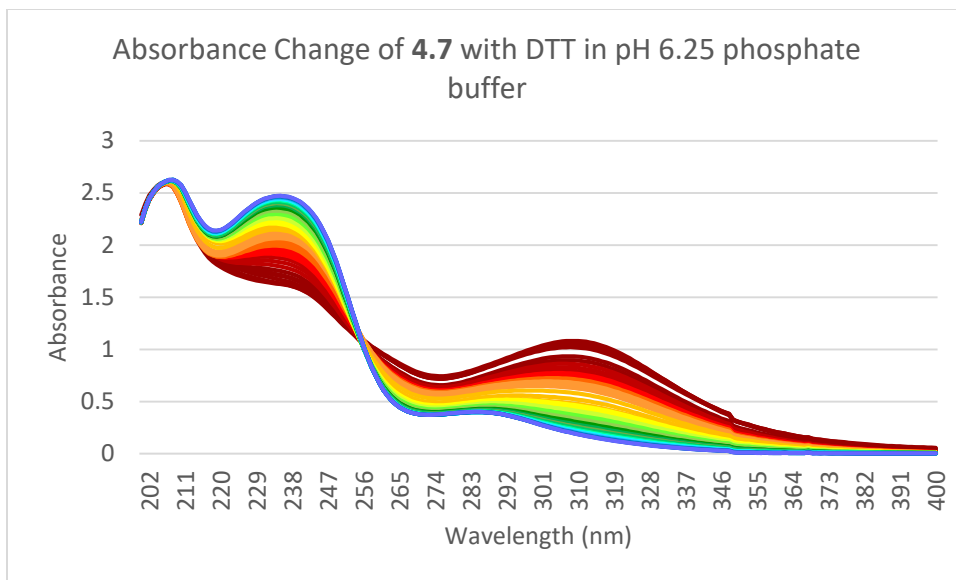


Figure 4.51. Absorbance change of **4.7** with DTT at pH 6.25. $t = 0$ is red, $t = 50$ hrs is purple.

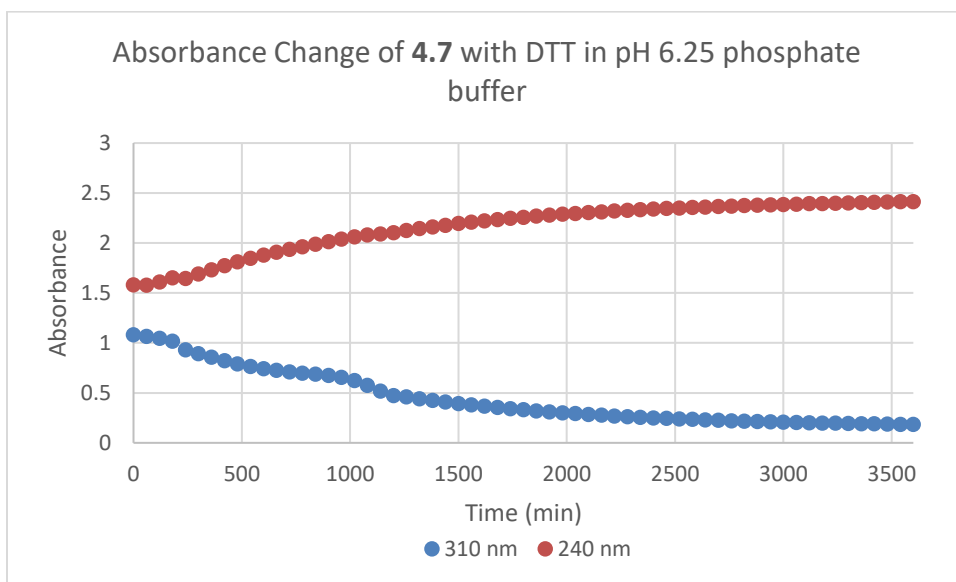


Figure 4.52. Absorbance change of **4.7** with DTT at pH 6.25.

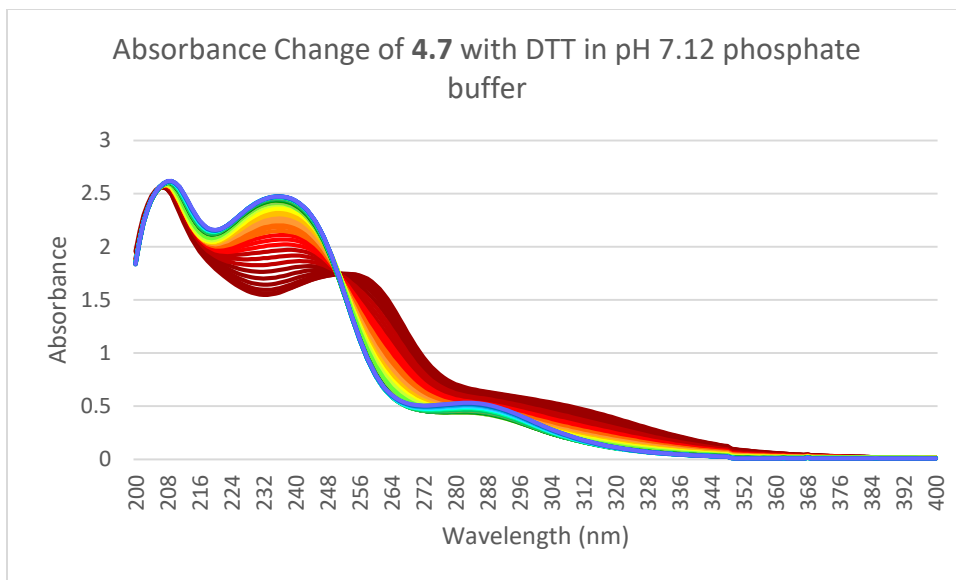


Figure 4.53. Absorbance change of **4.7** with DTT at pH 7.12. $t = 0$ is red, $t = 50$ hrs is purple.

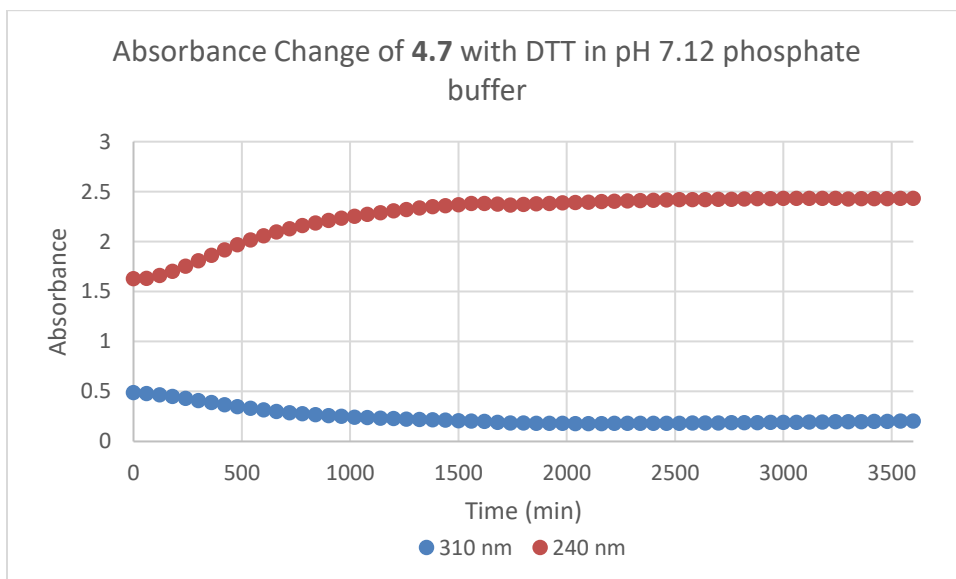


Figure 4.54. Absorbance change of **4.7** with DTT at pH 7.12.

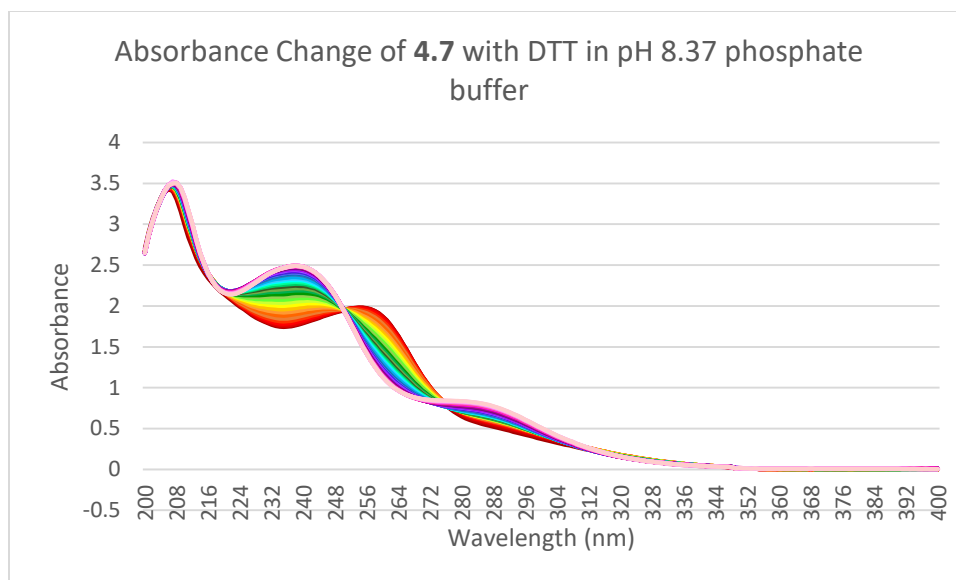


Figure 4.55. Absorbance change of **4.7** with DTT at pH 8.37. $t = 0$ is red, $t = 50$ hrs is purple.

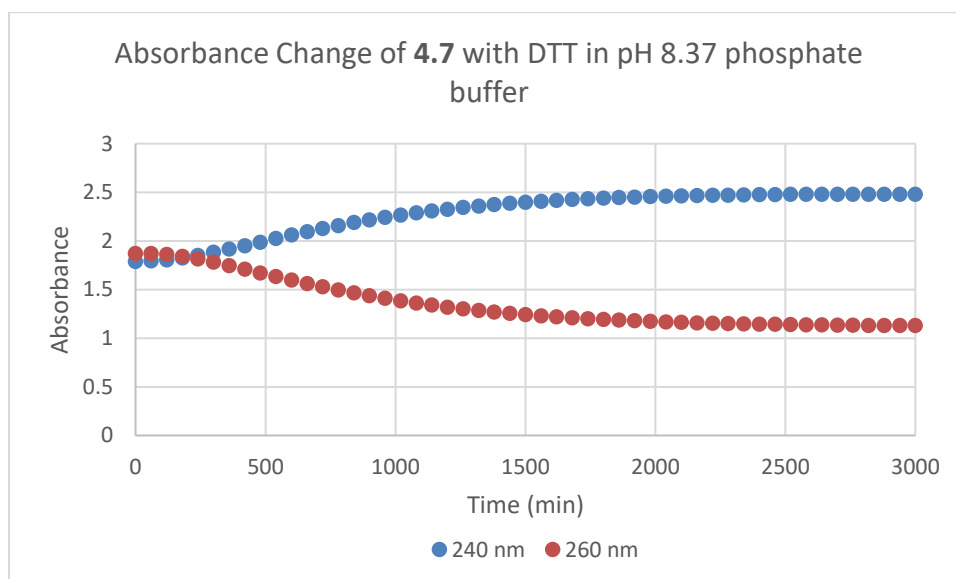


Figure 4.56. Absorbance change of **4.7** with DTT at pH 8.37.

4.5 CONCLUSION

We were able to expand upon an existing system for coupling and decoupling thiols and amines by introducing aryl amines. We also studied structure-activity relationships between

conjugate acceptors with a variety of anilines and the effect of these differently substituted anilines on the kinetics of the decoupling reaction. Reaction rates were analyzed using an advanced analysis software and were studied qualitatively over a range of pH's. We found that the electron-withdrawing nitro group greatly decreased the rate of decoupling, while the electron-donating methoxy group increased the rate. Additionally, the analysis of rates supports the conversion of **4.16** to **4.17** by showing a third rate constant that is independent of the type of aniline used in the conjugate acceptor. Future studies will focus on exploring the pH dependence of the decoupling reaction.

4.6 EXPERIMENTAL

Synthesis of **4.3**: Meldrum's acid (34.7 mmol, 5.0 g) was dissolved in 70 mL anhydrous DMSO under inert atmosphere. Triethylamine (72.8 mmol, 10.15 mL) was added, followed by carbon disulfide (38.2 mmol, 2.39 mL). After 15 min, methyl iodide (104 mmol, 6.48 mL) was added. This was stirred for 4 days at room temperature. Ice was added to precipitate the product. This was filtered and precipitate collected and purified via silica gel column chromatography (25% ethyl acetate/hexanes) to give 2.2 g product (26% yield). : $^1\text{H-NMR}$ (400 MHz, CDCl_3): δ = 2.54 (s, 6H), 1.62 (s, 6H).

Representative procedure for the synthesis of compounds **4.6-4.14**: **4.3** (0.0805 mmol, 20 mg) is dissolved in 9.6 mL 5:1 pH 7.2 phosphate buffer:acetonitrile. Aniline (0.0805 mmol) was added to the reaction mixture and a nitrogen sparged through for 16 hours. The reaction mixture was purified by reverse phase chromatography (acetonitrile:water).

4.6: $^1\text{H-NMR}$ (400 MHz, CDCl_3): δ = 7.45 (m, 2H), 7.37 (m, 1H), 7.32 (m, 2H), 2.28 (s, 3H), 1.77 (s, 6H). HRMS (ESI): m/z calculated for $\text{C}_{11}\text{H}_{16}\text{NO}_4$ $[\text{M}+\text{Na}]^+$: 244.1118, found 244.1116.

4.7: $^1\text{H-NMR}$ (400 MHz, CDCl_3): δ = 7.24 (d, 2H, $J=8.12$ Hz), 7.18 (m, 2H), 2.39 (s, 3H), 2.29 (s, 3H), 1.76 (s, 6H). $^{13}\text{C-NMR}$ (400 MHz, CDCl_3): δ = 178.11, 138.25, 134.56,

130.05, 125.19, 103.07, 85.83, 26.35, 21.13, 18.89. HRMS (ESI): m/z calculated for $C_{15}H_{17}NO_4S$ $[M-H]^-$: 306.08060, found 306.0801.

4.8: 1H -NMR (400 MHz, $CDCl_3$): δ = 7.20 (m, 2H), 6.93 (m, 2H), 3.83 (s, 3H), 2.30 (s, 3H), 1.75 (s, 6H). ^{13}C -NMR (400 MHz, $CDCl_3$): δ = 178.35, 159.19, 129.81, 126.81, 114.57, 103.05, 85.49, 55.52, 26.34, 18.87. HRMS (ESI): m/z calculated for $C_{15}H_{17}NO_5S$ $[M+Na]^+$: 346.07200, found 346.0721.

4.9: 1H -NMR (400 MHz, CD_3CN): δ = 7.32 (d, 2H, $J=8.52$ Hz), 6.81 (d, 2H, $J=8.02$ Hz), 2.35 (s, 3H), 1.38 (s, 6H). ^{13}C -NMR (400 MHz, CD_3CN): δ = 132.70, 126.91, 121.72, 103.32, 86.78, 26.41, 19.07, 8.59. HRMS (ESI): m/z calculated for $C_{14}H_{14}NO_4SBr$ $[M-H]^-$: 369.97540 and 371.97340, found 369.9753 and 371.9734.

4.10: 1H -NMR (400 MHz, CD_3OD): δ = 8.01 (m, 2H), 6.93 (m, 2H), 2.31 (m, 3H), 1.31 (s, 6H). ^{13}C -NMR (400 MHz, CD_3OD): δ = 164.99, 143.41, 123.71, 121.38, 102.10, 24.50, 13.71. HRMS (ESI): m/z calculated for $C_{14}H_{14}N_2O_6S$ $[M-H]^-$: 337.05000, found 337.0500.

4.11: 1H -NMR (400 MHz, CD_3OD): δ = 8.52 (m, 2H), 7.55 (m, 2H), 3.05 (s, 3H), 2.04 (s, 6H). ^{13}C -NMR (400 MHz, CD_3OD): δ = 175.03, 165.73, 131.68, 130.66, 129.68, 120.16, 114.94, 103.67, 78.73, 14.07. HRMS (ESI): m/z calculated for $C_{15}H_{15}NO_6S$ $[M-H]^-$: 336.05470, found 336.0538.

4.12: 1H -NMR (400 MHz, CD_3OD): δ = 7.13 (m, 2H), 6.79 (m, 2H), 2.97 (s, 6H), 2.35 (s, 3H), 1.71 (s, 6H). ^{13}C -NMR (400 MHz, CD_3OD): δ = 164.29, 125.59, 112.10, 109.99, 102.82, 39.24, 29.25, 24.92. HRMS (ESI): m/z calculated for $C_{16}H_{20}N_2O_4S$ $[M-H]^-$: 335.10710, found 335.1069.

4.13: 1H -NMR (400 MHz, $CDCl_3$): δ = 7.70 (d, 2H, $J=8.44$ Hz), 7.41 (d, 2H, $J=8.21$ Hz), 2.29 (s, 3H), 1.72 (s, 6H). ^{13}C -NMR (400 MHz, $CDCl_3$): δ = 192.66, 159.93, 133.43, 125.16, 103.50, 103.21, 103.01, 26.80, 26.45, 21.45, 19.02. HRMS (ESI): m/z calculated for $C_{15}H_{14}N_2O_4S$ $[M-H]^-$: 317.06020, found 317.0604.

4.14: HRMS (ESI): m/z calculated for $C_{14}H_{15}NO_5S$ $[M-H]^-$: 308.05980, found 308.0595.

Representative procedure for addition of NAC into 4.6-4.14: **4.3** (0.0805 mmol, 20 mg) is dissolved in 9.6 mL 5:1 pH 7.2 phosphate buffer:acetonitrile. Aniline (0.0805 mmol) was added to the reaction mixture and a nitrogen sparged through for 16 hours. N-Acetylcysteine (0.0805 mmol, 13.1 mg) was added and nitrogen sparged through solution until the reaction was complete by LCMS. Reaction mixture was purified by reverse-phase column chromatography (acetonitrile/water) and lyophilized.

4.6-NAC: HRMS (ESI): m/z calculated for $C_{18}H_{20}N_2O_7S$ $[M+Na]^+$: 431.08830, found 431.0872.

4.7-NAC: HRMS (ESI): m/z calculated for $C_{19}H_{22}N_2O_7S$ $[M+Na]^+$: 445.10400, found 445.1048.

4.8-NAC: HRMS (ESI): m/z calculated for $C_{19}H_{22}N_2O_8S$ $[M+Na]^+$: 461.09890, found 461.0998.

4.9-NAC: HRMS (ESI): m/z calculated for $C_{18}H_{19}BrN_2O_7S$ $[M+Na]^+$: 508.99890 and 510.99700, found 509.0000 and 510.99830.

4.10-NAC: HRMS (ESI): m/z calculated for $C_{18}H_{19}N_3O_9S$ $[M+Na]^+$: 476.07340, found 476.0730.

4.11-NAC: HRMS (ESI): m/z calculated for $C_{19}H_{20}N_2O_9S$ $[M+Na]^+$: 475.07820, found 475.0790.

4.12-NAC: HRMS (ESI): m/z calculated for $C_{20}H_{25}N_3O_7S$ $[M+Na]^+$: 474.13050, found 474.1292.

4.14-NAC: HRMS (ESI): m/z calculated for $C_{18}H_{20}N_2O_8S$ $[M+Na]^+$: 447.08330, found 447.0840.

4.17: 1H -NMR (400 MHz, CD_3OD): δ = 5.47 (ddd, 1H, $J=9.29, 7.93, 2.51$ Hz), 3.82 (td, 1H, $J=6.69, 2.49$ Hz), 3.43-3.56 (m, 2H), 2.84 (d, 2H, $J=6.70$ Hz), 1.68 (d, 6H, $J=3.54$ Hz).

Representative procedure for pH titrations: **AnCA** (500 μ M) was dissolved in 2:1 water:methanol and divided into 2 solutions. One solution was acidified with a drop of 12 M HCl and the other was basified with a drop of 7 M NaOH solution. The absorbance cuvette was

charged with the acidic solution. The pH was measured and the absorbance was then taken. Basic solution was titrated in and absorbance spectra taken at varying pH (every 0.3-1.0 pH units). Once the pH of the solution stopped increasing, acidic solution was titrated back in to measure additional pH values in order to more accurately determine the pK_a .

Representative procedure for kinetics experiments: **AnCA** was dissolved in 2:1 water:methanol (50 μ M). DTT was added to the solution and the solution was scanned every 30 min for 240 min then every 60 min until 2400 total minutes had passed.

Representative procedure for pH kinetics experiments: **AnCA** was dissolved in 2:1 buffer:methanol (100 μ M). DTT was added to the solution and the solution was scanned every 60 min.

4.7 ACKNOWLEDGEMENTS

Dr. Ken Johnson is very gratefully acknowledged for all his help with the kinetics analysis.

4.8 REFERENCES

- (1) Kolb, H. C.; Finn, M. G.; Sharpless, K. B. Click Chemistry: Diverse Chemical Function from a Few Good Reactions. *Angewandte Chemie International Edition* **2001**, *40* (11), 2004–2021.
- (2) Rostovtsev, V. V.; Green, L. G.; Fokin, V. V.; Sharpless, K. B. A Stepwise Huisgen Cycloaddition Process: Copper(I)-Catalyzed Regioselective “Ligation” of Azides and Terminal Alkynes. *Angewandte Chemie International Edition* **2002**, *41* (14), 2596–2599.
- (3) Cravotto, G.; Cintas, P.; Leonelli, C.; Mason, T. J.; Bang, J. H.; Suslick, K. S.; Mahamuni, N. N.; Adewuyi, Y. G.; Brenner, M. P.; Hilgenfeldt, S.; et al. Harnessing Mechanochemical Effects with Ultrasound-Induced Reactions. *Chem. Sci.* **2012**, *3* (2), 295–307.
- (4) Brantley, J. N.; Konda, S. S. M.; Makarov, D. E.; Bielawski, C. W. Regiochemical Effects on Molecular Stability: A Mechanochemical Evaluation of 1,4- and 1,5-Disubstituted Triazoles. *Journal of the American Chemical Society* **2012**, *134* (24), 9882–9885.
- (5) Kwart, H.; King, K. The Reverse Diels-Alder or Retrodiene Reaction. *Chemical Reviews* **1968**, *68* (4), 415–447.
- (6) Gandini, A. The Furan/maleimide Diels–Alder Reaction: A Versatile Click–unclick Tool in Macromolecular Synthesis. *Progress in Polymer Science* **2013**, *38* (1), 1–29.
- (7) Bielski, R.; Witczak, Z. Strategies for Coupling Molecular Units If Subsequent

- Decoupling Is Required. *Chemical Reviews* **2013**, *113* (3), 2205–2243.
- (8) Joshi, G.; Anslyn, E. V. Dynamic Thiol Exchange with β -Sulfido- α,β -Unsaturated Carbonyl Compounds and Dithianes. *Organic Letters* **2012**, *14* (18), 4714–4717.
- (9) Huang, X.; Chen, B. Synthesis of Bisalkylthiolydine Derivatives of Meldrum's Acid and Barbituric Acid. *Synthesis* **1986**, *1986* (11), 967–968.
- (10) Anslyn, E. V; Dougherty, D. A. *Modern Physical Organic Chemistry*; University Science Books, 2006.

Chapter 5: Synthesis of Piperlongumine and Analogs for Cellular Testing

5.1 INTRODUCTION

5.1.1 Piperlongumine Discovery and Anticancer Activity

Selective cytotoxicity in cancer treatment is essential for patient survival and wellbeing. This requires chemotherapeutics to be both selective and potent. While there are many cytotoxic compounds, selectivity is often difficult to achieve as cancer cells and normal cells have similar properties and environments.

In 2011, the small molecule piperlongumine, also known as piplartine, was reported to have excellent selectivity for cancer cells over normal cells during *in vitro* and *in vivo* studies.¹ (Figure 5.1) Piperlongumine was originally isolated in 1964 from the *Piper longum* plant but not studied in depth until more recently.²

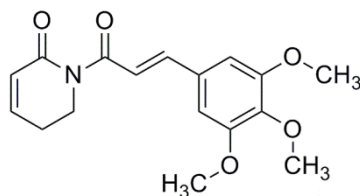


Figure 5.1. Piperlongumine (piplartine).

A mouse melanoma model was used to study piperlongumine's *in vivo* effects. (Figure 5.2) F10-B16 murine melanoma cells were injected subcutaneously and when the tumor size reached ~1 mm, the animals were treated for 21 days with either piperlongumine or a control. Cisplatin was used as a positive control and dimethylsulfoxide (DMSO) was used as the vehicle. Piperlongumine greatly reduced the size of the tumor without affecting healthy cells; however, it did require a higher dosage than cisplatin to induce apoptosis. Piperlongumine has shown to have excellent selectivity for cancer cells over normal cells, but it lacks the desired potency for chemotherapy treatment. (Figure 5.3)

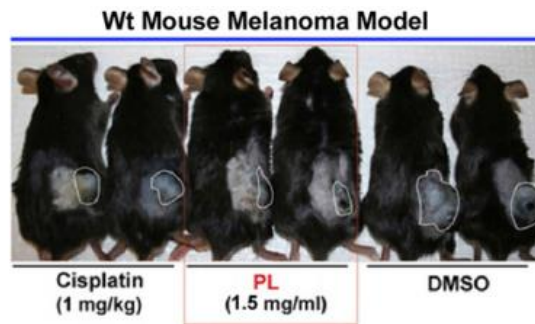


Figure 5.2. Mouse melanoma model.

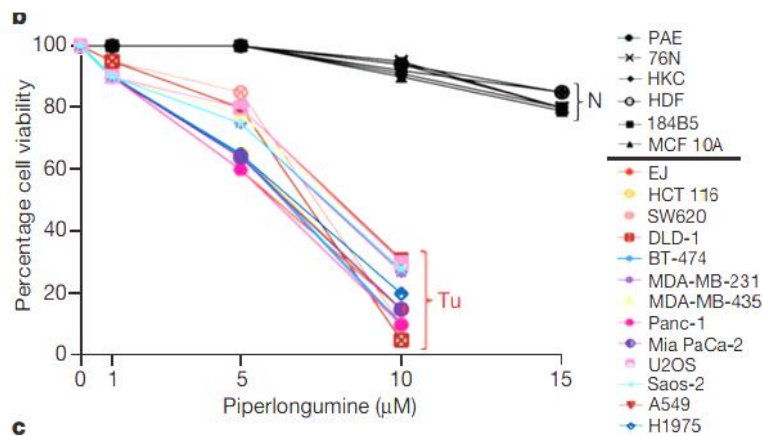


Figure 5.3. Piperlongumine tested in normal and tumor cells.

5.1.2 Reactive Oxygen Species and Cancer

Raj et al. showed that piperlongumine increases the level of reactive oxygen species (ROS) in tumor cells which leads to apoptosis.¹ ROS are discussed in more detail in Chapter 2, but are species such as peroxides, oxyanions, and nitric oxide that, in healthy cells, are byproducts of metabolism.³ These species are used to signal cell growth, differentiation, and inflammatory response as well as eliminate xenotoxins and regulate enzymes.

Levels of ROS are controlled by antioxidant molecules and enzymes in the cell, including glutathione, resveratrol, cytochrome P450, superoxide dismutase, glutathione peroxidase, and catalase.⁴ When this balance is disturbed, the cell experiences oxidative stress. Oxidative stress

can be caused by a variety of factors including environmental stressors, disease, and electron leakage from mitochondria. Mild levels of oxidative stress can be counteracted by antioxidants in the cell and, if necessary, reserve antioxidants can be upregulated as well. If the cell cannot modulate the level of ROS, these species can cause damage to proteins, lipids, and DNA. Oxidative damage to DNA can result in mutation, leading to apoptosis or malignant transformation.

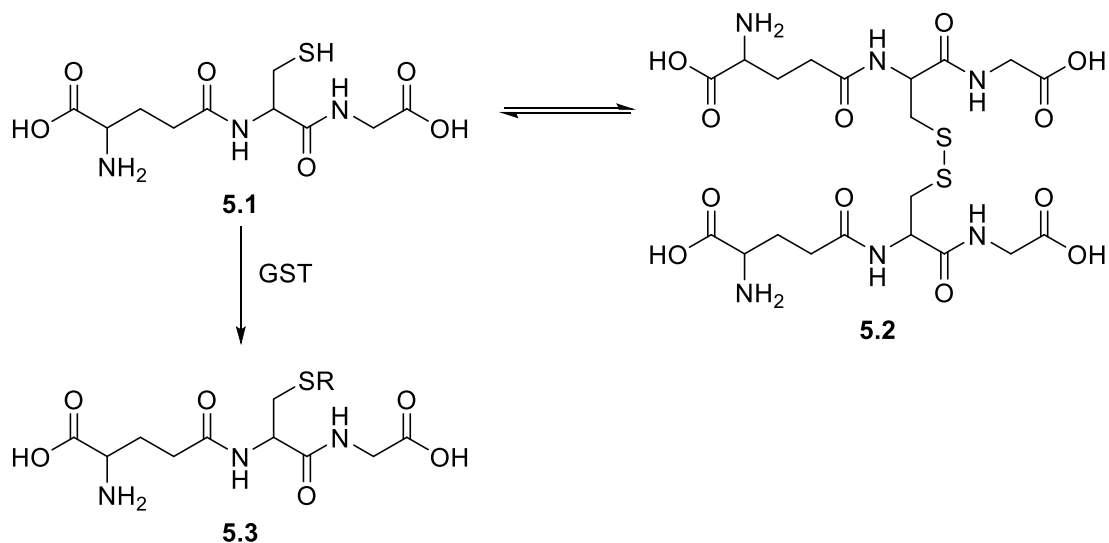
Cancer cells have been found to have higher levels of oxidant and antioxidant activity than normal cells. During mutation, oncogenic signals increase ROS to increase cellular proliferation.⁵ Other signals increase antioxidant pathways in order to minimize oxidative damage. Cancer cells with this increased level of oxidative stress are often resistant to many chemotherapeutics including paclitaxel, doxorubicin, cisplatin, and methotrexate.

ROS have recently become an appealing target for chemotherapy because the increased levels in tumor cells provide an opportunity for specific targeting of cytotoxicity.⁵ Approaching this method of treatment is difficult, however. Directly increasing ROS can cause mutations in healthy cells and dosing with antioxidants can lower the immune system. Piperlongumine is appealing because it indirectly increases the level of ROS in tumor cells.

5.1.3 Glutathione and the Suspected Mechanism of Action for Piperlongumine

Raj et al. showed that piperlongumine decreases the level of glutathione in tumor cells but not in normal cells. Glutathione **5.1** is the major ROS-scavenging system in cells and exists in equilibrium with the oxidized, disulfide glutathione dimer (**5.2**).⁴ (Scheme 5.1) In addition to scavenging radicals itself, glutathione is also a cofactor for antioxidant enzymes, such as glutathione *S*-transferases (GSTs), where it is covalently coupled to various substrates (**5.3**). To be an effective antioxidant in cells, reduced glutathione needs to be present in 100 times the amount of oxidized glutathione. Under oxidative stress, this ratio decreases to 10:1, but this amount of reduced glutathione is still capable of scavenging ROS. Further decrease in glutathione is problematic for the cell. Loss of glutathione has shown to decrease tumor cell

survival and increase drug sensitivity. Tumor cells are more sensitive to depletion of glutathione than normal cells due to their increased level of oxidative and antioxidative activity.



Scheme 5.1. Glutathione (**5.1**) is in equilibrium with oxidized glutathione (**5.2**). Only reduced glutathione can act as a cofactor to modify substrates “R” (**5.3**).

Piperlongumine has been shown to bind to multiple antioxidant proteins. The highest binding interaction was reported by Raj et al. to be glutathione S-transferase pi 1 (GSTP1).¹ GSTP1 covalently couples glutathione with substrates and is responsible for most xenobiotic detoxification in tumor cells. This protein is often overexpressed in solid and drug resistant tumor cells, making it an appealing target for chemotherapy.

The mechanism of action of piperlongumine remains unknown, but Adams et al.⁶ proposed a mechanism involving the different electrophilicities of the two Michael acceptors. (Figure 5.4) Adams et al. proposed that glutathione adds only to the more electrophilic olefin of the lactam (red). Then a glutathione-binding protein such as GSTP1 binds the glutathione-piperlongumine adduct and a cysteine residue adds to the cinnamic olefin (blue). The electrophilicity of the system is such that piperlongumine acts as a prodrug; only after glutathione adds to the first olefin does the second olefin react to inhibit antioxidant proteins.

This proposed mechanism of action has yet to be proven, but testing analogs with different functionalities could help support the proposed mechanism.

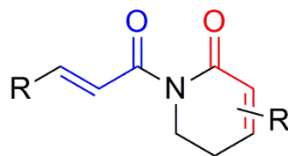


Figure 5.4. The two Michael acceptor's in piperlongumine. The red is proposed to react before the blue.

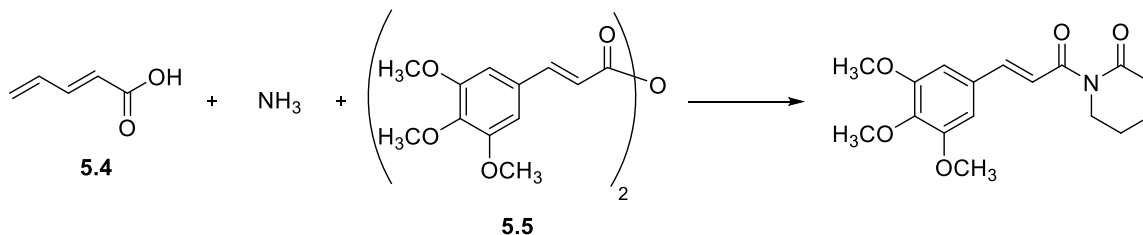
5.1.4 Probing the Mechanism of Action through Synthetic Analogs

Synthetic analogs need to have similar reactivity to the parent compound in order to function similarly. In particular, the two Michael acceptors must react in a similar fashion. If the cinnamic olefin is made to be too reactive, glutathione or another nucleophile will attack before a protein is able to. Adams et al. showed that although a dihydro-piperlongumine lacking the cinnamic olefin still increases ROS, it does not induce apoptosis in cells. Adams also showed that without the lactam olefin, the molecule shows no activity, so analogs must contain this moiety.

5.1.5 Prior Syntheses of Piperlongumine

Piperlongumine was first synthesized in 1984 by Boll et al. in order to verify the proposed structure.⁷ The lactam of piperlongumine was originally proposed as a piperidine ring, and then a saturated lactam, and then an unsaturated lactam, but with question as to the location of the double bond. Boll's synthesis verified the structure of piperlongumine. Boll et al. condensed ammonia with 2,4-pentadienoic acid (**5.4**) to give the unsaturated lactam in piperlongumine. (Scheme 5.2) This was then coupled to 3,4,5-trimethoxycinnamic anhydride (**5.5**). Boll's work is the most recent synthesis of piperlongumine reported except for a few mentions in patent literature.⁸ After verification of the structure of piperlongumine, there was little interest in the compound until the recent reports from Raj et al. of selective cytotoxicity.

Renewed interest has led to multiple publications in the past few years studying cytotoxicity and ROS increase.⁹



Scheme 5.2. Boll et al.'s synthesis of piperlongumine.

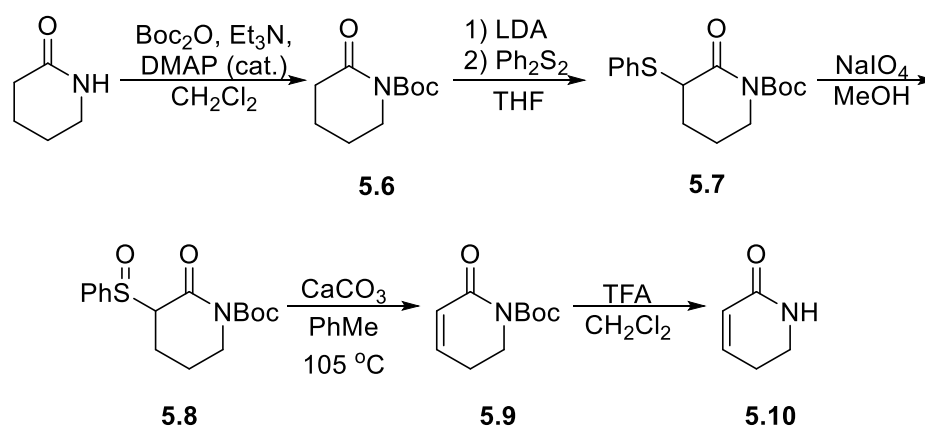
5.2 SYNTHESIS OF PIPERLONGUMINE AND ANALOGS

Piperlongumine has the desired selectivity of a chemotherapeutic but not the desired potency. The natural product has two Michael acceptors which are the proposed crux of its bioactivity. We varied the electronics and sterics of these Michael acceptors in order to increase potency and to test the mechanism of action. We intended to accomplish this by synthesizing piperlongumine and analogs via an adaptable, economical route.

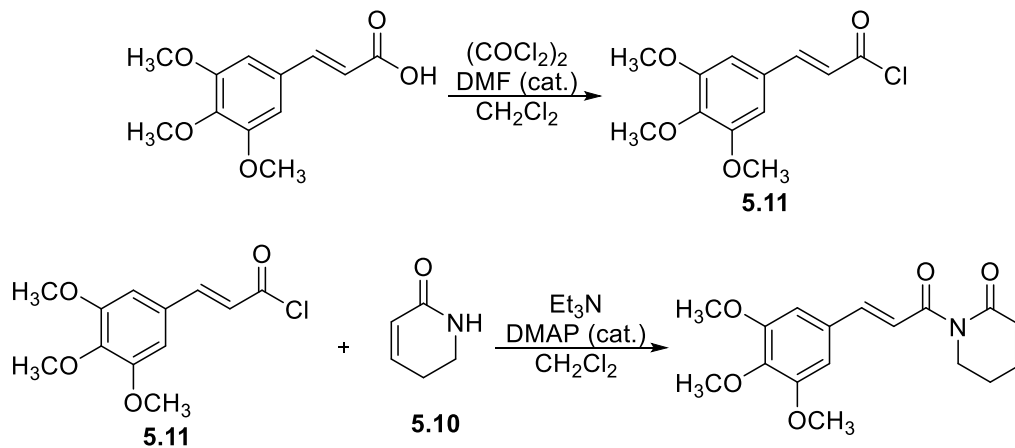
We synthesized piperlongumine through the dehydrogenation of commercially available δ -valerolactam followed by coupling to 3,4,5-trimethoxy-cinnamoyl chloride. The α,β -unsaturated lactam was first reported by Winter et al. using oxidative elimination of the α -phenylselenide.¹⁰ This was accomplished with LDA and phenylselenyl chloride, but the reaction gives a poor yield of only 30%. Starting material was not recoverable from this reaction as the lactam is thought to form the ketene and open the ring. Although oxidation with hydrogen peroxide provides the elimination in one step, overall yield of the end α,β -unsaturated lactam (**5.10**) was poor.

We modified this synthesis to improve the overall yield and economical viability by using phenyl disulfide. (Scheme 5.3) This simple change doubled the yield of the desired lactam **5.10**. Boc protection of δ -valerolactam proceeded in quantitative yield. This was followed by deprotonation and sulfenylation at the α -position to yield **5.7**. *m*CPBA was used to oxidize the

sulfide, but this gave a majority of the sulfone, which does not eliminate upon heating. We then switched to the less reactive NaIO₄, which gave us the sulfoxide **5.8** in modest yields, but with easily recovered starting material. The recovered sulfide can then be resubjected to the oxidation conditions without a decrease in yield of the sulfoxide. Heating in the presence of CaCO₃ provided the α,β-unsaturated lactam (**5.9**). After deprotection, the lactam was coupled to 3,4,5-trimethoxycinnamoyl chloride using triethylamine and 4-dimethylaminopyridine (DMAP). (Scheme 5.4) This yielded the natural product piperlongumine. This synthesis of piperlongumine has the advantage of being easily modified to include various substituents on either the acid chloride or lactam.

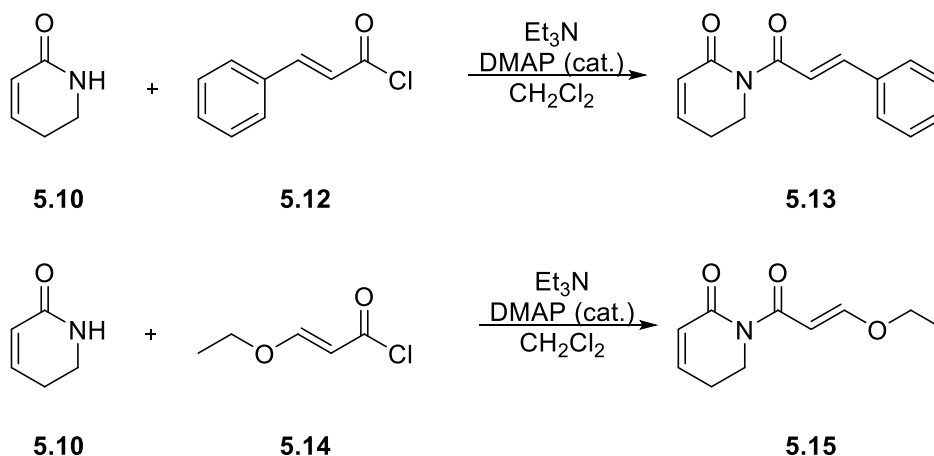


Scheme 5.3. Synthesis of the α,β-unsaturated lactam.



Scheme 5.4. Coupling of **5.11** and **5.10** to provide piperlongumine.

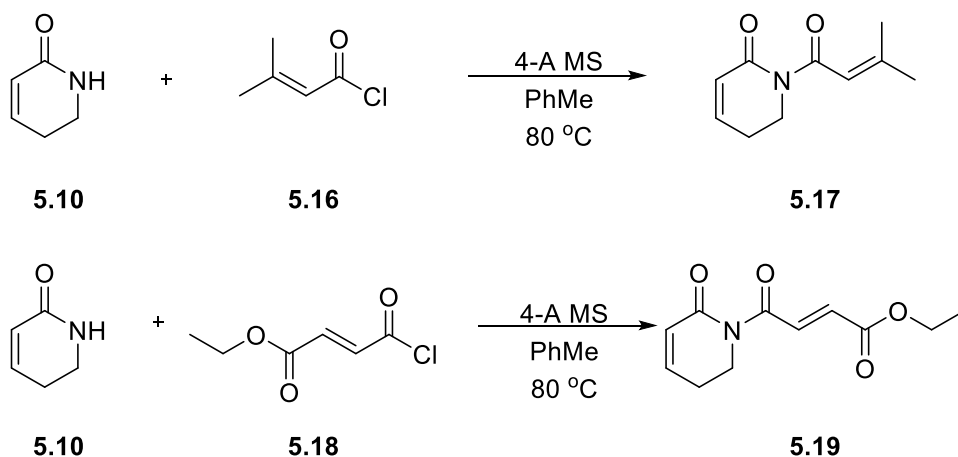
We used this methodology to make the cinnamic and 3-ethoxy acrylic derivatives of piperlongumine (**5.13** and **5.15**, respectively). (Scheme 5.5) However, when we applied these conditions to the coupling of 3,3-dimethylacryloyl chloride and **5.10**, we obtained recovered lactam and two unknown byproducts.



Scheme 5.5. Synthesis of **5.13** and **5.15**.

We then switched to using a procedure described by Baran¹¹ which involves heating the two substrates over 4-Å molecular sieves. (Scheme 5.6) Heating for 12 hours, filtration through

celite, followed by washing with aqueous NaHCO₃ and brine, yielded the desired coupling product **5.17**. This procedure was also used to successfully synthesize the ethyl fumarate analog **5.19**.



Scheme 5.6. Synthesis of **5.17** and **5.19**.

5.3 CONCLUSION

We were able to successfully synthesize piperlongumine and 4 analogs using a novel method. All of the described analogs were tested *in vitro* but with no significant activity compared to controls as measured by Dr. Bharat Aggarwal at MD Anderson Cancer Center using electrophoretic mobility shift assays (EMSA) and a NF- κ B-dependent reporter gene expression assay.

5.4 EXPERIMENTAL

5.4.1 General Procedures

Reactions were performed in flame-dried glassware using anhydrous technique under a positive pressure of nitrogen. Solvents (dichloromethane, tetrahydrofuran, and toluene) were purified using a Pure-Solv MD-5 Solvent Purification System (Innovative Technology). All other reagents were used directly without further purification. Analytical thin-layer chromatography (TLC) was carried out using 0.2 mm commercial silica gel plates (silica gel 60,

F254, EMD chemical) and visualized using a UV lamp and/or stained with CAM. Flash chromatography was performed using Silicycle SiliaFlash P60 (230-400 mesh) silica gel. Infrared spectroscopy was recorded on a Thermo Scientific Nicolet 380 FTIR using neat thin film technique. High-resolution mass spectra (HRMS) were performed at University of Texas-Austin Mass Spectrometry Center on a Agilent 6530 QTOF system equipped with a dual electrospray source and reported as m/z . ^{13}C and ^1H NMR were recorded on a Varian Mercury 400 MHz or Varian DirectDrive 400 MHz spectrometer. 2D NMR experiments were performed by the University of Texas-Austin NMR Laboratory on a Varian Inova 500 MHz spectrometer. Chemical shifts are reported in ppm using residual protium (δ 7.26 for CDCl_3) or carbon (δ 77.0 for CDCl_3) as an internal standard.

5.4.2 Synthetic Procedures

Synthesis of **5.6**: δ -Valerolactam (0.5 g, 5.04 mmol) was dissolved in dichloromethane (10.1 mL). Triethylamine (2.109 mL, 15.13 mmol), DMAP (0.062 g, 0.504 mmol) and di-tert-butyl dicarbonate (1.65 g, 7.57 mmol) were added to the stirring solution and this was allowed to stir at room temperature for 3 hrs. The crude reaction mixture was concentrated under reduced pressure to give an orange oil. This oil was purified via flash chromatography (20% ethyl acetate/hexanes) to give **5.6** as pale yellow crystals (0.98 g, 98%). mp 30-33 °C. ^1H NMR (400 MHz, CDCl_3) δ (ppm) 3.65 (t, 2H, J = 6.1 Hz), 2.50 (t, 2H, J = 7.2 Hz), 1.84-1.79 (m, 4H), 1.52 (s, 9H).

Synthesis of **5.7** using phenylselenium chloride: Diisopropylamine (0.531 mL, 3.76 mmol) was dissolved in THF (3 mL) and cooled to -78°C. *n*-BuLi (1.463 mL, 3.26 mmol) was added dropwise to the solution. This was stirred at -78 °C for 10 min then allowed to warm to 0 °C where the reaction was stirred for 30 min. The reaction was then cooled to -78 °C and transferred via cannula to a stirring solution of **5.6** (0.5 g, 2.51 mmol) in THF (3 mL) at -78 °C. This was stirred for 3 hours then transferred via cannula to a stirring solution of phenylselenium chloride (0.721 g, 3.76 mmol) in THF (3 mL) at -78 °C. The solution was allowed to gradually

warm to room temperature. This was quenched with H₂O (20 mL) and diluted with dichloromethane. The aqueous layer was extracted three times with dichloromethane (20 mL). The organic layers were combined, dried over Na₂SO₄, filtered and concentrated under reduced pressure to give an orange oil. This oil was purified by flash chromatography on silica gel (20% ethyl acetate/hexanes) to yield **5.7** as a yellow oil (0.27 g, 30%). ¹H NMR (400 MHz, CDCl₃) δ(ppm) 7.64 (dd, 2H, *J* = 5.5, 1.9 Hz), 7.33-7.23 (m, 3H), 3.95 (t, 1H, *J* = 5.8 Hz), 3.70-3.53 (m, 2H), 2.25-2.13 (m, 1H), 2.08-1.89 (m, 2H), 1.80-1.68 (m, 1H), 1.50 (s, 9H).

Synthesis of **5.9** using H₂O₂: A solution of 30% hydrogen peroxide in H₂O (5.64 mmol) was added to a stirring solution of **5.7** (1.00 g, 2.82 mmol) in THF (28.2 mL) at 0 °C. The reaction was stirred 15 min at 0 °C and then allowed to warm up to room temperature for 1 hour. The reaction mixture was then dissolved in dichloromethane (50 mL) and washed with a saturated aqueous solution of NaHCO₃. The aqueous layer was extracted three times with dichloromethane (20 mL). The organic layers were combined, dried over Na₂SO₄, filtered and concentrated under reduced pressure to give a pale yellow oil. This was purified by flash chromatography on silica gel (50% ethyl acetate/hexanes) to yield **5.9** as a pale yellow oil (0.44 g, 80%). ¹H NMR (400 MHz, CDCl₃) δ (ppm) 6.76 (dt, 1H, *J* = 9.9, 4.5 Hz), 5.93 (dt, 1H, *J* = 9.9, 1.9 Hz), 3.83 (t, 2H, *J* = 6.3 Hz), 2.41-2.35 (m, 2H), 1.51 (s, 9H).

Synthesis of **5.10**: **5.9** (1.63 g, 8.26 mmol) was dissolved in dichloromethane (69 mL) and trifluoroacetic acid (13.8 mL) was added dropwise. The reaction was stirred at room temperature for 1 hour then nitrogen was blown across the reaction to evaporate volatiles. The brown oil was purified via flash chromatography (5% MeOH/DCM) to give **5.10** as brown crystals (0.74 g, 92%). ¹H NMR (400 MHz, CDCl₃) δ (ppm) 7.19 (br s, 1H), 6.57 (dt, 1H, *J* = 9.9, 4.6 Hz), 5.81 (ddd, 1H, *J* = 9.9, 3.9 Hz, 1.8 Hz), 3.34 (td, 2H, *J* = 7.0, 2.8 Hz), 2.26 (tdd, 2H, *J* = 7.0, 4.6, 1.8 Hz).

Synthesis of **5.7** using phenyl disulfide: Diisopropylamine (0.844 mL, 6.02 mmol) was dissolved in THF (17 mL) and cooled to -78 °C. *n*-BuLi (3.17 mL, 5.52 mmol) was added dropwise to the solution. This was stirred at -78 °C for 10 min then allowed to warm to 0 °C

where the reaction was stirred for 30 min. The reaction was then cooled to $-78\text{ }^{\circ}\text{C}$ and transferred via cannula to a stirring solution of **5.6** (1.0 g, 5.02 mmol) in THF (17 mL) at $-78\text{ }^{\circ}\text{C}$. This was stirred for 3 hours then transferred via cannula to a stirring solution of phenyl disulfide (1.315 g, 6.02 mmol) in THF (17 mL) at $-78\text{ }^{\circ}\text{C}$. The solution was allowed to gradually warm to room temperature. This was quenched with H_2O (50 mL) and diluted with dichloromethane. The aqueous layer was extracted three times with dichloromethane (30 mL). The organic layers were combined, dried over Na_2SO_4 , filtered and concentrated under reduced pressure to give a yellow oil. This oil was purified by flash chromatography on silica gel (20% ethyl acetate/hexanes) to yield **5.7** as a yellow oil (1.08 g, 70%). ^1H NMR (400 MHz, CDCl_3) δ (ppm) 7.54 (m, 2H), 7.31 (m, 3H), 3.85 (td, 1H), 3.74 (m, 1H), 3.62 (m, 1H), 2.21 (m, 1H), 2.02 (m, 2H), 1.79 (m, 1H), 1.52 (s, 9H). IR (film, $\nu\text{ cm}^{-1}$) 747, 1147, 1250, 1292, 1367, 1716, 1770, 2977. HRMS (CI) calculated for $\text{C}_{16}\text{H}_{21}\text{NO}_3\text{S}$ $[\text{M}+\text{H}]^+$ 308.

Synthesis of **5.8**: Sulfide **5.7** (7.15 g, 23.26 mmol) was dissolved in methanol (233 mL) and sodium periodate added (4.88 g, 22.79 mmol). This suspension was stirred at room temperature overnight. The reaction was filtered and washed with methanol (50 mL). Methanol was removed under reduced pressure and the resulting slurry was dissolved in diethyl ether and dried over Na_2SO_4 . This was then filtered and concentrated under reduced pressure. The resulting oil was purified via flash chromatography (50% ethyl acetate/hexanes) to give **5.8** as a white powder (2.32 g, 31%). ^1H NMR (400 MHz, CDCl_3) δ (ppm) 7.50 (m, 2H), 7.44 (m, 3H), 4.22 (t, 1H), 3.71 (m, 1H), 3.64 (m, 1H), 2.32 (m 1H), 2.05 (m, 2H), 1.55 (s, 9H). IR (film, $\nu\text{ cm}^{-1}$) 1047, 1149, 1250, 1717, 1766, 2977. HRMS (CI) calculated for $\text{C}_{16}\text{H}_{21}\text{NO}_4\text{S}$ $[\text{M}+\text{H}]^+$ 324.

Synthesis of **5.9** from **5.8**: Sulfoxide **5.8** (2.32 g, 7.17 mmol) was dissolved in toluene (71.7 mL) and a scoop of CaCO_3 was added. This was heated to reflux overnight. After cooling to room temperature, volatiles were removed under vacuum and the resulting mixture was purified via flash chromatography (50% ethyl acetate/hexanes) to give **5.9** as a pale yellow oil (1.03 g, 73%). ^1H NMR (400 MHz, CDCl_3) δ (ppm) 6.76 (dt, 1H, $J = 9.9, 4.5$ Hz), 5.93 (dt, 1H, $J = 9.9, 1.9$ Hz), 3.83 (t, 2H, $J = 6.3$ Hz), 2.41-2.35 (m, 2H), 1.51 (s, 9H).

Synthesis of **5.11**: Procedure was adapted from Sibi et al.¹² 3,4,5-trimethoxycinnamic acid (10 g, 42.0 mmol) was dissolved in dichloromethane (420 mL). To this was added oxalyl chloride (4.32 mL, 50.4 mmol) and a drop of *N,N*-dimethylformamide. This was stirred at room temperature until bubbling had ceased. Volatiles were removed under reduced pressure and the crude acid chloride was used without further purification. **5.11** was a canary yellow powder (10.55 g, 98%). ¹H NMR (400 MHz, CDCl₃) δ (ppm) 7.76 (d, 1H), 6.79 (s, 2H), 6.55 (d, 1H), 3.90 (s, 9H). IR (film, ν cm⁻¹) 815, 993, 1127, 1746.

Synthesis of piperlongumine: **5.10** (0.034 g, 0.351 mmol) and **5.11** (0.075 g, 0.292 mmol) were dissolved in dichloromethane (2.92 mL) and triethylamine (0.123 mL, 0.877 mmol) and DMAP (0.0036 g, 0.029 mmol) were added. This was stirred overnight. Volatiles were removed under reduced pressure and the crude reaction was purified via flash chromatography (5% methanol/dichloromethane) to yield the desired product as a yellow solid (0.062 g, 67%). ¹H NMR (400 MHz, CDCl₃) δ (ppm) 7.65 (d, 1H), 6.78 (s, 2H), 6.68 (dt, 1H), 6.46 (d, 1H), 5.94 (m, 1H), 3.89 (s, 6H), 3.88 (s, 3H), 3.45 (dt, 2H), 2.38 (m, 2H). IR (film, ν cm⁻¹) 1126, 1633, 1681, 1687.

Synthesis of **5.12**: Cinnamic acid (0.444 g, 3.0 mmol) was dissolved in dichloromethane (3 mL). To this was added oxalyl chloride (0.309 mL, 3.60 mmol) and a drop of *N,N*-dimethylformamide. This was stirred at room temperature until bubbling had ceased. Volatiles were removed under reduced pressure and the crude acid chloride was used without further purification. **5.12** was a yellow solid (0.49 g, 99%).

Synthesis of **5.13**: **5.10** (0.05 g, 0.515 mmol) and **5.12** (0.071 g, 0.429 mmol) were dissolved in dichloromethane (4.29 mL) and triethylamine (0.18 mL, 0.129 mmol) and DMAP (0.006 g, 0.050 mmol) were added. This was stirred overnight. Volatiles were removed under reduced pressure and the crude reaction was purified via flash chromatography (5% methanol/dichloromethane) to yield the yellow solid **5.13** (0.061 g, 62%). ¹H NMR (400 MHz, CDCl₃) δ (ppm) 7.63 (d, 1H), 7.30 (m, 2H), 7.35 (m, 3H), 6.66 (dt, 1H), 6.47 (d, 1H), 5.90 (m, 1H), 3.43 (dt, 2H), 2.36 (m, 2H). IR (film, ν cm⁻¹) 1180, 1614, 1720, 2950.

Synthesis of **5.15**: **5.10** (0.050 g, 0.517 mmol) and **5.14** (0.058 g, 0.431 mmol) were dissolved in dichloromethane (4.3 mL) and triethylamine (0.181 mL, 1.29 mmol) and DMAP (0.005 g, 0.043 mmol) were added. This was stirred overnight. Volatiles were removed under reduced pressure and the crude reaction was purified via flash chromatography (50% ethyl acetate/hexanes) to yield the clear oil **5.15** (0.008 g, 10%). ¹H NMR (400 MHz, CDCl₃) δ (ppm) 7.74 (d, 1H), 6.87 (dt, 1H), 6.49 (d, 1H), 5.98 (m, 1H), 3.99-3.94 (m, 4H), 2.42 (m, 2H), 1.36 (t, 3H). ¹³C NMR (100 MHz, CDCl₃) δ (ppm) 169.1, 165.8, 163.2, 144.9, 126.2, 100.9, 66.8, 41.1, 24.8, 14.4, 8.6. IR (film, ν cm⁻¹) 1049, 1204, 1738, 2935. HRMS (CI) calculated for C₁₀H₁₃NO₃ [M+H]⁺ 196.

Synthesis of **5.17**: **5.10** (0.130 g, 1.341 mmol) and **5.16** (0.050 mL, 0.447 mmol) were dissolved in toluene (4.4.7 mL) over activated molecular sieves. The reaction was heated for 24 hours at 80 °C. The reaction mixture was filtered through celite and rinsed with ethyl acetate. The organic layer was washed with saturated aqueous NaHCO₃ and brine. The organic layer was dried over Na₂SO₄, filtered and concentrated under reduced pressure to yield the clear oil **5.17** (0.014 g, 17.5 %). ¹H NMR (400 MHz, CDCl₃) δ (ppm) 6.87 (dt, 1H), 6.48 (m, 1H), 5.98 (dt, 1H), 3.94 (t, 2H), 2.42 (m, 2H), 2.13 (d, 3H), 1.94 (d, 3H). ¹³C NMR (100 MHz, CDCl₃) δ (ppm) 168.8, 165.5, 154.3, 144.9, 125.9, 120.5, 41.1, 32.7, 27.7, 24.8, 21.1. IR (film, ν cm⁻¹) 1116, 1226, 1386, 1631, 1687. HRMS (CI) calculated for C₁₀H₁₃NO₂ [M+H]⁺ 180.

Synthesis of **5.19**: **5.10** (0.033 g, 0.338 mmol) and **5.18** (0.030 mL, 0.225 mmol) were dissolved in toluene (3 mL) over activated molecular sieves. The reaction was heated for 24 hours at 80 °C. The reaction mixture was filtered through celite and rinsed with ethyl acetate. The organic layer was washed with saturated aqueous NaHCO₃ and brine. The organic layer was dried over Na₂SO₄, filtered and concentrated under reduced pressure to yield the clear oil **5.19** (0.003 g, 6%). ¹H NMR (400 MHz, CDCl₃) δ (ppm) 7.67 (d, 1H), 6.97 (dt, 1H), 6.73 (d, 1H), 6.04 (m, 1H), 4.25 (q, 2H), 4.00 (t, 2H), 2.49 (m, 2H), 1.71 (t, 3H).

5.5 ACKNOWLEDGEMENTS

Dr. Bharat Aggarwal and Dr. Dionicio Siegel are gratefully acknowledged for their contributions to this work.

5.6 REFERENCES

- (1) Raj, L.; Ide, T.; Gurkar, A. U.; Foley, M.; Schenone, M.; Li, X.; Tolliday, N. J.; Golub, T. R.; Carr, S. a; Shamji, A. F.; Stern, A. M.; Mandinova, A.; Schreiber, S. L.; Lee, S. W. *Nature* **2011**, *475*, 231–4.
- (2) Chatterjee, A; Dutta, C. P. *Tetrahedron* **1967**, *23*, 1769–1781.
- (3) Trachootham, D.; Alexandre, J.; Huang, P. *Nature reviews. Drug discovery* **2009**, *8*, 579–91.
- (4) Armstrong, J. S.; Steinauer, K. K.; Hornung, B.; Irish, J. M.; Lecane, P.; Birrell, G. W.; Peehl, D. M.; Knox, S. J. Role of Glutathione Depletion and Reactive Oxygen Species Generation in Apoptotic Signaling in a Human B Lymphoma Cell Line. *Cell Death and Differentiation* **2002**, *9* (3), 252–263.
- (5) Liou, G.-Y.; Storz, P. Reactive Oxygen Species in Cancer. *Free radical research* **2010**, *44* (5), 479–496.
- (6) Adams, D. J.; Dai, M.; Pellegrino, G.; Wagner, B. K.; Stern, A. M.; Shamji, A. F.; Schreiber, S. L. *PNAS* **2012**, *109*, 15115–20.
- (7) Boll, P.M., Hansen, J., Simonsen, O. *Tetrahedron* **1984**, *40*, 171–175.
- (8) Yu, M.; Gao, Y. Process for preparation of piperlongumine and analogues. *Faming Zhuanli Shenqing* **2010**, 10pp.
- (9) Bezerra, D. P.; Pessoa, C.; De Moraes, M. O.; Saker-Neto, N.; Silveira, E. R.; Costa-Lotufo, L. V *European journal of pharmaceutical sciences* **2013**, *48*, 453–463.
- (10) Winter, D. K.; Drouin, A.; Lessard, J.; Spino, C. *The Journal of organic chemistry* **2010**, *75*, 2610–8.
- (11) Gutekunst, W. R.; Baran, P. S. *Journal of the American Chemical Society* **2011**, *133*, 19076–9.
- (12) Sibi, M. P.; Prabakaran, N.; Ghorpade, S. G.; Jasperse, C. P. *Journal of the American Chemical Society* **2003**, *125*, 11796–11797.

Appendix

A.1 CRYSTALLOGRAPHIC DATA

X-ray Experimental for C₁₇H₁₈BNO₃ (**3.3**): Crystals grew as clusters of pale yellow needles by slow evaporation from CH₂Cl₂. The data crystal was cut from a larger crystal and had approximate dimensions; 0.32 x 0.23 x 0.15 mm. The data were collected on a Rigaku SCX-Mini diffractometer with a Mercury 2 CCD using a graphite monochromator with MoK α radiation ($\lambda = 0.71075\text{\AA}$). A total of 1080 frames of data were collected using ω -scans with a scan range of 0.5° and a counting time of 26 seconds per frame. The data were collected at 100 K using a Rigaku XStream low temperature device. Details of crystal data, data collection and structure refinement are listed in Table 1. Data reduction were performed using the Rigaku Americas Corporation's Crystal Clear version 1.40.¹ The structure was solved by direct methods using SIR97² and refined by full-matrix least-squares on F² with anisotropic displacement parameters for the non-H atoms using SHELXL-97.³ Structure analysis was aided by use of the programs PLATON98⁴ and WinGX.⁵ The hydrogen atoms on carbon were calculated in ideal positions with isotropic displacement parameters set to 1.2xU_{eq} of the attached atom (1.5xU_{eq} for methyl hydrogen atoms). The hydrogen atoms on C7 and C24 were observed in a ΔF map and refined with isotropic displacement parameters.

The function, $\Sigma w(|F_o|^2 - |F_c|^2)^2$, was minimized, where $w = 1/[(\sigma(F_o))^2 + (0.0502*P)^2 + (1.0916*P)]$ and $P = (|F_o|^2 + 2|F_c|^2)/3$. $R_w(F^2)$ refined to 0.119, with $R(F)$ equal to 0.0486 and a goodness of fit, S , = 1.07. Definitions used for calculating $R(F)$, $R_w(F^2)$ and the goodness of fit, S , are given below.⁶ The data were corrected for secondary extinction effects. The correction takes the form: $F_{\text{corr}} = kF_c/[1 + (4.9(7)\times 10^{-6}) * F_c^2 \lambda^3/(\sin 2\theta)]^{0.25}$ where k is the overall scale factor. Neutral atom scattering factors and values used to calculate the linear absorption coefficient are from the International Tables for X-ray Crystallography (1992).⁷ All figures were generated using SHELXTL/PC.⁸ Tables of positional and thermal parameters, bond lengths and angles, torsion angles and figures are found elsewhere.

Table A1. Crystal data and structure refinement for **3.3**.

Empirical formula	C17 H18 B N O3
Formula weight	295.13
Temperature	100(2) K
Wavelength	0.71073 Å
Crystal system	monoclinic
Space group	P 21/n
Unit cell dimensions	a = 22.032(4) Å $\alpha = 90^\circ$. b = 6.0534(10) Å $\beta = 104.357(4)^\circ$. c = 22.854(4) Å $\gamma = 90^\circ$.
Volume	2952.8(8) Å ³
Z	8
Density (calculated)	1.328 Mg/m ³
Absorption coefficient	0.090 mm ⁻¹
F(000)	1248
Crystal size	0.320 x 0.230 x 0.150 mm
Theta range for data collection	3.136 to 27.503°.
Index ranges	-26 ≤ h ≤ 28, -7 ≤ k ≤ 7, -29 ≤ l ≤ 29
Reflections collected	27432
Independent reflections	6734 [R(int) = 0.0628]
Completeness to theta = 25.242°	99.8 %
Absorption correction	Semi-empirical from equivalents
Max. and min. transmission	1.00 and 0.821
Refinement method	Full-matrix least-squares on F ²
Data / restraints / parameters	6734 / 0 / 412
Goodness-of-fit on F ²	1.066
Final R indices [I > 2σ(I)]	R1 = 0.0486, wR2 = 0.1127
R indices (all data)	R1 = 0.0627, wR2 = 0.1195
Extinction coefficient	4.9(7) × 10 ⁻⁶
Largest diff. peak and hole	0.320 and -0.260 e.Å ⁻³

Table A2. Atomic coordinates ($\times 10^4$) and equivalent isotropic displacement parameters ($\text{\AA}^2 \times 10^3$) for **3.3**. $U(\text{eq})$ is defined as one third of the trace of the orthogonalized U_{ij} tensor.

	x	y	z	$U(\text{eq})$
C1	1534(1)	1744(2)	7209(1)	16(1)
C2	1980(1)	3063(3)	7593(1)	19(1)
C3	2246(1)	2409(3)	8185(1)	21(1)
C4	2081(1)	401(3)	8400(1)	21(1)
C5	1638(1)	-934(3)	8033(1)	18(1)
C6	1357(1)	-233(2)	7444(1)	17(1)
C7	838(1)	-1483(3)	7085(1)	17(1)
C8	-149(1)	-1731(2)	6262(1)	18(1)
C9	-109(1)	-2162(3)	5617(1)	26(1)
C10	-657(1)	-26(3)	6287(1)	29(1)
C11	-265(1)	-3862(3)	6564(1)	23(1)
C12	1648(1)	2292(2)	5686(1)	16(1)
C13	1918(1)	1855(3)	5215(1)	19(1)
C14	1938(1)	3589(3)	4812(1)	21(1)
C15	1700(1)	5653(3)	4893(1)	21(1)
C16	1433(1)	6095(2)	5379(1)	18(1)
C17	1412(1)	4380(2)	5769(1)	16(1)
C18	2800(1)	3673(2)	3408(1)	15(1)
C19	2377(1)	2444(3)	2976(1)	18(1)
C20	1773(1)	3215(3)	2730(1)	20(1)
C21	1580(1)	5254(3)	2902(1)	19(1)
C22	1986(1)	6493(3)	3336(1)	18(1)
C23	2587(1)	5674(2)	3598(1)	16(1)
C24	2972(1)	6811(2)	4110(1)	16(1)
C25	3821(1)	6826(2)	5068(1)	17(1)
C26	3454(1)	8706(3)	5262(1)	26(1)
C27	3890(1)	4906(3)	5514(1)	22(1)
C28	4453(1)	7638(3)	4999(1)	25(1)

C29	4277(1)	801(2)	3545(1)	15(1)
C30	4676(1)	-951(2)	3549(1)	17(1)
C31	5210(1)	-571(3)	3333(1)	20(1)
C32	5325(1)	1475(3)	3111(1)	20(1)
C33	4911(1)	3245(3)	3098(1)	18(1)
C34	4394(1)	2871(2)	3324(1)	15(1)
N1	464(1)	-712(2)	6600(1)	16(1)
N2	3462(1)	5933(2)	4464(1)	16(1)
O1	563(1)	1277(2)	6363(1)	19(1)
O2	1590(1)	891(2)	6134(1)	18(1)
O3	1191(1)	4414(2)	6278(1)	17(1)
O4	3691(1)	3945(2)	4342(1)	18(1)
O5	3729(1)	826(2)	3725(1)	16(1)
O6	3928(1)	4315(2)	3351(1)	17(1)
B1	1244(1)	2138(3)	6508(1)	17(1)
B2	3520(1)	3135(3)	3680(1)	16(1)

Table A3. Bond lengths [\AA] and angles [$^\circ$] for **3.3**.

C1-C2	1.396(2)	C8-C9	1.522(2)
C1-C6	1.406(2)	C8-C10	1.534(2)
C1-B1	1.587(2)	C9-H9A	0.98
C2-C3	1.391(2)	C9-H9B	0.98
C2-H2	0.95	C9-H9C	0.98
C3-C4	1.393(2)	C10-H10A	0.98
C3-H3	0.95	C10-H10B	0.98
C4-C5	1.380(2)	C10-H10C	0.98
C4-H4	0.95	C11-H11A	0.98
C5-C6	1.401(2)	C11-H11B	0.98
C5-H5	0.95	C11-H11C	0.98
C6-C7	1.445(2)	C12-O2	1.3600(17)
C7-N1	1.2923(19)	C12-C13	1.380(2)
C7-H7	0.952(18)	C12-C17	1.398(2)
C8-N1	1.5108(19)	C13-C14	1.403(2)
C8-C11	1.515(2)	C13-H13	0.95

C14-C15	1.385(2)	C26-H26C	0.98
C14-H14	0.95	C27-H27A	0.98
C15-C16	1.404(2)	C27-H27B	0.98
C15-H15	0.95	C27-H27C	0.98
C16-C17	1.377(2)	C28-H28A	0.98
C16-H16	0.95	C28-H28B	0.98
C17-O3	1.3677(18)	C28-H28C	0.98
C18-C19	1.394(2)	C29-O5	1.3697(18)
C18-C23	1.406(2)	C29-C30	1.375(2)
C18-B2	1.587(2)	C29-C34	1.399(2)
C19-C20	1.391(2)	C30-C31	1.403(2)
C19-H19	0.95	C30-H30	0.95
C20-C21	1.394(2)	C31-C32	1.386(2)
C20-H20	0.95	C31-H31	0.95
C21-C22	1.380(2)	C32-C33	1.403(2)
C21-H21	0.95	C32-H32	0.95
C22-C23	1.401(2)	C33-C34	1.380(2)
C22-H22	0.95	C33-H33	0.95
C23-C24	1.439(2)	C34-O6	1.3620(17)
C24-N2	1.2917(19)	N1-O1	1.3606(15)
C24-H24	0.953(18)	N2-O4	1.3612(15)
C25-N2	1.5102(18)	O1-B1	1.544(2)
C25-C28	1.522(2)	O2-B1	1.485(2)
C25-C26	1.524(2)	O3-B1	1.469(2)
C25-C27	1.528(2)	O4-B2	1.5448(19)
C26-H26A	0.98	O5-B2	1.467(2)
C26-H26B	0.98	O6-B2	1.4895(19)
C2-C1-C6	117.74(13)	C4-C3-H3	119.7
C2-C1-B1	126.36(14)	C5-C4-C3	120.15(14)
C6-C1-B1	115.68(13)	C5-C4-H4	119.9
C3-C2-C1	120.66(14)	C3-C4-H4	119.9
C3-C2-H2	119.7	C4-C5-C6	119.06(14)
C1-C2-H2	119.7	C4-C5-H5	120.5
C2-C3-C4	120.56(14)	C6-C5-H5	120.5
C2-C3-H3	119.7	C5-C6-C1	121.75(14)

C5-C6-C7	119.13(14)	C15-C14-H14	119.6
C1-C6-C7	118.95(13)	C13-C14-H14	119.6
N1-C7-C6	122.95(14)	C14-C15-C16	121.61(14)
N1-C7-H7	115.5(10)	C14-C15-H15	119.2
C6-C7-H7	121.4(10)	C16-C15-H15	119.2
N1-C8-C11	110.26(12)	C17-C16-C15	117.16(14)
N1-C8-C9	107.84(12)	C17-C16-H16	121.4
C11-C8-C9	110.60(13)	C15-C16-H16	121.4
N1-C8-C10	105.95(12)	O3-C17-C16	128.02(14)
C11-C8-C10	110.40(14)	O3-C17-C12	110.60(12)
C9-C8-C10	111.67(13)	C16-C17-C12	121.36(14)
C8-C9-H9A	109.5	C19-C18-C23	117.55(14)
C8-C9-H9B	109.5	C19-C18-B2	126.53(14)
H9A-C9-H9B	109.5	C23-C18-B2	115.76(13)
C8-C9-H9C	109.5	C20-C19-C18	120.81(14)
H9A-C9-H9C	109.5	C20-C19-H19	119.6
H9B-C9-H9C	109.5	C18-C19-H19	119.6
C8-C10-H10A	109.5	C19-C20-C21	120.70(14)
C8-C10-H10B	109.5	C19-C20-H20	119.7
H10A-C10-H10B	109.5	C21-C20-H20	119.7
C8-C10-H10C	109.5	C22-C21-C20	119.80(14)
H10A-C10-H10C	109.5	C22-C21-H21	120.1
H10B-C10-H10C	109.5	C20-C21-H21	120.1
C8-C11-H11A	109.5	C21-C22-C23	119.27(14)
C8-C11-H11B	109.5	C21-C22-H22	120.4
H11A-C11-H11B	109.5	C23-C22-H22	120.4
C8-C11-H11C	109.5	C22-C23-C18	121.74(14)
H11A-C11-H11C	109.5	C22-C23-C24	118.86(14)
H11B-C11-H11C	109.5	C18-C23-C24	119.15(13)
O2-C12-C13	127.46(14)	N2-C24-C23	123.07(14)
O2-C12-C17	110.75(13)	N2-C24-H24	115.2(10)
C13-C12-C17	121.75(14)	C23-C24-H24	121.5(10)
C12-C13-C14	117.26(14)	N2-C25-C28	107.83(12)
C12-C13-H13	121.4	N2-C25-C26	109.73(12)
C14-C13-H13	121.4	C28-C25-C26	110.69(13)
C15-C14-C13	120.85(14)	N2-C25-C27	106.29(12)

C28-C25-C27	111.89(13)	C33-C32-H32	119.6
C26-C25-C27	110.27(13)	C34-C33-C32	117.39(14)
C25-C26-H26A	109.5	C34-C33-H33	121.3
C25-C26-H26B	109.5	C32-C33-H33	121.3
H26A-C26-H26B	109.5	O6-C34-C33	127.86(14)
C25-C26-H26C	109.5	O6-C34-C29	110.47(12)
H26A-C26-H26C	109.5	C33-C34-C29	121.64(14)
H26B-C26-H26C	109.5	C7-N1-O1	122.04(12)
C25-C27-H27A	109.5	C7-N1-C8	126.12(13)
C25-C27-H27B	109.5	O1-N1-C8	111.63(11)
H27A-C27-H27B	109.5	C24-N2-O4	122.02(12)
C25-C27-H27C	109.5	C24-N2-C25	126.30(13)
H27A-C27-H27C	109.5	O4-N2-C25	111.54(11)
H27B-C27-H27C	109.5	N1-O1-B1	117.13(11)
C25-C28-H28A	109.5	C12-O2-B1	105.89(11)
C25-C28-H28B	109.5	C17-O3-B1	106.09(11)
H28A-C28-H28B	109.5	N2-O4-B2	117.95(11)
C25-C28-H28C	109.5	C29-O5-B2	105.95(11)
H28A-C28-H28C	109.5	C34-O6-B2	105.78(11)
H28B-C28-H28C	109.5	O3-B1-O2	106.10(12)
O5-C29-C30	128.04(13)	O3-B1-O1	104.67(12)
O5-C29-C34	110.70(12)	O2-B1-O1	108.29(12)
C30-C29-C34	121.24(14)	O3-B1-C1	118.59(13)
C29-C30-C31	117.47(14)	O2-B1-C1	111.59(12)
C29-C30-H30	121.3	O1-B1-C1	107.04(12)
C31-C30-H30	121.3	O5-B2-O6	105.89(12)
C32-C31-C30	121.39(14)	O5-B2-O4	103.74(11)
C32-C31-H31	119.3	O6-B2-O4	108.06(12)
C30-C31-H31	119.3	O5-B2-C18	119.27(13)
C31-C32-C33	120.85(14)	O6-B2-C18	111.97(12)
C31-C32-H32	119.6	O4-B2-C18	107.19(12)

Table A4. Anisotropic displacement parameters ($\text{\AA}^2 \times 10^3$) for **3.3**. The anisotropic

displacement factor exponent takes the form: $-2\pi^2 [h^2 a^{*2} U^{11} + \dots + 2 h k a^* b^* U^{12}]$

	U11	U22	U33	U23	U13	U12
C1	14(1)	17(1)	17(1)	-1(1)	7(1)	2(1)
C2	19(1)	18(1)	22(1)	-2(1)	9(1)	-3(1)
C3	16(1)	27(1)	20(1)	-6(1)	5(1)	-2(1)
C4	16(1)	30(1)	15(1)	0(1)	4(1)	2(1)
C5	16(1)	21(1)	20(1)	3(1)	6(1)	1(1)
C6	16(1)	18(1)	17(1)	-1(1)	5(1)	0(1)
C7	17(1)	16(1)	18(1)	2(1)	6(1)	1(1)
C8	14(1)	17(1)	21(1)	-1(1)	0(1)	-2(1)
C9	24(1)	33(1)	20(1)	-2(1)	2(1)	-7(1)
C10	17(1)	23(1)	42(1)	-6(1)	-1(1)	3(1)
C11	18(1)	22(1)	26(1)	2(1)	2(1)	-5(1)
C12	14(1)	16(1)	16(1)	1(1)	0(1)	-2(1)
C13	19(1)	16(1)	22(1)	-3(1)	5(1)	1(1)
C14	22(1)	25(1)	19(1)	-2(1)	8(1)	-4(1)
C15	24(1)	20(1)	19(1)	3(1)	5(1)	-3(1)
C16	19(1)	14(1)	21(1)	0(1)	4(1)	-1(1)
C17	14(1)	16(1)	16(1)	-1(1)	2(1)	-2(1)
C18	17(1)	16(1)	14(1)	2(1)	5(1)	-1(1)
C19	21(1)	18(1)	16(1)	-1(1)	6(1)	-2(1)
C20	19(1)	24(1)	16(1)	0(1)	3(1)	-5(1)
C21	14(1)	27(1)	16(1)	5(1)	3(1)	1(1)
C22	19(1)	18(1)	18(1)	3(1)	6(1)	3(1)
C23	16(1)	16(1)	16(1)	2(1)	5(1)	-1(1)
C24	16(1)	15(1)	17(1)	0(1)	5(1)	1(1)
C25	18(1)	18(1)	13(1)	-2(1)	1(1)	-1(1)
C26	29(1)	24(1)	22(1)	-7(1)	0(1)	3(1)
C27	28(1)	21(1)	16(1)	0(1)	4(1)	-2(1)
C28	23(1)	28(1)	21(1)	0(1)	1(1)	-7(1)

C29	14(1)	17(1)	12(1)	-2(1)	2(1)	-2(1)
C30	20(1)	14(1)	16(1)	-2(1)	3(1)	-2(1)
C31	18(1)	19(1)	21(1)	-5(1)	4(1)	2(1)
C32	18(1)	24(1)	20(1)	-4(1)	7(1)	-3(1)
C33	21(1)	17(1)	17(1)	-1(1)	4(1)	-4(1)
C34	16(1)	15(1)	13(1)	-2(1)	1(1)	1(1)
N1	16(1)	13(1)	18(1)	0(1)	4(1)	-1(1)
N2	18(1)	13(1)	16(1)	-1(1)	4(1)	1(1)
O1	18(1)	14(1)	22(1)	5(1)	2(1)	-2(1)
O2	22(1)	14(1)	17(1)	2(1)	6(1)	1(1)
O3	20(1)	15(1)	19(1)	2(1)	7(1)	1(1)
O4	20(1)	16(1)	16(1)	-2(1)	2(1)	6(1)
O5	16(1)	15(1)	18(1)	1(1)	6(1)	1(1)
O6	17(1)	13(1)	21(1)	2(1)	4(1)	1(1)
B1	16(1)	16(1)	20(1)	0(1)	4(1)	-1(1)
B2	18(1)	16(1)	16(1)	-1(1)	4(1)	-2(1)

Table A5. Hydrogen coordinates ($\times 10^4$) and isotropic displacement parameters ($\text{\AA}^2 \times 10^3$) for **3.3**.

	x	y	z	U(eq)
H2	2104	4421	7449	23
H3	2542	3341	8444	25
H4	2275	-51	8801	25
H5	1526	-2308	8177	22
H9A	8	-795	5442	39
H9B	-517	-2672	5376	39
H9C	208	-3297	5616	39
H10A	-633	355	6709	43
H10B	-1070	-650	6102	43
H10C	-592	1306	6066	43
H11A	72	-4913	6559	34
H11B	-667	-4493	6345	34
H11C	-276	-3561	6982	34
H13	2084	438	5164	23
H14	2117	3345	4480	25
H15	1717	6797	4613	25
H16	1275	7517	5436	22
H19	2503	1063	2847	22
H20	1488	2343	2441	24
H21	1171	5789	2722	23
H22	1859	7886	3456	21
H26A	3404	9910	4967	39
H26B	3682	9249	5659	39
H26C	3040	8170	5283	39
H27A	3476	4285	5501	33
H27B	4081	5440	5923	33
H27C	4156	3762	5404	33
H28A	4655	6471	4817	37

H28B	4719	8021	5397	37
H28C	4392	8946	4738	37
H30	4593	-2364	3692	20
H31	5499	-1741	3340	24
H32	5689	1683	2965	24
H33	4984	4645	2941	22
H7	735(8)	-2910(30)	7206(7)	19(4)
H24	2860(8)	8230(30)	4230(7)	21(4)

Table A6. Torsion angles [$^{\circ}$] for **3.3**.

C6-C1-C2-C3	1.1(2)	C19-C18-C23-C24	170.08(13)
B1-C1-C2-C3	-173.11(15)	B2-C18-C23-C24	-14.2(2)
C1-C2-C3-C4	1.5(2)	C22-C23-C24-N2	163.45(14)
C2-C3-C4-C5	-1.9(2)	C18-C23-C24-N2	-10.9(2)
C3-C4-C5-C6	-0.3(2)	O5-C29-C30-C31	179.25(13)
C4-C5-C6-C1	2.9(2)	C34-C29-C30-C31	1.1(2)
C4-C5-C6-C7	-172.14(14)	C29-C30-C31-C32	-1.5(2)
C2-C1-C6-C5	-3.3(2)	C30-C31-C32-C33	0.5(2)
B1-C1-C6-C5	171.50(14)	C31-C32-C33-C34	1.0(2)
C2-C1-C6-C7	171.78(13)	C32-C33-C34-O6	-179.04(13)
B1-C1-C6-C7	-13.4(2)	C32-C33-C34-C29	-1.4(2)
C5-C6-C7-N1	163.99(14)	O5-C29-C34-O6	-0.07(16)
C1-C6-C7-N1	-11.2(2)	C30-C29-C34-O6	178.35(12)
O2-C12-C13-C14	-178.47(14)	O5-C29-C34-C33	-178.10(12)
C17-C12-C13-C14	-1.0(2)	C30-C29-C34-C33	0.3(2)
C12-C13-C14-C15	0.6(2)	C6-C7-N1-O1	5.5(2)
C13-C14-C15-C16	0.3(2)	C6-C7-N1-C8	-168.59(13)
C14-C15-C16-C17	-0.8(2)	C11-C8-N1-C7	-1.5(2)
C15-C16-C17-O3	178.33(14)	C9-C8-N1-C7	-122.33(16)
C15-C16-C17-C12	0.3(2)	C10-C8-N1-C7	117.98(16)
O2-C12-C17-O3	0.09(17)	C11-C8-N1-O1	-176.10(12)
C13-C12-C17-O3	-177.73(13)	C9-C8-N1-O1	63.05(15)
O2-C12-C17-C16	178.45(13)	C10-C8-N1-O1	-56.65(15)
C13-C12-C17-C16	0.6(2)	C23-C24-N2-O4	7.4(2)
C23-C18-C19-C20	1.9(2)	C23-C24-N2-C25	-168.06(13)
B2-C18-C19-C20	-173.36(14)	C28-C25-N2-C24	-110.16(16)
C18-C19-C20-C21	1.2(2)	C26-C25-N2-C24	10.5(2)
C19-C20-C21-C22	-2.1(2)	C27-C25-N2-C24	129.71(15)
C20-C21-C22-C23	-0.1(2)	C28-C25-N2-O4	73.99(15)
C21-C22-C23-C18	3.3(2)	C26-C25-N2-O4	-165.37(12)
C21-C22-C23-C24	-170.94(14)	C27-C25-N2-O4	-46.15(15)
C19-C18-C23-C22	-4.1(2)	C7-N1-O1-B1	25.19(19)
B2-C18-C23-C22	171.62(13)	C8-N1-O1-B1	-159.94(12)

C13-C12-O2-B1	-177.73(15)	C6-C1-B1-O3	156.02(13)
C17-C12-O2-B1	4.61(16)	C2-C1-B1-O2	94.04(18)
C16-C17-O3-B1	176.98(15)	C6-C1-B1-O2	-80.25(16)
C12-C17-O3-B1	-4.80(16)	C2-C1-B1-O1	-147.64(14)
C24-N2-O4-B2	21.90(19)	C6-C1-B1-O1	38.07(17)
C25-N2-O4-B2	-162.04(12)	C29-O5-B2-O6	10.52(14)
C30-C29-O5-B2	174.95(14)	C29-O5-B2-O4	-103.15(12)
C34-C29-O5-B2	-6.77(15)	C29-O5-B2-C18	137.78(13)
C33-C34-O6-B2	-175.36(14)	C34-O6-B2-O5	-10.59(14)
C29-C34-O6-B2	6.77(15)	C34-O6-B2-O4	100.06(13)
C17-O3-B1-O2	7.36(15)	C34-O6-B2-C18	-142.12(12)
C17-O3-B1-O1	-107.05(12)	N2-O4-B2-O5	-169.16(11)
C17-O3-B1-C1	133.76(14)	N2-O4-B2-O6	78.74(15)
C12-O2-B1-O3	-7.31(15)	N2-O4-B2-C18	-42.10(16)
C12-O2-B1-O1	104.60(13)	C19-C18-B2-O5	-30.1(2)
C12-O2-B1-C1	-137.84(12)	C23-C18-B2-O5	154.65(13)
N1-O1-B1-O3	-171.40(11)	C19-C18-B2-O6	94.31(17)
N1-O1-B1-O2	75.75(15)	C23-C18-B2-O6	-80.98(16)
N1-O1-B1-C1	-44.70(16)	C19-C18-B2-O4	-147.35(14)
C2-C1-B1-O3	-29.7(2)	C23-C18-B2-O4	37.36(17)

A.2 REFERENCES

- (1) CrystalClear 1.40 (2008). Rigaku Americas Corporation, The Woodlands, TX.
- (2) SIR97. (1999). A program for crystal structure solution. Altomare, A., Burla, M. C., Camalli, M., Cascarano, G. L., Giacovazzo, C., Guagliardi, A., Moliterni, A. G. G., Polidori, G. and Spagna, R. *J. Appl. Cryst.* 32, 115-119.
- (3) Sheldrick, G. M. (2008). SHELXL97. Program for the Refinement of Crystal Structures. *Acta Cryst.*, A64, 112-122.
- (4) Spek, A. L. (1998). PLATON, A Multipurpose Crystallographic Tool. Utrecht University, The Netherlands.
- (5) WinGX 1.64. (1999). An Integrated System of Windows Programs for the Solution, Refinement and Analysis of Single Crystal X-ray Diffraction Data. Farrugia, L. J. *J. Appl. Cryst.* 32, 837-838.
- (6) $R_w(F^2) = \{\Sigma w(|F_o|^2 - |F_c|^2)^2 / \Sigma w(|F_o|^4)\}^{1/2}$ where w is the weight given each reflection.
 - a. $R(F) = \Sigma(|F_o| - |F_c|) / \Sigma |F_o|$ for reflections with $F_o > 4(\sigma(F_o))$.
 - b. $S = [\Sigma w(|F_o|^2 - |F_c|^2)^2 / (n - p)]^{1/2}$, where n is the number of reflections and p is the number of refined parameters.
- (7) International Tables for X-ray Crystallography (1992). Vol. C, Tables 4.2.6.8 and 6.1.1.4, A. J. C. Wilson, editor, Boston: Kluwer Academic Press.
- (8) Sheldrick, G. M. (1994). SHELXTL/PC (Version 5.03). Siemens Analytical X-ray Instruments, Inc., Madison, Wisconsin, USA.

References

- (1) Varshey, D. B.; Sander, J. R. G.; Friscic, T.; MacGillivray, L. R. Supramolecular Interactions. In *Supramolecular Chemistry: From Molecules to Nanomaterials*; Gale, P. A., Steed, J. W., Eds.; 2012; pp 9–24.
- (2) Nicolaou, K. C.; Sorensen, E. J. *Classics in Total Synthesis: Targets, Strategies, Methods*; VCH, 1996.
- (3) Corey, E. J. The Logic of Chemical Synthesis: Multistep Synthesis of Complex Carbogenic Molecules (Nobel Lecture). *Angewandte Chemie International Edition in English* **1991**, *30* (5), 455–465.
- (4) Steed, J. W.; Atwood, J. L.; Gale, P. A. Definition and Emergence of Supramolecular Chemistry. In *Supramolecular Chemistry: From Molecules to Nanomaterials*; Gale, P. A., Steed, J. W., Eds.; 2012; pp 3–8.
- (5) Gasparini, G.; Molin, M. D.; Lovato, A.; Prins, L. J. Dynamic Covalent Chemistry. In *Supramolecular Chemistry: From Molecules to Nanomaterials*; Gale, P. A., Steed, J. A., Eds.; 2012; pp 1497–1526.
- (6) Lorand, J. P.; Edwards, J. O. Polyol Complexes and Structure of the Benzeneboronate Ion. *The Journal of Organic Chemistry* **1959**, *24* (6), 769–774.
- (7) Bull, S. D.; Davidson, M. G.; van den Elsen, J. M. H.; Fossey, J. S.; Jenkins, A. T. A.; Jiang, Y.-B.; Kubo, Y.; Marken, F.; Sakurai, K.; Zhao, J.; et al. Exploiting the Reversible Covalent Bonding of Boronic Acids: Recognition, Sensing, and Assembly. *Accounts of chemical research* **2013**, *46* (2), 312–326.
- (8) James, T. D.; Samankumara Sandanayake, K. R. A.; Shinkai, S. Chiral Discrimination of Monosaccharides Using a Fluorescent Molecular Sensor. *Nature* **1995**, *374* (6520), 345–347.
- (9) Corbett, P. T.; Leclaire, J.; Vial, L.; West, K. R.; Wietor, J.-L.; Sanders, J. K. M.; Otto, S. Dynamic Combinatorial Chemistry. *Chemical Reviews* **2006**, *106* (9), 3652–3711.
- (10) Li, J.; Nowak, P.; Otto, S. Dynamic Combinatorial Libraries: From Exploring Molecular Recognition to Systems Chemistry. *Journal of the American Chemical Society* **2013**, *135* (25), 9222–9239.
- (11) Wojtecki, R. J.; Meador, M. A.; Rowan, S. J. Using the Dynamic Bond to Access Macroscopically Responsive Structurally Dynamic Polymers. *Nature Materials* **2011**, *10* (1), 14–27.
- (12) Michal, B. T.; Jaye, C. A.; Spencer, E. J.; Rowan, S. J. Inherently Photohealable and Thermal Shape-Memory Polydisulfide Networks. *ACS Macro Letters* **2013**, *2* (8), 694–699.

- (13) Von Delius, M.; Geertsema, E. M.; Leigh, D. A. These Molecules Are Made for Walking: A Synthetic Small Molecule That Can Walk down a Track. *Nature Chemistry* **2010**, *2* (2), 96–101.
- (14) Bandyopadhyay, A.; Gao, J. Targeting Biomolecules with Reversible Covalent Chemistry. *Current Opinion in Chemical Biology* **2016**, *34*, 110–116.
- (15) Ray, P. D.; Huang, B.-W.; Tsuji, Y. Reactive Oxygen Species (ROS) Homeostasis and Redox Regulation in Cellular Signaling. *Cellular Signalling* **2012**, *24*, 981–990.
- (16) Schieber, M.; Chandel, N. S. Review ROS Function in Redox Signaling and Oxidative Stress. *CURBIO* **2014**, *24*, R453–R462.
- (17) Chen, X.; Tian, X.; Shin, I.; Yoon, J. Fluorescent and Luminescent Probes for Detection of Reactive Oxygen and Nitrogen Species. *Chemical Society Reviews* **2011**, *40* (9), 4783.
- (18) Furchgott, R. F.; Zawadzki, J. V. The Obligatory Role of Endothelial Cells in the Relaxation of Arterial Smooth Muscle by Acetylcholine. *Nature* **1980**, *288* (5789), 373–376.
- (19) Ignarro, L. J.; Byrns, R. E.; Buga, G. M.; Wood, K. S. Endothelium-Derived Relaxing Factor from Pulmonary Artery and Vein Possesses Pharmacologic and Chemical Properties Identical to Those of Nitric Oxide Radical. *Circulation research* **1987**, *61* (6), 866–879.
- (20) Förstermann, U.; Sessa, W. C. Nitric Oxide Synthases: Regulation and Function. *European heart journal* **2012**, *33* (7), 829–37, 837a–837d.
- (21) Singh, S.; Gupta, A. K. Nitric Oxide: Role in Tumour Biology and iNOS/NO-Based Anticancer Therapies. *Cancer Chemotherapy and Pharmacology* **2011**, *67* (6), 1211–1224.
- (22) Kojima, H.; Urano, Y.; Kikuchi, K.; Higuchi, T.; Hirata, Y.; Nagano, T. Fluorescent Indicators for Imaging Nitric Oxide Production. *Angewandte Chemie International Edition* **1999**, *38* (21), 3209–3212.
- (23) Franz, K. J.; Singh, N.; Lippard, S. J. Metal-Based NO Sensing by Selective Ligand Dissociation. *Angewandte Chemie International Edition* **2000**, *39* (12), 2120–2122.
- (24) Yang, Y.; Seidlits, S. K.; Adams, M. M.; Lynch, V. M.; Schmidt, C. E.; Anslyn, E. V.; Shear, J. B. A Highly Selective Low-Background Fluorescent Imaging Agent for Nitric Oxide. *Journal of the American Chemical Society* **2010**, *132* (38), 13114–13116.
- (25) Corvaja, C. Introduction to Electron Paramagnetic Resonance. In *Electron Paramagnetic Resonance: A Practitioner's Toolkit*; Brustolon, M., Giamello, E., Eds.; 2009; pp 3–35.

- (26) Wikipedia: The Free Encyclopedia. Electron Paramagnetic Resonance https://en.wikipedia.org/wiki/Electron_paramagnetic_resonance (accessed Sep 6, 2016).
- (27) Hofer, P. Basic Experimental Methods in Continuous Wave Electron Paramagnetic Resonance. In *Electron Paramagnetic Resonance: A Practitioner's Toolkit*; Brustolon, M., Giamello, E., Eds.; 2009; pp 37–82.
- (28) Bowman, M. K. Pulsed Electron Paramagnetic Resonance. In *Electron Paramagnetic Resonance: A Practitioner's Toolkit*; Brustolon, M., Giamello, E., Eds.; 2009; pp 159–194.
- (29) Gescheidt, G. EPR Spectroscopy in the Liquid Phase. In *Electron Paramagnetic Resonance: A Practitioner's Toolkit*; Brustolon, M., Giamello, E., Eds.; 2009; p 128.
- (30) Alberti, A.; Macciantelli, D. Spin Trapping. In *Electron Paramagnetic Resonance: A Practitioner's Toolkit*; Brustolon, M., Giamello, E., Eds.; 2009; pp 287–323.
- (31) Hogg, N. Detection of Nitric Oxide by Electron Paramagnetic Resonance Spectroscopy. *Free radical biology & medicine* **2010**, *49* (2), 122–129.
- (32) Tickell, D. A.; Mahon, M. F.; Bull, S. D.; James, T. D. A Simple Protocol for NMR Analysis of the Enantiomeric Purity of Chiral Hydroxylamines. *Organic letters* **2013**, *15* (4), 860–863.
- (33) Pohjakallio, A.; Pihko, P. M. Enantioselective Synthesis of 2-Isoxazolines by a One-Flask Conjugate Addition/Oxime-Transfer Process. *Chemistry - A European Journal* **2009**, *15* (16), 3960–3964.
- (34) Kurtzweil, M. L.; Loo, D.; Beak, P. The Endocyclic Restriction Test: Determination of the Transition-Structure Geometry for the Transfer of Oxygen from N,N-Dialkylhydroxylamines to Triarylphosphines. *Journal of the American Chemical Society* **1993**, *115* (2), 421–427.
- (35) Ji, M.; Zhen, J.; Zhang, Q.; Chen, Y. Photolysis of N-Butyl Nitrite and Isoamyl Nitrite at 355 Nm: A Time-Resolved Fourier Transform Infrared Emission Spectroscopy and Ab Initio Study. *The Journal of chemical physics* **2009**, *130* (17), 174314.
- (36) Brisset, J.-L.; Pawlat, J. Chemical Effects of Air Plasma Species on Aqueous Solutes in Direct and Delayed Exposure Modes: Discharge, Post-Discharge and Plasma Activated Water. *Plasma Chemistry and Plasma Processing* **2016**, *36*, 355–381.
- (37) Sletten, E. M.; Bertozzi, C. R. From Mechanism to Mouse: A Tale of Two Bioorthogonal Reactions. *Accounts of Chemical Research* **2011**, *44* (9), 666–676.
- (38) Sahoo, H. Fluorescent Labeling Techniques in Biomolecules: A Flashback. *RSC Advances* **2012**, *2* (18), 7017.

- (39) Lang, K.; Chin, J. W. Bioorthogonal Reactions for Labeling Proteins. *ACS chemical biology* **2014**, *9* (1), 16–20.
- (40) Patterson, D. M.; Prescher, J. A. Orthogonal Bioorthogonal Chemistries. *Current Opinion in Chemical Biology* **2015**, *28*, 141–149.
- (41) Dean, K. M.; Palmer, A. E. Advances in Fluorescence Labeling Strategies for Dynamic Cellular Imaging. *Nature Chemical Biology* **2014**, *10* (7), 512–523.
- (42) Wikipedia: The Free Encyclopedia. DAPI <https://en.wikipedia.org/wiki/DAPI> (accessed Sep 23, 2016).
- (43) Hong, V.; Steinmetz, N. F.; Manchester, M.; Finn, M. G. Labeling Live Cells by Copper-Catalyzed Alkyne–Azide Click Chemistry. *Bioconjugate chemistry* **2010**, *21* (10), 1912–1916.
- (44) Agard, N. J.; Prescher, J. A.; Bertozzi, C. R. A Strain-Promoted [3 + 2] Azide–Alkyne Cycloaddition for Covalent Modification of Biomolecules in Living Systems. **2004**.
- (45) van Berkel, S. S.; van Eldijk, M. B.; van Hest, J. C. M. Staudinger Ligation as a Method for Bioconjugation. *Angewandte Chemie (International ed. in English)* **2011**, *50* (38), 8806–8827.
- (46) Rashidian, M.; Song, J. M.; Pricer, R. E.; Distefano, M. D. Chemoenzymatic Reversible Immobilization and Labeling of Proteins without Prior Purification. *Journal of the American Chemical Society* **2012**, *134* (20), 8455–8467.
- (47) Patterson, D. M.; Nazarova, L. A.; Prescher, J. A. Finding the Right (Bioorthogonal) Chemistry. *ACS Chemical Biology* **2014**, *9* (3), 592–605.
- (48) Ramil, C. P.; Lin, Q.; Shimomura, O.; Johnson, F. H.; Saiga, Y.; Tsien, R. Y.; Giepmans, B. N. G.; Adams, S. R.; Ellisman, M. H.; Tsien, R. Y.; et al. Bioorthogonal Chemistry: Strategies and Recent Developments. *Chemical Communications* **2013**, *49* (94), 11007.
- (49) Collins, B. E.; Metola, P.; Anslyn, E. V. On the Rate of Boronate Ester Formation in Ortho-Aminomethyl Functionalized Phenyl Boronic Acids. *Supramolecular chemistry* **2013**, *25* (2), 79–86.
- (50) Lorand, J. P.; Edwards, J. O. Polyol Complexes and Structure of the Benzeneboronate Ion. *The Journal of Organic Chemistry* **1959**, *24* (6), 769–774.
- (51) Bull, S. D.; Davidson, M. G.; van den Elsen, J. M. H.; Fossey, J. S.; Jenkins, A. T. A.; Jiang, Y.-B.; Kubo, Y.; Marken, F.; Sakurai, K.; Zhao, J.; et al. Exploiting the Reversible Covalent Bonding of Boronic Acids: Recognition, Sensing, and Assembly. *Accounts of chemical research* **2013**, *46* (2), 312–326.
- (52) Xu, X.-D.; Cheng, H.; Chen, W.-H.; Cheng, S.-X.; Zhuo, R.-X.; Zhang, X.-Z. In Situ Recognition of Cell-Surface Glycans and Targeted Imaging of Cancer Cells.

Scientific reports **2013**, *3*, 2679.

- (53) Nishiyabu, R.; Kubo, Y.; James, T. D.; Fossey, J. S. Boronic Acid Building Blocks: Tools for Self Assembly. *Chemical communications (Cambridge, England)* **2011**, *47* (4), 1124–1150.
- (54) Pérez-Fuertes, Y.; Kelly, A. M.; Johnson, A. L.; Arimori, S.; Bull, S. D.; James, T. D. Simple Protocol for NMR Analysis of the Enantiomeric Purity of Primary Amines. *Organic letters* **2006**, *8* (4), 609–612.
- (55) Schmidt, P.; Stress, C.; Gillingham, D.; Patterson, D. M.; Nazarova, L. A.; Prescher, J. A.; Saito, F.; Noda, H.; Bode, J. W.; Blackman, M.; et al. Boronic Acids Facilitate Rapid Oxime Condensations at Neutral pH. *Chem. Sci.* **2015**, *6* (6), 3329–3333.
- (56) Alfonta, L.; Zhang, Z.; Uryu, S.; Loo, J. A.; Schultz, P. G. Site-Specific Incorporation of a Redox-Active Amino Acid into Proteins. *Journal of the American Chemical Society* **2003**, *125* (48), 14662–14663.
- (57) Albers, A. E.; Okreglak, V. S.; Chang, C. J. A FRET-Based Approach to Ratiometric Fluorescence Detection of Hydrogen Peroxide. *Journal of the American Chemical Society* **2006**, *128* (30), 9640–9641.
- (58) Kolb, H. C.; Finn, M. G.; Sharpless, K. B. Click Chemistry: Diverse Chemical Function from a Few Good Reactions. *Angewandte Chemie International Edition* **2001**, *40* (11), 2004–2021.
- (59) Rostovtsev, V. V.; Green, L. G.; Fokin, V. V.; Sharpless, K. B. A Stepwise Huisgen Cycloaddition Process: Copper(I)-Catalyzed Regioselective “Ligation” of Azides and Terminal Alkynes. *Angewandte Chemie International Edition* **2002**, *41* (14), 2596–2599.
- (60) Cravotto, G.; Cintas, P.; Leonelli, C.; Mason, T. J.; Bang, J. H.; Suslick, K. S.; Mahamuni, N. N.; Adewuyi, Y. G.; Brenner, M. P.; Hilgenfeldt, S.; et al. Harnessing Mechanochemical Effects with Ultrasound-Induced Reactions. *Chem. Sci.* **2012**, *3* (2), 295–307.
- (61) Brantley, J. N.; Konda, S. S. M.; Makarov, D. E.; Bielawski, C. W. Regiochemical Effects on Molecular Stability: A Mechanochemical Evaluation of 1,4- and 1,5-Disubstituted Triazoles. *Journal of the American Chemical Society* **2012**, *134* (24), 9882–9885.
- (62) Kwart, H.; King, K. The Reverse Diels-Alder or Retrodiene Reaction. *Chemical Reviews* **1968**, *68* (4), 415–447.
- (63) Gandini, A. The Furan/maleimide Diels–Alder Reaction: A Versatile Click–unclick Tool in Macromolecular Synthesis. *Progress in Polymer Science* **2013**, *38* (1), 1–29.
- (64) Bielski, R.; Witczak, Z. Strategies for Coupling Molecular Units If Subsequent

- Decoupling Is Required. *Chemical Reviews* **2013**, *113* (3), 2205–2243.
- (65) Joshi, G.; Anslyn, E. V. Dynamic Thiol Exchange with β -Sulfido- α,β -Unsaturated Carbonyl Compounds and Dithianes. *Organic Letters* **2012**, *14* (18), 4714–4717.
- (66) Huang, X.; Chen, B. Synthesis of Bisalkylthiolydine Derivatives of Meldrum's Acid and Barbituric Acid. *Synthesis* **1986**, *1986* (11), 967–968.
- (67) Anslyn, E. V.; Dougherty, D. A. *Modern Physical Organic Chemistry*; University Science Books, 2006.
- (68) Raj, L.; Ide, T.; Gurkar, A. U.; Foley, M.; Schenone, M.; Li, X.; Tolliday, N. J.; Golub, T. R.; Carr, S. a; Shamji, A. F.; Stern, A. M.; Mandinova, A.; Schreiber, S. L.; Lee, S. W. *Nature* **2011**, *475*, 231–4.
- (69) Chatterjee, A; Dutta, C. P. *Tetrahedron* **1967**, *23*, 1769–1781.
- (70) Trachootham, D.; Alexandre, J.; Huang, P. *Nature reviews. Drug discovery* **2009**, *8*, 579–91.
- (71) Armstrong, J. S.; Steinauer, K. K.; Hornung, B.; Irish, J. M.; Lecane, P.; Birrell, G. W.; Peehl, D. M.; Knox, S. J. Role of Glutathione Depletion and Reactive Oxygen Species Generation in Apoptotic Signaling in a Human B Lymphoma Cell Line. *Cell Death and Differentiation* **2002**, *9* (3), 252–263.
- (72) Liou, G.-Y.; Storz, P. Reactive Oxygen Species in Cancer. *Free radical research* **2010**, *44* (5), 479–496.
- (73) Adams, D. J.; Dai, M.; Pellegrino, G.; Wagner, B. K.; Stern, A. M.; Shamji, A. F.; Schreiber, S. L. *PNAS* **2012**, *109*, 15115–20.
- (74) Boll, P.M., Hansen, J., Simonsen, O. *Tetrahedron* **1984**, *40*, 171–175.
- (75) Yu, M.; Gao, Y. Process for preparation of piperlongumine and analogues. *Faming Zhuanli Shenqing* **2010**, 10pp.
- (76) Bezerra, D. P.; Pessoa, C.; De Moraes, M. O.; Saker-Neto, N.; Silveira, E. R.; Costa-Lotufo, L. V *European journal of pharmaceutical sciences* **2013**, *48*, 453–463.
- (77) Winter, D. K.; Drouin, A.; Lessard, J.; Spino, C. *The Journal of organic chemistry* **2010**, *75*, 2610–8.
- (78) Gutekunst, W. R.; Baran, P. S. *Journal of the American Chemical Society* **2011**, *133*, 19076–9.
- (79) Sibi, M. P.; Prabakaran, N.; Ghorpade, S. G.; Jasperse, C. P. *Journal of the American Chemical Society* **2003**, *125*, 11796–11797.
- (80) CrystalClear 1.40 (2008). Rigaku Americas Corporation, The Woodlands, TX.

- (81) SIR97. (1999). A program for crystal structure solution. Altomare, A., Burla, M. C., Camalli, M., Cascarano, G. L., Giacovazzo, C., Guagliardi, A., Moliterni, A. G. G., Polidori, G. and Spagna, R. *J. Appl. Cryst.* 32, 115-119.
- (82) Sheldrick, G. M. (2008). SHELXL97. Program for the Refinement of Crystal Structures. *Acta Cryst.*, A64, 112-122.
- (83) Spek, A. L. (1998). PLATON, A Multipurpose Crystallographic Tool. Utrecht University, The Netherlands.
- (84) WinGX 1.64. (1999). An Integrated System of Windows Programs for the Solution, Refinement and Analysis of Single Crystal X-ray Diffraction Data. Farrugia, L. J. *J. Appl. Cryst.* 32. 837-838.
- (85) International Tables for X-ray Crystallography (1992). Vol. C, Tables 4.2.6.8 and 6.1.1.4, A. J. C. Wilson, editor, Boston: Kluwer Academic Press.
- (86) Sheldrick, G. M. (1994). SHELXTL/PC (Version 5.03). Siemens Analytical X-ray Instruments, Inc., Madison, Wisconsin, USA.